DISS. ETH NO. 24081

Thermal evolution of crustal-scale thrust zones in three collisional mountain regions: geospeedometry of inverted metamorphic gradients

A thesis submitted to attain the degree of

DOCTOR OF SCIENCES of ETH ZURICH

(Dr. sc. ETH Zurich)

presented by

STEFANIA CIOLDI

M.Sc. in Earth Science, ETH Zürich

born on 27.06.1983

citizen of Faido (TI), Switzerland

accepted on the recommendation of

Prof. Dr. Jean-Pierre Burg	ETH Zürich	examiner
Prof. Dr. Lucie Tajcmanová	ETH Zürich	co-examiner
Prof. Dr. Mark J. Caddick	Virginia Tech, USA	external examiner

2017

ALLA MIA FAMIGLIA

Contents

Abstract

Inverted Barrovian metamorphic sequences are reported to be one of the major consequences of syn-metamorphic ductile thrust zones. They have been observed and investigated in tectonic settings ranging from continent-continent collision (e.g. Kokchetav Massif (Kazakhstan), Great Caucasus (Russia), Yukon-Tanana (Canada), Massif Central (France), Alps (Switzerland), Alpine fault (New Zealand), Scandinavian Caledonides and Appalachians (U.S.)), to subduction zones (e.g. western Cordillera (U.S.), Shuksan Suite (North Cascades, NW U.S.) and Franciscan Complex (Coast Ranges, California, U.S.)). Despite advances in numerical models, kinematic simulations and interpretations explaining metamorphic inversion, limited agreement concerning the origin and the nature of metamorphic heat in collisional settings persists. The duration of peak metamorphic conditions should help deciphering tectonic processes active during metamorphism and orogenesis.

Three major ductile thrust faults with inverted metamorphic zonation have been studied following similar procedures and are presented separately: the Nestos Thrust Zone in the Rhodope Metamorphic Complex (Northern Greece), the Main Central Thrust in Sikkim Himalaya (NE India) and the inverted sequence of the Champtoceaux Complex, Armorican Massif (France). Considering different geological settings active at different times allows defining whether thermo-mechanical processes responsible for metamorphic inversion are limited to a local/regional interpretation or can be applied to other collisional systems.

Structures, pressure and temperature (*P*-*T*) conditions across the thrust zones, duration of peak-*T* conditions, links between mechanical and thermal evolution and considerations on the nature and origin of orogenic heat responsible for isograds inversion were evaluated combining detailed structural, petrological, geochemical, geochronological and geospeedometry investigations.

Garnet compositional zoning developed by fractionation and intracrystalline diffusion preserves quantitative records of pressure-temperature-time (*P*-*T*-*t*) history of metamorphic rocks. Durations of thermal peak were quantified applying: 1) inverse-fitting multicomponent (Fe – Mg – Ca – Mn) Fractionation and Diffusion in Garnet (FRIDGE) numerical model of smoothed garnet compositional profiles; 2) simple initial step function model of well-defined compositional discontinuities and/or complex garnet zoning patterns reflecting multiple metamorphic equilibrations. FRIDGE model of extensively diffused garnets, gives information about the prograde metamorphic path experienced by the rock and does not underestimate the duration of diffusion.

The Nestos Thrust is interpreted as Late Jurassic – Early Cretaceous suture zone, with top-to-SW shearing, separating the high-amphibolite facies Imbricate Terrane in the hanging wall from the greenschist to lower-amphibolite facies Lower Terrane in the footwall. U-Pb SHRIMP dating revealed

Late Jurassic – Early Cretaceous (*c*. 142 Ma) peak metamorphic conditions, Eocene granitoids intrusions in the Sidironero region and Late Eocene (*c*. 35 Ma) cooling on regional scale.

The inverted metamorphic zonation in Sikkim Lesser Himalaya (LH), associated with the Main Central Thrust (MCT), is confined in a relatively narrow (*c*. 5 km thick) zone parallel to the thrust. Phase equilibria modelling revealed inverted thermal isograds and normal pressure gradients moving upwards in the LH footwall toward the MCT. Zircon SHRIMP ages inferred Early- Middle Miocene (between 18 and 15 Ma) peak metamorphic conditions simultaneous with partial melting of magmatic and sedimentary rocks near the MCT.

The Champtoceaux Complex is interpreted as a segment of the Variscan suture zone of the collision between Laurussia and Gondwana continents. The inverted metamorphic sequence is localized at the contact between the Lower- and the Upper Allochthon. Phase equilibria modelling revealed an increase of temperature (*c*. 100 °C) and relatively uniform pressure conditions across *c*. 3 km thick pile of rocks.

Short-lived (from < 1 to 6 Ma) peak temperature conditions were recorded in the three investigated thrust zones applying both FRIDGE and simple step function models.

Considering similar metamorphic structures in the studied thrust zones, i.e. normal/nearly uniform pressures but inverted temperature gradients in the footwalls, the 1 to 3 km thick high grade zones parallel to the ductile thrusts and the transient duration of peak thermal pulse(s), viscous/shear-heating is deduced as a possible heat source responsible for temperature increase of 100 °C along the thrust and subsequent metamorphic inversion.

Riassunto

La zonazione inversa delle facies metamorfiche è considerata una delle principali conseguenze della tettonica di sovrascorrimento. Queste zone, dove gli elementi strutturali più elevati presentano un grado metamorfico maggiore, sono state osservate e studiate in contesti tettonici che variano da collisioni intra-continentali (ad esempio il massiccio di Kokchetav in Kazakistan, il Caucaso, lo Yukon-Tanana in Canada, il Massiccio Centrale in Francia, le Alpi svizzers, la falia Alpina in Nuova Zelanda, la Caledonia scandinava e gli Appalachi negli USA), a zone di subduzione (ad esempio la Cordillera occidentale degli USA, lo Shuksan Suite, North Cascades negli USA e il complesso di Franciscan in California). Nonostante i progressi nella modelizzazione numerica, le simulazioni geo-cinematiche e le interpretazioni mirate a spiegare l'inversione delle isograde, non è ancora stato raggiunto un accordo nel determinare la natura e l'origine del calore necessari per sviluppare una zona metamorfica inversa. Stimando la durata del picco termico, si possono stimare e meglio comprendere i processi tettonici attivi durante il metamorfismo ed orogenesi.

Tre falie sovrascorrenti con zonazione metamorfica invertita sono state studiate seguendo simili procedure e presentate separatamente: la falia di Nestos (*Nestos Thrust Zone*) nel complesso metamorfico di Rhodope (Grecia del nord), la falia principale centrale (*Main Central Thrust*) in Sikkim Himalaya (nord-est India) e la sequenza invertita nel complesso di Champtoceaux nel Massiccio armoricano (Francia). Il considerare sistemi tectonici diveresi attivi in tempi differenti permette di determinare se i processi termo-meccanici responsabili dell'inversione metamorfica sono limitati ad una interpretazione locale/regionale o possono essere applicati ad altri sistemi collisionali.

Le strutture, le condizioni di pressione e temperatura (*P-T*) nelle zone di sovrascorrimento, la durata del picco termico, le relazioni termo-meccaniche e considerazioni sulla natura ed origine del calore responsabile dell'inversione delle insograde, sono stati determinati combinando studi dettagliati sulle strutture, la petrologia, la geochimica, la geocronologia e la geospeedometria.

La zonatura composizionale dei granati, sviluppatasi durante la cristalizzazione e modificatasi per diffusione intracristallina, conserva informazioni quantitative sulle condizioni di pressione-temperatura-tempo (*P-T-t*) a cui le rocce metamorfiche sono state sottoposte. La durata del picco termico è stata quantificata applicando le seguenti tecniche: 1) il modello numerico FRIDGE, che genera profili composizionali computando il frazionamento e la diffusione dei cationi principali (Fe - Mg - Ca - Mn) di granati i cui profili sono estensivamente diffusi; 2) il modello dello "step" composizionale è stato applicato su granati in cui le discontinuità composizionali sono ben definite e/o presentano una zonazione complessa che rispecchia più stadi di equilibrio metamorfico. Il modello FRIDGE applicato a granati ampiamente diffusi, fornisce informazioni sul metamorfismo progrado subito dalla roccia e non sottovaluta la durata di diffusione.

La *Nestos Thrust Zone* è interpretata quale zona di sutura del Giurassico superiore e Cretaceo inferiore, con scorrimento top-to-SO, che separa le facies amphibolitche superiori del *Imbricate Terrane* nel hangingwall, dalle facies scisti verdi ad amfiboliti inferioni del *Lower Terrane* nel footwall. Le datazioni U-Pb SHRIMP hanno rivelato il picco del metamorpfismo durante il Giurassico e il Cretaceo inferiore (*c*. 142 Ma.), intrusioni di granitoidi nella regione Sidironero nel Eocene, e raffreddamento su scala regionale durante il tardo Eocene (*c*. 35 Ma).

La zonazione metamorfica inversa, osservata nell'unità *Lesser Himalaya* (LH) in Sikkim e associata al *Main Centra Thrust* (MCT), è confinata ad una zona ristretta (*c*. 5 km di spessore) parallela alla falia principale. *P-T* pseudosections hanno rivelato isograde termiche invertite e gradienti di pressione normali ascendendo il footwall LH verso la MCT. Gli zirconi datati con la SHRIMP indicano condizioni di picco del metamorfismo contemporaneo alla fusione parziale delle rocce magmatiche e sedimentarie nei pressi del MCT, durante il Miocene inferiore-centrale (tra i 18 e 15 Ma).

Il complesso di Champtoceaux è interpretato come un segmento della zona di sutura Varistica formatasi dalla collisione dei continenti Laurussia e Gondwana. La sequenza metamorfica invertita è localizzata al contatto tra il *Lower*- ed il *Upper Allochthon*. *P-T* pseudosection hanno rivelato un aumento di temperatura (*c*. 100 ° C) e pressione relativamente uniformi attraverso *c*. 3 km di spessore di rocce.

Le tre zone di sovrascorrimento studiate, applicando entrambe le tecniche di geospeedometria dello "step" composizinale e FRIDGE, indicano che le condizioni di picco termico sono di breve durata (da <1 a 6 Ma). Considerando le simili strutture metamorfiche, il gradiente normale/quasi uniforme di pressione, i gradienti di temperatura invertiti nelle footwalls, le zone di alto grado metamorfico confinate in 1 - 3 km di spessore parallele alla falia e la durata transitoria del picco termico, il riscaldamento di frizione evince come possibile fonte di calore responsabile dell'aumento delle condizioni di temperatura di 100 °C lungo le falie di sovrascorrimento e susseguente inversione metamorfica.

1. Introduction

Large-scale, dynamic geological processes such as continent-continent collision, subduction and ocean floor spreading are the cause of rock displacement and metamorphic reactions. During metamorphism, changes in pressure and temperature conditions trigger chemical reactions and modifications in phase stability, mineral composition and fabrics and are prime causes of metamorphism. Field observations and identification of metamorphic grade are first approaches for interpreting the tectonic evolution within crystalline terranes.

Portraying the changes in metamorphic grade is one of the main objectives of petrographical and lithological mapping. Places of equal metamorphic intensity are delimited with isograd (iso - equal, grad - grade) lines that separate metamorphic zones with different mineral assemblages. The principle of appearance (or disappearance) of particular index minerals to document metamorphic gradients was introduced by George Barrow (1893, 1912) in pelitic rocks of the Scottish Highlands (e.g. Bucher and Grapes, 2011, p. 120). The *Barrovian* (aka Intermediate Pressure) *sequence* in metapelitic rocks is characterized by the successive occurrence of chlorite – biotite – garnet – staurolite – kyanite – sillimanite. Barrow (1893) explained regional metamorphism as the thermal effect of a granitic intrusion, what is now called *contact metamorphism* (e.g. Winter, 2011, p. 424). The term of metamorphic grade was first introduced by Tilley (1924) who emphasized that the diversity in mineral composition of metamorphic rocks results from two independent variables: the rock composition and the grade of metamorphism, more specifically the particular pressure-temperature (P-T) conditions under which rocks have recrystallized (Tilley, 1924). As explained in Bucher and Grapes in the early twentieth century (2011, p. 119) P-T quantification was not reliable and temperature was considered to be the most important factor of metamorphism. For this reason, the metamorphic grade was often equated/confused with the thermal gradient. Eskola (1915, 1920, 1939), developed and improved the concept of *metamorphic facies* on the basis of relationships between rock composition and distinctive mineral assemblage in metabasic rocks. Since then, several additional facies and sub-facies have been proposed, reaching a general agreement for pressure and temperature limits (Fig. 1.1).

Today, the most important variables in rock metamorphism are attributed to variations in temperature, pressure and fluid content during large-scale tectono-thermal processes.

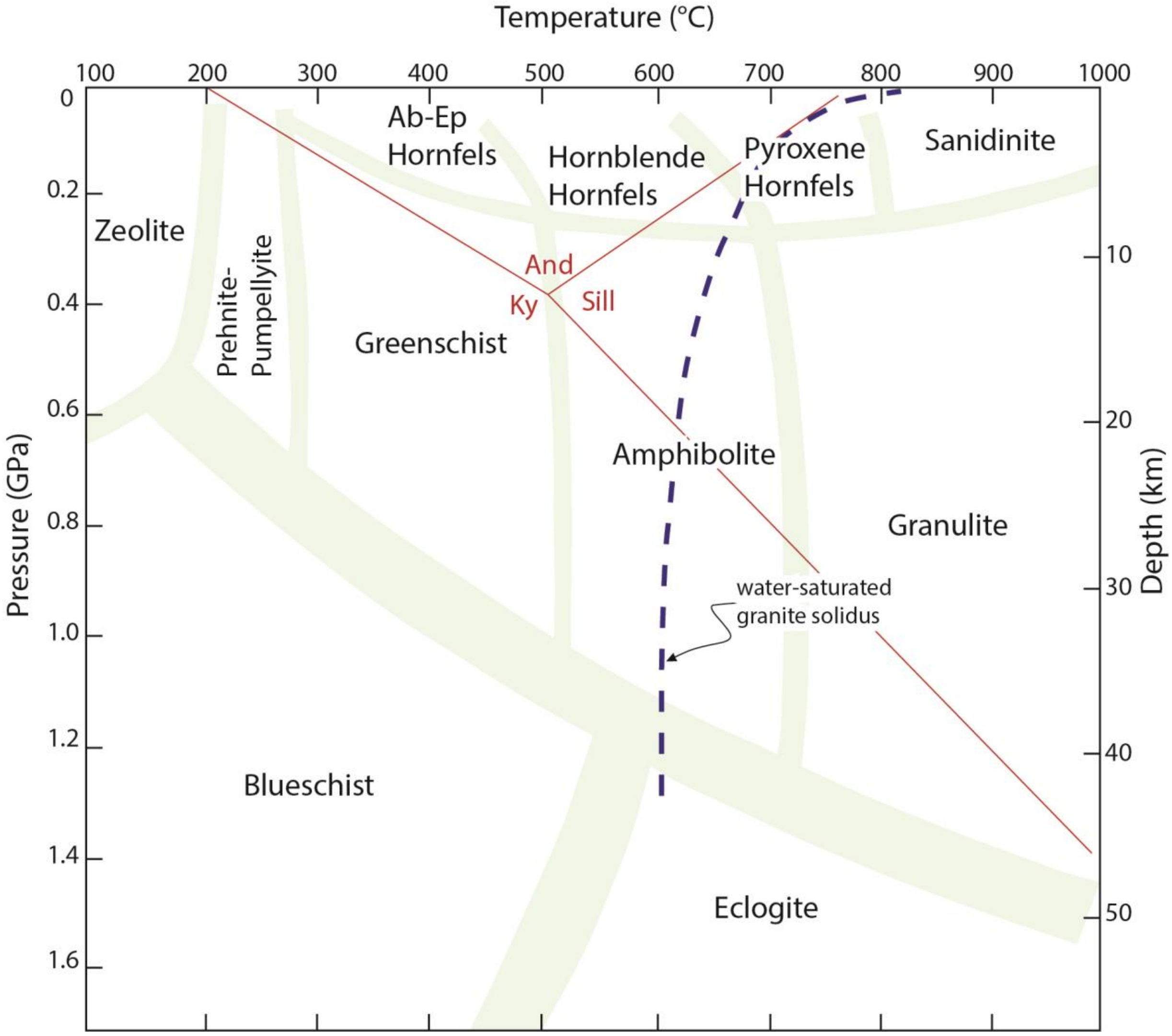

Figure 1.1. Pressure-temperature (*P*-*T*) diagram showing the generally accepted limits of the various metamorphic facies (modified *from Winter, 2010*). Mineral abbreviations after Kretz (1983).

1.1 Inverted metamorphic isograds

The phenomenon in which the metamorphic zones decrease in grade with structural depth is called *inverted metamorphic sequence*. Inverted Barrovian metamorphic isograds are reported to be one of the major consequences of large and possibly fast movements on syn-metamorphic thrust zones (Le Fort, 1975; Graham and England, 1976, England and Molnar, 1993). These thrust zones placed high grade over lower grade rocks (e.g. Tilley, 1925; Gansser, 1964; Le Fort, 1975; Burg *et al*., 1984, 1989; Searle and Rex, 1988, 1989; Cogné, 1990; England *et al.,* 1992; England and Molnar, 1993; Pitra *et al*., 2010) and occur in tectonic settings ranging from continent-continent collision (Andreasson and Lagerblad, 1980) to subduction zones (Peacock, 1987). Many thrust regions are several kilometres thick shear zones in which it is difficult to determine how dissipative heat sources were distributed when they were active (England and Molnar, 1993). Considering simple physical calculations, England and Molnar (1993) argued that several examples of inverted metamorphic gradients cannot be explained simply by the thrusting of hot over cold rocks without heat sources in the fault zone.

The most spectacular example of inverted metamorphic sequence is in the Himalayas across the Main Central Thrust (MCT; Frank *et al.*, 1973; Le Fort, 1975). The inverted isograds are mapped for more than 2200 km along the orogenic belt (e.g. Vannay and Grasemann, 2001) suggesting that some first-order process controlled this phenomena. Intensive efforts during the past decades have been dedicated to better constrain the tectono-thermal evolution of inverted isograds without reaching a common agreement.

Some authors attributed the inversion of isograds to local transient processes such as the ‘hot iron’ model, where a hot slab is thrusted (either in one or in multiple steps) over a cold one causing a regional ‘contact’ metamorphism (Fig. 1.2a; e.g. Le Fort, 1975), or viscous-heating along the thrust zone (Fig. 1.2b; e.g. Graham and England, 1976; Arita, 1983; England and Molnar, 1993; Burg and Schmalholz, 2008), or contact metamorphism due to magmatic intrusions at higher crustal levels (e.g. Himmelberg *et al.*, 1991). In these cases the temperature gradient is reversed, but the pressure gradient is normal.

Other authors explained inversion by post-metamorphic deformations of a former normal sequence. This would result from either large-scale folding (e.g. Mohan *et al.*, 1989; Searle and Rex, 1989; Swapp and Hollister, 1991; Stephenson *et al.*, 2001), or brittle/ductile superposition of high grade rocks over lower grade ones (e.g. Brunel and Andrieux, 1980; Andrieux *et al.*, 1981), or passive deformation of the isograds within the ductile shear zone (Fig, 1.2c; e.g. Hubbard, 1996; Gibson *et al.*, 1999; Grasemann and Vannay, 1999), or ductile extrusion of a wedge (Fig. 1.2d; Hodges *et al.*, 1993, 1996) or hot channel flow (Fig. 1.2e; Grujic *et al.*, 1996; Vannay and Grasemann, 2001; Beaumont *et al.*, 2001, 2004; Jamieson *et al.*, 2002, 2004).

The main difficulty is to estimate the thermal budget and constrain the thermal source: where does the heat come from? It is essential to consider quantitatively the physics of heat transfer on small and large scales (e.g. England and Molnar, 1993, Schott *et al.*, 2000; Burg and Gerya, 2005; Faccenda *et al.*, 2008; Burg and Schmalholz, 2008; Gerya *et al.*, 2008). Progresses in numerical modelling of thermo-mechanical processes give essential simulations of kinetics but fail in estimating the source of heat needed to reach peak metamorphic conditions obtained with thermobarometric methods (e.g. Jamieson *et al.*, 1998; Engi *et al.*, 2001). Figuring out the thermal structure in an orogenic setting can be fundamental because it effects rheological properties and thus the deformational evolution (Schott *et al.*, 2000; Jamieson *et al.*, 2002).

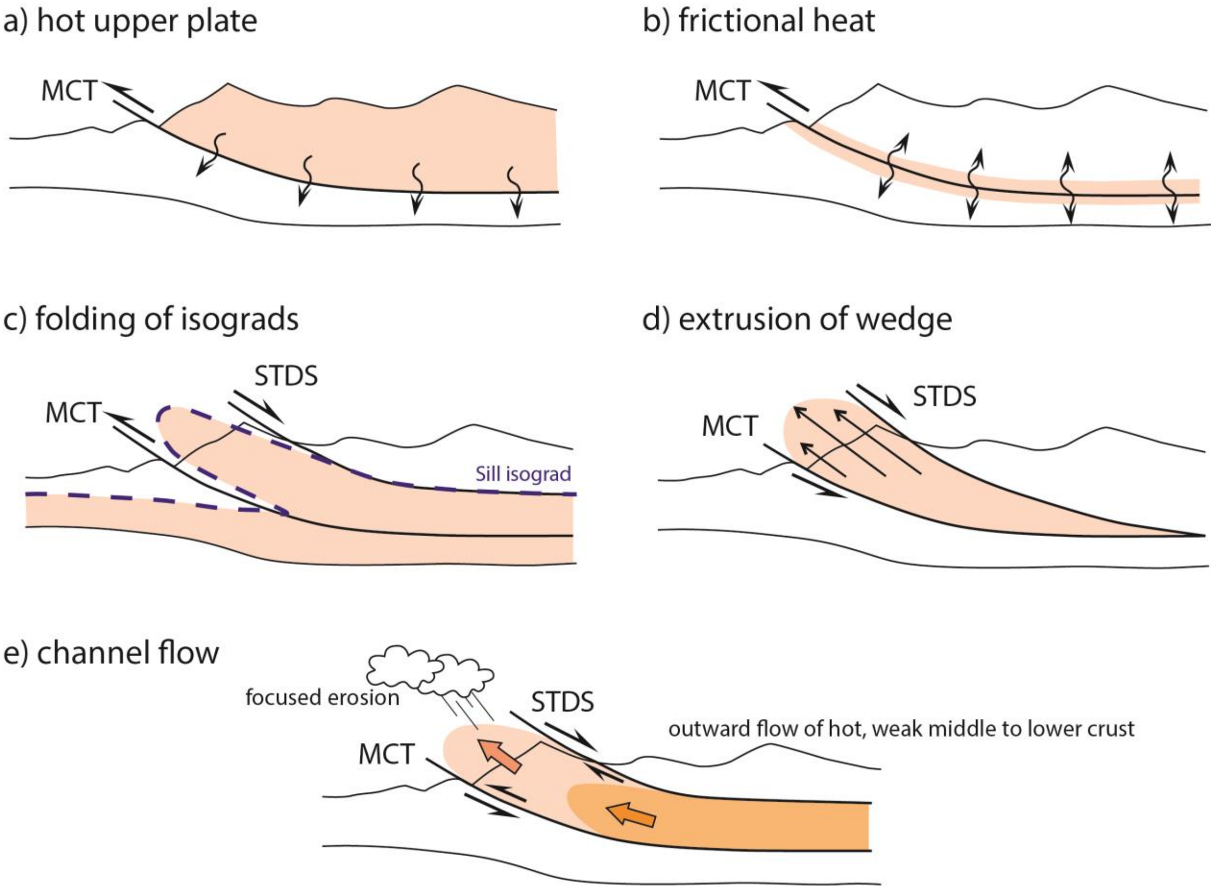

Figure 1.2. Schematic summary of tectonic models for the formation of inverted metamorphic zone in the Himalayas. **a)** Heating by a hot upper plate (e.g. Le Fort, 1975). **b)** Frictional heating (e.g. *Graham and England, 1976; Arita, 1983; England and Molnar, 1993; Burg and Schmalholz, 2008).* **c)** Folding of isograds (e.g. *Hubbard, 1996; Gibson* et al.*, 1999; Grasemann and Vannay, 1999).* **d)** Extrusion of a crustal wedge (e.g. *Hodges* et al.*, 1993, 1996; Grujic* et al.*, 1996; Vannay and Grasemann, 2001).* **e)** Ductile extrusion/channel flow with dynamic coupling between mid-crustal and surface processes (e.g. *Jamieson et al., 2002, 2004*; *modified from Jamieson et al., 2004*).

Beside the interpretation of the source/s of heat, another problem is the estimation of the duration of the thermal event. Previous models of conductive thermal relaxation in tectonically thickened crust predict that the attainment of metamorphic peak conditions should span few tens of million years (e.g. Thompson and England, 1984). Recent structural, petrologic, isotopic and diffusion studies suggest that some metamorphic processes may operate over much shorter timescales (few millions of years; Kröner *et al.*, 1998; Oliver *et al.*, 2000; Schott *et al.*, 2000; Camacho *et al.*, 2005; Dewey, 2005; Ague and Baxter, 2007; Caddick *et al.*, 2010). This has broad implications because Barrovian metamorphic sequences are common in mountain belts of any age. In fact, the thermo-mechanical evolution, i.e. the origin and the nature of regional metamorphic heat in collisional settings remain an important gap in understanding orogenic processes.

In this study, the main focus is placed on estimating the duration of peak metamorphic conditions associated with isograds inversion. The applied geological chronometer is *garnet geospeedometry* (Lasaga, 1983). Garnets are a potential chronometer and their compositional zoning formed by intracrystalline diffusion, is an excellent quantitative indicator to estimate the rate of element diffusion within the mineral, constraining the timescales of thermal events. Results should yield indications on the tectonic processes active during metamorphism and orogenesis (Lasaga, 1983; Spear *et al.*, 1984; Perchuk and Phillipot, 1997; Ague and Baxter, 2007; Viete *et al.,* 2011, Ague and Carlson, 2013).

1.2 Aim of the thesis

The PhD thesis combines the investigation of tectonic setting of previously reported inverted metamorphic isograds related to crustal-scale thrusting with the analysis of diffusion zonation in garnet crystals. The aim is to understand the link between mechanical and thermal evolutions of major ductile thrust zones, clarify the timescale of peak temperature conditions and constrain the nature and the origin of orogenic heat responsible for metamorphic inversion.

Estimating the duration of the peak metamorphic condition can improve interpretations of the genesis of inverted isograds across major thrust faults, the potential heat source in the *P-T-t* (*t* for time) path and the related deformation processes.

1.3 Methods

To achieve the objectives of this work, a multidisciplinary approach was necessary. This allows to complement, corroborate or refute published information.

1.3.1 Field work

Geological mapping and rock sampling across major thrust faults were fundamental to interpret and compile existing information on tectonic settings. Detailed description of the rock types, their field relations and structures are necessary to constrain the investigated thrusts zones.

1.3.2 Mineralogy, petrology and geochemistry

Mineralogical and petrological observation are essential to determine peak mineral assemblages. Microscopic observations were carried out using transmitted light microscopy, cathodoluminescence and electron microprobe (EMPA).

Geochemical analyses were performed to measure bulk rock compositions of samples used for peak *P-T* estimates. Major elements contents were obtained using a Panalytical Axios wave-length dispersive spectrometer (WDXRF, 2.4 KV) at ETH Zürich. Rock samples were crushed in fine powder, mixed with *Fluxana* (Lithiumtetraborat 66.5%, Lithiummetaborat 33.5%) in a ratio of 1:5 and melted with an Eagon 2 fusion instrument at the ETH Zürich. The homogeneous glass beads were analysed for SiO_2, TiO_2, Al_2O_3, Fe_2O_3, MgO, MnO, CaO, Na_2O and K_2O. The content of H_2O was estimated from loss of ignition (LOI) during the melting stage of the glass beads preparation.

Minor and trace elements in whole rocks were analysed with Perkin Elmer Elan 6100 DRC laser ablation inductively coupled plasma mass spectrometer (LA-ICP-MS) at the ETH Zürich. The homogeneous glass beads were analysed for *Rb*, *Ba*, *Sr*, *Nb*, *Zr*, *Hf*, *Y*, *Ga*, *Zn*, *Cu*, *Co*, *V*, *Sc*, *La*, *Ce*, *Nd*, *Pb*, *Th* and *U*. Mineral chemical compositions were obtained using the electron microprobe JEOL-8200 at ETH Zürich. Operating conditions for spot analyses were 15 kV accelerating voltage, 20 nA current, beam size < 5 µm and 20s counting time. Minerals were analyzed for SiO_2, TiO_2, Al_2O_3, FeO, MgO, MnO, CaO, Na_2O, K_2O and Cr_2O_3.

1.3.3 Geochronology

Absolute ages are essential to reconstruct the regional thermo-tectonic evolution of inverted metamorphic zonations. U-Pb sensitive high resolution ion microprobe (SHRIMP) and Laser Ablation ICP-MS zircon geochronology are accurate records of multiple high temperature geological events.

Zircons were extracted after high voltage electrical discharge in the SelFrag apparatus (http://www.selfrag.com) at the ETH Zürich. Advantages of this method, compared to the classical mechanical crushing, are to obtain clean surfaces and to preserve the natural grain size. Zircon fractions were separated with methylene iodide heavy liquid and hand-picked. In-situ U-Pb analyses were performed using a SHRIMP II at the Center of Isotopic Research (CIR) at VSEGEI, Saint Petersburg. The ages are presented in Concordia (Watherill, 1956) and Tera-Wasserburg diagrams (Tera and Wasserburg, 1972). Additional U-Pb ages of two samples (*R13-013* and *R15-011*) from the Rhodope Metamorphic Complex collected during a second field campaign, have been measured with LA-ICP-MS at the ETH Zürich.

$^{40}Ar/^{39}Ar$ dating was performed to constrain cooling below 350-400 °C. White mica grains were extracted from micaschists with shockwaves produced in the SelFrag apparatus. The single crystal grains were selected after magnetic separation and final hand picking. $^{40}Ar/^{39}Ar$ step-heating analyses were performed at the Geological Survey of Norway, Trondheim.

1.3.4 Garnet crystals preparation

For garnet diffusion-growth zoning analysis euhedral crystals in different sizes (few mm up to 15 mm) were hand (hammer and mason) extracted from the rocks. The detached grains were mounted in epoxy “pills” and polished until the core of the crystal. This procedure was required to respect the geometry of radial diffusion and warrant as precise as possible the application of numerical modelling. The polished pills were coated by carbon (~30 µm). Major element (Mg, Mn, Ca and Fe) concentration maps were performed to image their within-grain distribution. Compositional profiles were obtained using the electron microprobe JEOL JXA-8200 at the ETH Zürich and were programmed avoiding garnet inclusions and cracks.

1.3.5 Diffusion modelling: garnet geospeedometry

The term *geospeedometry* was introduced by Lasaga in 1983. Geospeedometry is a complementary method to geothermobarometry and can be used to constrain pressure – temperature - time (P-T-t) history. The fundamental quantity considered in exchange reactions or activity-composition relations is not changes in free energy ($\Delta G°$) or enthalpy ($\Delta H°$) but the *kinetic* response (diffusivity) of minerals (Lasaga, 1983).

Diffusional studies in crystals may predict duration (t) of tectono-metamorphic processes in collisional systems. The overgrowth of a mineral on itself leads to a development of crystals with compositional contrasts between core and rim. This compositional gradient will generate diffusion. A common assumption is that thermodynamics of the minerals is known and the composition of the core of the crystal can be used to estimate peak-T conditions (Lasaga, 1983). If diffusion rates, temperature and initial concentration profiles are well constrained, diffusion modelling then allows estimating the maximal duration (t) of peak-T.

The next section illustrates the theoretical basis of transport phenomena and provides a brief background on what diffusion is and why it can be beneficial in understanding metamorphic events and geological processes. The last part of the section presents the garnet diffusion modelling applied in this study.

1.3.5.1 Fundamentals of diffusion

Diffusion is a thermally activated mass transfer phenomenon. It induces random Brownian motions of particles at atomic-scale (atoms, ions and molecules) causing the uniform distribution of the species in space during time (e.g. Zhang, 2010). In other words, according to the second law of thermodynamics, a system in a non-equilibrium state will evolve toward equilibrium with time.

There are different types of diffusion mechanisms. In solids, diffusion is divided in volume, grain boundary and surface diffusion (e.g. Ganguly, 2002). Factors that can influence diffusion are the diffusing species, the host solid, temperature and microstructures.

The simplest description of mass transfer at molecular scale is the Fick's first law (Fick, 1855), which relates the flux of the diffusing substance with the concentration gradient (or chemical potential gradient):

$$J = -D \cdot \frac{dC}{dx} \tag{1}$$

where J $[mol\ m^{2}\ s^{-1}]$ is the diffusive mass flux, D $[m^{2}\ s^{-1}]$ is the diffusion coefficient, C $[mol\ m^{-3}]$ is the concentration of the considered component, x is distance; hence, dC/dx is the concentration gradient; the negative sign indicates that the direction of the flux is opposite to the direction of the concentration gradient. D indicates the "rate" of diffusion and depends upon the pressure, temperature, composition of the system and oxygen fugacity (fO_2).

The Fick's second law considers the concentration profile (concentration gradient) as a function of space and time where D usually is assumed as a constant independent of x and C:

$$\frac{dC}{dt} = D \cdot \frac{d^2C}{dx^2} \tag{2}$$

If more than one chemical species are present in the system, the diffusion coefficient D cannot be treated as constant or composition independent. In a *multi-component system* the diffusion flux of any component does not depend only on its own concentration or chemical potential gradient but also on those of all other diffusing components (Ganguly, 2002; Zhang, 2010). The Fick's first law can then be extended to a system of n components arranged in matrix form:

$$\begin{bmatrix} J_1 \\ J_2 \\ \cdots \\ J_{n-1} \end{bmatrix} = - \begin{bmatrix} D_{11}\ D_{12} \ldots\ldots D_{1(n-1)} \\ D_{21}\ D_{22} \ldots\ldots D_{2(n-1)} \\ \cdots\cdots\cdots\cdots \\ D_{(n-1)1} \cdots\ D_{(n-1)(n-1)} \end{bmatrix} \cdot \begin{bmatrix} \frac{\partial C_{11}}{\partial x} \\ \frac{\partial C_{21}}{\partial x} \\ \cdots \\ \frac{\partial C_{n-1}}{\partial x} \end{bmatrix} \tag{3}$$

This matrix considers n-1 equations since in an n-components system the concentration of one component is fixed by those of others at any given point.

The diffusion coefficient matrix is calculated using the Wendt formulation (1965):

$$D_{ij} = D_i^0 \delta_{ij} - \left[\frac{D_i^0\, X_i}{\sum_{k=1}^{n} D_k^0\, X_k}\right] \cdot \left(D_j^0 - D_n^0\right) \tag{4}$$

where D^0 is the self-diffusion coefficient for the component i, n is the number of the components, and $\delta_{ij} = 0$ when $i \neq j$ and 1 when $i = j$ (Ague and Baxter, 2007).

For active diffusion to occur, the temperature should be high enough to overcome energy barriers to atomic motion. Diffusivity D is a strong function of temperature following the empirical Arrhenius relation (1889):

$$D = D_0 \cdot e^{-E/RT} \tag{5}$$

where E $[J\ mol^{-1}]$ is the activation energy, R $[J\ K^{-1} mol^{-1}]$ the universal gas constant, T $[K]$ the absolute temperature and D_0 $[m^{2}\ s^{-1}]$ is a constant (maximal diffusion coefficient).

The effective diffusion length (l_{eff}) is a fundamental material property. It is the average distance travelled in one direction by a particle from the point at which it is formed to the point at which it is absorbed:

$$l_{eff} = \sqrt{Dt} \tag{6}$$

The average distance is proportional to the square root of the time t and diffusion coefficient D. All three values are temperature-dependent.

1.3.5.2 Geological applications

Diffusion processes within a mineral preserve important records of the thermal and physical-chemical history of the host rock (Ganguly, 2002). Therefore, it is possible to interpret and understand thermal histories, closure temperatures, apparent equilibrium temperatures and cooling rates from diffusion properties (Zhang, 2008).

Chemical zonation generated during crystal growth is modified by diffusional relaxation at temperature above a nominal diffusional closure temperature range, which for any element depends on cooling rate and grain size (Dodson, 1973). The extent of diffusion profiles depends strongly on temperature and time over which diffusion was effective (Ganguly, 2002). Garnet from lower-T greenschist facies rocks ($T < 600$ °C) would have diffusion coefficients an order of magnitude or more smaller than garnet from high grade rocks (Ague and Baxter, 2007).

In summary, the growth zoning in metamorphic garnets is convenient to reconstruct the P-T path and tectonic evolution during garnet crystallization (Kohn, 2003). Investigating such a zonation allows to: (1) calculate the rate of element diffusion within the mineral, (2) extrapolate the duration of thermal events, and (3) provide clues on the tectonic processes active during metamorphism and orogenesis (Lasaga, 1983; Spear *et al.*, 1984; Ague and Baxter, 2007; Viete *et al.*, 2011). Many experimental studies have been carried out for a better understanding of diffusion mechanisms, self-diffusion coefficients, activation energies and multicomponent diffusion in several minerals (e.g. Lasaga, 1979; Ghiorso, 1987; Chakraborty and Ganguly, 1991, 1992; Sheng *et al.*, 1992; Chakraborty *et al.*, 1994; Lasaga and Jiang, 1995; Chakraborty, 1997; Ganguly *et al.*, 1998; Mungall *et al.*, 1998). Intracrystalline diffusion quantification can be problematic and controversial because it depends on a variety of factors such as compositional variations within mineral solid solutions, initial boundary conditions, fluids, experimental calibrations of diffusion coefficients and the correct interpretation of observed diffusion profile (Ague and Baxter, 2007).

As explained by Ganguly (2002), the most critical point is the application of experimental data to natural systems. Mineral composition of crystals used in the laboratory experiments, physical variables as temperature, pressure or fO_2 may undeniably not represent natural conditions. Numerical simulations of mechanisms and kinetics of crystallization are ongoing and in constant evolution making this topic very innovative.

1.3.5.3 Garnet diffusion modelling

The study of garnet zoning profiles combined with mineral chemistry from the other minerals of the assemblage are excellent indicators of *P-T-t* path of metamorphic events (Spear and Silverstone, 1983; Spear *et al.*, 1984). Nevertheless, as will be explained hereafter, substantial assumptions and simplifications are necessary (Ague and Baxter, 2007; Schwarz *et al.*, 2011; Gaidies *et al.*, 2011; Ketchman and Carlson, 2012).

Garnet is a common mineral in ultramafic to felsic bulk rock compositions. Its stability spans from T < 300 to 2000 °C and from atmospheric pressure up to 25 GPa (Baxter and Scherer, 2013). The garnet composition is represented by the formula $X_3Y_3(SiO_4)_3$, where *X* is *Ca (Grossular), Mg (Pyrope), Fe (Almandine)* or *Mn (Spessartine)* and *Y* is *Fe, Al, Cr* or *Ti*. In metapelites, garnet is mostly represented and zoned by the major elements $(Fe, Ca, Mg, Mn)_3Al_2(SiO_4)_3$. All garnet species have similar physical properties with unique chemical and mechanical peculiarities. Diffusional rates of intracrystalline diffusion are slow enough to retain a complete record in the zoning of the major elements. Furthermore, garnet crystals are isotropic so that diffusion has no directional dependence which is a considerable advantage in multicomponent zoning modelling. The dodecahedral crystal habit allows to simplify the geometry of the crystal in a sphere with radial diffusion. In multicomponent diffusion all major cations *Fe*, *Mg*, *Mn* and *Ca* are treated as dependent on each other in order to maintain the stoichiometry:

$$\begin{pmatrix} \frac{\partial X_1}{\partial t} \\ \frac{\partial X_2}{\partial t} \\ \frac{\partial X_3}{\partial t} \end{pmatrix} = \frac{1}{r^2}\frac{\partial}{\partial r}\left[r^2 \begin{pmatrix} D_{11} & D_{12} & D_{13} \\ D_{21} & D_{22} & D_{23} \\ D_{31} & D_{32} & D_{33} \end{pmatrix} \cdot \begin{pmatrix} \frac{\partial X_1}{\partial r} \\ \frac{\partial X_2}{\partial r} \\ \frac{\partial X_3}{\partial r} \end{pmatrix} \right] \qquad (7)$$

where *X* represents the mole fraction of a component, *r* the radius of the sphere and index 1, 2 and 3 are any three of the four components (almandine, grossular, pyrope and spessartine).

Diffusion is strongly temperature dependent (Eq. 5). The maximum of diffusion potential occurs at or near peak-*T* conditions experienced by a rock. Peak-*T* conditions are estimated from a combination of thin section observations, garnet-biotite (Grt-Bt) Fe-Mg exchange conventional thermometer, phase equilibria modelling and isopleths garnet chemical compositions.

Garnet diffusion depends also on oxygen fugacity fO_2 (Ganguly *et al.* 1998). In the absence of fO_2 evolution during diffusion, fO_2 is assumed to follow the graphite buffer, which is a reasonable considering that high fO_2 would shift the diffusion coefficients to larger values; then, the apparent time estimates would be shorter (Eq. 6).

Depending on the shape of measured garnet profiles, two different approaches have been applied to obtain maximal timescale estimate: (1) *initial step function* and (2) *FRactIonation-Diffusion in GarnEt (FRIDGE)* model.

1. ***Initial step function***: Garnet radial multicomponent diffusion modelling in a sphere (Eq.7) is computed with the method of Ague and Baxter (2007). For initial conditions, we employed an *initial step function* of garnet composition across core-rim compositional variation boundaries (Fig. 1.3a).

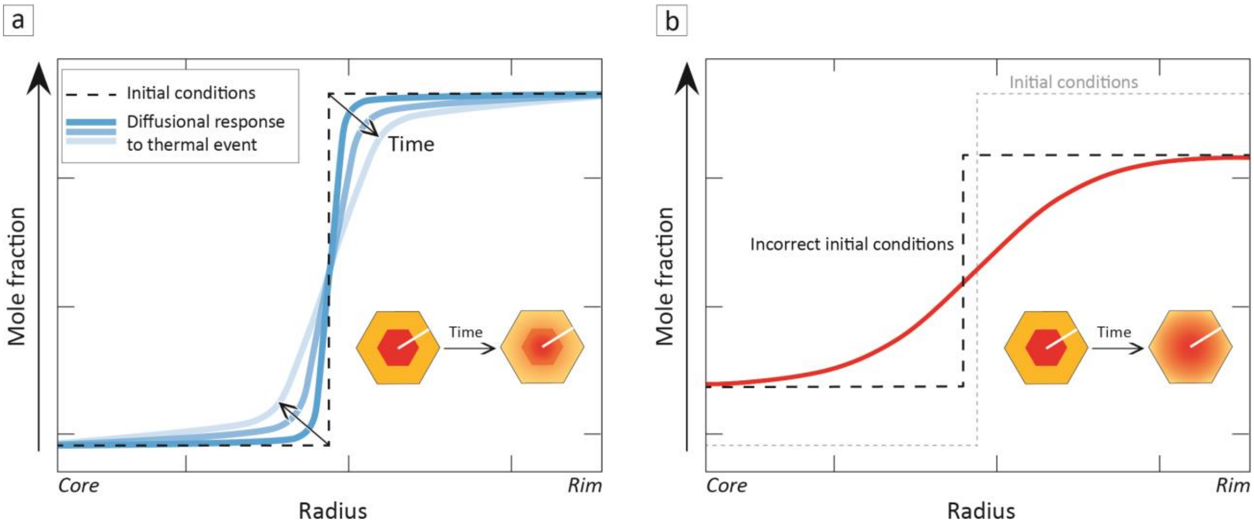

Figure 1.3. Mole fraction relaxation profile during time of a step function. a) Estimated duration = maximal time that garnet was at peak *T* conditions. The longer garnet is held at given *T*, the more diffusional smoothing of internal zoning will be. **b)** By extensive relaxation predictions of initial compositions conditions are incorrect, duration is underestimated (*modified from Ague and Carlson, 2013*).

This procedure ensures that the time estimation is maximal. The initial compositional variation is interpreted as growth zoning. The pre-existing compositional step function undergoes diffusional relaxation during peak-*T* conditions and compositional profiles are considered “frozen” during cooling. The model estimates the time needed to match the calculated simulation curves with the measured garnet profiles.

If garnet composition profiles are significantly re-equilibrated, core concentrations do not represent the initial composition and the prediction of a step function is unattainable (Fig. 1.3b). Profile fitting using the measured smoothed values as initial conditions would underestimate the duration of peak metamorphic conditions (Ague and Baxter, 2007; Ague and Carlson, 2013) making an additional approach necessary.

2. ***Fractionation and diffusion in garnet (FRIDGE)***: The second approach is an inverse fitting model considering fractionation and diffusion in garnet (FRIDGE) for the four major elements simultaneously. Diffusion is strongly temperature dependent and more effective at temperature above

600 °C. FRIDGE numerical model starts calculations from a given bulk rock composition and a *P*-*T*-*t* path. The *P*-*T* path is extrapolated from garnet core compositions and near rim conditions given from conventional geothermobarometry (garnet-biotite (Fe-Mg) thermometry, garnet-alumosilicate-plagioclase-quartz (GASP), garnet-plagioclase-biotite-muscovite-quartz (GPBMQ) and garnet-plagioclase-muscovite-quartz (GPMQ) Geobarometry) supported by phase equilibria modelling.

The model assumes that a garnet crystal is fractionated from the given bulk rock composition as soon as it crystalizes along a *P*-*T*-*t* path (Fig. 1.4). The matrix recrystallized at successive *P*-*T* conditions is in equilibrium with the successive garnet's rim maintaining garnet's rims. This means that during each growth step the matrix has a bulk rock composition different from that in the previous step and the matrix composition is always homogeneous. Along the *P*-*T*-*t* path, garnet crystal diffuses as soon as it fractionated. The output of FRIDGE's calculations are the garnet profiles for each of the four major elements. Assumptions and limitations of FRIDGE are homogeneous crystal distribution and small variations in garnet size.

In FRIDGE the given *P*-*T* path is not limited to few points but it is defined through the computer mouse in a graphical user interface (GUI). FRIDGE uses the functions of the software Perplex_X_07 (Connolly, 2005), ensuring the last thermodynamic data, updated diffusion coefficients and allows to fractionate other mineral phases along the prograde *P*-*T* path.

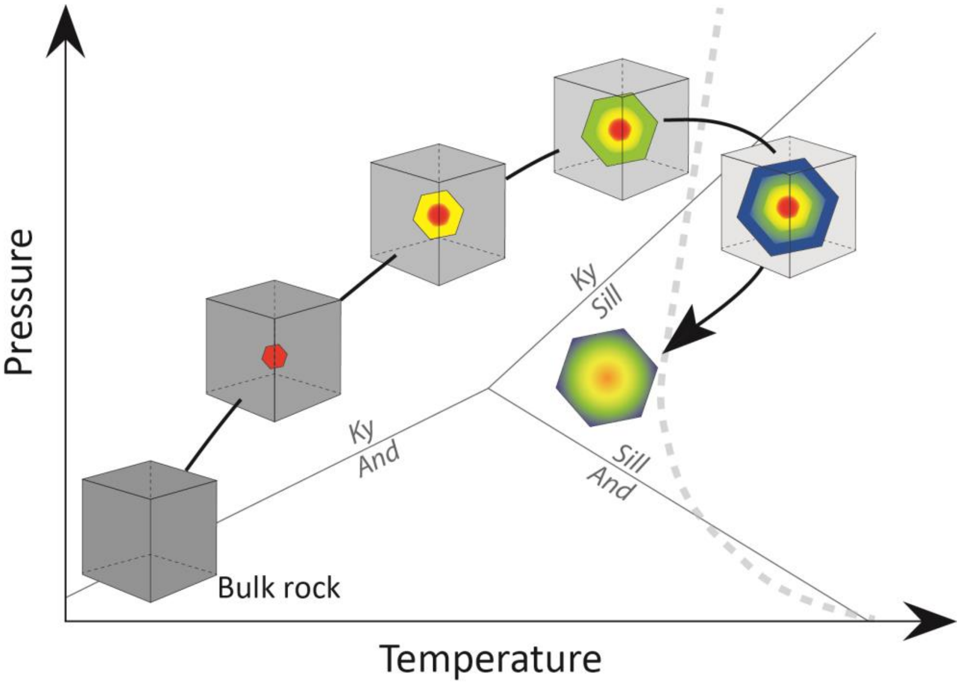

Figure 1.4. Principle of FRactIonation and Diffusion in GarnEt (FRIDGE) inverse fitting model. Garnet is fractionated from the bulk rock as soon as it is formed. The matrix recrystallizes at the new *P*-*T* conditions. The rim of garnet is always in equilibrium with the matrix. Diffusion is active during the *P*-*T*-*t* path but effective at *T* > 600 °C.

The purpose of this research is to estimate the maximal time at peak-*T* conditions and not the duration of the complete thermal/s (heating-cooling) event/s. In other words, garnet compositional profiles initiate “to smooth” at $T > 600$ °C. This process (diffusivity *D*) is faster at higher *T* conditions and slow down during cooling (cf. Eq. 5). We assume that the actual garnet compositional profile represents the result of diffusion occurred exclusively at the peak-*T* conditions estimated with petrological thermometry and pseudosection calculations. Therefore, the estimates of peak metamorphic conditions duration represent the maximal timespan.

1.4 Study areas

Three cases of inverted metamorphic profiles have been studied: the Nestos Thrust zone in the Rhodope (Greece), the High Himalaya in Sikkim (India) and the Variscan Champtoceaux Complex (Brittany, France). Considering different geological settings with different ages makes it possible to recognize whether the thermo-mechanical processes responsible for metamorphic inversion are reduced to a local/regional explanation or can be applied to other collisional systems.

1.4.1 The Nestos Thrust Zone in the Rhodope Metamorphic Complex (Northern Greece)

The first case-study is the Nestos Thrust Zone (NTZ) in the Rhodope Metamorphic Complex (RMC). The RMC is located in north-northeastern Greece and southern Bulgaria and lies between the north-verging Balkanides to the northeast and the south-west verging Hellenides to the southwest (Fig. 1.5). The northern boundary of the Rhodope Massif is represented by the Maritza dextral strike-slip fault, which deformed late Jurassic granitoids during Late Cretaceous (Rieser *et al.*, 2008). To the south, the RMC disappears below Miocene to recent sediments of the Aegean Sea.

The Metamorphic Complex is a 300 x 300 km open antiform composed by medium- to high-grade metamorphic rocks, abundant granitoid intrusions partly covered by sedimentary and volcanic rocks (Fig. 1.6a; Didier *et al.*, 2014). The Massif is interpreted as a segment of the Alpine-Himalaya sutures exposing an association of both large-scale thrusting and pervasive exhumation tectonics (Burg *et al.*, 1990; Burg *et al.*, 1996; Ricou *et al.*, 1998; Burg, 2012). Orogeny started in the early Cretaceous with the continuous northward subduction of microcontinents below the southern margin of Eurasia causing the progressive closure of the Tethys Ocean (Ricou *et al.*, 1998; Jolivet and Brun, 2010). Early Cretaceous collision between the Drama continental fragment and the Moesian platform (a part of Europe) caused the south-southwest thrusting and stacking of nappes forming a crustal-scale duplex structure (Fig. 1.6b; Robertson et *al.*, 1991; Burg et *al.*, 1996; Ricou *et al*., 1998; Burg, 2012).

Shortening, crustal thickening and deep subduction caused high pressure (HP) regional metamorphism (Burg *et al*., 1996a; Liati *et al*., 2004) and locally, within the thrust sheets, ultra-high pressure (UHP) conditions (Ricou *et al*., 1998, Krenn *et al*., 2000) where micro- and nano-diamonds inclusions in garnet porphyroblasts have been observed (Mposkos and Kostopoulos, 2001).

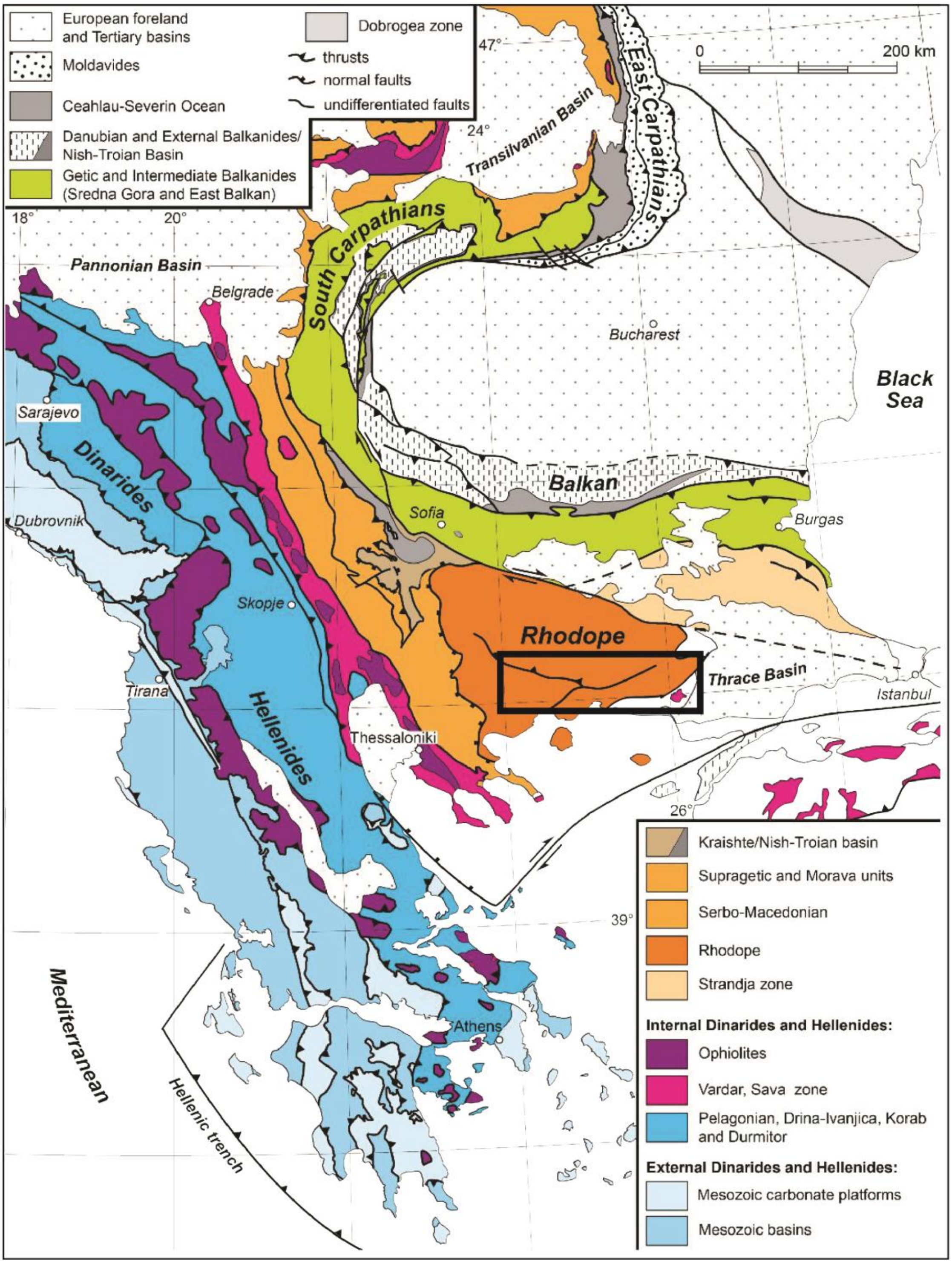

Figure 1.5. Location of the Rhodope Metamorphic Complex (RMC) in the Alpine system of southern Europe (*after Burg, 2012*). Black sector: study area.

During Early Eocene, in the northeastern Rhodope Massif, the subduction/collisional context converted into an extensional tectonism (e.g. Bonev *et al.,* 2006). Structural and geochronological studies confirmed that the crystalline RMC metamorphic core complexes were exhumed during a protracted Cenozoic extensional history (Bonev *et al*., 2006a; Brun and Sokoutis, 2007). Eocene-Oligocene extension developed grabens, metamorphic domes and voluminous magmatism and volcanism (e.g. Baker and Liati, 1991; Jones *et al*., 1992; Burg, 2012). Middle Miocene through Early Pliocene crustal extension produced later grabens and detachment faults during two events initiated in the Rhodope Massif and migrated southwards: (1) syn-orogenic or syn-thickening extension and (2) post-orogenic, slab-rollback driven extension (e.g. Dinter and Royden, 1993; Sokoutis *et al.,* 1993, Brun and Faccenna (2008); Burg, 2012; Schenker *et al*., 2012).

The RMC is subdivided into three main ”Terranes”, from the lowest to the uppermost structural position: the Lower Terrane, the Middle (Imbricate) Units and the Upper Terrane (Fig. 1.6a). The Lower Terrane (also called Drama window) is constituted of thick layers of marbles with schist interlayers, leucocratic orthogneisses, and paragneisses interlayered with thin (few meters) marbles, micaschists and minor amphibolites. The Middle (Imbricate) Units incorporate several lithologies such as migmatitic orthogneisses containing leucogranite veins, lenticular bodies of eclogites and peridotites in paragneisses, minor graphitic marbles, micaschists within metamorphosed gabbros, diorites and felsic orthogneiss that overlain the thick massive marble of the Lower Terrane (e.g. Ivanov *et al.*, 1988; Burg *et al.,* 1996 and references therein). The Middle Units are intruded by Upper Cretaceous to Middle Tertiary granitic intrusions (Ovtacharova *et al.*, 2003). Rocks of the Upper Allochthon are mostly quartzo-feldspatic migmatites containing bodies of basic and ultramafic rocks, including eclogites retrogressed into amphibolite facies (e.g. Burg, 2012).

The north-dipping Nestos Thrust Zone (NTZ), in Central Rhodope, can be traced for about 100 km from Xanthi in the east to the Mesta Basin to the west. The NTZ is interpreted as a major suture separating the Lower Allochthon unit in the footwall from the high grade, eclogites-bearing migmatitic Imbricate Units in the hanging wall (Burg *et al*., 1996; Nagel *et al.,* 2011). It consists of a > 1 km thick pile of mylonites displaying top-to-the-south sense of shear criteria (e.g. Kilias and Mountrakis, 1990; Burg *et al.,* 1996). Ages of accretion of terranes during the closure of the Tethys ocean have been proposed from Jurassic to Eocene (e.g. Ricou *et al*., 1998; Turpaud and Reischmann, 2010; Krenn *et al*., 2010).

The NTZ developed inverted isograds, in the lowest structural level of the Lower Terrane, from greenschist facies up to sillimanite-bearing migmatites against the thrust zone (e.g. Papanikolaou and Panagopoulos, 1981; Mposkos *et al*., 1989; Burg *et al*., 1996).

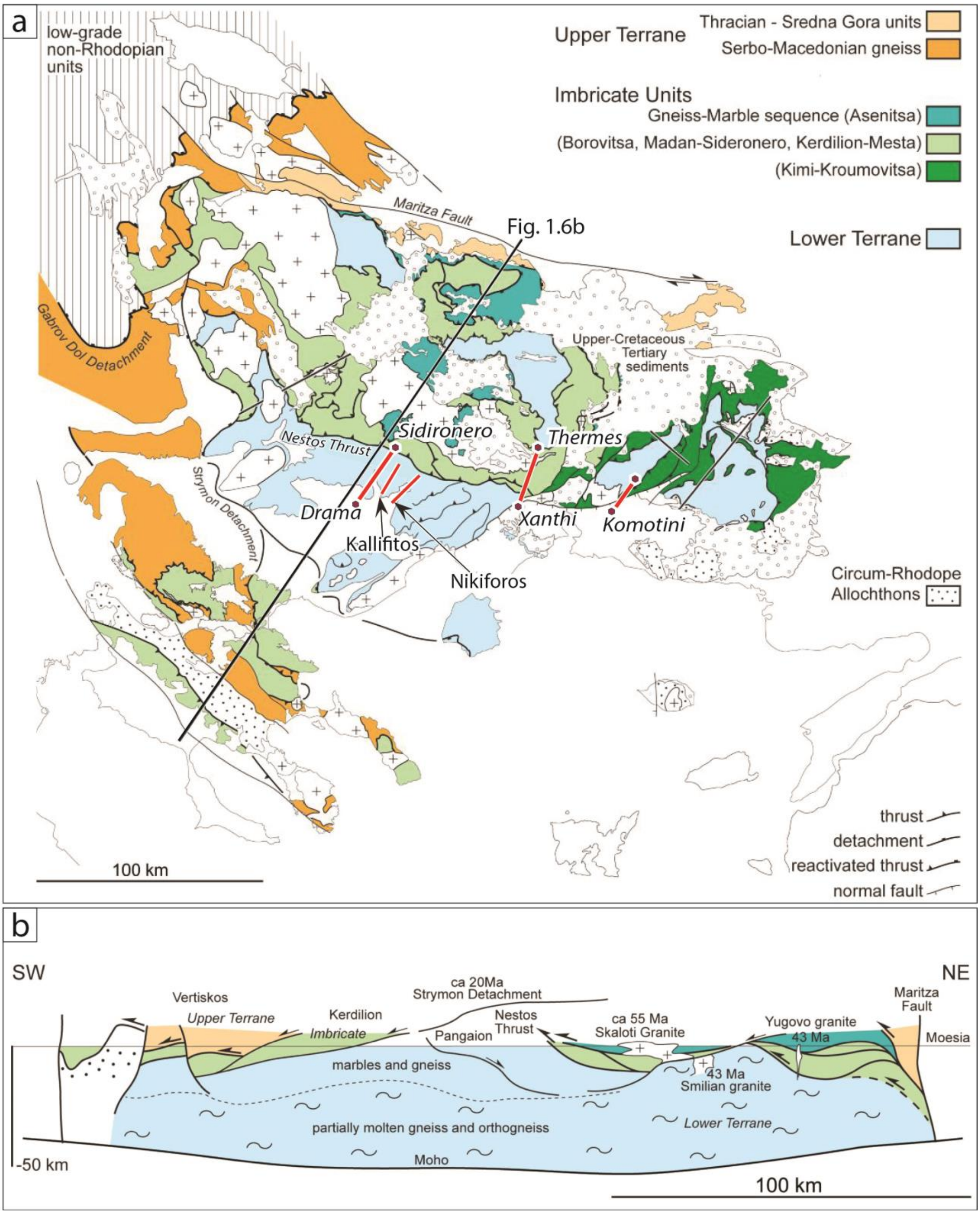

Figure 1.6. **a)** Simplified geological map of the Rhodope massif showing the main tectonic units and the localities of the considered sections Sidironero, Kallifitos, Nikiforos, Xanthi and Komotini (red lines, from west to the east). Black line represents the cross-section presented in **b)** simplified cross-section to illustrate the crustal duplex (*modified from Burg, 2012*).

This work considered five sections across the Nestos Thrust in the regions of (from east to west) Drama, Kallifitos, Mesochori, Xanthi, and Komotini (Fig. 1.6a). Major attention was dedicated to the Drama, Xanthi and Komotini transverses, where garnet-bearing metapelite have been collected for petrographic observations, bulk rock compositions, mineral chemistry, geochronology and garnet fractionation/diffusion modelling.

1.4.2 Main Central Thrust, Sikkim (NE India)

The Himalayan orogen is a classic example of continent-continent collision zone and plays a central role in understanding orogenesis. Closure of the Tethys Ocean and subduction of the Indian subcontinent beneath the Tibetan Plateau caused collision between the Indian and the Eurasian plates since 60-50 Ma, generating the 2400 km long (from Pakistan in the west through north-western India, Nepal, Bhutan, south-eastern Tibet and northeastern India) and 250 to 400 km wide Himalayan mountain (including the southern Tibet suture zone) range (Le Fort, 1975). The amount of Indian continental lithosphere consumed in the Himalayas is estimated from paleomagnetic data (Patriat *et al.,* 1984; Chen *et al.,* 1993; Patzelt *et al.,* 1996) and from thermo-mechanical modelling (Chemenda *et al.,* 2000; Yin and Harrison, 2000) to be about 1000 to 1500 km. Because of the vast range of the orogenic belt and its high elevation, geologic evolutions may have also affected the climate at global scale (Molnar *et al.*, 1993) and perhaps the chemistry of oceans (e.g. Richter *et al.*, 1992). Simultaneously, climate changes may have influenced erosional rates altering the dynamic of the orogenic system (Beaumont *et al*., 1992).

The orogenic history, uplift and exhumation processes in the Himalaya remain subjected to various interpretations depending on approaches that have been applied such as magnetic records (e.g. Sangode *et al*., 1996, 2004), stratigraphy, structures and tectonic (e.g. Stöcklin, 1980; Burg and Chen, 1984; Rowley, 1996; DeCelles *et al*., 2001), biostratigraphy (e.g. Singh, 1981; Hughes, 1999; Yin and Enay, 2004; Wang *et al*., 2013) and geochronology (e.g. Catlos *et al*., 2001; DeCelles *et al.*, 2004; Anczkiewicz *et al*., 2014; Mottram *et al*., 2014).

The Himalaya belt has been simplified into four major units, which are from the lowest structural level in the south to the highest in the north (Fig. 1.7): the Molasse of the Sub Himalayas (Siwaliks), the Lesser Himalayas (LH), the Higher Himalayas (HH) and the Tethys Himalayas (TH). These major units are separated by three north-dipping major faults, from south to the north: the Main Boundary Thrust (MBT) between the Siwaliks Molasse and schists and gneiss of the LH (Johnson *et al*., 1982, 1985; Brookfield, 1993); the Main Central Thrust (MCT) between LH and HH and the low-angle South Tibetan Detachment System (STDS) between the HH and the low-grade TH metasediments in the north (Burg et *al*., 1984; Burchfiel *et al*., 1992). These structures converge into a basal décollement known as the Main Himalayan Thrust (MHT; Zhao *et al*., 1993; Nelson *et al.*, 1996; Harrison *et al.*, 1998; Vanney and Grasemann, 2001).

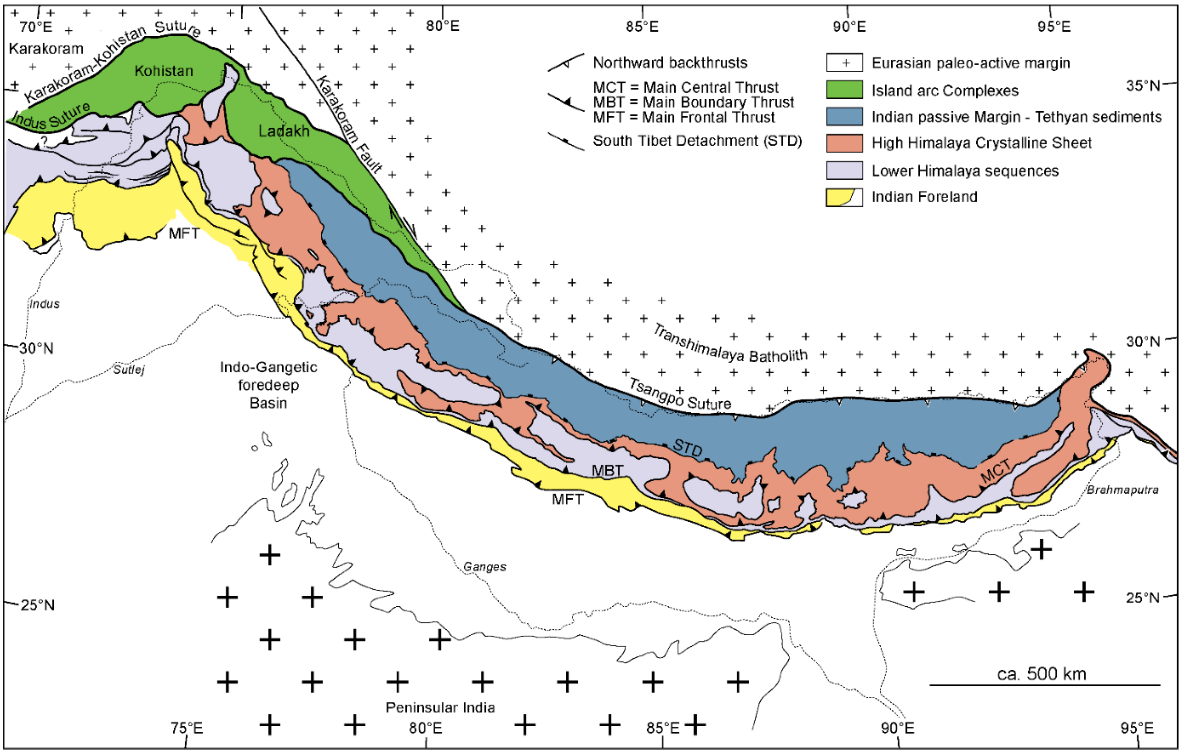

Figure 1.7. Simplified geological map of the Himalaya belt. Main boundary Thrust (MBT); Main Central Thrust (MCT; South Tibetan Detachment System (STDS). Black sector: location of the study area in Sikkim (*after Burg: http://www.files.ethz.ch/structuralgeology/jpb/vorlesungen.htm).*

This study focused on the MCT, one of the major intracontinental fault zones that accommodated a minimum of 140, maybe as much as 500 km of displacement of post-collisional convergence between India and Eurasia (Gansser, 1964; Gansser, 1981; Arita, 1983; Pêcher, 1989; Schelling and Arita, 1991; Srivastava and Mitra, 1994; Catlos *et al.*, 2001). It represents a thick, from 1.5 km up to 10 km (e.g. Grasemann and Vannay, 1999; Stephenson *et al.*, 2000) ductile north-dipping shear zone. Rocks of the LH footwall display inverted metamorphism with increasing metamorphic grade towards higher structural levels adjacent to the MCT over the entire length of the Himalayas (e.g. Heim and Gansser, 1939; Le Fort, 1975; Pêcher, 1977; Hodges *et al.*, 1988; Searle and Rex, 1989). *P-T* conditions and origin of inverted isograds remain debated issues concerning the heat source of the metamorphism, the origin of the inverted isograds, the ages of deformation events, and the relationship between metamorphism, deformation and magmatism (Neogi *et al.*, 1998).

A favourable location to study the MCT is Sikkim (Fig. 1.8), which is located in the north-eastern Himalayas bounded by Nepal to the west, Tibet (China) to the north and to the east, Bhutan to the southwest and the state of West Bengal in the south. The region exposes a complete inverted Barrovian sequence from chlorite-biotite to kyanite-sillimanite grade from south to north, where higher metamorphic grades lie at higher structural levels (Sinha-Roy, 1982; Arita, 1983; Mohan *et al.*, 1989; Hodges, 2000; Vannay and Grasemann, 2001; Harris *et al.*, 2004; Dasgupta *et al.*, 2004, 2009; Rubatto *et al.*, 2013).

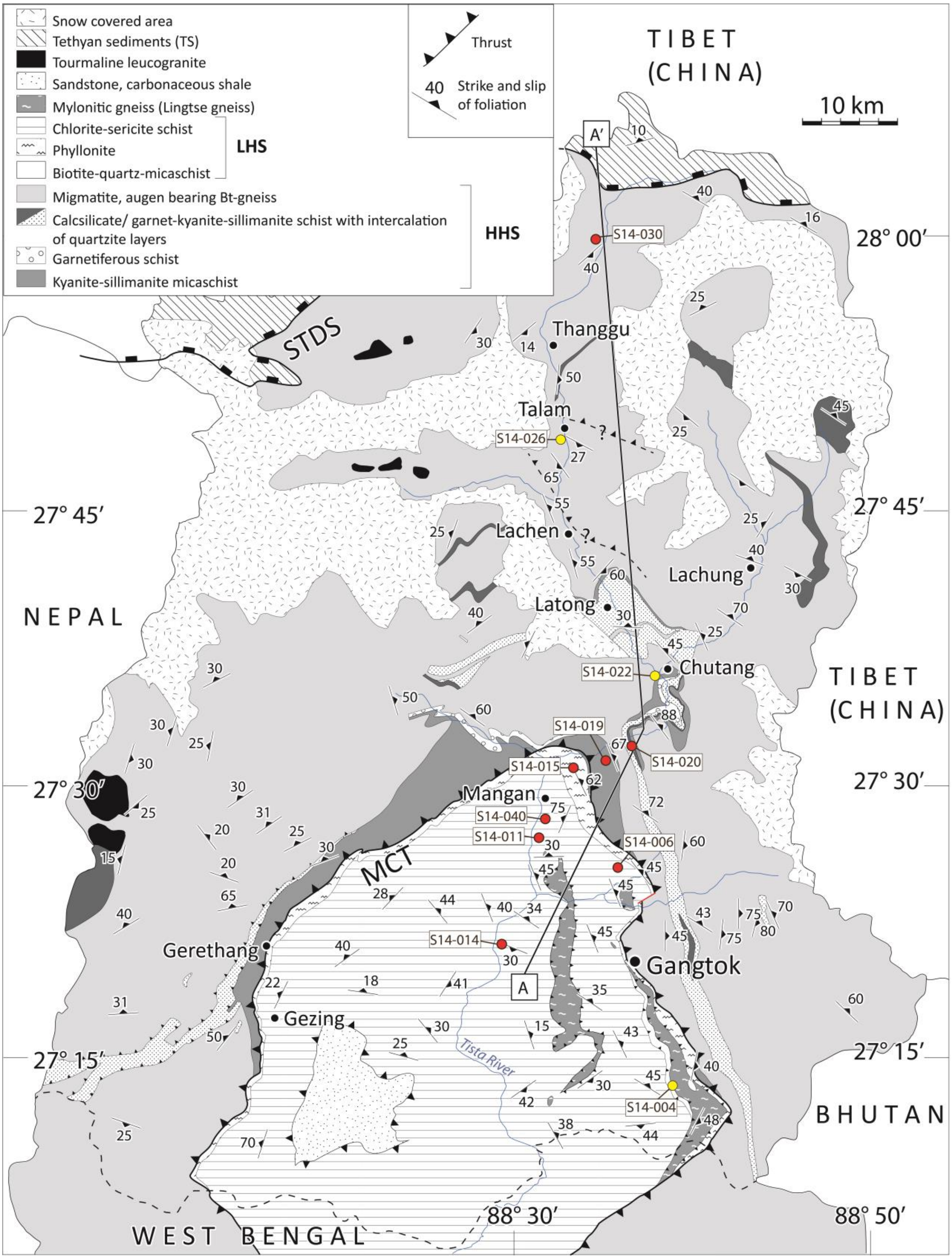

Figure 1.8. Simplified geological map of Sikkim Himalaya with major lithological and structural units. A-A' = trace of the investigated geological profile (Fig. 3.3). Numbered red circles: samples locations; yellow circles: samples for geochronology studies (*modified after Ghosh, 1956; Acharryya and Ray, 1977; Lal et al., 1981 and Ray, 2000*).

The Sikkim Himalaya is subdivided into a series of domains disposed around an antiformal half-window (Fig. 1.8), from the south to the north: the Sub Himalayan complex, which comprises weakly metamorphosed molasse-type deposits of the Siwaliks followed by a thin boundary of Carboniferous-Permian carbonates (Buxa Formation) and a thick sedimentary sequence of dominantly pelites with subordinate psammite and wacke (Daling Group) representing the LH (Gansser, 1964; Sinha-Roy, 1982; Dasgupta *et al.*, 2009; Faak *et al.*, 2012). The overlying HH unit consists of medium to high grade crystalline rocks (from schists to migmatites) with minor calc-silicate and metabasite layers. The grade of metamorphism in the HH decreases upward toward the overlying TS (Dasgupta *et al.*, 2004; Faak *et al.*, 2012).

Particular attention has been dedicated to the Gangtok-Thangu (SSW-NNE) *c.* 85 km long section. Rock samples were systematically collected across the MCT for petrographic observations, bulk rock compositions, minerals chemistry, geochronology and geospeedometry studies.\

1.4.3 Champtoceaux Complex, Armorican Massif (Brittany)

The Armorican Massif is part of the Variscan collision belt between Laurussia (alias Laurentia *and* Baltica) and the northern margin of Gondwana. Armorica was a microcontinent that rifted away from Gondwana and is now squeezed between the two main land masses. The Armorican Massif is divided into four main domains separated by Late Carboniferous transcurrent shear zones (Jégouzo, 1980; Gumiaux *et al.*, 2004): the Léon domain to the north-west; the North-; the Central-; and the South-Armorican domains (Fig. 1.9).

As summarized by Ballèvre *et al.* (2009) these domains differ by the strain accumulated during Devonian and Carboniferous. The North- and the Central-Armorican domains were part of the continental crust and moderately sheared between two suture zones, whereas the Léon and the South-Armorican have been strongly reworked during the Variscan orogeny (Ballèvre *et al.*, 2009).

The Champtoceaux Complex is a crustal-scale thrust zone in the South Armorican domain between the Nort-Sur-Erdre Fault (NSEF) to the north and the South-Armorican Shear Zone (SASZ) to the south (Fig. 1.10). It consists of stacked, strongly deformed eclogite-bearing gneisses and micaschists (Ballèvre *et al.*, 1989) exhumed during Early Carboniferous (Bosse *et al.*, 2000) and refolded by a large, east-west trending antiform (Marchand, 1981). The complex is interpreted as the trace of the Variscan suture zone between Armorica and Gondwana (e.g. Ballèvre et al., 2009; Pitra *et al.*, 2010) and has been divided into four major units (Fig. 1.10), from bottom to top: the lowermost Parautochthon metagrauwackes of unknown age (Mauves unit) overthrust by the Lower Allochthon. The Lower Allochthon is composed essentially by Ordovician orthogneisses including well-preserved eclogite lenses derived from doleritic dykes (Cellier Unit; Godard, 1988) overlain by garnet-chloritoid-chlorite micaschists (Lower Micaschists), fine-grained Ordovician orthogneisses (St. Mars Unit) and garnet-staurolite micaschists (Upper Micaschist). The Middle Allochton is composed, from bottom to top, by strongly deformed garnet-bearing amphibolites with serpentinized peridotite lenses (Folies Siffait Unit) overlain by metaperidotites and metagabbros (Drain Unit). The upper part of the Middle Allochton consists of chloritoid-chlorite micaschists and amphibolites (Hâvre Unit; Pitra *et el.*, 2010). The Upper Allochthon is formed by migmatitic orthogneisses with few, poorly preserved eclogite lenses and rare metapelites (Pitra *et al.*, 2010). These formations are overlain by metagreywackes of the Mauges Unit (Ballèvre *et al.*, 1989, 2002; Bosse *et al.*, 2000; Pitra *et al.*, 2010).

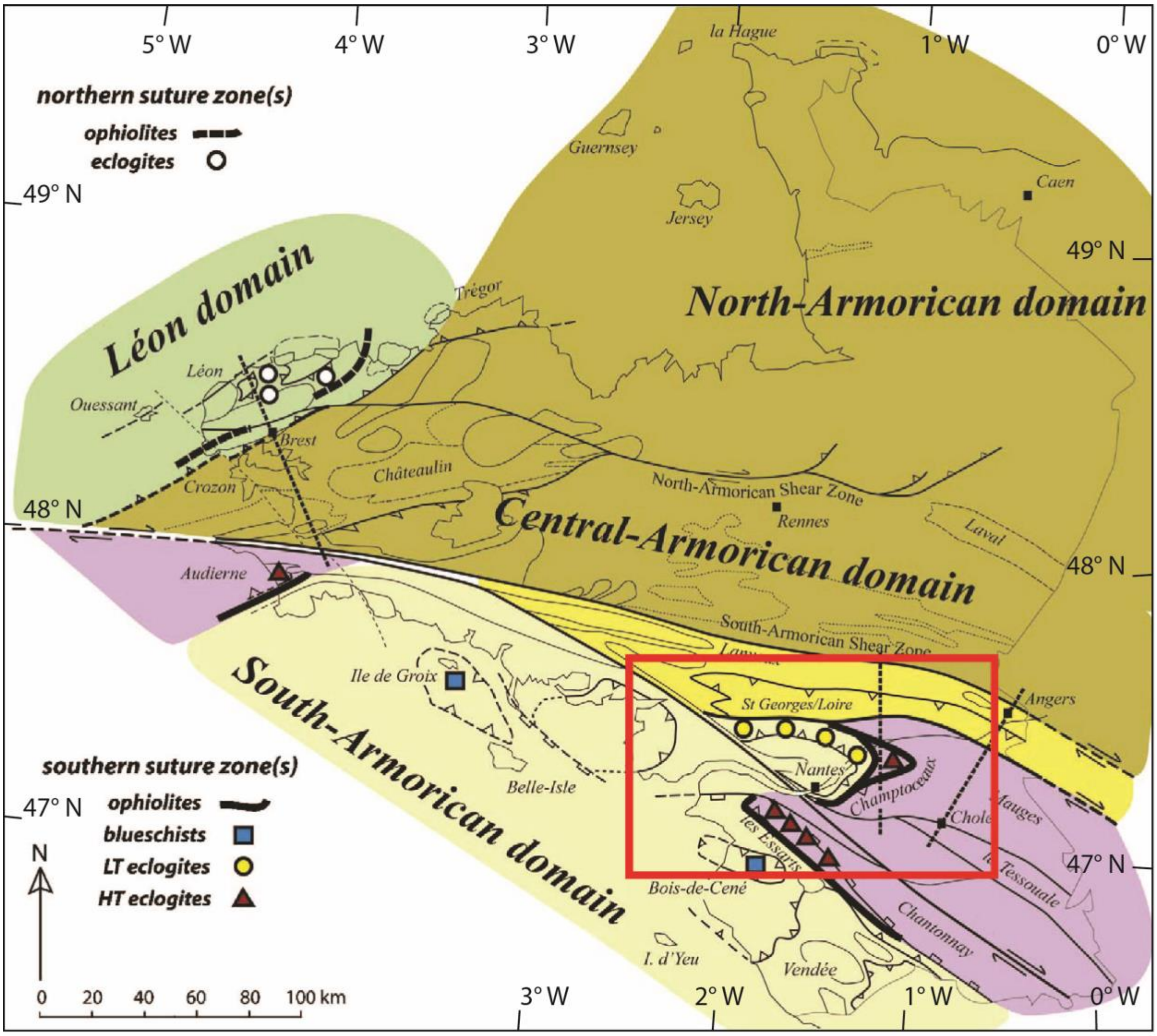

Figure 1.9. Structure of the Armorican Massif. Late Carboniferous shear zones separates the different domains with contrasting deformation histories. Paleozoic rocks of the Armorican Massif were deformed during the Variscan orogeny. Red frame: location of Champtoceaux field study area (*modified from Ballèvre et al., 2009*).

Four main deformational events have been described in the Champtoceaux Complex (Pitra *et al.* 2010; and references therein): ductile deformation (D1) is locally observed in mostly undeformed eclogites lenses. Eclogites host rocks display a penetrative main foliation linked to the D2 event. The third deformation (D3) is related to localized ductile- to semi-ductile shear bands in the Hâvre (Middle Allochton) and Mauges (Upper Allochton) units. The final deformational stage (D4) is associated to dextral strike-slip South-Armorican Shear Zone coeval with Upper Carboniferous two-mica leucogranites intrusions (e.g. Carron *et al.*, 1994). A correlated dextral strike-slip fault system in the north-eastern part of the complex resulted in the regional open fold with easterly-plunging axes (e.g. Pitra *et al.*, 2010).

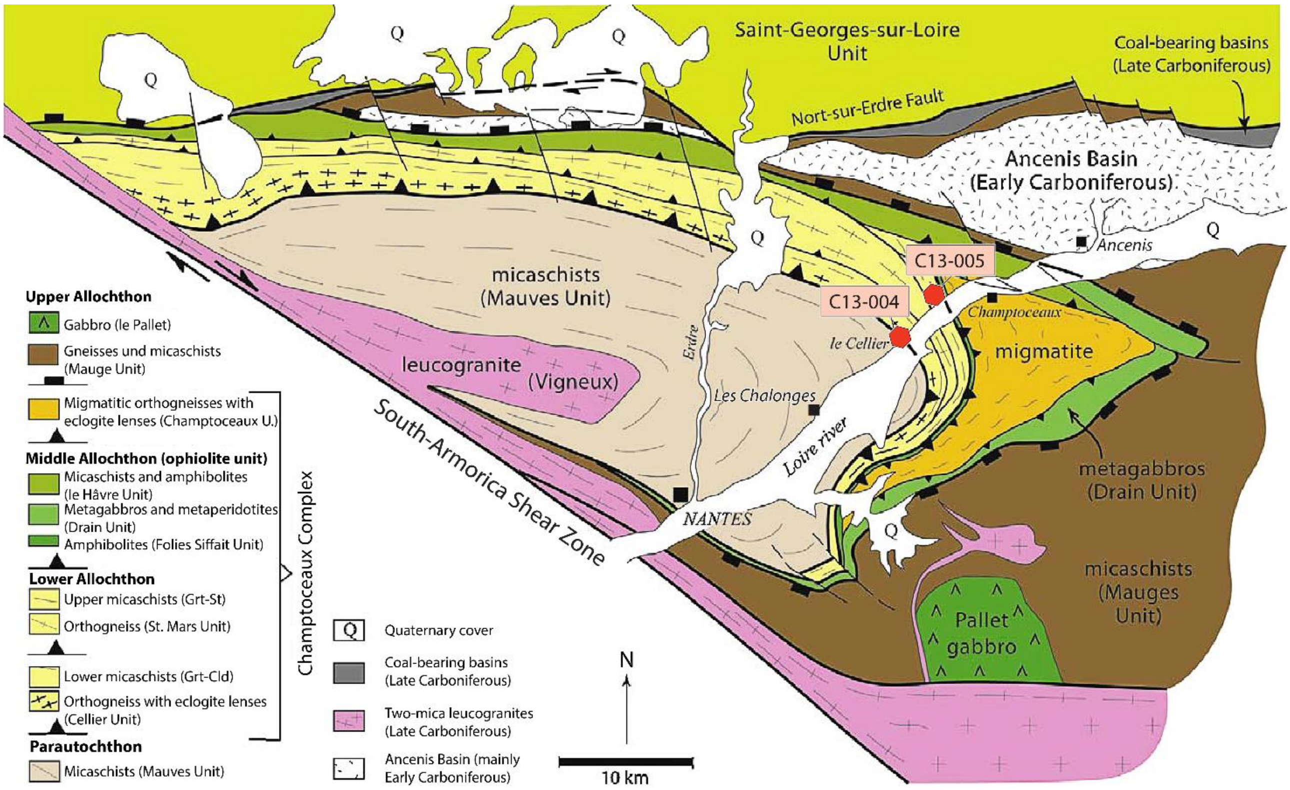

Figure 1.10. Simplified geological and structural map of the Champtoceaux Complex. The Nort-sur-Erdre Fault bounds to the north an antiformal stack of nappes. Two of them (the Cellier and the Champtoceaux Units) contain eclogite lenses, deriving from doleritic dykes intruding a thinned continental crust (*from Ballèvre et al., 2009*).

The *c.* 15 km long investigated section is along the Loire river, starting from Les Chalonges locality in the south-west and finishing near the Ancenis commune in the north-east (Fig. 1.10). The cross-section shows an upward increase in metamorphic grade. From bottom to top, the inverted metamorphic zonation starts in the biotite-chlorite metagreywackes of the Parautochthon ($T < 500$ °C) and increases to garnet-chloritoid-chlorite and garnet-staurolite-biotite assemblages in the Lower Allochthon micaschists (Pitra *et al.*, 2010). Temperature conditions reach $T > 650$ °C in the

Champtoceaux migmatitic orthogneisses, toward the boundary with the Upper Allochthon, (e.g. Ballèvre *et al.*, 2009; Pitra *et al.*, 2010). Pressure conditions (between 0.7 and 1.0 GPa) along the investigated section, suggest that the inverted metamorphic zone in the Champtoceaux Complex is due to the emplacement of a hot nappe over colder units (Pitra *et al.* 2010).

Garnet-bearing rock samples were systematically collected across the transverse for petrographic observations, bulk rock compositions, minerals chemistry and geospeedometry studies.

1.5 Outline of the thesis

This PhD thesis presents field work results, geochronological data and garnet fractionation/diffusion numerical modelling simulations.

Chapter II is dedicated to the inverted metamorphic zonation across the Nestos Shear Zone in the Rhodope Metamorphic Complex. Field observations, structural and petrological descriptions are complemented with U-Pb SHRIMP zircon ages, which specify regional partial melting during the Early Cretaceous (*c.* 144 Ma). This age is in disagreement with some previous assertions, which argued that leucosomes in this region crystallized in the Late Eocene (42-35 Ma). Beside geochronology, *P*-*T* conditions of NTZ rocks were estimated with conventional geothermobarometry supported by phase equilibria modelling and mineral composition contours. Garnet crystals display smoothed composition profiles requiring an inverse-fitting numerical model considering Fractionation and Diffusion in GarnEt (FRIDGE). The model predicts 2 to 6 Myr long peak-*T* conditions.

Chapter III is dedicated to the Main Central Thrust (MCT) in Sikkim, NE India. Geological mapping and detailed geological structural sections define metamorphic conditions estimated using convectional geothermobarometry and phase equilibria modelling including the use of garnet and biotite compositional isopleths for *P*-*T* conditions estimates. Results are consistent with literature. Garnets from different tectonic levels display different compositional zonings in major divalent cations Fe, Mg, Ca and Mn. Compositional profiles of garnet porphyroblasts from the lower part of Lesser Himalaya were (garnet-zone) were simulated with FRIDGE numerical modelling. Garnet porphyroblasts from the MCT exhibit complex zoning patterns reflecting multiple growth. Core compositions in these garnets are almost homogenized making the FRIDGE approach unreliable. In these cases multicomponent diffusion modelling in a sphere was applied with the step function approach. Best-fit garnet compositional profile simulations predict 3 to 6 Myr long peak metamorphic conditions.

Chapter IV focuses on the inverted metamorphic zones in the Champtoceaux region. Difficulties in the Champtoceaux region were the poorly exposed outcrops and the minor amount of large (few mm) zoned garnets. Most of the analysed garnets are fine graine d aggregates with completely homogenized compositional profiles. Few garnet porphyroblasts from the Upper Micaschist in the Lower Allochton formation were suitable for the purpose of this study. Step function garnet diffusion modelling predicted short 0.8 to 3.5 Myr maximal duration for peak metamorphic conditions.

Chapter V combines results of the three investigated collisional settings presented in the thesis to offer a general conclusion. Possible heat sources responsible for the metamorphic inversion and thermo-mechanical scenarios are discussed. This is followed by a brief outlook describing open questions for future research.

2. Conditions, timing and duration of peak metamorphic conditions across the inverted metamorphic sequence of the Nestos Thrust Zone, Central Rhodope (Northern Greece)

Abstract

Thrust tectonics and inverted metamorphic gradients are major consequences of large and likely fast movements of crustal blocks in compressional environments. The purpose of this study is to investigate the tectonic setting and the duration of peak metamorphic conditions of the inverted metamorphic zonation related to crustal-scale thrusting at the Nestos Thrust Zone in the Rhodope Metamorphic Complex, Northern Greece.

Conventional geothermobarometry, phase equilibria modelling and garnet chemical compositions indicate upwards increase of temperature from *c.* 670 up to *c.* 750 °C at pressure of 0.85 ± 0.15 GPa. Peak metamorphic conditions are coincident with top-to-SSW shearing and the main fabric formation.

U-Pb Sensitive High Resolution Ion Microprobe (SHRIMP) zircon geochronology on leucosomes from migmatitic orthogneisses specifies regional metamorphic (re)crystallization during Late Jurassic - Early Cretaceous (*c.* 142 Ma) and Eocene (*c.* 51 Ma) granitoid magmatism. ^{40}Ar/^{39}Ar dating yields Late Eocene - Early Oligocene (40 - 30 Ma) cooling (< 350 – 400 °C) in Drama and Xanthi regions where local thermo-deformation events are linked to late and post-orogenic intrusions.

Garnet geospeedometry is applied on syn-tectonic garnets to determine the absolute time of peak thermal perturbation during deformation. Inverse-fitting numerical model considering Fractionation and Diffusion in GarnEt (FRIDGE) simulates garnet major cations (Fe – Mg – Ca – Mn) composition profiles by introducing *P*-*T*-*t* path and XRF derived bulk-rock composition of a specific sample. The model calculates pre-diffusion cations configuration and simultaneous diffusional relaxation at $T >$ 600 °C. Numerical simulations are then compared with measured garnet profiles.

FRIDGE results reveal short lived (2 - 8 Myr) peak metamorphic conditions. The short-lived thermal perturbation suggests that viscous/shear-heating may be responsible for the inversion of isograds across the Nestos Thrust Zone in the Rhodope collisional system.

2.1 Introduction

Estimating the duration of peak metamorphic conditions may improve interpretations of inverted isograds across major faults. Models of conductive thermal relaxation in tectonically thickened crust suggest that peak metamorphic conditions should last at least *c*. 40 million years in collisional orogenic belts (Thompson and England, 1984). However, structural, petrologic, isotopic and intracrystalline diffusion studies suggest that metamorphic processes may operate over much shorter timescales (less than a few millions of years; Camacho *et al.*, 2005; Dewey, 2005; Ague and Baxter, 2007; Caddick *et al.*, 2010). This implies that the thermo-mechanical evolution, the origin and the nature of regional metamorphic heat in collisional settings remain enigmatic and represent an important gap in understanding orogenic processes.

The purpose of this study is to investigate the tectonic setting of inverted metamorphic zones related to crustal-scale thrusting along the Nestos Thrust Zone (NTZ) in the Rhodope Metamorphic Complex, Northern Greece (Fig. 2.1). The motivation is to contribute to the understanding of the link between mechanical and thermal evolutions of this ductile thrust zone and clarify the nature and the origin of orogenic heat.

The analytical tool applied to estimate the duration of peak temperature (T) conditions is garnet geospeedometry (Lasaga, 1983), which considers modifications in garnet compositional zoning caused by intracrystalline diffusion during metamorphism (Lasaga, 1983; Spear *et al.*, 1984; Perchuk and Phillipot, 2000; Ague and Baxter, 2007; Caddick *et al.*, 2010; Viete *et al.*, 2011, Ague and Carlson, 2013).

2.2 Geological setting

The Rhodope Metamorphic Complex (RMC) is a *c*. 300 x 300 km open antiform bounded to the southwest by the Dinarides - Hellenides in Greece and to the north by the Balkan Belt in Bulgaria (e.g. Burchfiel, 1980, Burg *et al.*, 1996). It is bordered to the west by the Serbo-Macedonian Massif, to the east it disappears below Eocene-Oligocene (locally Maastrichtian) sedimentary cover (Ricou *et al.*, 1998), and to the south it plunges in the Aegean Sea (Fig. 2.1).

The RMC is a segment of the Alpine-Himalaya orogenic belt formed during collision between the "Drama" continental fragment and the Moesian platform during Late Jurassic and Early Cretaceous times, causing south-southwest thrusting and stacking of nappes (Robertson *et al.*, 1991, Burg *et al.*, 1996; Ricou *et al.*, 1998, Burg, 2011). The RMC is simplified in three major structural levels: the Lower, the Middle (Imbricate) and the Upper Terranes (Fig. 2.1, Burg *et al.*, 1990).

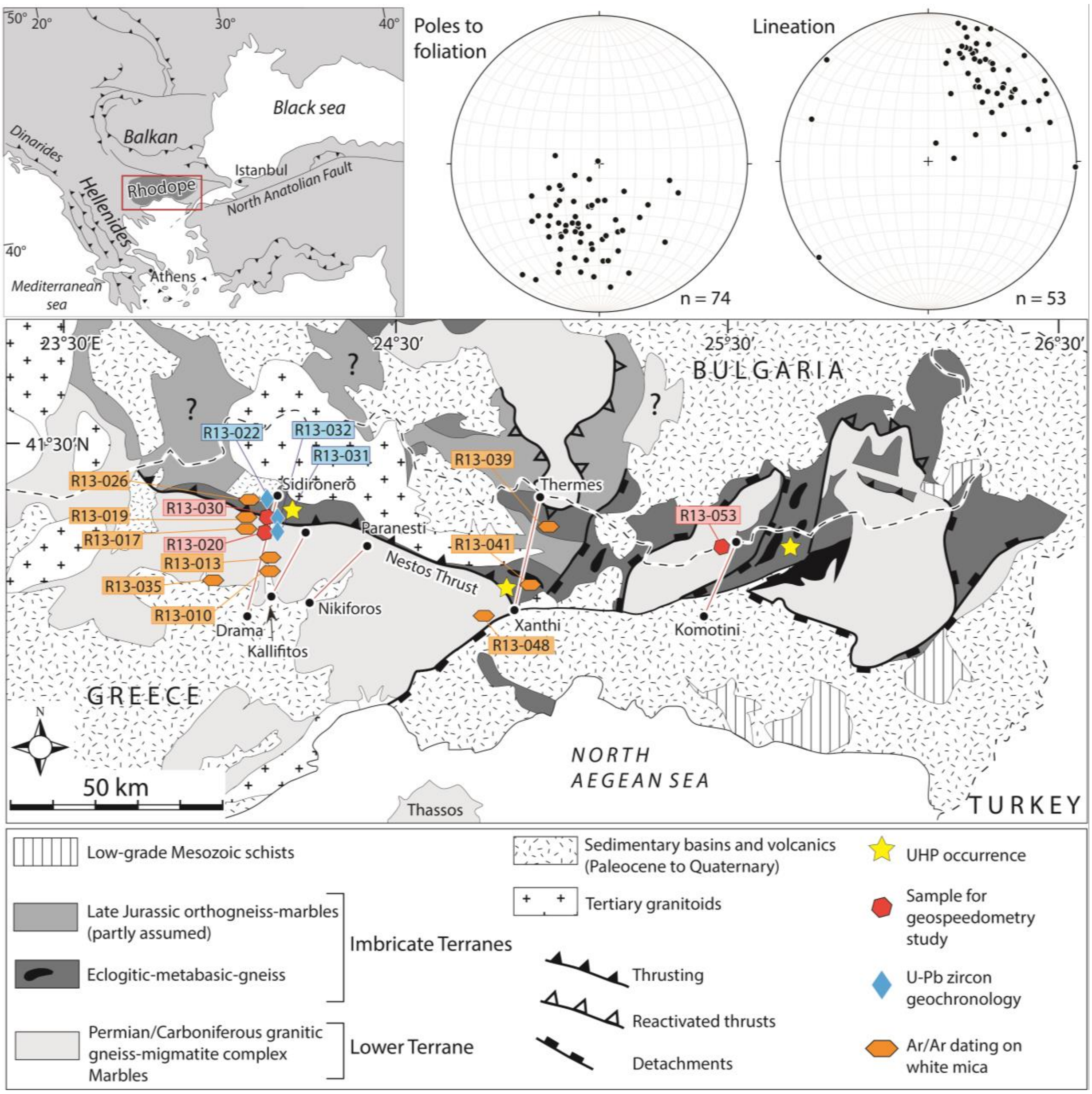

Figure 2.1. Sketch map of the main tectonic units of the Rhodope Metamorphic Complex (*modified after Burg et al., 1996; Turpaud, 2006; Krenn et al., 2010*) and locations of the investigated sections. Yellow stars: locations of garnets-bearing micro- and nanodiamonds inclusions related to Ultra-High Pressure (UHP) (*after Liati, 2005; Turpaud, 2006; Perraki et al., 2006*). Red dots: locations of garnet-bearing rocks used for geospeedometry studies. Blue diamond: samples for zircon U-Pb dating. Orange bullets: samples for ^{40}Ar/^{39}Ar cooling dating. On top: (*left*) location of the RMC; (*right*) stereographic projections of poles to foliation and stretching lineations considering Drama, Kallifitos, Nikiforos and Xanthi sections (lower hemispheres, n = number of measurements, program: Stereonet).

The Lower Terrane (also called Drama window) is mainly composed of, from bottom to top, orthogneisses, massive sequence of marbles interlayered with schists, leucocratic orthogneisses and paragneisses interlayered with marbles and micaschists. Metamorphic facies varies up-section from upper greenschist to amphibolite facies (e.g. Papanikolaou and Panagopoulos, 1981; Mposkos *et al*., 1989; Burg *et al*., 1996; Burg, 2011).

The Middle (Imbricate) Terranes consist of several imbricate slivers of migmatitic orthogneisses, lenticular bodies of amphibolitized eclogites and peridotites, paragneisses, micaschists and marbles (e.g. Ivanov *et al.*, 1988; Burg *et al.*, 1996 and references therein). These imbricates represent a dismembered suture within the SSW thrust placing the high grade rocks over low grade Lower Terrane (Burg et *al.*, 1996; Burg, 2011). The suture interpretation is based on amphibolites with oceanic affinities (Kolceva *et al.*, 1986; Liati, 1986; Barr *et al.*, 1999) and ultramafic lenses associated to high pressure (HP) and ultra-high pressure (UHP) metamorphic conditions (e.g. Burg *et al*., 1996a; Ricou *et al*., 1998; Krenn *et al*., 2000; Liati *et al.*, 2004). Exsolution of quartz, rutile, apatite, micro- and nano-diamonds inclusions in garnet porphyroblasts have been reported in places (Fig. 2.1; Mposkos and Kostopoulos, 2001; Liati 2005; Schmidt *et al*., 2010) and interpreted as consequences of UHP conditions peak metamorphic event in the RMC (Mposkos and Kostopoulos, 2001; Perraki *et al.*, 2006). The Imbricates are intruded by Late Cretaceous to Middle Tertiary granitic intrusions (Ovtacharova *et al*., 2003).

The Upper Allochthon is mostly composed by quartzo-feldspatic migmatites containing bodies of basic and ultramafic rocks, including eclogites retrogressed into amphibolite facies (e.g. Burg, 2011).

Thrusting converted into extensional tectonics during Maastrichtian-Paleocene in eastern Rhodope (Bonev *et al.,* 2006). Structural and geochronological studies confirmed that the crystalline RMC includes Cenozoic metamorphic core complexes exhumed during a protracted extensional history since Late Cretaceous until Late Neogene (Bonev *et al.,* 2006; Brun and Sokoutis, 2007). Eocene-Oligocene extension developed grabens, metamorphic domes and voluminous magmatism and volcanism (e.g. Baker and Liati, 1991; Jones *et al*., 1992; Burg, 2011). Middle Miocene through Early Pliocene extension produced later grabens and detachment faults predominantly on the southern flank of the RMC (e.g. Dinter and Royden, 1993; Sokoutis *et al.*, 1993, Burg, 2011).

The north-dipping Nestos Thrust Zone (NTZ) extends for about 100 km from Xanthi to the east to the Mesta basin to the west. It is a > 1 km thick pile of mylonites with bulk top-to-the-south sense of shear criteria (e.g. Kilias and Mountrakis, 1990; Burg *et al.*, 1996) between the Lower Terrane in the footwall and high grade, eclogites-bearing migmatitic Imbricates in the hanging wall (Burg *et al*., 1996; Nagel *et al*., 2011). Inverted isograds, starting from greenschist facies in the lowest structural level of the Lower Terrane, up to sillimanite-bearing migmatites toward north against the NTZ (e.g. Mposkos *et al*., 1989; Burg *et al*., 1996).

Five sections across the NTZ have been studied: Drama, Xanthi, Kallifitos, Mesochori and Komotini. Locations and structural measurements are presented in Fig. 2.1. Rock samples were collected along the Drama, Xanthi and Komotini sections for petrographic observations, bulk rock compositions, minerals chemistry, geochronology and garnet fractionation/diffusion modelling. Geothermobarometry supported by phase diagram section calculations was carried on pelitic samples. Leucocratic dikes and leucosome from migmatitic orthogneisses located north of Drama were dated to constrain the ages of zircon (re)crystallization during peak metamorphic conditions. ^{40}Ar/^{39}Ar dating on white micas defining the foliation was performed to determine cooling ages.

2.3 Lithological and structural characteristics

Along the Kallifitos and Mesochori sections (Fig. 2.1) massive marbles and orthogneisses are the dominant rock type. Garnet-bearing rocks were not found. Therefore, focus has been given to the *c*. 21 km long SSW-NNE Drama - Sidironero transverse across the Lower- and the Imbricate Terranes (Fig. 2.2). Along this section rocks are well exposed offering a complete exposition of the inverted Barrovian sequence. The metamorphic grade increases from low grade chlorite-epidote-biotite in the south, to medium grade biotite-garnet-kyanite upward against the NTZ, and migmatites in the Imbricate Terrane hanging wall.

Structures and main lithologies representing the Lower and the Imbricate Terranes are described from the bottom (in the south) toward higher structural levels (in the north), following the inverted sequence from low grade up to medium- high-grade metamorphic rocks (Fig. 2.2). Sample description, mineral assemblages and locations are given in Table 2.1.

Additional garnet-bearing rocks from the Imbricate Terranes across the Xanthi section and in the Komotini area were investigated as elements of comparison for *P-T* conditions estimates and/or garnet geospeedometry study.

2.3.1 Field relations, structural descriptions

All lithologies exhibit an intense penetrative foliation striking 033° ± 15°E and dipping 35° ± 14°N, but becomes almost vertical to the north, near the Sidironero locality (Figs. 2.1 and 2.2). Elongated biotite, white micas and strained feldspar mineral define the NNE-SSW stretching lineation (Fig. 2.1). Rocks are rich in kinematic indicators that persistently reveal top-to-SSW sense of shear (e.g. Kilias and Mountrakis, 1990). The NNE-dipping gneissic pile is overprinted by extensional detachment shear zones and intruded by pre-, syn-, and post-foliation granitoids (e.g. Burg, 2011).

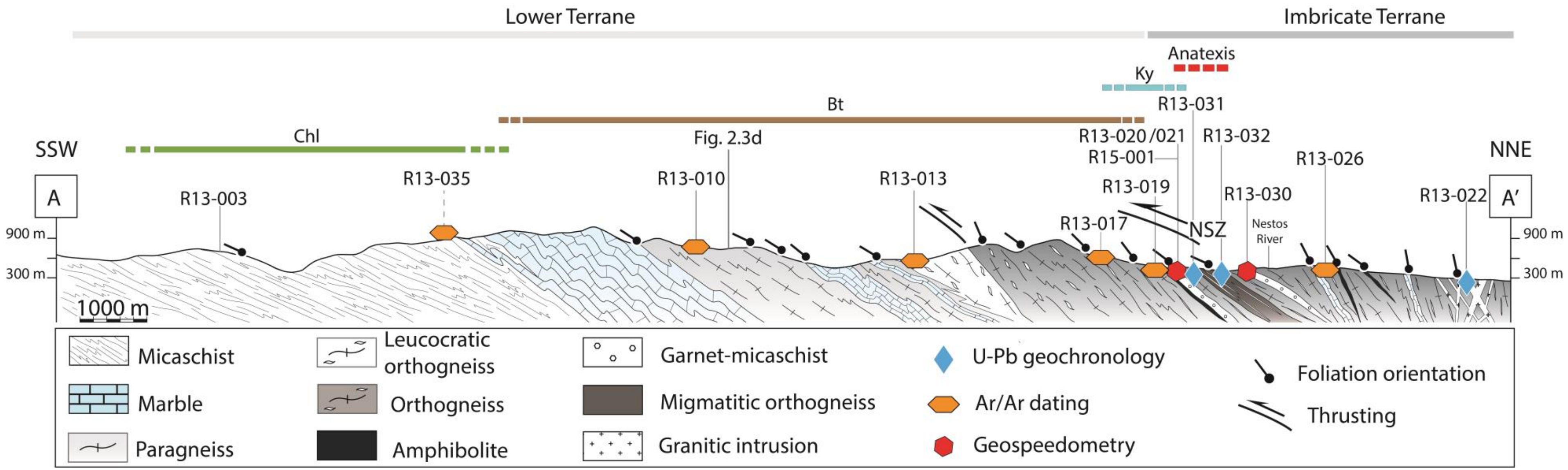

Figure 2.2. Drama-Sidironero cross section (location Fig. 2.1) across the Nestos Thrust Zone (NTZ) showing the inverted metamorphic zone. Sample location for $^{40}Ar/^{39}Ar$ dating (orange bullets), U-Pb SHRIMP geochronology (blue diamonds) and garnet geospeedometry investigations (red dots).

2.3.1.1 Lower Terrane

Micaschists (metamarls): Micaschists are one of the dominant rock types in the southern part of the Drama - Sidironero section (Fig. 2.2). This lithology is heterogeneous in grain-size and composition, in particular in biotite content yielding weathering colour variations from light-brow – orange in the south to brown – dark-grey towards north. Moving upwards, they locally contain up to 50 cm thick interlayered marble sheets, interpreted as the original sedimentary transition from terrigenous to carbonate sediments. Folds are generally facing SSW (Fig. 2.3a) indicating a normal succession in the south-south westward sheared area.

Marbles: Moving northwards up-section graphitic marble layers (up to 50 cm thick), interlayered within micaschists (metamarls), thicken in a 1.5 km thick marble sheet (Fig. 2.2). The fine- to middle-grained marbles are variably foliated and folded (Fig. 2.3b). Up-section, 10 up to 30 m thick metacarbonate layers are interlayered with the overlaying paragneisses (Fig. 2.2). This alternation of marbles and paragneisses may represent the original sedimentary evolution.

Paragneisses: About 1.5 km thick sequence of paragneisses overlies and is interlayered with marbles (Fig. 2.2) suggesting continuity in the sedimentary transitional zone. Paragneisses are heterogeneous in composition and grain size. Normal graded bedding is occasionally defined by changes in grain size and/or chemical composition, i.e. weathering colours (Fig. 2.3c). Paragneisses become more psammitic (± calcite) up-section and are interlayered with fine grained pelitic layers rich in white mica (Figs. 2.3d and location in 2.2).

Orthogneisses: c. 2 km thick non-migmatitic orthogneisses represent old intrusions in paragneisses. They are leucocratic at the base (albite-gneiss unit of Krohe and Mposkos, 2002). Contacts with the lower paragneisses are intrusive. The upper part is predominantly composed by augen- and biotite-gneisses locally displaying drag-folds showing top-to-south direction of shearing (Fig. 2.3e). Contact between albite-gneiss and biotite-gneiss is strongly tectonized. Upwards, approaching the NTZ, orthogneisses display mylonitic textures characterized by fine grains and strongly strained feldspar porphyroclasts.

Garnet-micaschists: 15 to 30 m thick layers of garnet-micaschists occur above orthogneisses in the Drama-Sidironero traverse (Fig. 2.2). These micaschists are strongly foliated, boudinaged and interlayered with thin (up to few metres) mylonitic orthogneisses and meter scale amphibolite layers (Fig. 2.3f). This mylonitic zone is interpreted as the tectonic boundary between the Lower- and the Imbricate Terrane, i.e. the NTZ (Fig. 2.2). Similar lithologies have been mapped in the Xanthi region and are described in details by Krenn *et al.* (2010) and in Turpaud and Reischmann, (2010).

Table 2.1 Provenence, mineral assemblage, metamorphic grade and purpose of the investigated samples

Sample*	Coordinates	Structural unit	Rock type	Mineral assemblage	Metamorphic grade	Purpose
R13-010	N 41° 15' 54.6" E 24° 12' 31.0"	Lower Terrane	Metapsammite	qtz, pl, ms, bt, op	greenschist facies	Ar/Ar dating
R13-013	N 41° 17' 09.6" E 24° 12' 33.5"	Lower Terrane	Metapsammite	qtz, pl, ms, chl, op	greenschist facies	Ar/Ar dating
R13-017	N 41° 19' 17.6" E 24° 12' 37.3"	Lower Terrane	Orthogneiss	pl, qtz, ms, bt, op	greenschist facies	Ar/Ar dating
R13-019	N 41° 20' 15.1" E 24° 12' 24.8"	Lower Terrane	Orthogneiss	pl, qtz, kfs, bt, op	amphibolite facies	Ar/Ar dating
R13-020	N 41° 20' 18.5" E 24° 12' 29.2"	Lower Terrane	Grt-amphibolite	grt, amph, pl, qtz, bt, op	amphibolite facies	*P*-*T* estimates Geospeedometry
R13-022	N 41° 21' 49.3" E 24° 13' 21.9"	Imbricate Terrane	Leucogranit	pl, qtz, kfs, bt, op	amphibolite facies	U-Pb Geochronology
R13-026	N 41° 21' 12.0" E 24° 12' 15.0"	Imbricate Terrane	Orthogneiss	pl, kfs, qtz, ms, bt epi, op	amphibolite facies	Ar/Ar dating
R13-030	N 41° 20' 47.6" E 24° 11' 55.9"	NSZ	Grt-micaschist	grt, bt, ms, pl, kfs qtz, op	amphibolite facies	*P*-*T* estimates Geospeedometry
R13-031	N 41° 20' 25.3" E 24° 12' 28.6"	NSZ	Migmatitic orthogneiss	pl, kfs, qtz, bt	amphibolite facies	U-Pb Geochronology
R13-032	N 41° 20' 28.4" E 24°12' 20.4"	NSZ	Migmatitic orthogneiss	pl, kfs, qtz, bt	amphibolite facies	U-Pb Geochronology
R13-035	N 41° 15' 24.1' E 24° 01' 28.4"	Lower Terrane	Micaschist	mu, pl, qtz, kfs bt, op	amphibolite facies	Ar/Ar dating
R13-037	N 41° 21' 19.6" E 24° 58' 07.9"	Imbricate Terrane	Grt-ky-micaschist	grt, ky, bt, ms, pl, kfs, qtz, op	amphibolite facies	*P*-*T* estimates
R13-039	N 41° 17' 59.8' E 24° 57' 39.1"	Imbricate Terrane	Migmatitic orthogneiss	pl, kfs, qtz, bt	amphibolite facies	Ar/Ar dating
R14-041	N 41° 11' 22.4" E 24° 51' 38.4"	Imbricate Terrane	Grt-micaschist	grt, pl, kfs, ms, bt, qtz, ttn, ap, op	amphibolite facies	Ar/Ar dating
R13-048	N 41° 06' 45.0" E 24° 45' 31.4"	Imbricate Terrane	Metapsammite	pl, qtz, kfs, ms, op	amphibolite facies	Ar/Ar dating
R13-053	N 41° 14' 38.0" E 25° 30' 37.1"	Imbricate Terrane	Grt-ky-micaschist	pl, qtz, kfs, ms, bt, ap, zrn, op	amphibolite facies	*P*-*T* estimates Geospeedometry

*From south toward north

Mineral abbrevation as Kretz (1983): qtz - quartz; pl - plagioclase; kfs - K feldspar; bt - biotite; ms - muscovite; chl - chlorite; grt - garnet; st - staurolite; ky - kyanite; sil - sillimanite; mag - magnetite; ap - apatite; zrn - zircon; epi - epidote; ttn - titanite; op - opaque.

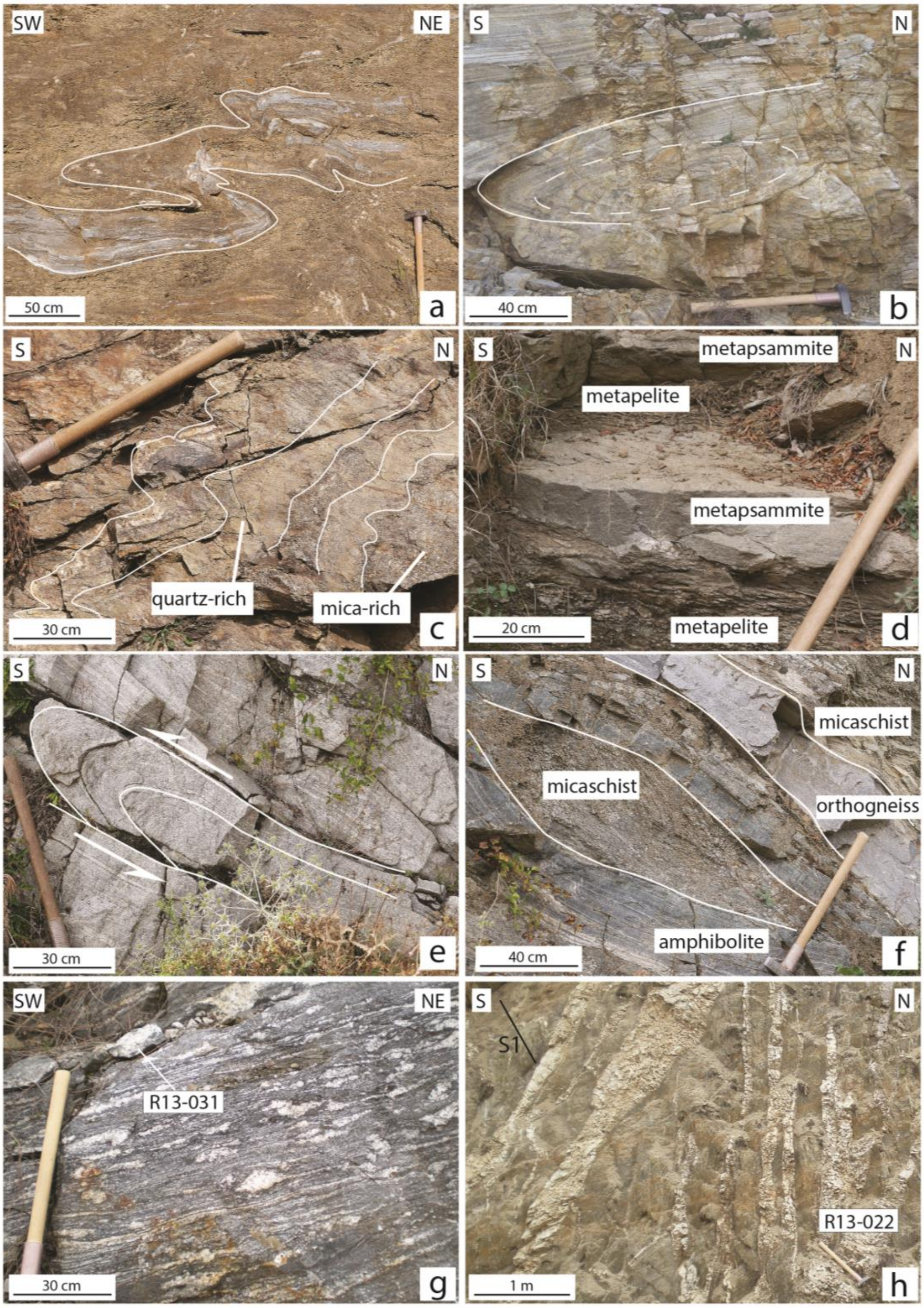

Figure 2.3. **a)** *(41°12’09.5”, 24°10’57.4”)* Folded marble layer within micaschist (metamarls). **b)** *(N41°16’11.2”, E24°12’29.0”)* Graphitic marble display a closed sheath-fold. **c)** *(N41°16’03.3”, E24°12’00.8”)* Sedimentary layering in paragneisses emphasized by white lines. **d)** *(N41°15’59.0”, E24°12’00.7”)* Metapsammite interlayered with fine grained metapelite. **e)** *(N41°15’59.0”, E24°12’00.7”)* Drag-fold along a shear plane in migmatitic orthogneiss. **f)** *(N41°20’30.9”, E24°12’49.0”)* Ductile shear zone in the Imbricate Terrane with micaschists asymmetric boudin. Micaschists alternate with amphibolite and orthogneisses layers. **g)** *(N41°20’25.3”, E24°12’28.6”)* Migmatitic orthogneiss. Sample *R13-031* collected for U-Pb geochronology. **h)** *(N41°21’49.3”, E24°13’21.9”)* Granitoid dikes in orthogneisses. Sample *R13-022* for U-Pb geochronology.

2.3.1.2 Intermediate thrust sheet

Migmatitic-orthogneisses: From 50 up to 70 m thick sheets of migmatitic-orthogneiss are observed in the north part of Drama-Sidironero section in the NTZ hanging wall (Fig.2.2). The rock is greyish, coarse grained and mainly composed of quartz, plagioclase, alkali feldspar and biotite. The texture is equigranular and fluidal. Leucosomes range from few mm up to 20 cm in thickness and define the main gneissic layering (Fig. 2.3g). They locally cut the foliation and delineate fold hinges. Samples *R13-031* (Fig. 2.3g) and *R13-032* (Fig. 2.2) were collected from different structural levels for geochemistry analysis and U-Pb SHRIMP zircon geochronology presented in section 2.5.

Amphibolite and metabasite lenses: Along the Drama section, foliated to mylonitic mafic lenses have been observed on the south and north side of the Nestos river (Fig. 2.2). These rocks are predominantly composed of hornblende, plagioclase, quartz, epidote ± diopside, titanite and locally garnet porphyroblasts. Garnets from a mafic body near the NTZ (*R13-020*) have been investigated for geospeedometry (Fig. 2.1).

Calc-silicate: Calc-silicates occur as 10 - 30 m thick layers within orthogneisses north of the Nestos River in the Intermediate Terrane (Fig. 2.2). Microscopic observation reveals that middle- to coarse grained calcite is infiltrated by veins of fibrous wollastonite.

Granitic intrusion: Further north, near the Sidironero locality, biotite-gneisses are intruded by syn- to post-tectonic coarse-grained leucocratic granitoids displaying folds and boudinage structures. These rocks are related to the Skaloti pluton located in the north part of Sidironero (Fig. 2.1). The intrusive contacts are discordant to the main regional foliation (Fig. 2.3h). Rock sample *R13-022* was collected for bulk-rock chemical composition and U-Pb SHRIMP geochronological dating (section 2.5).

2.3.2 Mineralogical description

Six representative rocks from low grade zone (*R13-003* and *R13-015*) in the south, to the medium-high grade NTZ shear zone in the north (*R13-020*, *R13-021*, *R15-001* and *R13-030*) are described. Mineral assemblages and sample locations are given in Table 2.1 bulk rock compositions are given in Table 2.2. Particular attention is given to garnet-bearing rocks. Garnet-micaschist samples (*R13-021; R15-001; R13-030*) were collected at different horizons for bulk-rock and mineral chemistry, garnet porphyroblast investigations and fractionation/diffusion modelling.

R13-003: Micaschists have a main foliation defined by fine grained muscovite, stilpnomelane and elongated plagioclase and quartz crystals. The presence of calcite, abundant muscovite, chlorite ± gypsum suggest a calcareous clay-rich (marl) protolith (Fig. 2.4a). Locally the rock is cut by mm thick calcite veins. Up-section, chlorite is replaced by biotite, denoting increase in metamorphic conditions.

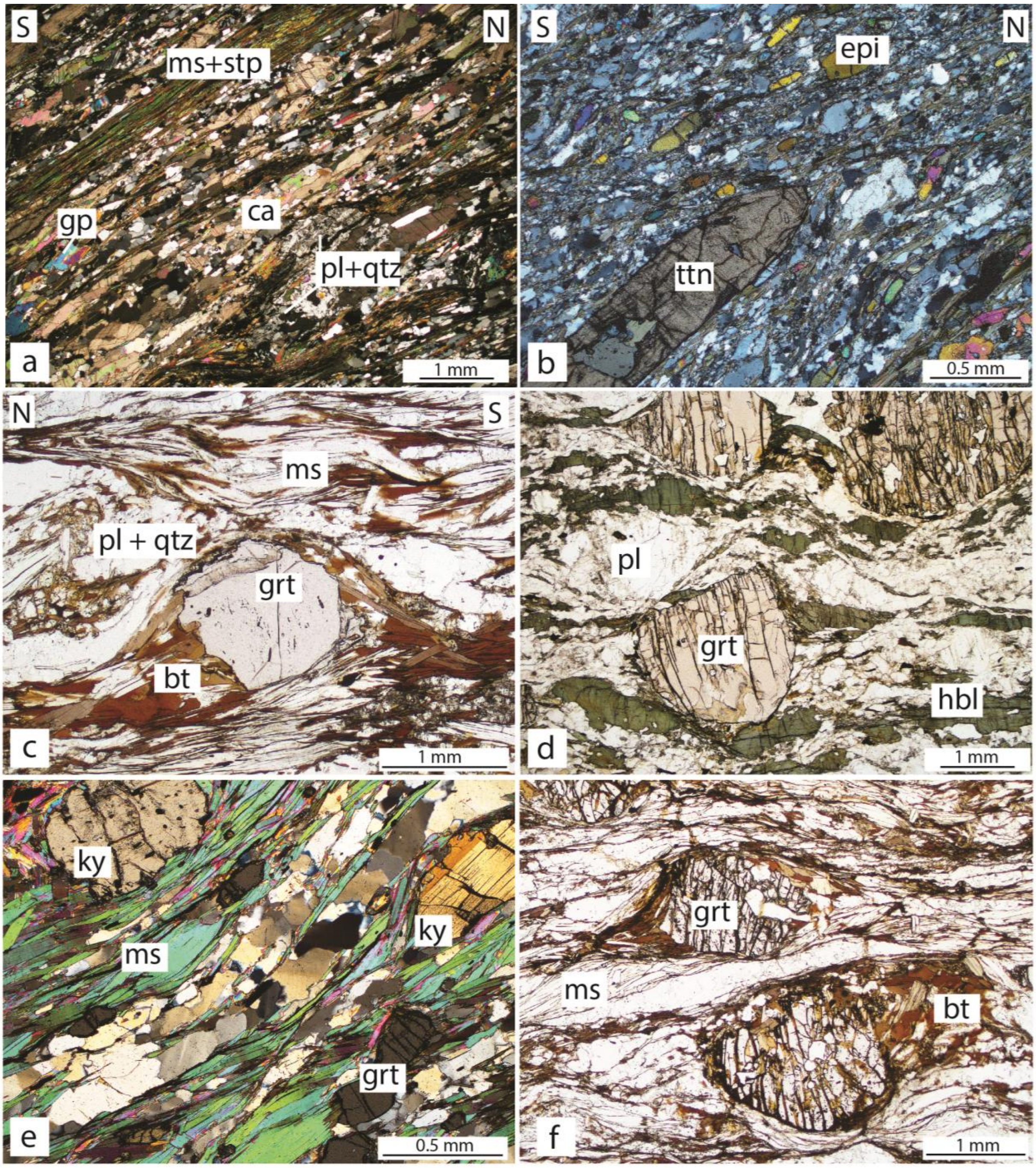

Figure 2.4. Photomicrographs of representative rocks upward through the inverted metamorphic zone of the Nestos Thrust Zone. Mineral abbreviations as in Kretz (1983). **a)** *R13-003* Fine grained metamarls (cross-polarized light). **b)** *R13-015* Fine-grained orthogneiss with foliation defined by elongated epidote, recrystallized quartz and titanite (cross-polarized light). **c)** *R13-021* Pre- to syn-Kinematic garnet with biotite stain shadow. **d)** *R13-020* Garnet amphibolites **e)** *R15-001* Main foliation in garnet micaschist defined by muscovite, recrystallized quartz and elongated kyanite (cross-polarized light). **f)** *R13-030* Fractured garnets, rich in quartz inclusions, partially pseudomorphed to biotite (transmitted light).

R13-015: Foliation of bottom fine-grained orthogneiss horizons is defined by equigranular elongated epidote, recrystallized quartz, plagioclase, biotite, K-feldspar and large titanite crystals (Fig. 2.4b).

R13-020: Amphibolite lenses in garnet-micaschists are mostly composed by plagioclase, amphibole, minor quartz, ilmenite and rutile (Fig. 2.4d). Garnet porphyroblasts ranging from < 1mm to 4 mm in size. Garnet fractures are filled with biotite and chlorite. Cores display large quartz and minor rutile inclusions.

R13-021: Main foliation of middle- to coarse-grained garnet-micaschists collected at upper structural level of the Lower terrane against the NTZ (Fig. 2.2) is defined by biotite, white mica, minor elongate plagioclase and recrystallized quartz grains (Fig. 2.4c). Biotite occurs along cracks and/or replaces garnet rims. Quartz inclusion patterns define an internal schistosity connected to the matrix foliation. This textural relation suggests syn-tectonic crystallization of garnet.

R15-001 and R13-030: Garnet-kyanite micaschists *R15-001* from higher structural level of footwall near the NTZ is characterized by rounded from < 1 mm to 12 mm in size garnets and up to 2 mm long euhedral kyanite crystals (Fig. 2.4e). Kyanite is observed only in few horizons. Garnet porphyroblasts sizes and distribution are heterogeneous. Inclusions are mostly quartz, plagioclase and ilmenite. Kyanite is found in few layers. Micaschists *R13-030* was collected above migmatitic orthogneisses, south of the Nestos River (Fig. 2.2). These schists are characterized by < 1 mm to 5 mm, idioblastic to xenoblastic large porphyroblasts generally rich in quartz, plagioclase, biotite and ilmenite inclusions (Fig. 2.4f). No alumina silicate was found. Biotite replaces rims or large volume of garnet crystals. A general characteristic is garnet fragmentation.

Similar garnet-kyanite micaschists were observed in Xanthi, Thermes and Komotini regions (Fig. 2.1) and described in Krenn *et al*. (2010). Garnet porphyroblasts range from < 1 to 10 mm in diameter in Komotini section and from few mm up to 10 cm in the Xanthi region (e.g. Krenn *et al*., 2010).

Table 2.2 XRF-derived and effective bulk rock compositions

Sample		R13-010	R13-011	R13-013	R13-017	R13-019	R13-020		R13-022	R13-026	R13-030	
							XRF	Effective			XRF	Effective
SiO2	wt.%	76.20	49.96	79.91	75.39	75.24	59.10	58.42	75.29	74.05	71.12	70.58
TiO2	wt.%	0.28	2.16	0.17	0.09	0.17	0.70	0.70	0.01	0.34	0.33	0.33
Al2O3	wt.%	11.51	13.91	11.01	14.02	12.85	14.32	13.93	15.41	12.37	15.01	14.71
FeO	wt.%	2.21	13.54	1.18	1.02	1.68	9.82	9.27	0.07	3.32	2.40	1.99
MnO	wt.%	0.02	0.21	0.01	0.04	0.02	0.13	0.11	0.00	0.04	0.06	0.05
MgO	wt.%	0.74	5.95	0.24	0.16	0.65	5.13	5.07	0.02	0.77	0.77	0.70
CaO	wt.%	0.12	9.39	0.08	0.56	0.38	6.62	6.50	2.30	0.61	2.00	1.92
Na2O	wt.%	1.69	2.67	1.02	3.42	3.83	3.10	3.10	5.75	3.00	3.88	3.88
K2O	wt.%	4.50	0.53	4.92	4.17	4.48	0.28	0.28	1.07	4.60	3.48	3.48
LOI	wt.%	1.41	1.45	1.26	1.08	0.60	0.48	0.48	0.49	0.64	0.73	0.73
Total		98.68	99.78	99.80	99.94	99.90	99.67	97.86	100.40	99.75	99.78	98.37
Traces (Input=Output)												
Rb	ppm	156.40	19.90	172.10	305.20	117.60	10.30		20.80	171.90	128.00	
Ba	ppm	868.00	102.70	821.00	103.40	289.10	41.80		230.60	661.70	464.20	
Sr	ppm	117.50	259.70	86.10	58.40	57.60	148.50		312.50	45.00	167.50	
Nb	ppm	9.90	7.40	6.00	22.80	9.90	4.00		2.50	11.30	10.60	
Zr	ppm	133.70	149.90	83.10	43.40	204.90	37.70		0.00	501.70	99.10	
Hf	ppm	7.30	6.90	4.50	3.80	8.30	4.20		3.40	17.30	5.90	
Y	ppm	17.00	37.00	14.20	6.90	37.40	25.00		1.60	70.90	17.40	
Ga	ppm	29.20	36.70	24.20	42.20	33.70	15.20		22.60	35.00	33.30	
Zn	ppm	28.00	109.40	20.20	35.60	34.10	47.00		3.90	98.80	39.60	
Cu	ppm	7.40	52.40	2.20	8.30	3.30	38.90		0.00	12.40	4.20	
Ni	ppm	16.70	28.40	8.90	10.20	8.90	33.80		1.30	19.60	16.00	
Co	ppm	12.50	42.10	19.90	18.30	18.10	42.70		20.30	12.20	16.50	
Cr	ppm	16.00	178.60	9.90	3.10	5.30	35.90		2.10	5.80	12.80	
V	ppm	38.60	352.00	28.70	8.00	10.20	287.20		1.20	15.30	40.00	
Sc	ppm	2.80	43.50	6.40	5.80	4.80	35.00		2.20	14.60	5.60	
La	ppm	38.70	0.00	25.20	12.70	40.50	0.00		1.70	57.50	9.60	
Ce	ppm	63.40	64.80	45.90	0.00	71.20	0.00		0.00	156.70	28.50	
Nd	ppm	28.50	29.80	23.50	6.80	31.10	14.40		9.10	58.70	17.50	
Pb	ppm	45.60	38.70	41.00	44.50	43.10	6.40		13.10	47.00	49.70	
Th	ppm	20.30	0.00	9.20	3.90	18.00	2.80		0.10	20.10	10.50	
U	ppm	2.40	0.00	1.20	3.70	2.70	0.00		0.00	2.60	1.40	
W	ppm	n.d.	n.d.	n.d.	n.d.	n.d.	183.70		n.d.	n.d.	n.d.	

Table 2.2 (continued)

Sample		**R13-031**	**R13-032**	**R13-037**	**R13-039**	**R13-041**	**R13-048**	**R13-053**		**R15-001**
								XRF	Effective	
SiO2	wt.%	73.82	72.94	66.95	72.32	77.49	81.08	57.55	56.81	56.69
TiO2	wt.%	0.12	0.17	0.75	0.21	0.52	0.11	1.08	1.08	1.03
Al2O3	wt.%	14.70	14.00	16.41	14.83	11.24	10.57	23.73	23.31	22.82
FeO	wt.%	0.74	1.33	5.69	1.76	3.95	0.55	6.80	6.22	7.98
MnO	wt.%	0.01	0.04	0.08	0.04	0.08	0.01	0.13	0.06	0.51
MgO	wt.%	0.27	0.40	1.94	0.47	1.28	0.15	3.66	3.62	1.76
CaO	wt.%	1.37	1.64	1.43	2.26	0.65	0.58	1.49	1.34	0.60
Na2O	wt.%	6.68	2.83	1.18	4.01	1.96	2.44	2.83	2.83	1.30
K2O	wt.%	1.73	5.68	3.21	3.17	1.61	3.18	2.13	2.13	4.54
LOI	wt.%	0.46	0.36	1.70	0.91	1.33	1.34	0.90	0.90	1.89
Total		99.89	99.40	99.34	99.99	100.11	100.00	100.30	98.31	99.11
Traces (Input=Output)										
Rb	ppm	19.30	162.10	119.10	102.00	65.60	95.40	65.00		208.40
Ba	ppm	159.40	557.40	815.90	786.90	303.60	361.30	323.80		681.50
Sr	ppm	87.10	203.70	149.20	367.50	124.60	54.60	262.70		78.70
Nb	ppm	0.80	4.90	15.10	7.40	9.30	5.40	15.40		22.40
Zr	ppm	83.10	59.80	225.10	115.10	202.90	76.10	176.10		185.90
Hf	ppm	2.40	3.80	5.20	7.00	8.70	5.40	2.30		5.60
Y	ppm	9.70	14.60	35.60	13.50	16.10	8.10	32.10		37.10
Ga	ppm	15.90	13.40	19.90	34.00	30.40	27.50	25.90		29.80
Zn	ppm	8.60	21.10	98.60	38.90	49.70	15.10	71.30		131.20
Cu	ppm	2.50	2.30	19.30	8.50	6.60	1.00	13.50		33.00
Ni	ppm	8.70	9.70	35.80	6.30	32.40	5.30	97.90		42.90
Co	ppm	13.20	12.40	19.10	15.60	19.30	15.70	24.70		26.80
Cr	ppm	0.00	0.00	46.10	4.20	48.10	9.60	172.50		94.40
V	ppm	10.00	21.70	81.60	16.30	71.60	8.70	146.30		143.40
Sc	ppm	0.80	1.70	12.30	4.80	8.50	2.30	17.60		17.40
La	ppm	3.40	14.40	60.00	17.20	16.90	16.20	59.60		58.60
Ce	ppm	8.80	19.60	100.80	48.50	46.80	14.20	115.40		135.70
Nd	ppm	10.70	10.20	35.90	24.10	23.60	12.70	56.70		48.20
Pb	ppm	15.30	35.80	25.10	55.40	42.80	40.80	23.40		39.70
Th	ppm	0.00	19.30	16.00	13.00	9.70	12.80	20.10		18.70
U	ppm	0.60	11.60	3.90	1.90	1.00	1.20	2.00		3.70
W	ppm	292.40	192.90	81.10	n.d.	n.d	n.d	123.10		117.30

2.4 Metamorphic evolution, *P-T* estimates

Accurate *P-T* conditions estimates are essential for the garnet fractionation/diffusion model since diffusion is strongly temperature dependent and significant at $T > 600$ °C. Reconstructing prograde metamorphic conditions is often problematic because mineral compositions may reflect both prograde and retrograde reactions. Retrograde metamorphism is a major source of uncertainty when applying conventional thermobarometry based on Fe-Mg exchange because resetting of mineral chemistry during cooling and retrograde reactions (Frost and Chacko, 1989). Therefore, peak metamorphic conditions were estimated from a combination of thin section observations, garnet-biotite (Grt-Bt) Fe-Mg exchange thermometer and garnet-alumosilicate-plagioclase-quartz (GASP) barometer, phase diagram section calculations and isopleths of garnet and biotite chemical composition.

Minerals chemical compositions have been analysed for SiO_2, TiO_2, Al_2O_3, FeO, MgO, MnO, CaO, Na_2O, K_2O and Cr_2O_3 using the electron microprobe JEOL JXA-8200 at the ETH Zürich. Operating conditions for spot analyses were 15 kV accelerating voltage, 20 nA sample current, 40 s counting time per element and beam size < 5 µm.

2.4.1 Thermobarometry

Thermobarometric calculations were made with least weathered pelitic samples *R15-001* from the Lower Terrane kyanite-zone and *R13-030* from the NTZ shear zone (Fig. 2.2). Garnet concentration maps performed with the microprobe, revealed thin (few µm) retrograde corona due to exchange reactions between garnet and matrix (Frost and Chacko, 1989; Kohn and Spear, 2000). In order to obtain peak-*T* information, quantitative analyses have been performed taking into account the retrogressed thin rims and measurements (minimum of three for each pair) were carried out a few µm from the contact between the two phases. In absence of biotite in contact with garnet porphyroblasts, measurements have been performed considering biotite from the matrix.

Representative average EMPA mineral chemical compositions used for garnet-biotite peak-*T* calculations and garnet-aluminosilicate-plagioclase-quartz (GASP) are given in Table 2.3; *P* and peak-*T* results from different calibrations are summarized in Fig. 2.5.

Sample *R15-001* yielded peak-*T* estimates of 650 ± 25 °C and pressures between 0.8 ± 0.1 GPa. Average peak-*T* of different calibrations for sample *R13-030* yields temperatures of 730 ± 30 °C and pressures between 0.8 and 0.95 GPa, revealing uniform pressure conditions and temperature increase across *c*. 800 m thick pile of rocks.

Table 2.3 Representative microprobe mineral compositions used to estimate peak-T and P conditions

Sample*	R15-001				R13-030			
	Gt	Bt	Mu	Pl	Gt	Bt	Mu	Pl
No. Meas.	3	3	3	6	3	3	3	3
SiO_2	37.60	35.50	45.42	65.51	38.19	35.94	47.66	61.46
TiO_2	0.02	1.94	0.56	0.02	0.08	2.27	0.71	0.02
Cr_2O_3	0.03	0.01	0.02	0.01	0.03	0.07	0.03	0.01
Al_2O_3	21.26	18.56	34.54	19.98	21.39	17.71	33.39	22.47
FeO	32.66	17.57	2.24	0.09	29.06	17.64	1.12	0.02
MnO	3.21	0.18	0.01	0.01	0.34	0.13	0.18	n.d
MgO	4.69	10.38	0.59	n.d.	5.85	10.51	0.74	0.01
CaO	0.97	0.12	0.03	1.34	5.33	0.00	0.00	4.95
Na2O	0.03	0.21	1.03	10.29	0.00	0.12	0.45	8.05
K2O	n.d	7.16	10.12	0.09	0.01	8.73	9.19	0.16
Total	100.49	91.62	94.55	97.33	100.28	93.12	93.47	97.15

*From south to north
n.d. = not detected

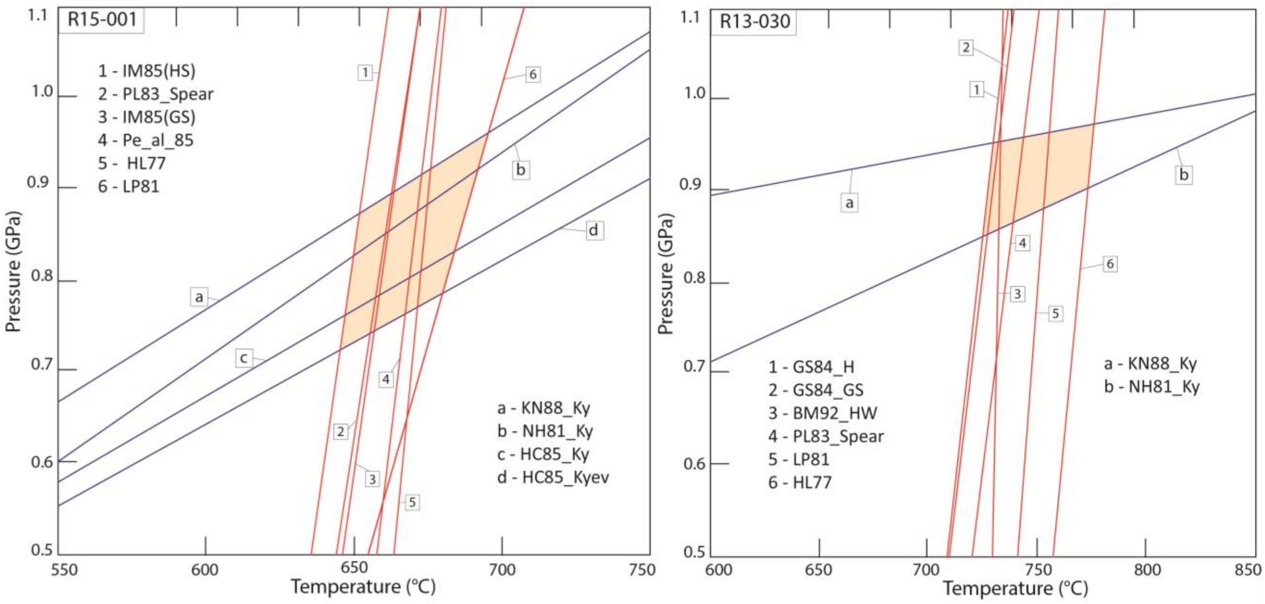

Figure 2.5. Thermo-barometric results for samples *R15-001* (*left*) and *R13-030* (*right*). Pressures (blue lines) and temperatures (red lines) estimated applying the following calibrations: BM92-HW - Bhattacharya et al. (1992); HC85 - Hodges and Crowley (1985); HL77 - Holdaway and Lee (1977); IM85(HS)/(GS) - Indares and Martignole, 1985; KN88 - Koziol and Newton (1988); LP81 - Lavrent'eva and Perchuk (1981); NH81 - Newton and Haselton (1981); PL83_Spear - Perchuk and Lavrent'eva (1983); Pe_al_85 - Perchuk et al., 1985.

2.4.2 P-T diagram section calculations

Pseudosections represent stability fields of coexisting minerals in the *P-T* space for a specific bulk-rock composition. XRF bulk-rock compositions were obtained using a Panalytical Axios wave-length dispersive XRF spectrometer (WDXRF, 2.4 kW) at ETH Zürich. Phase diagram sections were calculated using the software Perplex_X_07 (Connolly, 2005), the thermodynamic database of Holland and Powell (1998, updated 2004) and mineral solution models listed in Table 2.4. Pseudosections and isopleths of mineral compositions were calculated in the system Na_2O-CaO-K2O-FeO-MgO-Al_2O_3-SiO_2-H_2O-MnO (NCKFMASHMn). Water (H_2O) content was estimated from loss of ignition (LOI) occurred during glass-bead preparation (Table 2.2).

Table 2.4 Solid solutions used in the equilibrium phase diagram calculations

Mineral phase	Solution model	Reference
amphibole	GlTrTsMr	Massonne and Willner, 2008
biotite	Bio (TCC)	Tajcmanová *et al*., 2009
chlorite	Chl (HP)	Holland and Powell, 1998
chloritoid	Ctd (HP)	White *et al*., 2000
cordierite	hCrd	Holland and Powell, 1998
epidote	Ep (HP)	Holland and Powell, 1998
feldspar	San	Waldbaum and Thompson 1968
garnet	Gt (GCT)	Ganguly *et al.,* 1996
ilmenite	IlHm (A)	Andersen and Lindsley, 1988
magnetite	MtUl (A)	Andersen and Lindsley, 1988
melt	melt (HP)	Holland and Powell, 1998
muscovite	Mica (CHA)	Coggon and Holland, 2002
orthopyroxene	Opx (HP)	Powell and Holland, 1999
plagioclase	Pl (h)	Newton *et al*., 1980
staurolite	St (HP)	Parameters from Thermocalc

Most appropriate rocks for phase diagram section calculations and *P-T* estimates are samples *R15-001*, *R13-020* from higher structural levels of Lower Terrane, *R13-030* from the NTZ shear zone and *R13-053* from the Imbricate Terrane in the Komotini region (Figs. 2.1 and 2.2). Phase diagram sections of samples *R15-001* and *R13-30* are displayed in Fig. 2.6 (samples *R13-020* and *R13-053* in Appendix A1). Garnets in samples *R13-020* and *R13-030* display concentric compositional zoning. Therefore, garnet core chemical compositions were extracted from the XRF derived bulk rock in order to estimate the effective equilibrium composition (Table 2.2). Garnet amount (vol. %) was estimated from thin sections, rock sample surface and Perplex modal calculations (Appendix A2).

Assuming spherical garnet porphyroblasts, the average of core composition and its volume (starting from the core till the abrupt change in chemical composition observed in compositional profiles) were subtracted from the bulk rock. In order to ensure radial compositional profiles, garnet porphyroblasts have been separated from the rock and polished until reaching the core of the crystal. Garnet major elements maps and composition profiles were obtained using the electron microprobe.

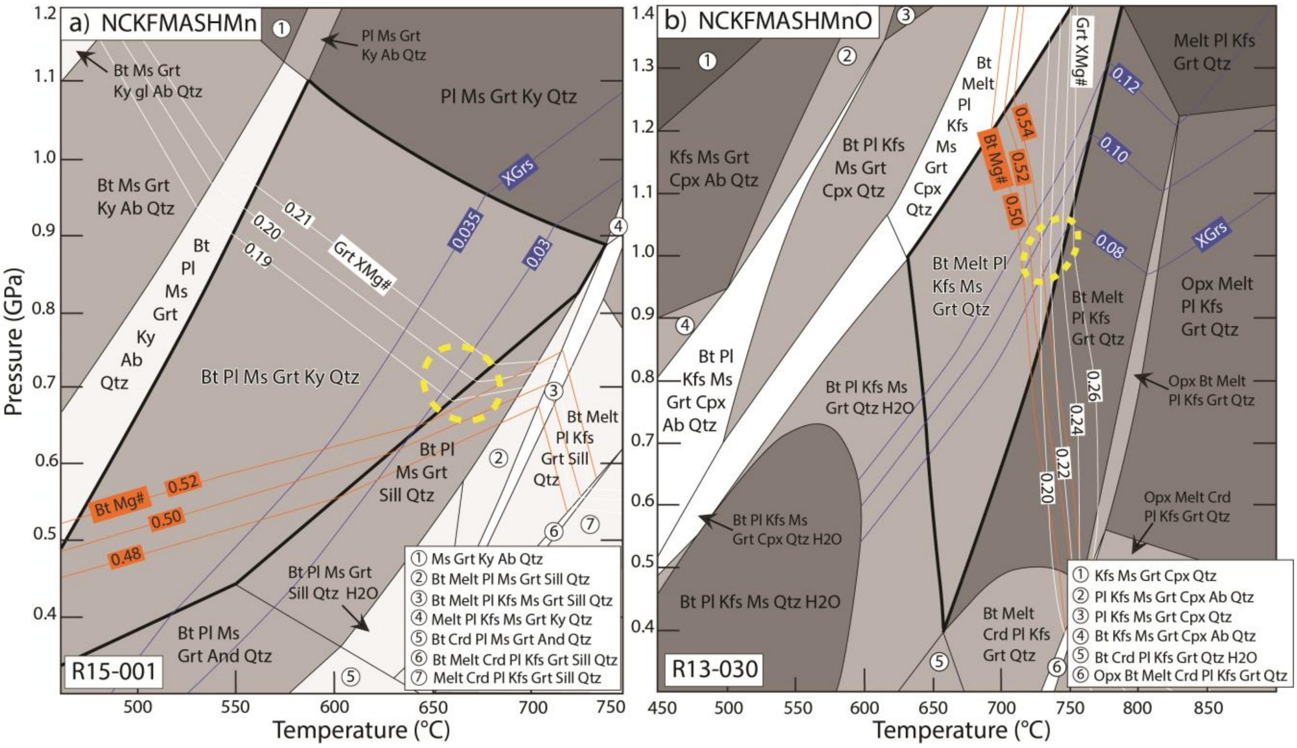

Figure 2.6. *P*-*T* pseudosections calculated in the NCKFMASHMn system for samples *R15-001* (a) and *R13-030* (b). Bold line: sample assemblage stability field. Orange lines: Mg# biotite composition. Blue lines: garnet grossular (*X*Grs) composition isopleths. Green lines: garnet Mg# (Grt *X*Mg#) chemical contour. Dashed ellipse: estimated *P*-*T* conditions. Bulk rock compositions are given in Table 2.3. Same greyscale = same amount of stable phases.

The element maps of garnet porphyroblasts from sample *R15-001* revealed homogeneous chemical compositions, consequently, effective bulk rock composition estimate was not required.

Peak mineral assemblage stability field of sample *R15-001* ranges between *T* < 450 and 740 °C and between *P* < 0.3 and 1.1 GPa. Biotite *X*Mg# (between 0.48 and 0.52) and garnet isopleths (*X*Mg#: 0.19-0.21 and grossular contour *X*Grs: 0.03-0.035) intersect the stability field at 670 ± 20 °C for 0.65-0.7 GPa (Fig. 2.6a).

The stability field of peak mineral assemblage of sample *R13-030* covers large T-conditions from 640 to 770 °C and pressures from 0.4 to > 1.4 GPa (bold field in Fig. 2.6b). Grossular content (*X*Grs) ranges between 0.08 and 0.12, whereas garnet *X*Mg# is 0.20 to 0.26. Garnet (*X*Mg# and *X*Grs) and biotite (*X*Mg#: 0.50-0.54) isopleths intersect the stability field at 750 ± 30 °C and 1.05 ± 0.05 GPa. These conditions are within a phase field that includes melt, but its modal proportion calculated with Perplex is < 7 vol% (Appendix A3).

These *P*-*T* conditions are consistent with conventional thermobarometric estimates (Fig. 2.5). Garnet amphibolite *R13-020* and garnet micaschist *R13-030*, both from the Drama section, yield similar peak-*T* (735 ± 25 °C) and pressures (0.85 ± 0.05 GPa; Appendix A1). Sample *R13-053* from Komotini yielded temperatures between 720 - 760 °C and pressures at 1.3 ± 0.1 GPa (Appendix A1).

2.5 Geochronology

To constrain the thermotectonic evolution of the inverted metamorphic zonation in the NTZ, reliable geochronological data are essential. U-Pb Sensitive High Resolution Ion Micro Probe (SHRIMP) allows measuring isotopic ratios of compositional domains of zircon single grains previously imaged with backscattered electrons and cathodoluminescence (CL). Zircons have been processed and separated at the ETH Zürich using high voltage electrical discharge in the SelFrag apparatus (http://www.selfrag.com), sieving and heavy liquids separation procedures. Advantage of SelFrag, compared to mechanical crushing, is to obtain clean surfaces and to preserve the natural grain size. In situ U-Pb analyses were performed using a SHRIMP II in the Center of Isotopic Research (CIR) at VSEGEI, Saint-Petersburg.

Focus has been given to migmatitic orthogneisses *R13-031* (Fig. 2.3e) and *R13-032* collected near the Sidironero locality (Figs. 2.1 and 2.2).

In addition, one granitic intrusion (*R13-022,* Figs. 2.2 and 2.3f) was dated to determine its possible origin and nature and to understand if the pluton intrusion may have contributed as heat source to the inverted metamorphic zonation along the NTZ. Nine samples including orthogneisses, paragneisses and schists were collected for ^{40}Ar/^{39}Ar dating on white mica, which offers a key to the thermotectonic evolution between 350 and 400°C: six samples from Drama-Sidironero transverse (*R13-035, R13-010, R13-013*, *R13-017*, *R13-019* and *R13-026*) and three from the Xanthi section (Fig. 2.1; *R13-039*, *R13-041* and *R13-048*).

White mica grains were extracted from micaschists with shockwaves produced in the SelFrag apparatus. Single crystal grains were selected after magnetic separation and final hand picking. White micas from samples *R13-013*, *R13-017* and *R13-039* were separated at different grain sizes (between 63-125 µm and 125-350 µm) to determine whether different grain sizes may represent different recrystallization stages. ^{40}Ar/^{39}Ar dating with step-heating technique was performed at the Geological Survey of Norway, Trondheim.

Mineral assemblages and sample locations are listed in Table 2.1 and bulk rock compositions of samples for U-Pb and ^{40}Ar/^{39}Ar geochronology are given in Table 2.2, geochronological results are resumed in table 2.5.

2.5.1 Cathodoluminescence (CL) imaging and zircon characteristics

Leucosome R13-031: Sample *R13-031* was taken from 5-15 cm thick leucosome lenses near the bottom of a migmatitic orthogneiss layer (Figs. 2.2 and 2.3g). Samples are homogeneous, middle- to coarse-grained. CL-images show homogeneously shaped zircons (Fig. 2.7a *left*). Crystals are rounded-prismatic, slightly elongate, euhedral to subhedral with rounded edges. They are 150-250 µm wide and 200-500 µm long. They display two different types of zoning: Some crystals show patchy irregular zoning surrounded by a thin, less luminescent rim; and oscillatory zoning in the core truncated by an irregular highly luminescent rim (e.g. zircon 031-5, Fig. 2.7a *left*). No inherited xenocrystic zircons was observed.

Leucosome R13-032: Sample *R13-032* was collected in a fold hinge zone from the migmatitic orthogneiss layer in the Imbricate Terrane (Fig. 2.2). CL-images show two main zircon populations (Fig. 2.7b *left*). A small population (1) shows patchy irregular zoning with irregular, high luminescent rims (i.e. zircon 032-2, Fig. 2.7b *left*). The larger population (2) shows a volumetrically dominant regular oscillatory zoning in the core truncated by heterogeneous irregular rim. In general, rims are thicker at grain terminations. Grain size varies between 160-380 µm in length and 70-200 µm in width.

Granitic intrusions R13-022: Sample *R13-022* was extracted from granitic dikes discordant to the orthogneisses of the Imbricate Terrane (Fig. 2.2; Fig. 2.3f). CL-imaging shows a homogeneous zircon population with sharp and straight edges and variable elongation. Larger zircons are 200 - 250 µm long and 90 - 110 µm wide euhedral, prismatic crystals, whereas needle acicular zircons crystals are 100 - 300 µm long and 70 - 90 µm wide (Fig. 2.7c *left*). Many crystals exhibit patchy, inherited cores surrounded by well-developed oscillatory zoning. Some zircons display xenocrystic cores.

2.5.2 U-Pb zircon SHRIMP results

R13-031: Ten rim and ten core data points were obtained from ten zircon grains. Th/U ratios vary between 0.03 and 0.24. Ten oscillatory core zones give ages of 143.4 ± 1 Ma, ten rims yielded 141.0 ± 0.7 Ma (Fig. 2.7a *right*).

R13-032: The two zircon populations have been dated. Eleven oscillatory zoned core- and twelve homogeneous rim-spots were measured in ten zircon grains. Th/U ratios vary between 0.02 and 0.37. Two core ages of minor population (1) give Late Jurassic - Early Cretaceous ages (between 144.7 ± 1.2 and 142.4 ± 1.4 Ma). The second zircon domain (2) yielded Late-Carboniferous concordant ages (295.6 ± 1.9 Ma) for five oscillatory cores. Three core spots yielded ages scattering between 340.5 ± 2.2 and 306.8 ± 2.2 Ma, while one other spot yielded Permian ages (269.7 ± 1.9 Ma). Eleven analysis of the outer metamorphic rim for both populations yield a concordant age of 142.43 ± 1.0 Ma (Fig. 2.7b *right*). One outer rim age from population (2) give Early Jurassic ages (181.2 ± 1.8 Ma).

R13-022: Six oscillatory cores and fourteen sector-zoned outer parts of ten grains give variable Th/U ratios between 0.02 and 0.42. Six core analyses yielded Early Eocene concordant ages (53.33 ± 0.36 Ma). Intermediate and outer oscillatory zones yielded similar concordant ages at 50.88 ± 0.26 Ma.

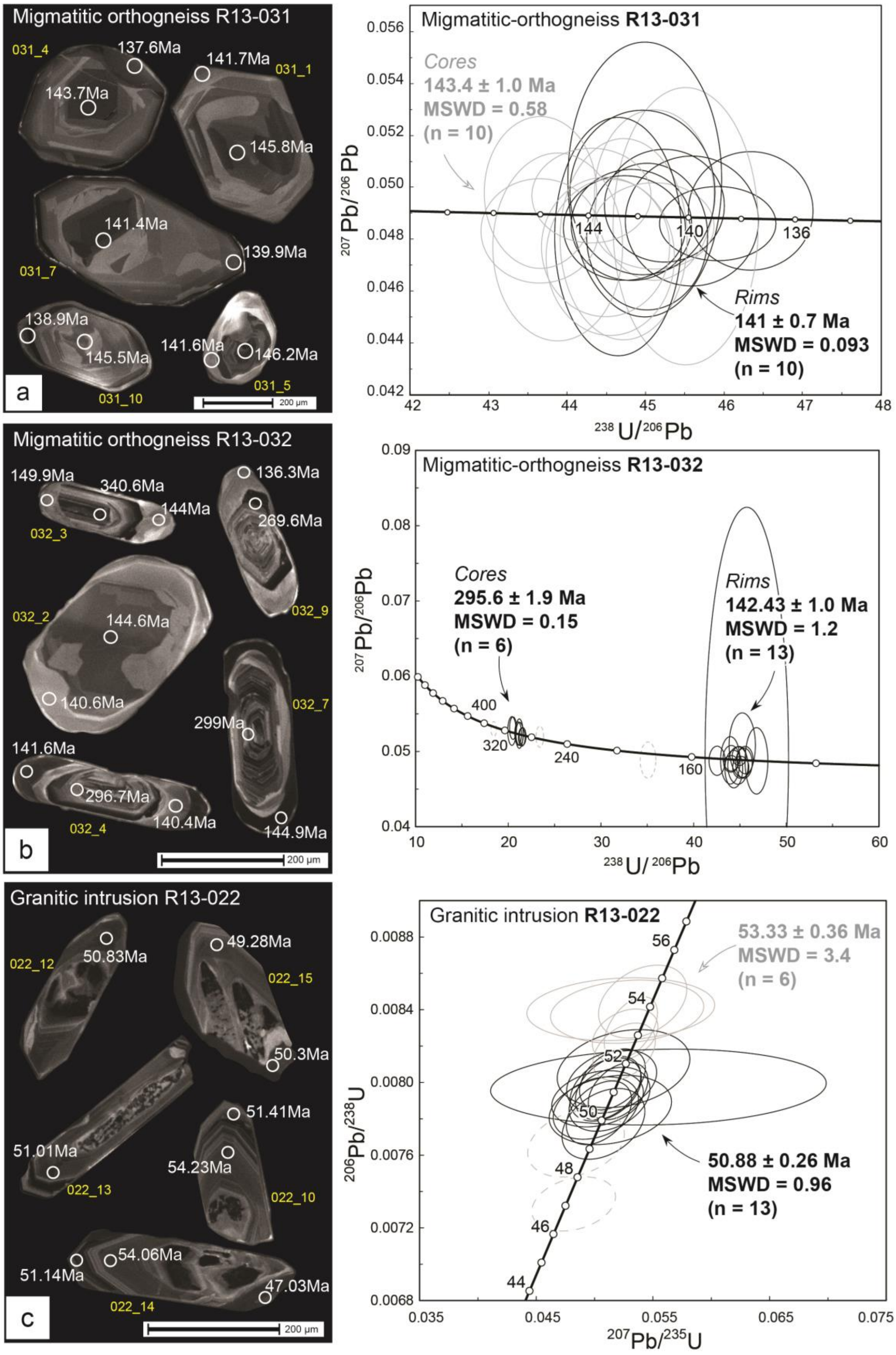

Figure 2.7. *Left:* Cathodoluminescence (CL) images of representative zircons used for U-Pb SHRIMP geochronology. White rings: spot measurements and corresponding ^{206}Pb/^{238}U ages in Ma. *Right:* Associated Concordia diagrams. Uncertainties for individual analysis are at 1σ level. Uncertainties in calculated Concordia ages are at 2σ level. Grey ellipse: core ages. Black ellipse: rim ages. Dashed ellipse: not considered.

2.5.3 ^{40}Ar/^{39}Ar dating results

^{40}Ar/^{39}Ar ages are summarized in Table 2.5 and results are shown in Fig. 2.8 (Appendix A4 for all samples) as age spectra diagrams (Turner *et al.,* 1996) and uncertainties are given at 2σ level.

Samples from both Drama and Xanthi regions show flat spectra between 0 up to 80-90% of ^{39}Ar release, with Early Oligocene mean ages (*c*. 35 Ma). 160 and 63 µm white micas from *R13-013* and *R13-017* (Drama region) yielded *c.* 1 Ma younger ages than that of larger grains (250-160 µm). In sample *R13-039* (Xanthi locality) age difference is smaller (*c.* 0.3 Ma) and larger grains (250-160 µm) are younger.

Table 2.5 Summary of U-Pb SHRIMP and 40Ar/39Ar dating results

U-Pb SHRIMP Geochronology

Rock type	Zircon characteristic	Core ages (Ma)	Rim age (Ma)
Migmatitic orthogneiss			
R13-031	Rounded-prismatic zircons, patchy irregular cores, irregular rims	143.4 ± 1.0 Ma	141.0 ± 0.7 Ma
Migmatitic orthogneiss			
R13-032	Euhedral zircons, oscillatory cores, thick irregular rims	295.6 ± 1.9 Ma	142.43 ± 1.0 Ma
Granitoid intrusion			
R13-022	Patchy cores surrounded by well developed oscillatory zoning	53.33 ± 0.36 Ma	50.88 ± 0.26 Ma

40Ar/39Ar dating

Sample	Grain size (µm)	Age ± 1.96σ	Sample	Grain size (µm)	Age ± 1.96σ
R13-010**	250-160	35.05 ± 0.17	R13-026***	250-160	35.65 ± 0.18
R13-013**	250-160	35.95 ± 0.09	R13-035**	250-160	37.69 ± 0.21
	160-63	35.01 ± 0.11	R13-039***	250-160	36.77 ± 0.08
R13-017***	250-160	35.34 ± 0.19		160-63	37.25 ± 0.15
	160-63	36.23 ± 0.17	R13-041*	250-160	34.15 ± 0.29
R13-019***	250-160	36.07 ± 0.15	R13-048**	250-160	34.36 ± 0.07

* Micaschists, ** Paragneisses *** Orthogneisses

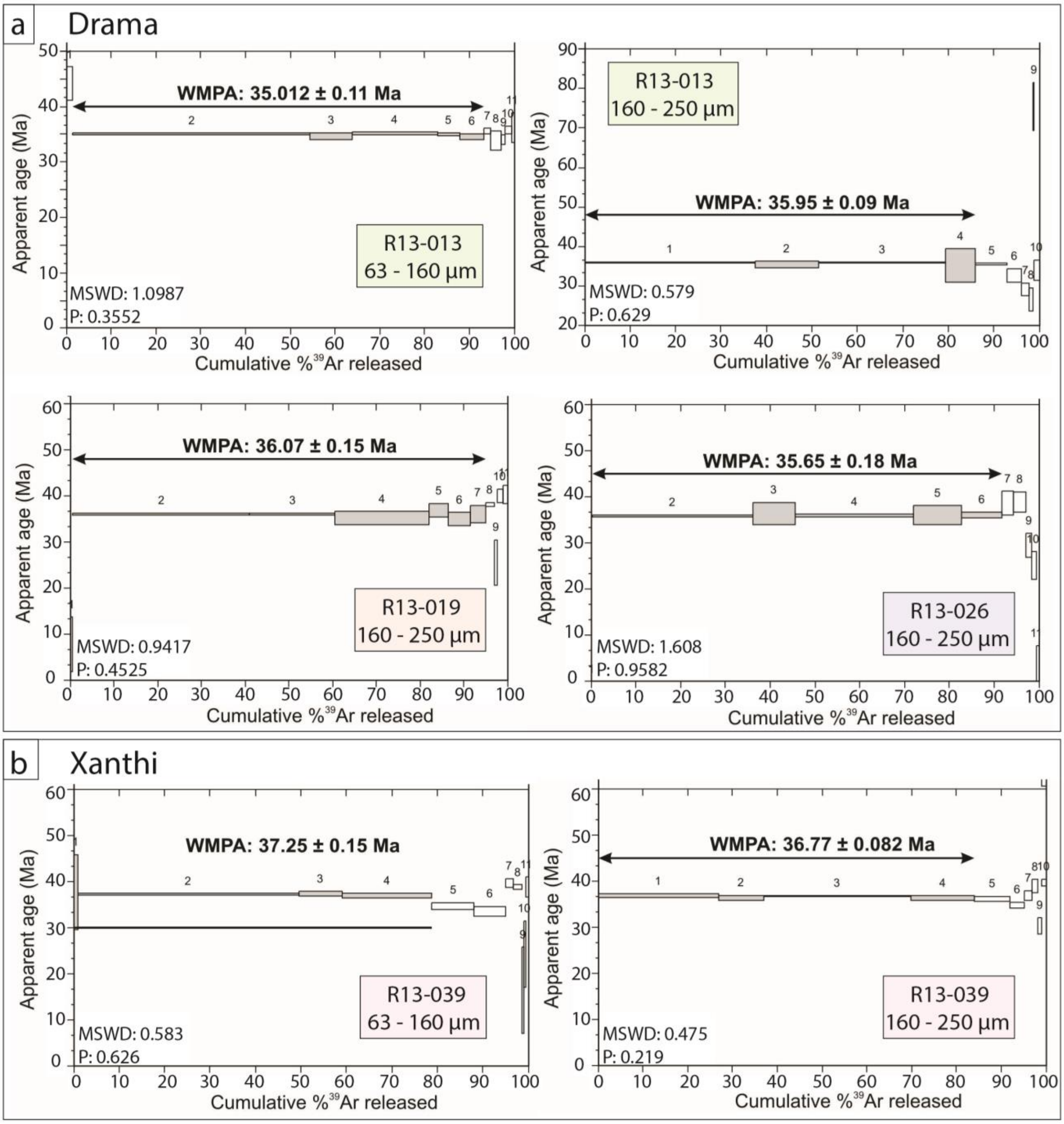

Figure 2.8. Representative ^{40}Ar/^{39}Ar step-heating ages. Uncertainties are given at 2σ level. (**a**) Drama-Sidironero section and (**b**) Xanthi region. Constant concentration profiles indicate no diffusion or later heating events. Plateau ages are similar for different grain sizes from same sample (*R13-013* and *R13-039*). ^{40}Ar/^{39}Ar dating with step-heating technique was performed at the Geological Survey of Norway, Trondheim.

2.6 Garnet geospeedometry

2.6.1 Garnet diffusion modelling approach

Garnet geospeedometry considers the kinetic response of minerals to pressure, temperature and composition (*P*-*T*-*X*) changes during time. Chemical zonation generated during crystal growth is often modified by diffusional relaxation at temperature above a nominal diffusional closure temperature range, which for any element depends on cooling rate and grain size (Dodson, 1973).

Investigations on diffusive elements in garnet porphyroblasts allow calculating the rate of element diffusion within the mineral, estimating the absolute time-dependent thermal evolution and contributing to the interpretation of syn-metamorphic tectonic processes (Lasaga, 1983; Spear *et al.*, 1984; Ague and Baxter, 2007; Caddick *et al.*, 2007; Viete *et al.*, 2011). Diffusivity D depends on temperature following the empirical Arrhenius relation (1889; Eq. 1):

$$D = D_0 \cdot e^{-E/RT} \tag{1}$$

where E *[J mol^{-1}]* is the activation energy, R *[J K^{-1}mol^{-1}]* the universal gas constant, T *[K]* the absolute temperature and D_0 *[m^2 s^{-1}]* is a constant (maximal diffusion coefficient).

Garnet is stable over wide temperature, pressure and bulk composition ranges and is acceptably represented by the major elements $(\mathrm{Fe, Ca, Mg, Mn})_3\mathrm{Al}_2(\mathrm{SiO}_4)_3$. All garnet species have similar physical properties. Limited intracrystalline diffusion rates permit to retain a complete record in the zoning of the major cations and reaction history can be used to obtain *P*-*T* path of the rock during garnet growth (Spear and Selverstone, 1983).

The isotropic nature of garnet is a considerable advantage in multicomponent zoning modelling because diffusion has no directional dependence. Furthermore, the dodecahedral crystal habit allows approximating the porphyroblast shape to a sphere. Radial multicomponent Fe/Mg-Ca-Mn diffusion modelling in a sphere is computed with the method of Lasaga (1983), where all major cations (Fe, Mg, Mn and Ca) are treated as interdependent to maintain stoichiometry (Eq. 2):

$$\begin{pmatrix} \frac{\partial X_1}{\partial t} \\ \frac{\partial X_2}{\partial t} \\ \frac{\partial X_3}{\partial t} \end{pmatrix} = \frac{1}{r^2}\frac{\partial}{\partial r}\left[r^2 \begin{pmatrix} D_{11} & D_{12} & D_{13} \\ D_{21} & D_{22} & D_{23} \\ D_{31} & D_{32} & D_{33} \end{pmatrix} \begin{pmatrix} \frac{\partial X_1}{\partial r} \\ \frac{\partial X_2}{\partial r} \\ \frac{\partial X_3}{\partial r} \end{pmatrix} \right] \tag{2}$$

where X represents the mole fraction of a component, r the radius of the sphere (porphyroblast) and indexes 1, 2 and 3 are any three of the four components (almandine, grossular, pyrope and spessartine).

The diffusion duration is formulated as:

$$t = \frac{\Delta L_D^2}{2D} \tag{3}$$

where t is time, ΔL_D is diffusion length and D is diffusivity.

In order to respect zonation geometries and ensure the application of radial diffusion numerical modelling, garnet crystals (sizes from 4 mm up to 18 mm) were manually extracted from the rocks (hammer and mason), mounted in epoxy “pills” and polished until exposing the core of the crystal. The polished pills were coated with carbon (~30 µm).

2.6.2 Fractionation and diffusion modelling in garnet (FRIDGE)

The program FRIDGE (Fractionation and Diffusion in GarnEt) generates modeled compositional profiles of garnet from a given bulk rock composition assuming chemical fractionation and simultaneous diffusion along a *P-T-t* path. During the fractionation of garnet crystal, and therefore the sequestration of some elements, the bulk rock composition is in continuous modification along the metamorphic path and always in equilibrium with the transient rim composition.

The modeled profiles ($C_{r,j}^{mod}$) are compared with the observed ones ($C_{r,j}^{obs}$) and a *P-T-t* path is chosen when the mismatch between modeled and measured profile is minimized. The minimization is evaluated through the following cost function:

$$\chi^2 = \sum\sum\left(C_{r,j}^{mod} - C_{r,j}^{obs}\right)^2 \tag{4}$$

Several parameters control the shape of garnet compositional profiles. The *P-T* path controls the composition of the newly-crystallized garnet rims, whereas the time spent at high-*T* conditions plays an important role in the extent of diffusion, i.e. two garnets following same *P-T* path would have different compositional profiles depending on the time spent at peak-*T* conditions. Other parameters that may influence results are uncertainties of diffusion coefficients and their dependency on oxygen fugacity fO_2. Diffusion coefficients slightly increase with increasing oxygen-fugacity difference from the graphite buffer (French and Eugster, 1965). If oxygen fugacity is overestimated, the apparent time estimates may be significantly shorter than estimates with the appropriate fO_2 (Ganguly *et al.*, 1998; Carlson, 2006) since the garnets would homogenize faster. In the absence of graphite that would buffer the fO_2 in the rock, the estimate of fO_2 is not straightforward and need not be constant throughout the rock evolution. Therefore, it is assumed that fO_2 follows the graphite buffer, which ensures that the calculated duration of peak metamorphic temperatures is a maximal estimate. Intra-granular diffusion of Mg, Fe, Ca, and Mn as a function of temperature is based upon diffusivity coefficients given by Carlson (2006). Advantage of FRIDGE, compared to the *step function* model (e.g. Ague and Baxter 2007), is that FRIDGE gives information about the prograde path and it does not underestimate the time-of-diffusion for garnets which profiles are smoothly zoned (Ague and

Carlson, 2013). Restriction of the model are the assumptions of small variation in garnet sizes and homogeneous crystal distribution.

2.6.3 Garnet compositional zoning

Garnet chemical composition maps and profiles were obtained using the electron microprobe. Garnet Mg, Mn, Ca and Fe concentration maps identify growth/diffusion zoning or complete homogenization. Such maps have been performed on 46 garnet porphyroblasts from eight garnet-bearing rock samples: *R13-020, R13-021, R13-030 and R15-001* from Drama, *R13-038, R13-040 and R13-041* from Xanthi and *R13-053* from the Komotini section. Rock samples and garnets porphyroblasts considered for fractionation/diffusion modelling study are presented in Table 2.1 and representative garnet compositional maps are shown in Fig. 2.9. Radial garnet composition profiles were analysed for SiO_2, TiO_2, Al_2O_3, FeO, MgO, MnO, CaO, Na_2O, K_2O and Cr_2O_3 avoiding garnet inclusions and cracks. Figurative garnet compositional profiles selected for geospeedometry studies are presented in Fig. 2.10.

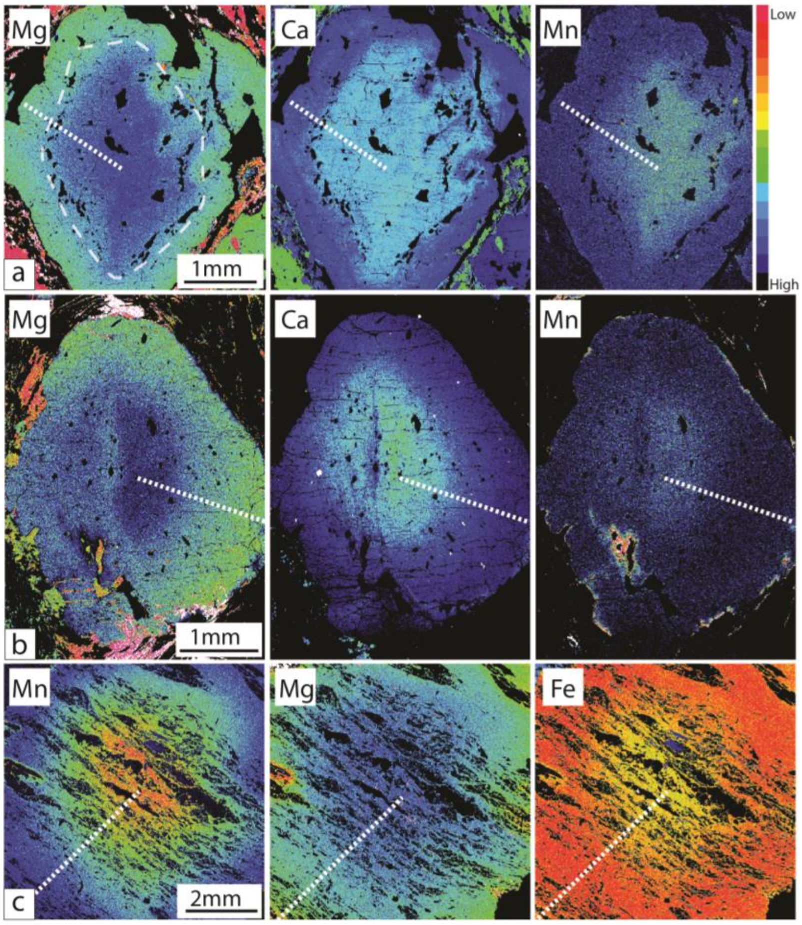

Figure 2.9. Representative garnet major element (Ca, Mg, Mn and Fe) concentration maps. Sample locations are presented in Table 2.1 and Fig. 2.2. Strait dashed lines: measured garnet chemical profile (Fig. 2.10). **a)** Porphyroblast from *R13-020* garnet-amphibolite. **b)** Zoned garnet in sample *R13-030.* **c)** Garnet from Komotini display quartz inclusions trails

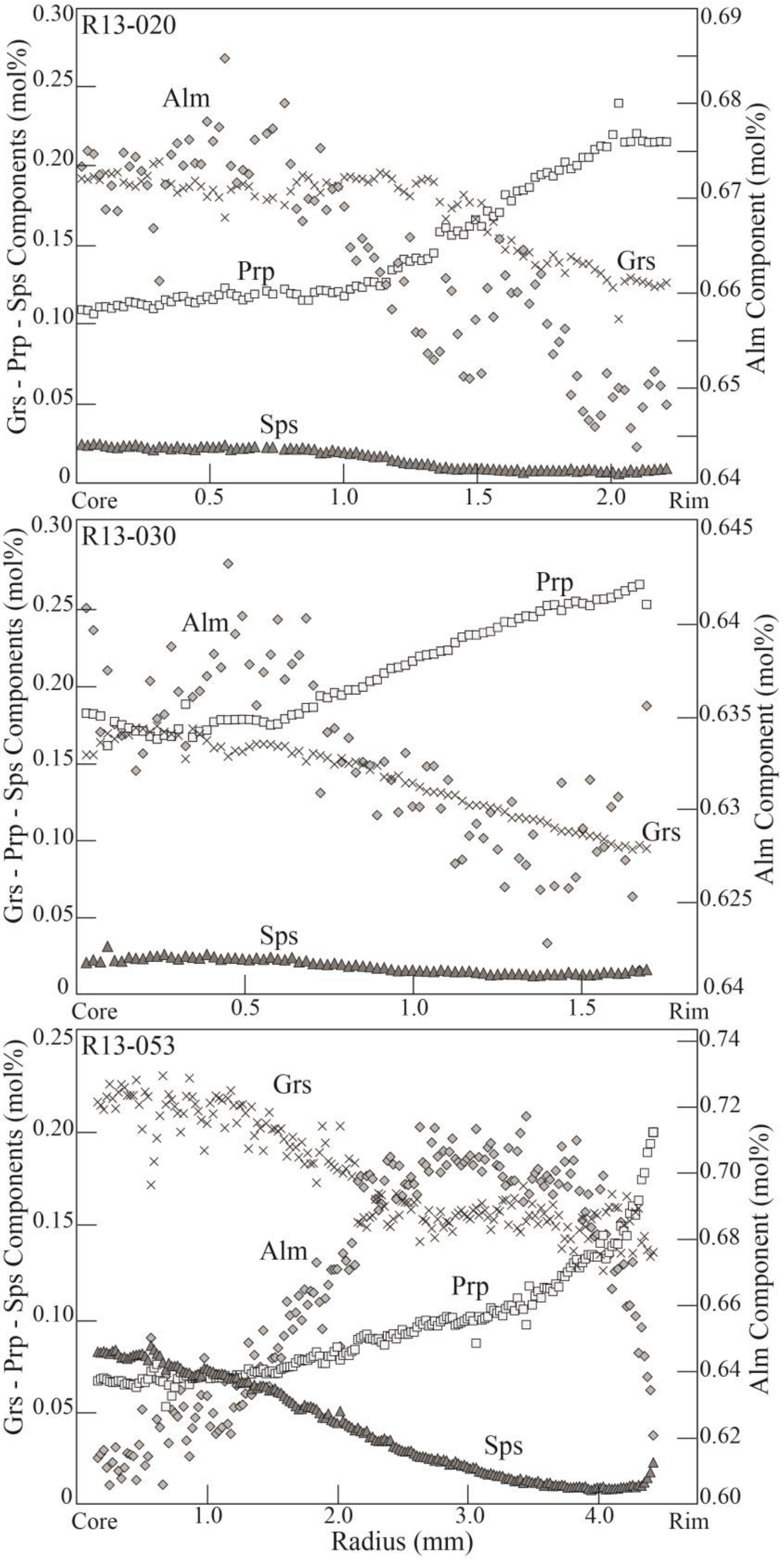

Figure 2.10. Representative chemical zoning profiles for almandine (Alm), pyrope (Prp), spessartine (Sps) and grossular (Grs) from core to rim in samples *R13-020*, *R13-030* and *R13-053* (Fig. 2.9).

Generally crystal rim boundaries (few µm) shown resorption textures characterized by sharply *X*Mg# drop and *X*Mn increase due to diffusional exchange between garnet and rock matrix during retrograde metamorphism (Kohn and Spear, 2000). Therefore, outermost rims were not considered for peak-*T* time duration estimates.

Garnet porphyroblasts from the Xanthi section are chemical equilibrated or display patchy zoning patterns, which geometries are not convenient for radial diffusion modelling.

Garnet crystals from Drama and Komotini regions display concentric compositional zoning. Typically, from core to rim, almandine (Alm) and pyrope (Prp) increase, whereas spessartine (Sps) and grossular (Grs) decrease (Fig. 2.10). The bell-shape profile of Mn and *X*Mg# decrease are characteristic of prograde growing zone without internal diffusion (Hollister, 1969).

2.6.4 Duration of peak temperature conditions

The representative FRIDGE calculation of garnet fractionation/diffusion modelling for sample *R13-030* is shown in Fig. 2.11 (Appendix A5 for all garnets considered). FRIDGE fractionation/diffusion modelling results are summarized in Table 2.6. For each garnet porphyroblast *P-T* paths were implemented twice, considering maximal and minimal values of peak-*T* estimates. This apparent redundancy was necessary to better understand the influence of temperature on intracrystalline diffusion and the consequences on time duration estimates. FRIDGE calculations applied to samples *R13-020*, *R13-030* (Drama) and *R13-053* (Komotini) predict peak-*T* conditions ranging from 2 to 6 Myr in the Drama region, and between 3 and 8.3 Myr north of Komotini locality.

Table 2.6 Summary of FRIDGE fractionation/diffusion modelling results

Rock type Sample		Peak *T* [°C] min	 max	Time duration (Myr) at *T*min	 *T*max
Grt-amphibolite (Drama)					
R130-020	Grt-A	710	750	6.8 Ma	2.2 Ma
	Grt-C	710	750	5.3 Ma	2.0 Ma
Grt micaschist (Drama)					
R13-030	Grt-A	720	780	5.7 Ma	3.4 Ma
	Grt-B2	720	780	4.4 Ma	2.0 Ma
Grt-ky micaschist (Komotini)					
R13-053	Grt-1	720	760	7.4 Ma	3.2 Ma
	Grt-C1	720	760	8.3 Ma	2.9 Ma

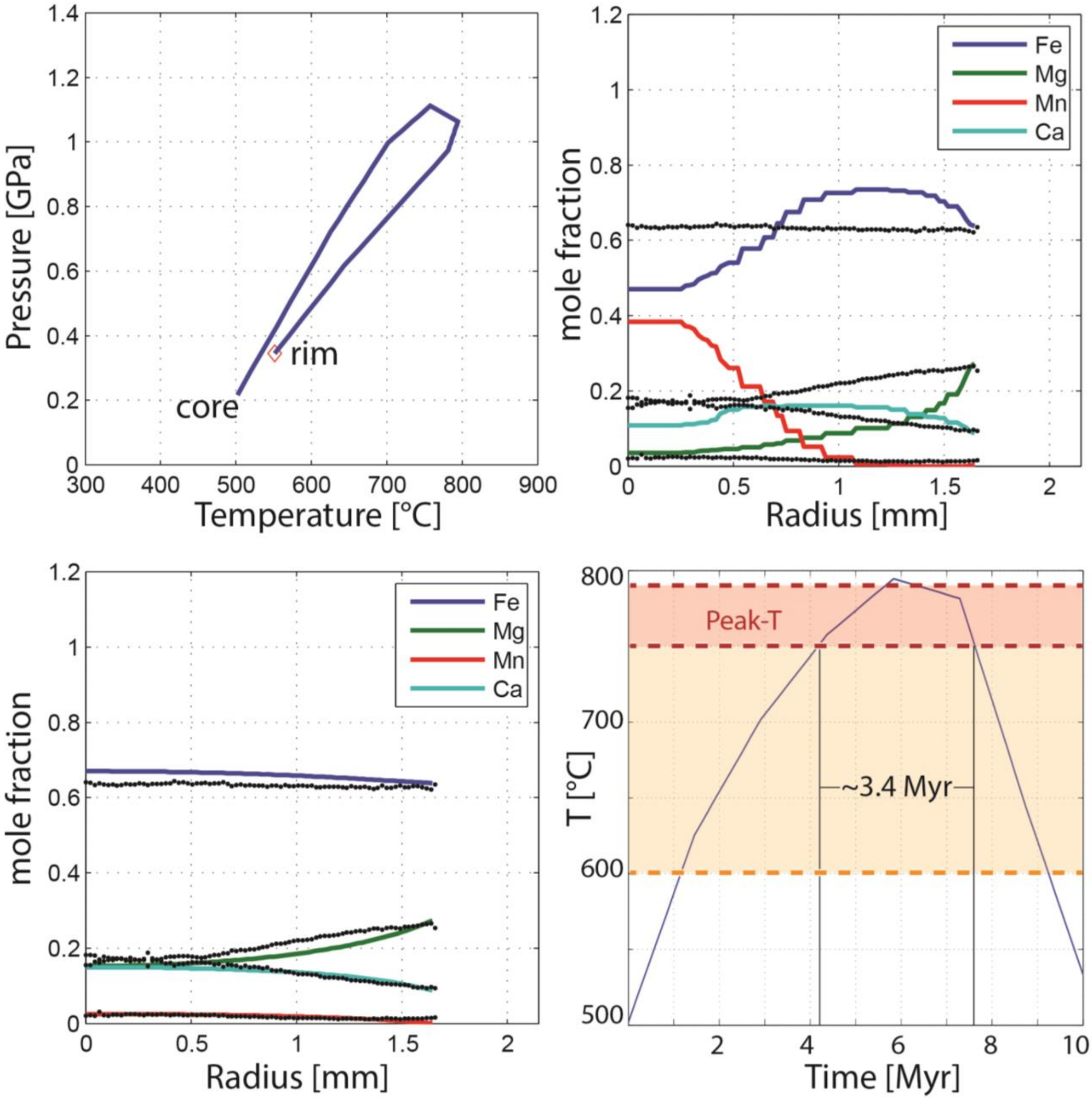

Figure 2.11. FRIDGE numerical model results for sample *R13-030* (Grt - A). Black dots: measured profiles from core to rim. **a)** Estimated pressure-temperature-time (*P*-*T*-*t*) path from petrographic observation, phase diagram sections and *P*-*T* estimates. **b)** Simulated garnet fractionation without intracrystalline diffusion for the four major cations along the given *P*-*T*-*t* path. **c)** Result of garnet fractionation with diffusivity activated at *T* = 600 °C. **d)** Temperature-time (*T*-*t*) diagram representing the duration (Myr) of peak-*T* conditions. Orange sector: diffusivity active at *T* = 600 °C. Red sector: diffusivity at peak-*T* (*T* ~ 750°C).

2.7 Discussion

2.7.1 Geochronology

Samples *R13-031* and *R13-032* from migmatitic orthogneisses yielded Early Cretaceous (144.7 ± 1.2 - 142.4 ± 1.4 Ma) metamorphic rim ages. Equivalent rim and core ages of sample *R13-031* suggest zircon crystallization during partial melting. Zircons from sample *R13-032* have Late Carboniferous - Early Permian (between 340.5 ± 2.2 and 295.6 ± 1.9 Ma) oscillatory cores ages. Older oscillatory cores are related to the orthogneiss protolithic rock. Equivalent Late Carboniferous - Early Permian orthogneisses ages and Late Jurassic - Early Cretaceous metamorphic (re)crystallization ages obtained in this study have been previously obtained by Turpaud and Reischmann (2010) in central Rhodope.

Liati (2005) reported four different metamorphic events from different regions of Rhodope, i.e. Late Jurassic (*c*. 149 Ma) north of Xanthi (Central Rhodope), Late Cretaceous (*c*. 73 Ma) near Kimi (East Rhodope), Mid Eocene in Sidironero (*c*. 51 Ma) and Late Eocene (*c*. 42 Ma) in Thermes (Central Rhodope), and interpreted these age heterogeneity as evidence of multiple subductions and multiple metamorphic cycles during orogeny. In this study, zircons from migmatitic leucosomes revealed one Earliest Cretaceous (*c*. 145 - 142 Ma) metamorphic event in the Sidironero region. Mid Eocene ages (~ 50 Ma) are obtained from discordant granitoid intrusions (*R13-022*, Fig. 2.3h), associated with the Skaloti pluton to the north (Fig. 2.1; geochronological data review in Burg, 2011). Late Cretaceous and Mid Eocene metamorphic ages presented by Liati (2005) are contemporaneous with voluminous Tertiary granitoid intrusions. Therefore, the Cenozoic ages reported by Liati may reflect the metamorphic overprint due to the voluminous magmatism.

Homogeneously distributed Late Eocene (*c*. 35 Ma) cooling (< 350 – 400 °C) ages obtained from white mica ^{40}Ar/^{39}Ar dating along the Drama and Xanthi sections (Fig. 2.1 and Table 2.5) are associated with post magmatic cooling (review in Burg, 2011). Different grain-sizes (between 160 - 63 µm and 250 - 160 µm) do not yield different ages, suggesting that different white mica grain-sizes are not related to multiple cooling stages.

Equivalent Earliest Cretaceous (*c*. 145 Ma) peak metamorphic (re)crystallization and Eocene (between *c*. 50 and 35 Ma) cooling ages have been reported in previous studies in central (e.g. Liati, 1986; Liati and Kreuzer, 1990; Kaiser-Rohrmeier *et al*., 2004; Krenn *et al.,* 2010; Turpaud and Reischmann, 2010) and in eastern Rhodope (e.g. Bonev *et al*., 2010; Bonev and Stampfli, 2011; Bonev *et al.,* 2013, Moulas *et al*., 2016 submitted). These coherent results suggest that western Rhodope, i.e. Sidironero region, experienced with central (Xanthi area) and eastern Greek Rhodope (Kimi region) a common tectonometamorphic evolution (e.g. Krenn *et al*., 2010, Moulas *et al.*, 2016 submitted).

2.7.2 P-T estimates and peak-T duration

Peak-*T* and pressure conditions increase from 670 ± 30 °C at *c*. 0.7 GPa (*R15-001*) up to 730 ± 20 °C at *c*. 1.0 GPa (*R13-030*) moving up-section across an about 800 m thick pile of rocks. Results reveal an inverted thermal gradient and upward increase in pressure conditions moving upwards in Lower Terrane against the NTZ in the Drama – Sidironero transverse. In the investigated samples, feldspar anorthite content (X_{An}= Ca/ (Ca+Na+K)) does not intersect the peak mineral assemblage stability fields (out of *P-T* diagram section). Plagioclase may represents either a relic of a previous stable mineral assemblage, or (re)crystallized during the retrograde path. Possible pressure overestimation of sample *R13-030* due to the steep slope of garnet *X*Mg#, biotite *X*Mg# and *X*Grs compositional contours has to be taken into account in interpretations. Moreover, the syn-tectonic mineral assemblage (Bt – Pl – Kfs – Mu – Grt – Qtz) is stable in a large *P-T* stability field and therefore, not supportive for more accurate pressure constraint (Fig. 2.6b). Therefore, we assume that the investigated rocks equilibrated at nearly uniform pressure of 0.85 ± 0.15 GPa.

Upper-amphibolite facies conditions estimates are comparable with those of previous studies in central and in eastern Rhodope (e.g. Mposkos, 1989; Mposkos and Liati, 1993; Machev and Kolcheva, 2008; Krenn *et al*., 2010; Moulas *et al*., 2013; Moulas *et al*., 2016 submitted). In the Imbricate Terrane of the investigated sections high grade metamorphic rocks with microdiamond inclusions in garnets were reported (Fig. 2.1; Mposkos and Kostopoulos, 2001). No diamonds have been found during this study.

The duration of peak-*T* conditions helps in deducing the heat source and mechanisms responsible for metamorphic isograds inversion. Detailed petrographic observations and garnet compositional zoning revealed that garnet porphyroblasts grew syn-kinematically with the peak mineral assemblage in the prograde path. Therefore, diffusion occurred during syn-tectonic peak metamorphic conditions. Due to the impossibility to determine and quantify chemical relaxation during heating and cooling events, and/or distinguish different thermal episodes, it is assumed that measured compositional profiles resulted from diffusional modifications taking place at peak-*T* conditions. This assumption infers maximum time estimate for peak-*T* duration (Ague and Baxter, 2007).

Intracrystalline diffusion starts to modify garnet compositional profiles at medium grade metamorphic conditions (*T* > 600 °C). Diffusion is efficient at high grade conditions (*T* > 700 °C; Arrhenius, 1889; Eq. 1). If compositional zoning is extensively diffused, core concentrations may have dropped below they initial values (e.g. Ague and Carlson, 2013). Fitting of compositional profiles using attenuated values as initial conditions, e.g. by employing the simple step function method (Ague and Baxter, 2007), would underestimate the duration of diffusion, i.e. would yields diffusivity time shorter than that actually experienced (e.g. Ague and Baxter, 2007; Caddick *et al.*, 2010; Ague and Carlson, 2013).

Fractionation and Diffusion in Garnet (FRIDGE) inverse fitting modelling overcomes time underestimation. FRIDGE calculates "pre-diffusion" garnet compositional profiles (from a specific

bulk rock composition) and simultaneously simulates diffusional relaxation (starting at T = 600 °C) along a given *P-T-t* path, assuming continuous equilibration between the growing garnet rim and the matrix. The *P-T-t* path is implemented with the support of phase diagram sections, i.e. peak *P-T* estimates and petrographic observations. The optimal *P-T-t* path is predicted by taking into account (as fix parameter) the previously estimated peak *P-T* condition and varying the *P-T* path and/or duration time until the mismatch between calculated and observed profile is minimized (Eq. 4).
FRIDGE garnet fractionation and diffusion modelling using diffusivity of Carlson (2006) predicts short-lived (between 2 and 8 Myr) peak-*T* conditions along the NTZ.

2.7.3 Tectonic implications

Garnets grew syn-tectonically in the prograde path and in equilibrium with peak mineral assemblages. Rotated clasts, asymmetric pressure shadows, fabric asymmetry consistently display top-to-SSW sense of shearing associated to the NTZ. Ductile deformation at the thrust occurred at peak-*T* of *c.* 750 °C and pressure at *c.* 1.0 GPa indicating that these rocks were already at lower crustal conditions in the Earliest Cretaceous. Equivalent internal structures, metamorphic conditions, U-Pb zircon metamorphic dating and ^{40}Ar/^{39}Ar cooling ages previously inferred in central (Xanthi, Thermes) and in eastern (Kimi) Rhodope (e.g. Reischmann and Kostopoulos, 2002; Liati, 2005; Bauer *et al.*, 2007; Krenn *et al*., 2010; Turpaud and Reischmann, 2010; Moulas *et al.*, 2016 submitted), suggest that the NTZ may be interpreted as a coherent intracontinental suture zone extending for more than 150 km between the Imbricate Terrane and the Lower Terrane (e.g. Krenn *et al.*, 2010).

The thermal inversion in the Drama – Sidironero section may be caused by the emplacement (either in one or in multiple steps) of hot material over the cool footwall (Le Fort, 1975), or by shear- or viscous-heating along the thrust (e.g. Graham and England, 1976; England and Molnar, 1993; Stüwe, 1998; Burg and Gerya, 2005; Burg and Schmalholz, 2008; Schmalholz et *al.,* 2014; Schmalholz and Duretz, 2015). In these scenarios the temperature gradient is reversed, whereas the pressure gradient is normal/nearly uniform. Considering the resulted transient (2 - 8 Myr) nature of the thermal perturbation and the metamorphic architecture of the thrust, viscous heating is hypothesized as most plausible heat source that generated inverted isograds across the NTZ.

The large number of equilibrated garnet porphyroblasts, their variations in radial size (from < 1 mm up to 9 mm) and heterogeneous spatial distribution across the NTZ, may indicate that garnets grew at different metamorphic stages. Completely equilibrated garnets may have crystallized at the initial stage of metamorphism before reaching peak conditions, whereas porphyroblasts displaying compositional zoning crystallized at/near peak-*T* conditions.

2.8 Conclusion

The Drama - Sidironero section exhibits an inverted metamorphic sequence between the Lower Terrane footwall and Imbricate Terrane hanging-wall, starting from greenschist facies in the south and increasing to upper-amphibolite grade in the north against the Nestos Thrust Zone. Peak-*T* conditions increase from 670 ± 30 °C up to 730 ± 20 °C across 800 m thick pile of rocks that equilibrated at pressures of 0.85 ± 0.15 GPa. Garnet porphyroblasts are in equilibrium with the matrix and have grown in the Earliest Cretaceous (*c*. 145 - 142 Ma) peak metamorphic overprint associated to top-to-SSW thrusting. Mid Eocene (~ 50 Ma) granitoid intrusions are related to the widespread Tertiary magmatic activity in the Rhodope. Post magmatic cooling (< 350 – 400 °C) occurred during Early Oligocene (*c*. 35 Ma). Structures, petrology, metamorphic conditions and geochronological data support previous statements of one single subduction-exhumation cycle started before Late Jurassic.

FRIDGE garnet compositional profile modelling reveals that rocks have been held at peak-*T* conditions for maximum time of 2 to 8 Myr. The metamorphic structure of the Nestos Thrust Zone, i.e. inverted isograds and nearly uniform pressures, the localized (800 m) high grade zone parallel to the thrust and the transient (2 to 8 Myr) duration of peak-*T* conditions, suggest viscous/shear-heating to be responsible for metamorphic inversion of the Nestos Thrust Zone.

Acknowledgements

The authors are grateful to Schenker F. P. for his precious help, support during field work and valuable suggestions. Thanks to Lüchinger R. and Pirovino F. for their efficient work and excellent quality thin sections. The authors were supported by ETH Zürich, Research ETH-14 11-1.

3. Short-lived formation of the inverted metamorphic sequence across the Himalayan Main Central Thrust (MCT), Sikkim, NE India

Abstract

This study investigates the tectonic setting and the timescale of inverted isograds related to crustal-scale thrusting at the Main Central Thrust in the Sikkim region, northeast India. The aim is to contribute to the understanding of the link between mechanical and thermal evolution of major thrust zones and to clarify the nature and the origin of orogenic heat by applying garnet geospeedometry.

Garnet compositional zoning is used as a gauge for rate estimates of element diffusion within the mineral. Convectional geothermobarometry supported by phase equilibria modelling and garnet chemical compositions indicate an inverted thermal- and a normal pressure-gradient within increasing structural levels in the Lesser Himalaya footwall of the Main Central Thrust. Pressure - temperature (*P*-*T*) path obtained in the garnet-zone were modelled with inverse-fitting numerical model considering Fractionation and Diffusion in GarnEt (FRIDGE). The numerical model calculates garnet composition profiles by introducing pressure-temperature-time (*P*-*T*-*t*) paths and the bulk-rock composition of a specific sample. Simulations were then compared with measured garnet profiles.

Due to the complexity of zoning patterns related to different metamorphic stages, garnets from staurolite-, kyanite- and sillimanite-zone were not suitable for the FRIDGE approach. A simple diffusion step function was then applied. Results indicate 3 to 5.7 Myr short peak metamorphic conditions. This short duration does not allow thermal re-equilibration but preservation of inverted metamorphic gradients. Zircon SHRIMP ages show that peak metamorphic conditions near the Main Central Thrust were reached between *c*. 18 and 15 Ma.

Considering the normal pressure gradient, the narrowness (2 to 5 km) of high grade rocks (kyanite- and sillimanite-zone) and the short duration of peak-*T* conditions within the Main Central Thrust, it is contend that viscous-heating explains localized and short-lived metamorphic conditions along crustal thrust zones like the Main Central Thrust.

3.1 Introduction

Inverted Barrovian metamorphic isograds are reported to be one of the major consequences of large and possibly fast movements on syn-metamorphic crustal-scale thrust zones (e.g. Le Fort, 1975; Graham and England, 1976, England and Molnar, 1993). Such thrust zones place high metamorphic grade rocks over lower grade rocks (e.g. Gansser, 1964; Le Fort, 1975; Burg *et al*., 1984, 1989; Searle *et al.*, 1988, Searle and Rex, 1989; Cogné, 1990; England *et al*., 1992; England and Molnar, 1993; Pitra *et al*., 2010) and occur in tectonic settings ranging from continent-continent collision (Andreasson and Lagerblad, 1980) to subduction zones (Peacock, 1987). The most documented example of inverted metamorphic sequences is in the Himalayas across the Main Central Thrust (MCT, Fig. 3.1; e.g. Gansser, 1964, Frank *et al*., 1973; Le Fort, 1975; Vannay and Grasemann, 1998; Hodges, 2000; Caddick *et al*., 2007; Kohn, 2008). Many interpretations, numerical models and kinematic simulations have been proposed to explain metamorphic zone inversion. For example, large scale folding of isograds (e.g. Searle and Rex, 1988; Swapp and Hollister, 1991; Stephenson *et al*., 2001) and brittle/ductile superposition of high grade rocks over lower grade ones (e.g. Brunel and Andrieux, 1980; Andrieux *et al*., 1981). In these cases, the pressure gradient is also inverted. Other authors interpreted the inversion of isograds as a syn-kinematic process such ductile thrusting related to either ductile extrusion (e.g. Gibson *et al*., 1999; Grasemann and Vannay, 1999; Grujic *et al*., 1996; Jamieson *et al*., 2002, 2004), or the ‘hot-iron’ model, where a hot slab is thrust over a cold one (Le Fort, 1975), or viscous-heating (e.g. England and Molnar, 1993; Burg and Schmalholz, 2008). In these cases the temperature gradient is inverted, but the pressure gradient is normal.

The main difficulty is to determine the thermal source needed to reach peak temperature (T) conditions obtained from petrological thermobarometric methods next the major thrusts (e.g. Jamieson *et al.*, 1998; Engi *et al.*, 2001) and simultaneously, consider quantitatively the physics of the heat transfer on small and large scales (e.g. England and Molnar, 1993, Schott *et al.*, 2000; Burg and Gerya, 2005; Faccenda *et al.*, 2008; Burg and Schmalholz, 2008; Gerya *et al.*, 2008).

Beside the interpretation of heat source(s), another question concerns the duration of the peak thermal event. Previous models of conductive thermal relaxation in tectonically thickened crust predicted that the attainment of metamorphic peak conditions should span few tens of million years (e.g. Thompson and England, 1984). Recent structural, petrologic, isotopic and diffusion studies suggest that some metamorphic processes may operate over much shorter timescales (few millions of years; Kröner *et al*., 1998; Oliver *et al.*, 2000; Schott *et al.*, 2000; Camacho *et al.*, 2005; Dewey, 2005; Caddick *et al.*, 2010; Chu and Ague, 2015) or even < 1 Ma (Ague and Baxter, 2007, 2013). This discrepancy reflects that thermo-mechanical evolution, origin and nature of regional metamorphic heat in collisional settings remain important limitations in understanding orogenic processes. Figuring out the thermal structure and duration of peak-*T* conditions in an orogenic setting can be fundamental for the interpretation of rheological properties and thus deformational evolution (Schott *et al.*, 2000; Jamieson *et al.*, 2002).

In this study, the applied geological chronometer is garnet geospeedometry (Lasaga, 1983) with the step function method described in Ague and Baxter (2007). Garnet compositional zoning, formed by intracrystalline diffusion, is a rare indicator to estimate the rate of element diffusion within the mineral and thus constrain the timescales of metamorphic conditions during orogenesis (Lasaga, 1983; Spear *et al.*, 1984; Perchuk and Phillipot, 1997; Ague and Baxter, 2007; Viete *et al.*, 2011, Ague and Carlson, 2013; Chu and Ague, 2015).

3.2 Geological setting and stratigraphy

Our case study is in the Sikkim Himalaya. Collision between India and Eurasia caused the closure of the Tethys Ocean and the subsequent 2400 km long Himalayan orogen (Le Fort, 1975; Gansser, 1981; Pêcher, 1989).

The Himalayan belt is divided into four major units separated by three north-dipping major fault zones (Fig. 3.1) from the south to the north, i.e. from the structural bottom to top:

- The Main Boundary Thrust (MBT) between the Neogene Siwalik Molasse of the Sub-Himalaya and the Middle Proterozoic Lesser Himalaya (LH).
- The Main Central Thrust (MCT) accommodates the Late Proterozoic high grade metamorphic rocks of the Higher Himalaya (HH) unit over the LH unit.
- The low-angle South Tibetan Detachment System (STDS) separates the HH unit in the footwall from the low-grade Cambrian to Middle Eocene Tethyan Himalaya metasediments (TS) in the hanging wall, to the north. These fault zones converge into a basal décollement, the Main Himalayan Thrust (MHT; Pandey *et al*., 1995; Warren *et al.*, 2013). MCT and STDS have opposite senses of shear and have been synchronously active in the Early Miocene (e.g. Burg *et al*., 1984; Burchfield *et al*., 1992).

The MCT accommodated from 140 (Schelling and Arita, 1991) or perhaps up to more than 500 km (Coward and Butler, 1985; Srivastava and Mitra, 1994) of displacement. This major thrust zone is well known for the inverted isograds mapped over the entire length of the Himalayas (Heim and Gansser, 1939; Gansser, 1964; Le Fort, 1975; Searle, 1986; Hodges *et al*., 1988; Vannay and Grasemann, 2001; Caddick *et al*., 2007). The precise structural placement and timing of thrusting along the MCT has created a great amount of confusion reflecting different approaches by different workers (e.g. Searle *et al.*, 2008). In the present work, the MCT was mapped in relation to metamorphic reactions, first appearance of index minerals (successively upward garnet, staurolite, kyanite and sillimanite; Heim and Gansser, 1939; Le Fort, 1975; Pêcher, 1977; Searle and Rex, 1989) and zones of high strain, which along the Himalayan belt varies from 2 to 3 km in thickness (e.g. Searle *et al.*, 2008).

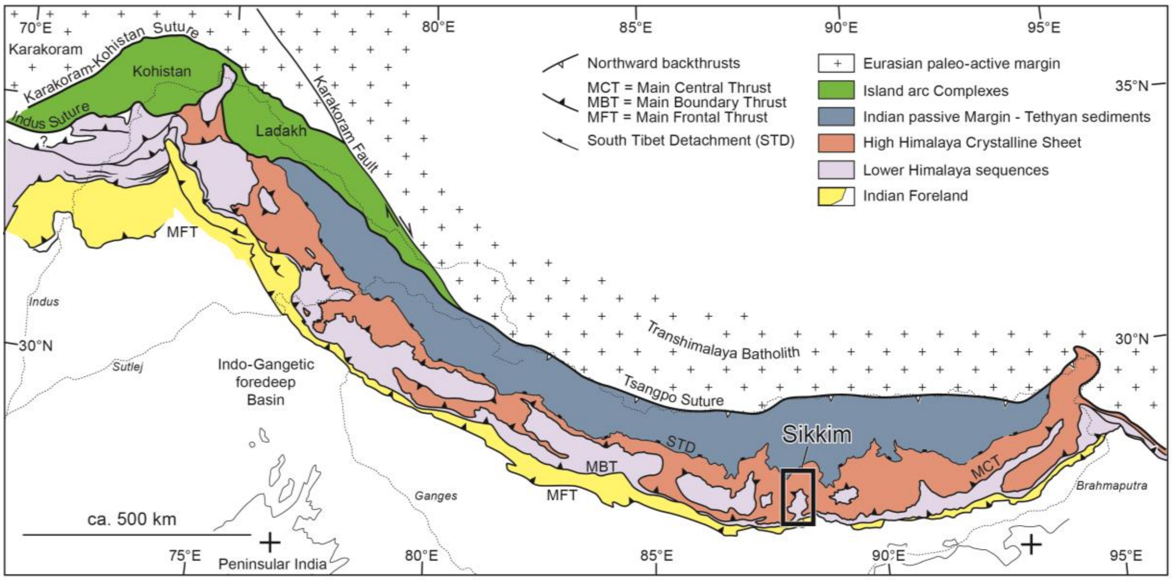

Figure 3.1. Simplified geological map of the Himalaya Belt. Main Boundary Thrust (MBT); Main Central Thrust (MCT; South Tibetan Detachment (STD). Black frame: location of the study area in Sikkim (*modified from Burg: http://www.files.ethz.ch/structuralgeology/jpb/vorlesungen.htm*).

In Sikkim, the main Himalayan units (LH, HH and TS) are arranged in an arcuate, N-S-trending antiform (Fig. 3.2) displaying N-S mineral stretching lineation. The region represents and optimal location to study the MCT and associated metamorphic evolution thanks to excellent exposures of the ductile shear zones and to the complete inverted Barrovian sequence in the LH. The metamorphic grade increases from low chlorite-biotite in the south, to medium biotite-garnet-staurolite-kyanite grade toward the MCT, and kyanite-sillimanite high grade rocks within the MCT shear zone (Sinha-Roy, 1982; Arita, 1983; Mohan *et al.*, 1989; Hodges, 2000; Catlos *et al.*, 2001; Vannay and Grasemann, 2001; Harris *et al.*, 2004; Dasgupta *et al.*, 2004, 2009; Rubatto *et al.*, 2013; Mottram *et al.*, 2014; Gaidies *et al.*, 2015). The High Himalaya (HH) hanging wall crystalline series are characterized by medium- to high-grade metasedimentary series, leucogranites and gneisses with migmatites (e.g. Neogi *et al.*, 1998; Catlos *et al.*, 2004). The grade of metamorphism decreases upward the HH toward the overlying unmetamorphosed TS (e.g. Dasgupta *et al.*, 2004; Faak *et al.*, 2012).

This study describes the Gangtok-Thanggu (SSW-NNE) *c.* 85 km long section across the MCT (A - A’ on Fig. 3.2; Fig. 3.3). Rock samples were systematically collected along the section for petrographic observations, bulk rock compositions, minerals chemistry, geochronology and geospeedometry studies. Conventional geothermobarometry supported by phase diagram section calculation was carried out on pelitic samples. Leucocratic intrusions and leucosomes from migmatitic orthogneisses were sampled to constrain ages of partial melting. Particular attention was dedicated to garnet-bearing rocks from the LH metasediments and from the sillimanite-zone from the MCT shear zone for geospeedometry investigations.

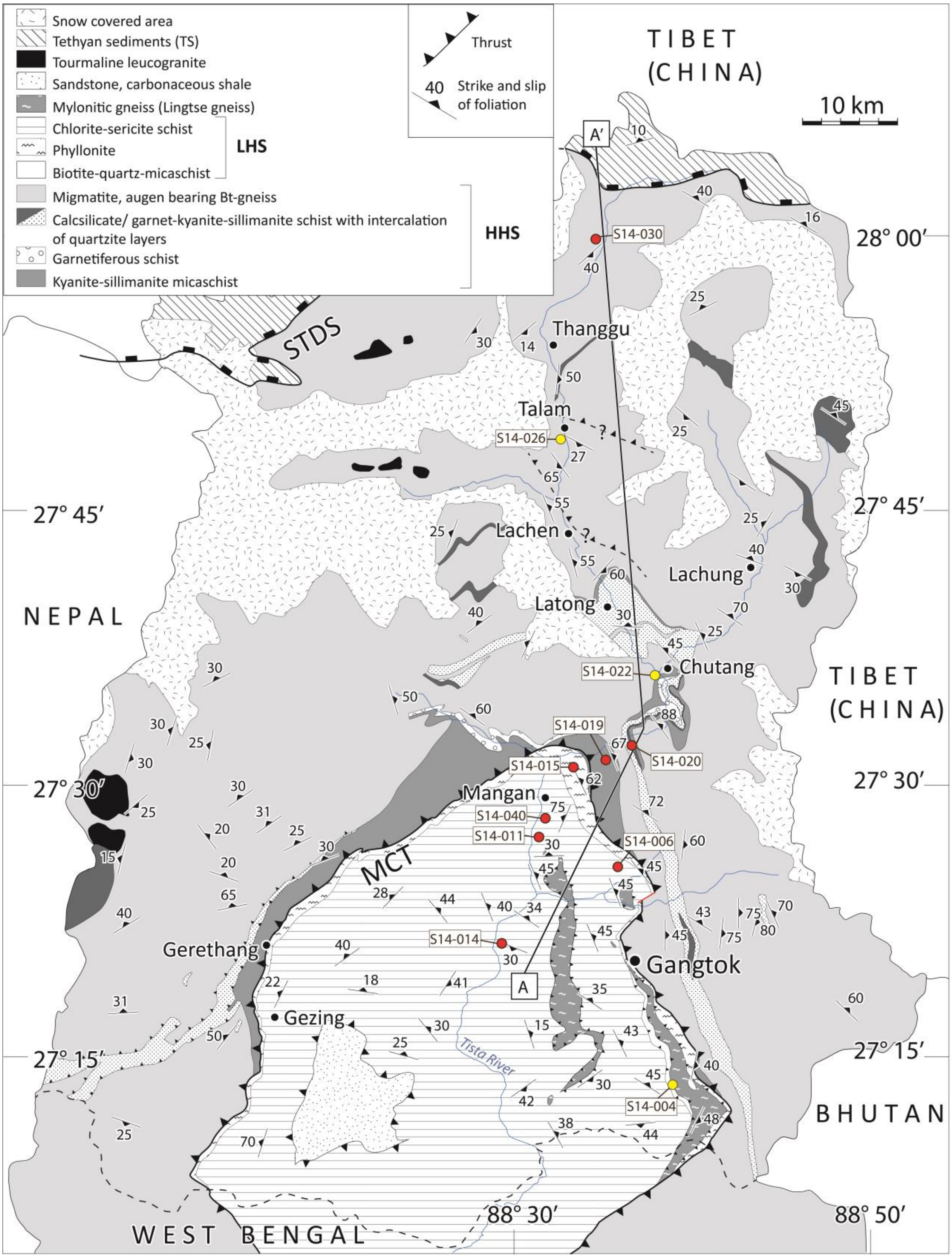

Figure 3.2. Simplified geological map of Sikkim Himalaya with major lithological and structural units (*modified after Ghosh, 1956; Acharryya and Ray, 1977; Lal et al., 1981 and Ray, 2000).* A-A' = trace of the investigated geological profile (Fig. 3.3). Numbered red circles: samples locations; yellow circles: samples for geochronology studies.

3.3 Lithological characterisation and sample description

Ten rock samples representing the spectrum of the LH and the HH in the Sikkim region were selected for this study. Sample location, mineral assemblages, metamorphic grade and their applications are summarized in Table 3.1 and located in Fig. 3.2.

Table 3.1 Provenence, mineral assemblage, metamorphic grade and purpose of the investigated samples

Sample*	Coordinates	Structural unit	Rock type	Mineral assemblage	Metamorphic grade	Purpose
S14-011	N 27° 27' 52.50" E 88° 31' 25.80"	LH	Grt-micaschist	grt, mu, chl, bt, pl, qtz, op	greenschist facies	*P-T* estimates Fractionation mod.
S14-040	N 27° 28' 38.20" E 88° 31' 44.90"	LH	Grt-micaschist	grt, mu, bt, chl, pl, qtz, op	greenschist facies	*P-T* estimates Fractionation mod.
S14-004	N 27° 13' 51.50" E 88° 40' 08.60"	LH	Leucogranite	pl, qtz, ksp, bt, ap, zrc, op	amphibolite facies	U-Pb Geochronology
S14-006	N 27° 26' 43.40" E 88° 36' 34.90"	LH	Grt-st-micaschist	grt, st, bt, mu, pl, qtz, chl, op	amphibolite facies	*P-T* estimates Geospeedometry
S14-015	N 27° 31' 04.90" E 88° 33' 43.40"	LH/MCT	Grt-ky-st-micaschist	grt, ky, st, mu, bt, pl, qtz, chl, op	amphibolite facies	*P-T* estimates Geospeedometry
S14-019	N 27° 31' 48.10" E 88° 36' 24.50"	MCT/HH	Grt-sill-micaschist	grt, sill, bt, mu, pl, qtz, mt, op	amphibolite facies	*P-T* estimates Geospeedometry
S14-020	N 27°32' 21.70" E 88° 36' 54.30"	HH	Grt-sill-bt schist	grt, bt, mu, sill, qtz, pl st, scp, op	amphibolite facies	*P-T* estimates
S14-022	N 27° 36' 0.70" E 88° 38' 55.70"	HH	Leucogranite	pl, qtz, ksp, mu, bt, tur, ap, zrc, op	amphibolite facies	U-Pb Geochronology
S14-026	N 27° 49' 34.40" E 88° 32' 55.00"	HH	Leucogranite	pl, qtz, ksp, mu, bt, ap, zrc, op	amphibolite facies	U-Pb Geochronology
S14-030	N 27° 58' 57.00" E 88° 35' 08.60"	HH	Migmatitic paragneiss	grt, sill, bt, pl, ksp, qtz, op	upper amphibolite facies	*P-T* estimates

*From south toward north

Mineral abbrevation: qtz - quartz; pl - plagioclase; ksp - alkali feldspar; bt - biotite; mu - muscovite; chl - chlorite; grt - garnet; st - staurolite; ky - kyanite; sill - sillimanite; mt - magnetite; ap - apatite; zrc - zircon; epi - epidote; op - opaque; tur - tourmaline; scp - scapolite

3.3.1 Field observations, structural features

The southern bottom of the studied section is in the LH fine- to middle-grained metapsammite and metagraywackes (Fig. 3.3) in which original bedding (from few centimetres up to few decimetres thick) (Fig. 3.4a) is well preserved. The main foliation is sub- parallel to the north-dipping bedding. Rocks are massive, mainly composed of quartz, feldspar, chlorite and minor white mica. Fold axes trend 122° ± 10°E, plunging of 45° ± 8°N. Metapsammite and metagraywackes are intercalated with few decimetres thick metapelitic layers.

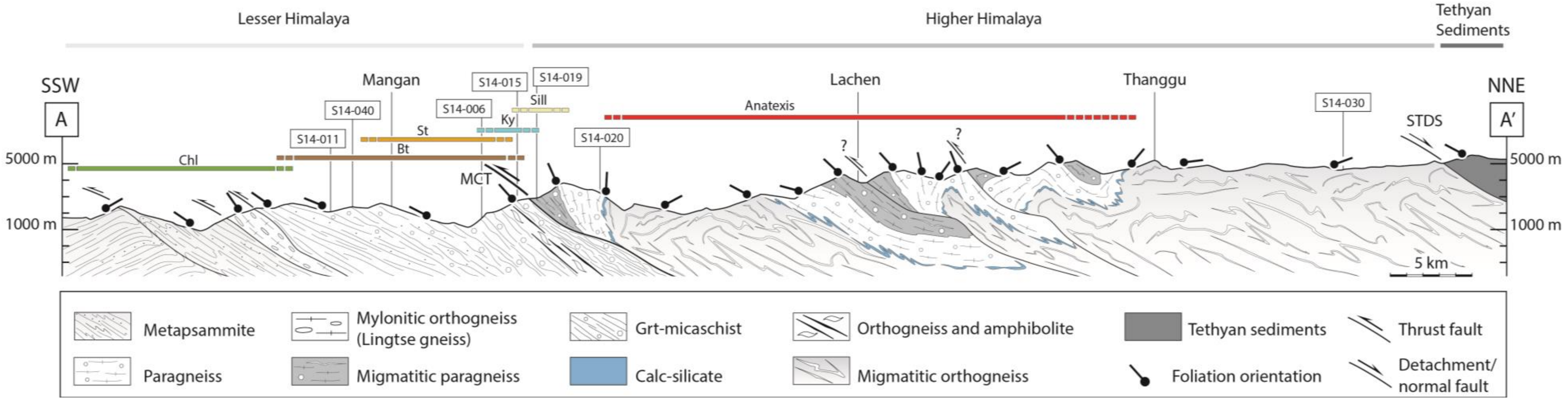

Figure 3.3. Cross section through the Sikkim (location Fig. 3.2) Lesser Himalaya with metamorphic index minerals of the inverted metamorphic zones. Repetition of High Himalaya lithologies is interpreted as tectonic imbrication. Mangan, Lachen and Thanggu localities are correctly positioned along the longitude, but not in elevation.

Moving upward in the pile, heading north, the metamorphic grade increases from greenschist to lower amphibolite facies indicated by abundant biotite and large (up to 7 mm in diameter) rounded euhedral garnet crystals. Garnet-micaschists are strongly foliated and locally folded. Asymmetric recrystallized quartz ribbons and S-C-type fabrics indicate top-to-the-south sense of shear (Fig. 3.4b).

The LH includes bodies of orthogneisses, known as Lingtse Gneiss, mostly exposed at the base of the eastern MCT (Fig. 3.2). Along the studied section a *c.* 50 m thick, N-S sheet of Lingtse Gneiss was mapped between the kyanite bearing phyllonite of the LH and the garnet-sillimanite schist of the MCT shear zone. The porphyroclastic, medium- to coarse-grained orthogneiss gneiss exhibits a N-S lineated L-tectonite (Fig. 3.4c). Similar orthogneisses form tectonic wedges at different levels of the LH stratigraphy (Sinha Roy, 1974).

The HH is composed of crystalline rocks, from sillimanite-bearing pelitic schists, garnet-bearing paragneisses to pelitic migmatites, migmatitic orthogneisses with minor calc-silicate layers, sporadic quarzite and metabasite bodies. We interpret the repetition of garnet-bearing paragneisses, migmatitic paragneisses and migmatitic orthogneisses as post metamorphic, thrust imbrication (Fig. 3.3; e.g. Schelling, 1992; Catlos *et al.*, 2004; Robinson *et al.*, 2006).

Calc-silicate layers range from few meters up to tens of meters in thickness and are folded with dominant south vergence (Fig. 3.4d).

About 10 km to the north of the MCT, near Chungthang locality (Fig. 3.2) fine- to medium-grained leucocratic, few decimetres thick veins cut the main foliation of migmatitic orthogneisses (Fig. 3.4e). Similar leucocratic dykes were observed in the LH, to the south of Gangtok, and in the northern part of the HH (Fig. 3.2). Samples (*S14- 026*, *S14-022* and *S14-004*, Fig. 3.2) were collected for geochemistry analysis and U-Pb SHRIMP zircon geochronology presented in section 3.5.

Migmatitic orthogneisses are dominant in the Latong region and in the Thanggu territory in the northeast part of the section (Fig. 3.2). Leucosomes are predominantly composed of quartz, feldspar, minor biotite and locally garnet and tourmaline. Melt segregation took place along foliation planes indicating partial melting occurred under differential stress (Fig. 3.4f).

Figure 3.4. a) (N27°14’11.1”/E88°38’13.1”) Original layering in LH metapsammite emphasized by white lines. **b)** (N27°28’38.2”/E88°31’44.9”) LH garnet-micaschist in the chlorite-lower amphibolite zone. Asymmetric quartz ribbons and S-C-type fabrics indicating top-to-the-south sense of shear (arrows). **c)** (N27°31’03.5”/E88°34’59.3”) Mylonitic orthogneiss in the LH observed near MCT. **d)** Sub-isoclinal S-vergent folds in calc-silicate layers of the HH (courtesy of Jalutharia H.). **e)** (N27°36’00.7”/ E88°38’55.7”) Fine- to middle-grained leucogranitic veins crosscutting main foliation of a migmatitic orthogneiss. Sample *S14-022* collected for U-Pb geochronology. **f)** (N27°54’26.1”/ E88°31’05.5”) Migmatitic orthogneiss in the HH.

3.3.2 Mineralogical description

Mineral assemblages in low- to high-grade metapelites are given in Table 3.1. We describe six rocks representative for the metamorphic zones from the low-grade LH in the south, through the MCT shear zone to the high-grade HH hanging wall. Particular attention is given to peak mineral assemblages and textural relations of garnet bearing rocks in order to specify the *P*-*T*-path of the rock, which is necessary for geospeedometry diffusion modelling.

Sample *S14-011* is located in the lower part of the garnet-zone (Fig. 3.2). Sub-euhedral garnet porphyroblasts, up to 6 mm in diameter, overgrew a foliation preserved as quartz, ilmenite and minor staurolite inclusions patterns connected to the external foliation. This textural relation suggests syn-tectonic crystallization of garnet. These garnets have been subsequently fractured and partly replaced by chlorite and quartz (Fig. 3.5a).

Garnets in sample *S14-040* are euhedral, 1-7 mm in diameter. Patterns of quartz and ilmenite inclusions are usually curved and in continuity with the rock foliation indicating syn-tectonic garnet growth (Fig. 3.5b). The rock foliation is crenulated with white mica and biotite on the crenulation cleavage. Chlorite is mostly observed around garnet as a retrograde product.

Garnet-staurolite-micaschist *S14-006* in the staurolite-zone is characterized by rounded, 1 - 4 mm in size garnet crystals and up to 5 mm long euhedral staurolite. Most staurolite crystals lay within the main foliation and define the N-S mineral lineation; few are randomly oriented. These textural relationships suggest syn- to late-tectonic crystallization. Garnets show quartz and ilmenite inclusion-rich cores and inclusion-free rims (Fig. 3.5c). Core inclusion patterns are straight defining an internal schistosity disconnected from the matrix foliation. Inclusion patterns and inclusion free rims suggest that garnets growth during different metamorphic stages.

North of Mangan (Fig. 3.2) the kyanite-zone is characterized by garnet-kyanite-phyllonites (sample *S14-015*). Up to 1 cm long kyanite crystals on foliation planes define the N-S mineral lineation. Rare, up to 1 mm long staurolite crystals parallel and across the rock foliation are syn- to late-deformation. In these rocks a general increase in garnet amount and crystal size is observed. Garnet porphyroblasts are euhedral, up to 10 - 15 mm in size. Cores are generally inclusion-rich. Inclusion patterns of quartz, chlorite and minor biotite mimic a foliation (Fig. 3.5d). The outermost rims are inclusions-free.

Sample *S14-019* was collected in the strongly sheared sillimanite-zone delineating the MCT (Fig. 3.2). Sillimanite forms fibrolitic-matted aggregates intergrown with biotite (Fig. 3.5e). Garnet morphologies vary from idioblastic to xenoblastic. Grains are up to 4 mm in diameter and locally replaced by biotite. As in samples *S14-006* and *S14-015*, garnet crystals exhibit two distinct growth zones with inclusions-rich cores and inclusion-free rims, indicating a polymetamorphic evolution (Inger and Harris, 1992, Gaidies *et al.,* 2006).

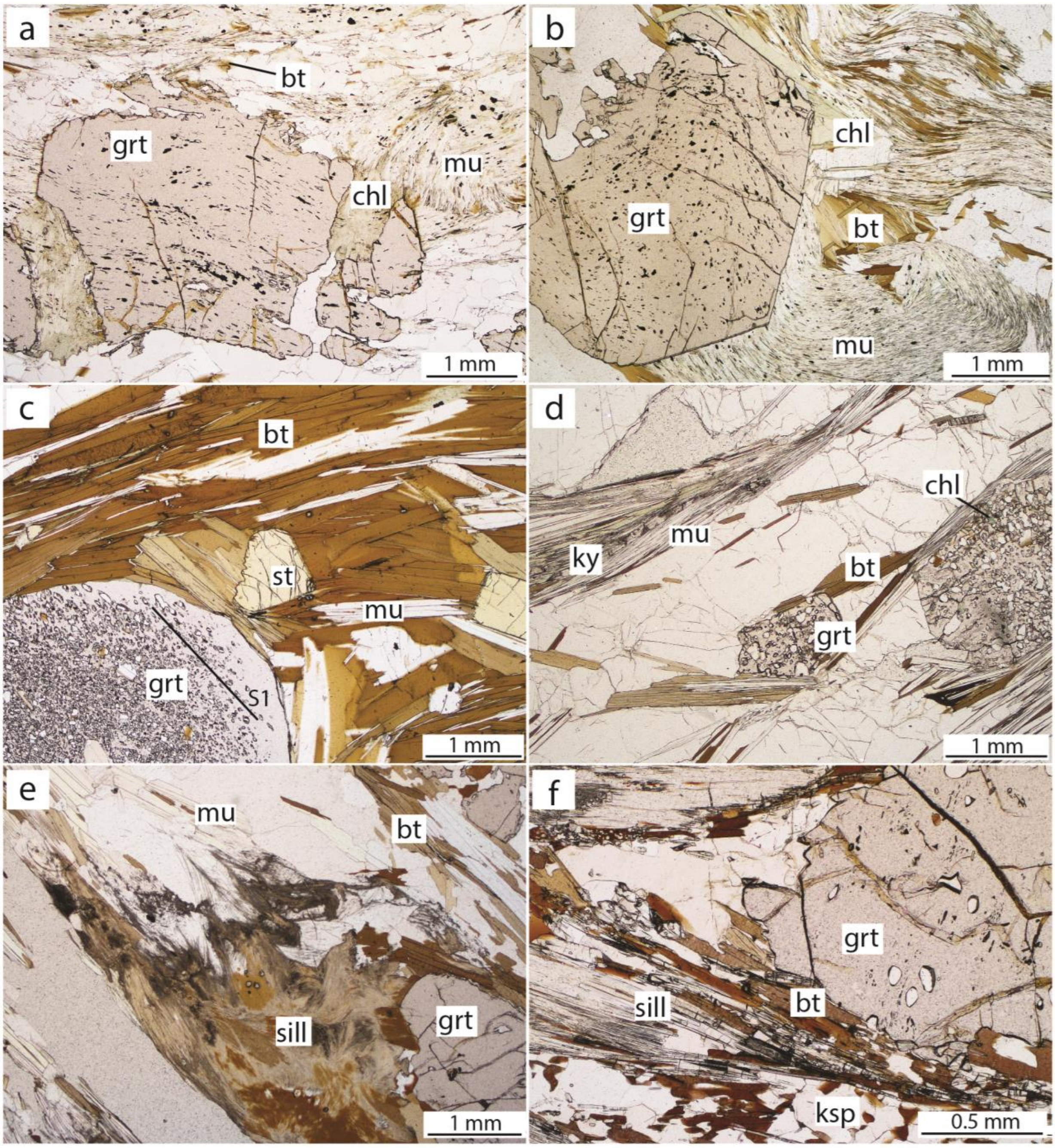

Figure 3.5. Photomicrographs of studied metamorphic samples located in Fig. 3.2 and 3.3. Mineral assemblages and abbreviations in Table 3.1. **a)** ***S14-011*** Garnet with inclusion trails defining internal foliation. **b)** ***S14-040*** Garnet with curved inclusions trails symptomatic for syn-tectonic crystal growth. **c)** ***S14-006*** Garnet-staurolite schist. Inclusions in garnet defining an internal S1 discordant to the external rock foliation. **d)** ***S14-015*** Kyanite, muscovite and biotite defining the main rock foliation. **e)** ***S14-019*** Sillimanite fibrolitic-matted aggregates intergrown with biotite in the MCT shear zone. **f)** ***S14-030*** composed of garnet, acicular sillimanite, biotite and K-feldspar. Muscovite is absent.

Opaque minerals are abundant in garnet core and in the matrix. Mineralogical evidences (magnetite inclusions) indicate that Fe^{3+} content should be considered for *P-T* estimations (subchapter 3.4.2).

Sample *S14-030* was collected in the HH (Fig. 3.2). Biotite and acicular prismatic sillimanite define the main foliation (Fig. 3.5f). The absence of muscovite suggests reaction of white mica with quartz and/or plagioclase to form K-feldspar and sillimanite.

3.4 Peak temperature conditions

Diffusion is exponentially temperature dependent and it is effective at $T > 600$ °C. Peak metamorphic conditions along the studied geological section were estimated from a combination of thin section observations, garnet-biotite Fe-Mg exchange thermometer, phase equilibria calculations and, when suitable, isopleths for garnet and biotite chemical compositions.
The major source of uncertainty with thermobarometry based on Fe-Mg exchange is the resetting of mineral chemistry during cooling and retrograde metamorphism (Frost and Chacko, 1989). Consequently, it is important to corroborate this approach with phase equilibria modelling based on minimization of Gibbs free energy. Representative average EMPA chemical compositions of garnet, biotite, muscovite and plagioclase used for garnet-biotite geothermometry, garnet-alumosilicate-plagioclase-quartz (GASP), garnet-plagioclase-biotite-muscovite-quartz (GPBMQ) and garnet-plagioclase-muscovite-quartz (GPMQ) geobarometry are given in Table 3.2.

Pseudosections and isopleths were calculated in the chemical system of Na_2O-CaO-K_2O-FeO-MgO-Al_2O_3-SiO_2-H_2O-MnO (NCKFMASHMn) for samples *S14-011* and *S14-015*. The chemical system (NCKFMASHMnO) including ferric iron (Fe_2O_3), was used for magnetite bearing samples *S14-040*, *S14-006* and *S14-019*. Phase diagram sections have been calculated using the software Perplex_X_07 (Connolly, 2005), the database of Holland and Powell (2004 update) and mineral solution models listed in Table 3.4. The systems were considered saturated with respect to SiO_2 and H_2O in order to model the prograde path. Whole-rock bulk compositions (Table 3.5) were obtained with X-Ray Fluorescence (XRF) analysis at the ETH Zürich. Effective bulk rock compositions were recalculated in order to constrain peak *P-T* conditions after the sequestration of garnet core compositions of zoned porphyroblasts (Table 3.5). Estimates of peak T-conditions from conventional geothermobarometry were then compared with *P-T* pseudosections calculations.

Table 3.2 Representative microprobe mineral compositions used to estimate peak-T and P conditions

Sample*	Mineral	SiO2	TiO2	Cr2O3	Al2O3	FeO	MnO	MgO	CaO	Na2O	K2O	Total
S14-011	Grt	36.93	0.09	0.04	21.38	37.43	0.33	2.42	3.56	0.02	n.d.	102.18
	Bt	35.62	1.40	0.02	18.81	21.28	0.03	9.16	0.05	0.18	8.76	95.30
	Mu	46.57	0.26	0.04	38.08	0.94	0.02	0.57	0.04	1.20	8.59	96.31
	Pl	64.15	0.05	n.d.	22.71	0.41	0.01	n.d.	2.90	9.44	0.06	99.72
S14-040	Grt	36.63	0.09	0.01	21.36	37.04	0.04	2.76	2.94	0.01	0.01	100.89
	Bt	36.00	1.54	0.01	19.20	19.87	0.02	10.41	0.04	0.34	8.33	95.74
	Mu	45.77	0.30	0.03	38.60	0.73	0.00	0.45	0.01	1.90	7.90	95.69
	Pl	62.80	0.02	n.d.	22.68	0.03	0.00	n.d.	4.06	8.46	0.08	98.13
S14-006	Grt	37.23	0.06	n.d.	21.70	37.12	0.29	3.96	0.98	0.02	n.d.	101.37
	Bt	35.67	1.43	0.03	19.77	20.06	0.01	9.80	0.01	0.37	8.84	95.99
	Mu	46.30	0.44	0.02	38.13	1.20	0.07	0.68	0.02	1.49	8.56	96.91
	Pl	64.12	0.03	n.d.	21.29	0.01	0.00	0.00	2.88	9.25	0.12	97.72
S14-015	Grt	37.73	0.06	0.01	21.26	37.05	0.10	4.71	1.47	0.03	0.01	102.43
	Bt	36.44	2.18	0.01	19.75	20.22	0.01	9.81	0.01	0.30	7.58	96.31
	Mu	46.23	0.65	0.02	37.27	1.21	0.01	0.75	0.01	1.21	8.91	96.26
	Pl	61.34	0.03	n.d.	24.00	0.02	0.01	n.d.	5.08	8.08	0.11	98.67
S14-019	Grt	37.45	0.06	0.02	21.90	37.01	0.45	3.45	1.48	0.01	0.00	101.82
	Bt	35.24	2.84	0.02	21.93	23.67	0.02	7.75	0.03	0.31	8.84	100.65
	Mu	46.07	0.90	0.02	37.22	1.51	0.00	0.74	0.01	0.72	9.39	96.58
	Pl	63.59	0.03	0.01	22.84	0.07	0.01	0.00	3.88	8.84	0.11	99.39
S14-020	Grt	39.26	0.07	0.01	21.86	30.72	0.13	7.81	2.67	0.02	n.d.	102.56
	Bt	37.25	1.01	0.08	18.38	12.90	0.02	16.78	0.03	0.59	7.72	94.76
	Pl	60.39	0.04	n.d.	24.68	0.05	0.01	0.00	5.68	7.93	0.06	98.84
S14-030	Grt	38.14	0.06	0.01	21.66	32.12	2.08	5.40	1.45	n.d.	0.01	100.92
	Bt	34.91	4.75	0.01	17.81	18.98	0.04	9.65	0.05	0.09	9.34	95.61
	Pl	62.45	0.04	0.02	23.29	0.15	0.01	0.00	4.01	8.61	0.31	98.90

*From south to north

3.4.1 Conventional geothermobarometry

Garnet major element concentration maps previously performed with the microprobe (details in 3.6.2), provided evidence for compositional zoning and thin (few µm) retrograde outer rims related to exchange reactions between garnet porphyroblasts and matrix (Frost and Chacko, 1989; Kohn and Spear, 2000). To obtain peak-*T* conditions, quantitative analyses of garnet-biotite pairs (minimum of three measurements for each pair) were performed taking into account the retrogressed thin rims, i.e. few µm from the grains boundary contact. Biotite compositions have been measured in garnet inclusions in the prograde zone (near-rim) and paired with the surrounding garnet. In absence of biotite-inclusions, measurements have been performed considering biotite next to garnet and/or biotite from the matrix. Results of calculated pressures and peak-*T* for several calibrations are summarized in Table 3.3 and showed in Fig. 3.6.

Table 3.3 Peak temperature and pressure estimates for metapelites

Sample*	S14-011	S14-040	S14-006	S14-015	S14-019	S14-020	S14-030
Peak temperature [°C]							
	P = 0.9 GPa	P = 0.65 GPa	P = 0.6 GPa	P = 0.6 GPa	P = 0.73 GPa	P = 0.75 GPa	P = 0.85 Gpa
TH76	580	550	746	725	799	652	820
HL77	555	536	704	686	744	620	757
LP81	579	563	700	686	730	730	740
FS78	540	515	775	745	841	638	860
HS82	576	546	784	761	859	664	875
PL83 (Spear)	569	548	682	668	715	620	728
BM92_HW	520	560	680	675	718	590	694
BM92_GS	460	565	670	673	715	552	648
PL85	627	590	693	690	743	660	755
Pressure [GPa]	T = 560 °C	T = 550 °C	T = 680 °C	T = 660 °C	T = 720 °C	T = 650 °C	T = 750 °C
H90_R5	0.91	0.65	0.63	0.6	0.74	1.06	1.06
H90_R6	0.9	0.65	0.56	0.53	0.65	1.04	0.98
HC85_Fe	0.86	0.69	0.62	0.61	0.74	0.74	_
HC89_Mg	0.88	0.63	0.61	0.56	_	_	_
NH81_Ky	_	_	_	0.57	_	_	_
NH81_Sill	_	_	_	_	0.73	0.74	0.76
HC85_Ky	_	_	_	0.61	_	_	_
HC85_Ky_ev	_	_	_	0.63	_	_	_
HC85_Sill	_	_	_	_	0.72	0.77	0.72
HC85_Sill_ev	_	_	_	_	0.75	0.79	0.76
KN88_Ky	_	_	_	0.66	_	_	_
KN88_Sill	_	_	_	_	0.81	0.84	0.84
K89_ky	_	_	_	0.7	_	_	_
K89_Sill	_	_	_	_	0.87	0.87	0.94

* From south toward north

Calibration abbrevation: TH76 - Thompson (1976); HL77 - Holdaway and Lee (1977); LP81 - Lavrent'eva and Perchuk (1981); HS82 - Hodges and Spear (1982); PL83 - Perchuk and Lavrent'eva (1983); B92-HW/GS - Bathacharya et al. (1992); FS78 - Ferry and Spear (1978); H90_R5 - Hoisch (1990); HC85 - Hodges and Crowley (1985); NH81 - Newton and Haselton (1981); KN88 - Kozio and Newton (1988); K89 - Koziol (1989); PL85 - Perchuk et al., 1985. Uncertainties are ± 40 °C, ± 50 MPa.

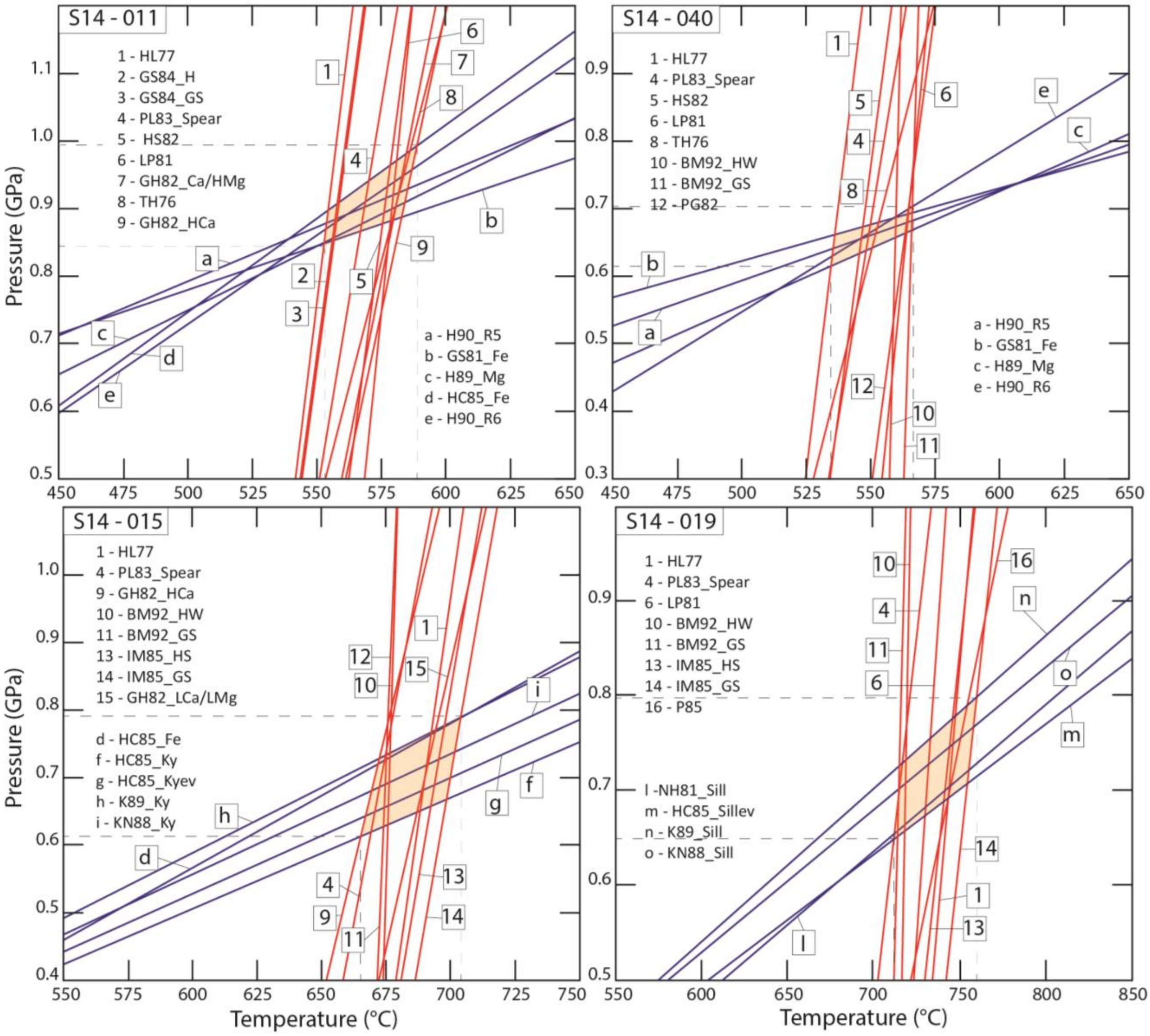

Figure 3.6. Summary of conventional thermobarometric calculations for samples *S14-011*, *S14-040*, *S14-15* and *S14-019* (Figs. 3.2 and 3.3). Orange sectors: *P*-*T* estimate range. Blue lines: pressures. Red lines: temperatures. Calibration abbreviations are presented in Table 3.3.

Sample *S14-011* at the entrance into the garnet-zone yielded an average peak-*T* of 568 ± 12 °C and pressure of 0.9 ± 0.07 GPa (Fig. 3.6a). Similar temperature conditions have been recorded in sample *S14-040* (between 509 and 578 °C) at pressure of 0.66 ± 0.05 GPa (Fig. 3.6b). Estimated peak-*T* in the staurolite-zone (sample *S14-006*) span between 649 and 704 °C and pressures at 0.66 ± 0.04 GPa. Average peak-*T* of different calibrations in the kyanite-zone (sample *S14-015*) gave temperatures of 660 ± 25 °C and pressures at 0.6 ± 0.06 GPa (Fig. 3.6c). Sillimanite-bearing rock *S14-019* from the MCT shear zone yielded peak-*T* of 730 ± 20 °C at 0.77 ± 0.05 GPa (Fig. 3.6d). Sample *S14-020* from the HH recorded temperatures between 620 and 730 °C and pressures between 0.76 and 1.06 GPa. Sample *S14-030* from the northernmost part of the section (Fig. 3.2) yielded temperatures between 740 and 860 °C and pressures ranging from 0.76 to 1.06 GPa.

3.4.2 P-T pseudosection

Phase equilibria calculations (pseudosections) are based on minimization of Gibbs free energy, where mineral assemblage stability fields, for a specific bulk rock composition, are represented in the *P-T* space. Pseudosections were constructed for samples *S14-011*, *S14-040*, *S14-006*, *S14-015* and *S14-019*.

Garnet porphyroblasts in these samples show concentric compositional zoning profiles. In order to estimate the effective equilibrating bulk compositions, XRF-derived bulk rock analyses have been corrected (Table 3.3) as follows: modal proportion of garnet was estimated from thin sections, rock sample surface and Perplex modal calculations (Appendix B1). Garnet compositional profiles and XRF analyses were recalculated in molar proportions. Volume (vol. %) of garnet cores were estimated from garnet chemical composition maps and profiles, obtained from the electron microprobe. Assuming a spherical geometry, garnet core average compositions have been removed from the total XRF bulk analyses.

Table 3.4 Solid solutions used in the equilibrium phase diagram calculations

Mineral phase	Solution model	Reference
amphibole	GlTrTsMr	Massone and Willner, 2008
biotite	Bio (TCC)	Tajcmanová *et al*., 2009
chlorite	Chl (HP)	Holland *et al*., 1998
chloritoid	Ctd (HP)	White *et al*., 2000
cordierite	hCrd	Holland and Powell, 1998
epidote	Ep (HP)	Holland and Powell, 1998
feldspar	San	Waldbaum and Thompson 1968
garnet	Gt (GCT)	Ganguly *et al.*, 1996
ilmenite	IlHm (A)	Andersen and Lindsley, 1998
magnetite	MtUl (A)	Andersen and Lindsley, 1998
melt	melt (HP)	White *et al*., 2007
muscovite	Mica (CHA)	Coggon and Holland, 2002
orthopyroxene	Opx (HP)	Powell and Holland, 1999
plagioclase	Pl (h)	Newton *et al*., 1981
staurolite	St (HP)	Parameters from Thermocalc

Table 3.5 XRF-derived and effective bulk rock compositions of acidic rocks

Sample*	S14-011		S14-040		S14-006		S14-015		S14-019		S14-004**	S14-022**	S14-026**
Major oxides (wt%)	XRF	Effective	XRF	Effective	XRF	Effective	XRF	Effective	XRF	Effective			
SiO_2	57.48	56.95	50.64	49.73	58.90	57.15	60.62	60.13	65.37	65.15	73.19	76.08	73.01
TiO_2	0.68	0.67	0.81	0.81	0.48	0.47	0.64	0.63	0.75	0.75	0.07	0.02	0.12
Al_2O_3	21.79	21.49	25.97	25.43	17.96	16.96	20.22	19.95	17.98	17.85	14.83	14.85	14.46
FeO	7.66	7.14	9.02	8.16	12.60	10.81	6.77	6.31	6.03	5.80	0.77	0.50	1.16
MgO	2.32	2.29	2.51	2.47	3.21	3.09	2.04	1.99	1.35	1.33	0.19	0.07	0.22
MnO	0.04	0.01	0.07	0.00	0.12	0.07	0.05	0.03	0.04	0.03	0.01	0.02	0.02
CaO	0.53	0.48	0.56	0.47	0.61	0.55	0.47	0.44	0.35	0.34	1.60	0.95	0.71
Na_2O	1.27	1.27	1.64	1.64	1.04	1.04	0.69	0.69	0.94	0.94	4.40	4.16	3.79
K_2O	4.26	4.26	4.91	4.91	3.32	3.32	5.13	5.13	4.27	4.27	3.89	1.89	4.72
LOI	3.17	3.17	3.08	3.08	1.06	1.06	2.59	2.59	1.91	1.91	0.33	1.00	0.63
Total	99.21	97.73	99.21	96.69	99.30	94.53	99.22	97.90	98.99	98.38	99.26	99.53	98.84
Traces (ppm)													
Rb	217.80		267.50		189.20		225.10		240.00		99.00	176.60	364.70
Ba	698.80		933.40		435.70		843.90		696.40		399.50	16.30	234.10
Sr	101.90		117.30		41.40		79.90		115.10		98.10	22.00	78.20
Nb	18.00		20.00		13.40		14.10		15.90		0.00	7.00	13.90
Zr	125.30		179.90		98.90		123.90		204.40		37.40	21.20	65.60
Hf	2.80		7.90		0.00		6.00		5.00		1.20	0.00	0.90
Y	32.70		45.20		35.00		24.80		38.80		33.20	16.40	18.70
Ga	29.20		33.70		22.00		29.30		23.60		11.00	16.10	19.30
Zn	97.00		95.30		65.70		46.60		92.70		5.00	8.40	38.80
Cu	50.90		2.50		28.30		27.60		23.10		3.80	0.00	1.10
Ni	43.00		42.50		35.80		36.10		28.10		1.90	6.70	5.60
Co	25.60		26.50		23.40		19.10		20.00		14.00	9.00	11.40
Cr	81.00		94.80		49.70		66.40		55.20		0.00	0.00	0.00
V	85.60		105.20		68.70		87.30		89.40		8.10	2.90	3.00
Sc	18.90		22.10		15.30		15.60		16.50		2.60	1.90	0.70
La	69.50		89.30		41.20		67.10		45.90		5.50	7.80	20.90
Ce	117.70		175.90		88.90		103.60		100.10		0.00	20.80	19.00
Nd	44.70		59.50		38.60		42.10		41.60		3.10	0.40	10.00
Pb	28.70		34.40		9.30		14.70		39.70		20.10	29.90	62.90
Th	32.80		35.70		18.10		25.70		23.00		0.00	0.00	14.30
U	3.30		3.40		5.40		4.00		3.00		3.70	1.80	12.30
W	63.20		68.20		102.50		62.50		115.80		210.00	162.00	235.20

* From south toward north against the MCT

**Samples for geochronology studies

The presence of ferric (Fe^{3+}) iron can affect phase relations in a rock and its amount is in general a good indicator of redox budget of a system (Evans, 2006; Diener and Powell, 2010). Isothermal pseudosections *P*-*X* (Fe_2O_3) were calculated for magnetite-bearing rocks *S14-040*, *S14-006* and *S14-019* (Fig. 3.7). Changes of Fe^{3+} content in the bulk composition are expressed in terms of *X* (Fe_2O_3), from pure Fe^{2+} (*X* (Fe_2O_3) = 0) to pure Fe^{3+} (*X* (Fe_2O_3) = 1.0), in function of *P* at a fixed *T* previously estimated with thermometric calculations.

In sample *S14-040* the intersection of garnet *X*Mg# (*X*Mg = Mg/ (Mg + Fe)), grossular (*X*Grs = Ca/ (Ca+Mg+Mn+Fe)) and spessartine (*X*Sps = Mn/ (Ca+Mg+Mn+Fe)) contours in the *P*-*X*(Fe_2O_3) diagram section at *T* at 570 °C, indicates Fe^{3+} content of *c*. 0.1 and *P* at 1.3 GPa (Fig. 3.7a). Garnet *X*Mg# and *X*Grs isopleths intersect the stability field of sample *S14-006* at *c*. 0.2 *X*(Fe_2O_3) and *P* at 0.7 GPa (T = 640 °C; Fig. 3.7b).

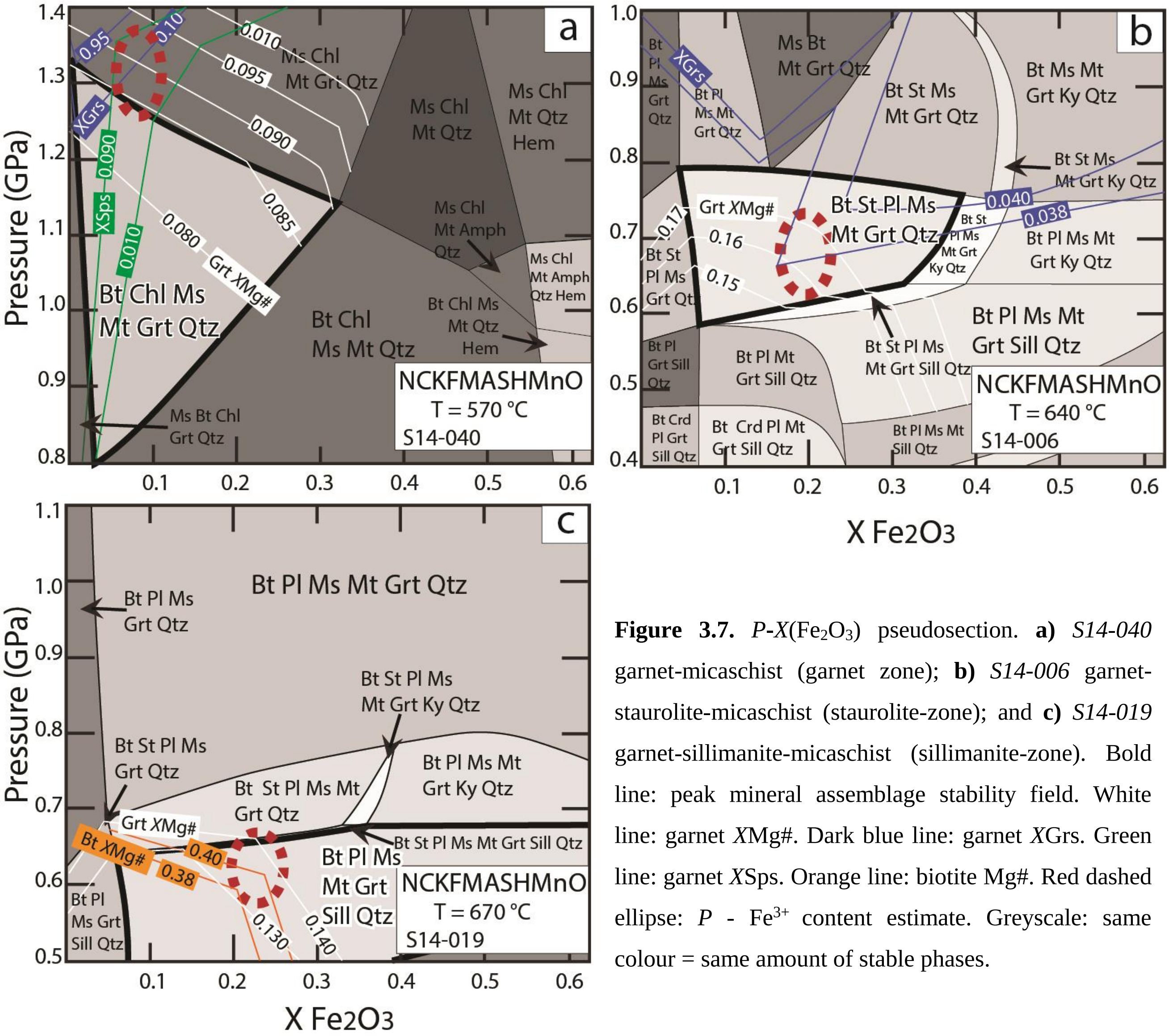

Figure 3.7. *P*-*X*(Fe_2O_3) pseudosection. **a)** *S14-040* garnet-micaschist (garnet zone); **b)** *S14-006* garnet-staurolite-micaschist (staurolite-zone); and **c)** *S14-019* garnet-sillimanite-micaschist (sillimanite-zone). Bold line: peak mineral assemblage stability field. White line: garnet *X*Mg#. Dark blue line: garnet *X*Grs. Green line: garnet *X*Sps. Orange line: biotite Mg#. Red dashed ellipse: *P* - Fe^{3+} content estimate. Greyscale: same colour = same amount of stable phases.

The mineral assemblage stability field of sample *S14-019* ranges from 0.08 to > 0.6 X (Fe_2O_3) (Fig. 3.7c). Biotite Mg# and garnet *X*Mg# contours intersect at *c*. 0.25 X (Fe_2O_3) and P at c. 0.65 GPa (T = 670 °C; Fig. 3.7c).

The *P-T* range of peak mineral assemblage of sample *S14-011* covers T-conditions from 520 to 600 °C and P > 1.4 GPa (bold field in Fig. 3.8a). Biotite in the matrix and adjacent to garnet have similar compositions with *X*Mg# between 0.43 and 0.45. Grossular content (*X*Grs) ranges between 0.06 and 0.07, whereas garnet *X*Mg# is 0.10 to 0.11. Garnet (*X*Mg# and *X*Grs) and biotite (Mg#) isopleths intersect the stability field at 570 ± 20 °C and 1.0 ± 0.05 GPa. Feldspar has an anorthite content (X_{An}= Ca/ (Ca+Na+K)) of 0.15 - 0.24 indicating that it is not in equilibrium with the system and may represents either a relic of a previous stable mineral assemblage, or it (re)crystallized during the retrograde path.

The peak assemblage of sample *S14-040* coincides with a large stability field between 490 and 610 °C and pressures from 0.55 to 1.4 GPa (Fig. 3.8b). Garnet isopleths (*X*Mg# between 0.09 and 011, Xgrs range between 0.08 and 0.09) and biotite Mg# (about 0.48) constrain peak-*T* between 560 and 580 °C at about 1.1 GPa. As in sample *S14-011*, feldspar anorthite content (X_{An} at about 0.209) is not stable at peak metamorphic conditions and, as sample *S14-011*, may have (re)crystallized during deformation.

Peak mineral assemblage stability field of sample *S14-006* ranges between 550 and 650 °C. Biotite Mg# and garnet isopleths intersect the stability field at 630 - 640 °C and 0.58 - 0.68 GPa (Fig. 3.8c).

Temperature and pressure estimates for sample *S14-015* range from 650 to 670 °C and 0.65 to 0.82 GPa (Fig. 3.8d). The stability field including staurolite occurs at slightly lower *P-T* conditions (few °C and 0.06 GPa).

Due the uncertainty of Fe^{3+} estimate in sample *S14-019* (Fig. 3.7c), *P-T* pseudosections were calculated with 0.2, 0.25 and 0.3 Fe^{3+} content. Results do not evidences divergences between the three *P-T* phase diagram sections. In Fig. 3.8e is presented the pseudosection result with a Fe^{3+} content of 0.25. Intersections of grossular and garnet Mg# compositional contours in the stability field of sample *S14-019* bracket peak temperature conditions between 640 and 670°C and pressures between 0.5 and 0.6 GPa (Fig. 3.8e). Pseudosections predict partial melting for this bulk rock composition at these conditions. In the field we did not find evidence of partial melting.

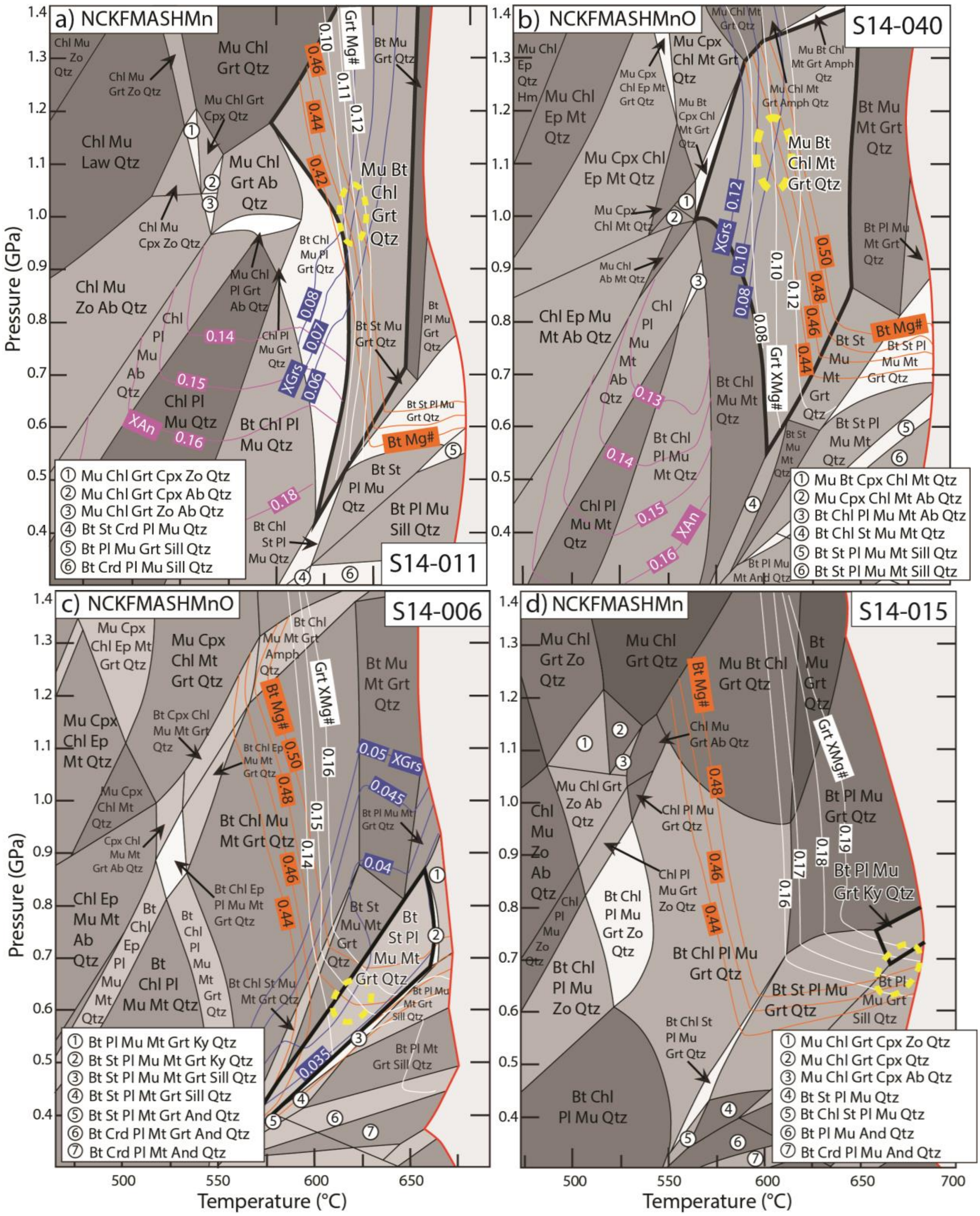

Figure 3.8. Calculated (NCKFMASHMn ± O) P-T pseudosection for metapelitic rocks from the LH inverted metamorphic region. Bold line: mineral assemblage stability field. White lines: garnet *X*Mg#. Blue lines: *X*grossular (*X*Grs). Orange lines: biotite *X*Mg#. Pink lines: *X*anorthite (*X*An). Dashed ellipse: estimated P-T conditions. From south toward north: **a)** S14-011 garnet-biotite-zone LH; **b)** S14-040 garnet-biotite-zone LH; **c)** S14-006 garnet-staurolite-zone LH; **d)** S14-015 garnet-kyanite ± staurolite zone LH. **e)** S14-019 garnet-sillimanite zone. Effective bulk rock compositions in Table 3.5. Same greyscale = same amount of stable phases.

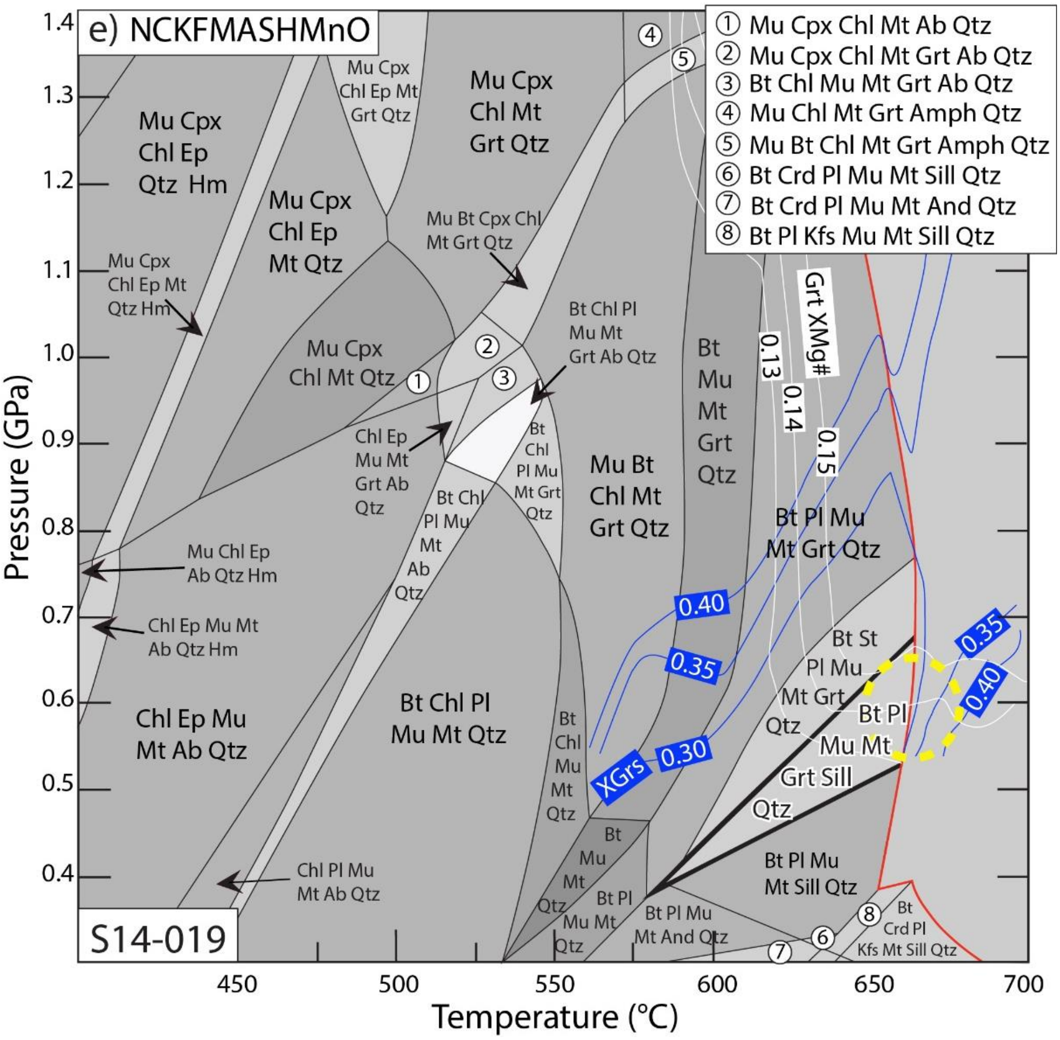

Figure 3.8. Continued

3.5 Zircon U-Pb geochronology

Three samples, from south to north: *S14-004*, *S14-022*, *S14-026*, have been selected to date partial melting and leucocratic granitic intrusions (Fig. 3.2). Mineral assemblages are given in Table 3.1 and bulk rock chemical composition in Table 3.5. Zircons have been processed and separated at the ETH Zürich using high voltage electrical discharge in the SelFrag apparatus (http://www.selfrag.com), sieving and heavy liquid separation procedures. In situ U-Pb analyses were performed using a Sensitive High resolution Ion Microprobe (SHRIMP) II in the Center of Isotopic Research (CIR) at VSEGEI, Saint-Petersburg.

3.5.1 Zircon characteristics in cathodoluminescence (CL) images

Leucosome S14-004: Sample *S14-004* was collected to the south of Gangtok (Fig. 3.2) from migmatitic lenses in the grt-phyllonite zone. The rock is massive, homogeneous, fine- to middle grained. CL-images show two main zircon populations, both containing xenocrysts (Fig. 3.9a *left*). The main population is represented by euhedral, needle acicular zircons crystals with sharp and straight edges, 200-260 µm long and 70-90 µm wide. Cores and rims display well-developed regular oscillatory zoning with variable luminescence. The second population is similar in size and shape but is characterized by a homogeneous or weakly zoned irregular metamorphic rim, irregular to patchy cores and parallel fractures trails healed by low-luminescence material (zircon 004-16, Fig. 3.9a). Self-induced micro fractures are attributed to rapid decompression (Rudnick and Williams, 1987) and their generation is a function of the degree of metamictization and confining pressure (Lee and Tromp, 1995).

Leucogranite S14-022 was taken from the 20 to 30 cm thick veins cutting the migmatitic orthogneiss near Chungtang locality (Figs. 3.2 and 3.4e). The rock is homogeneous, middle- to coarse-grained. XRF whole-rock bulk composition is peraluminous (Table 3.5).
This sample is characterized by three zircon populations (Fig. 3.9b *left*). One is constituted by 180-200 µm large rounded cores with variable zoning overgrown by a thin unzoned or weakly zoned rim. These rims are interpreted as metamorphic growth that may have involved melts of migmatitic origin. A second population is characterized by rounded-prismatic, euhedral to subhedral crystals with rounded edges. They are 120- 270 µm long and 70-130 µm wide. Cores exhibit two different types of CL zoning: patchy irregular or weakly regular zoning. The third population is dominated by acicular 200-250 µm long and 60-70 µm wide crystals with sharp edges and well-developed magmatic oscillatory zoning.

Leucogranite S14-026: Sample S14-026 was collected near Talam village, southward of Thanggu in the HH unit (Fig. 3.2). The leucogranitic outcrop is about 25 to 40 m thick; contacts with the host-rock are not exposed. The rock is massive, homogeneous, middle- to coarse-grained, slightly foliated. Whole rock geochemistry indicates a peraluminous granite (Table 3.5).
Cathodoluminescence (CL) images show a heterogeneous zircon population (Fig. 3.9c *left*). The dominant population is characterized by prismatic, euhedral crystals with variable elongation (from 100 to 400 µm), from 100 to 170 µm wide and sharp and straight edges. Most crystals exhibit patchy, chaotic oscillatory cores surrounded by a thin well-developed magmatic oscillatory zoning. Some zircons contain xenocrysts. A second population is characterized by prismatic, 200 -300 µm long and 80-100 µm wide crystals, with slightly rounded edges. Irregular thin metamorphic rims surround weakly oscillatory or patchy cores. Few rounded grains, 80 to 120 µm in size, show an unzoned metamorphic rim too thin for SHRIMP analyses.

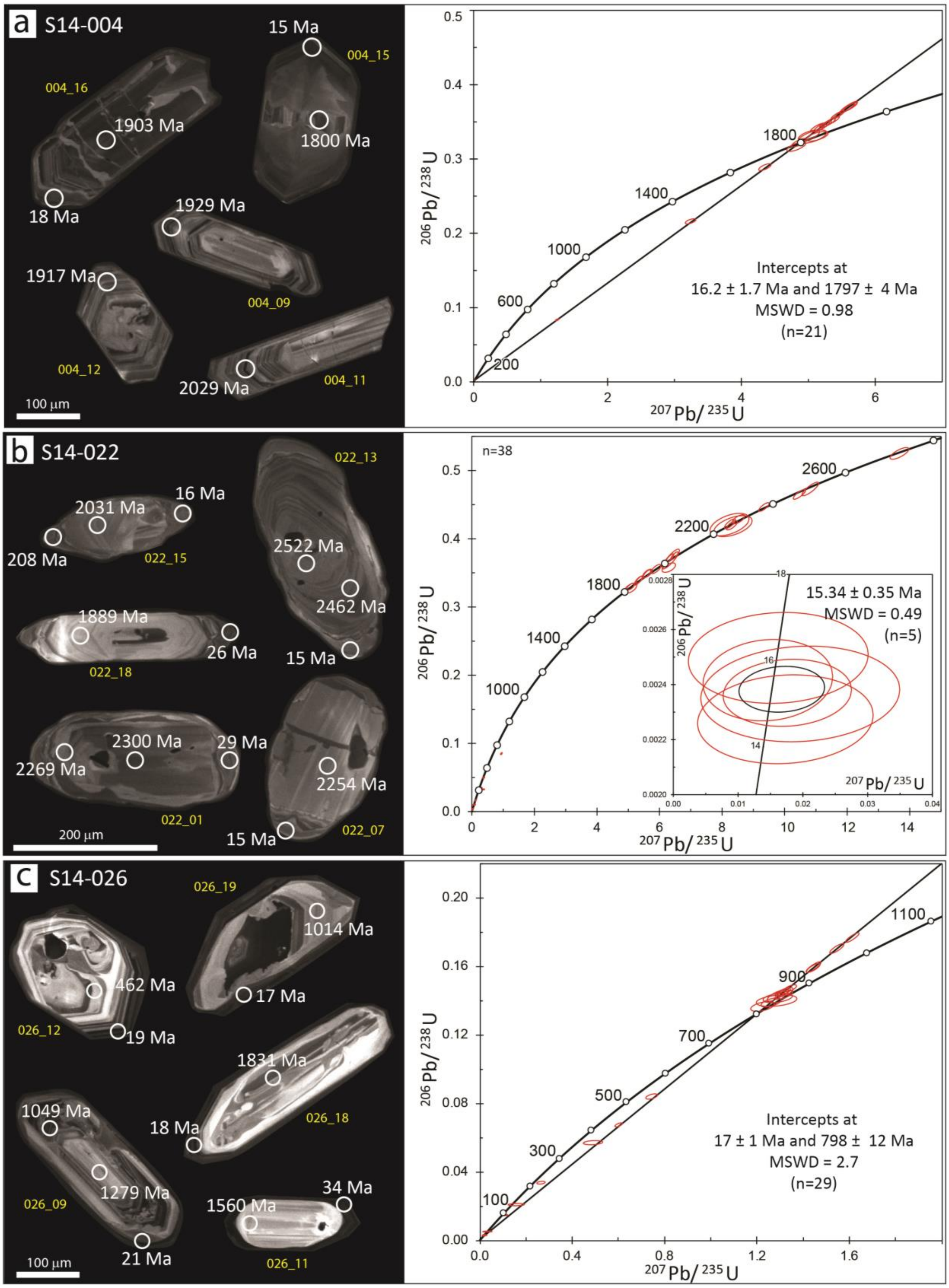

Figure 3.9. *Left*: Cathodoluminescence (CL) images of representative zircon crystals used for U-Pb SHRIMP dating. Circles represent measurement spots and numbers indicate ^{206}Pb/^{238}U ages in Ma. *Right*: Related Concordia diagrams. Uncertainties for the individual analysis are at the 1σ level, whereas the uncertainties in calculated Concordia ages are reported at 2σ level.

3.5.2 U-Pb results

Ages are presented on Concordia diagrams (Fig. 3.9; Wetherill, 1956) and summarized in Table 3.6. Uncertainties of individual analyses are at the 1σ level; uncertainties in calculated Concordia ages are reported at 2σ level.

S14-004: Seven homogeneous to patchy cores were measured in sixteen zircons including all observed populations. Th/U ratios range from 0.23 to 1.05 and yielded Early Proterozoic ages between 1907 and 1637 Ma. Ten spots analyses of oscillatory intermediate zones with Th/U ratios of 0.02-0.29 yielded eight Early Proterozoic (2030 - 1898 Ma), one Middle Proterozoic (1262 ± 3 Ma) and one Cambrian age of 517 ± 3 Ma. Four magmatic outer rim spots with Th/U ratios between 0.001 and 0.14 yielded two Early Proterozoic ages (2021 and 1773 Ma), while the other two spots yielded Middle Miocene ages (15 ± 0.3 Ma). One spot analysis of outer metamorphic rim yielded also a Miocene age of 18 ± 0.3 Ma.

S14-022: Sixteen data points were obtained from cores of eighteen zircons, counting all observed populations, with Th/U ratios between 0.14 and 0.89. Two spots give late Archean ages (2745 and 2522 Ma; fourteen points yielded Early Proterozoic ages (between 2380 and 1827 Ma). Seven intermediate oscillatory zones from seven zircons with Th/U ratios of 0.01-0.45 present four Early Proterozoic (between 2462 and 1889 Ma), one Late Cambrian (527 ± 3.8 Ma), one Early Jurassic (208 ± 2.1 Ma) and one early Cretaceous (110 ± 1.4 Ma) ages. Fifteen analyses of thin metamorphic outer rims yielded low Th/U ratios of 0.01-0.02. One point yielded Late Carboniferous age of 313 ± 2.7 Ma, two points provide Late Triassic ages of 222 and 207 Ma, three points give Cretaceous ages between 99 and 65 Ma and three points yielded Oligocene ages between 32 and 26 Ma. One spot gives Early Miocene age of 21± 0.4 Ma. A cluster of five spots yielded a concordant age of 15.34 ± 0.35 Ma (Fig. 3.9b *right*).

S14-026: Nineteen zircon grains have been selected for dating involving all populations. Thirteen core spots with Th/U ratios between 0.05-0.92 yielded twelve Early to Late Proterozoic ages (1831 ± 12 to 825 ± 7 Ma) and one Ordovician age of 462 ± 3 Ma. Five spots in the intermediate oscillatory zones yielded Th/U ratios of 0.08-0.65 and ages between 1049 ± 6 and 872 ± 6 Ma. Two spots in homogeneous metamorphic rims yielded late Proterozoic ages (864-860 ± 6 Ma, Th/U values 0.04-0.34). Six homogeneous metamorphic rims with Th/U ratios of 0.03-0.28 yielded ages spanning from Cambrian (520 ± 4 Ma), Silurian (412-430 Ma), Late Triassic (213 ± 2 Ma), Early- and Late Cretaceous (133-94 Ma); one spot gives an age of 17 ± 0.3 Ma (Th/U ratio 0.005). Three spots in rims provide Early Miocene ages (Th/U values 0.005-0.018). Six oscillatory rims analyses with Th/U ratios 0.006-0.018 yielded one Oligocene age (34 ± 0.4 Ma) and five early Miocene ages (18-19 Ma).

Table 3.6 Main field and zircon characteristics of the investigated samples

Rock type Sample*	Formation	Field characteristic	Zircon characteristic	Core ages (Ma)	Intermediate oscillatory zone (Ma)	Rim age (Ma)
Leucogranite S14-026	Melt derived from a sedimentary precursor	Coarse-grained, slightly foliated	Oscillatory zoned cores, thin magmatic/metamorphic rim few detrital rounded grains	1831 ± 12 - 825 ± 7	1049 ± 6 - 872 ± 7	[a] 34 ± 0.4-18.4 ± 0.9 [b] scattering between 520 and 17 Ma
Leucogranite S14-022	Melt derived from a sedimentary precursor	Discordant to the host migmatitic orthogneiss, coarse-grained	Detrital rounded zircons, sector and oscillatory cores, thin metamorphic rim	2745 ± 15 - 1827 ± 15	scattering between 2462 and 110 Ma	[b] 15.34 ± 0.35
Leucosome S14-004	Melt derived from melting of a granitoid precursor	Leucocratic, coarse grained, massive melt pocket	Well-developed oscillatory zoned cores and thin metamoprhic rim	1907 ± 14 -1637 ± 9	scattering between 2030 and 517 Ma	[a] 15 ± 0.3 Ma [b] 18 ± 0.3 Ma

* From north to south

[a] Rims diplaying oscillatory zoning; [b] Homogeneous metamoprhic outer rim

3.6 Garnet geospeedometry

The extent of diffusion profiles are strongly dependent on temperature and timescale over which diffusion was effective (Ganguly, 2002). The investigation of chemical zonation in minerals allows to: (1) calculate the rate of element diffusion within the mineral, (2) extrapolate the timescales of thermal events, and (3) provide indications on the tectonic processes active during metamorphism and orogenesis (Lasaga, 1983; Spear *et al.*, 1984; Ague and Baxter, 2007; Viete *et al.,* 2011).

3.6.1 General approach and sample preparation

Garnet chemical zoning develops in response on pressure, temperature and composition (*P*-*T*-*X*) changes during time. Garnet is a very common mineral and in metapelite is mostly represented and zoned by the major elements $(Fe, Ca, Mg, Mn)_3Al_2(SiO_4)_3$. All species have similar physical properties and intracrystalline diffusion rates are slow enough to retain a complete record in the zoning of the major elements. Furthermore garnet crystals are isotropic so that diffusion has no directional dependence which is a considerable advantage in multicomponent zoning modelling. The dodecahedral crystal habit allows to simplify the geometry of the crystal to a sphere (Eq. 1). In radial multicomponent diffusion all major cations Fe, Mg, Mn and Ca are treated as interdependent on each other in order to maintain the stoichiometry of the mineral composition:

$$\begin{pmatrix} \frac{\partial X_1}{\partial t} \\ \frac{\partial X_2}{\partial t} \\ \frac{\partial X_3}{\partial t} \end{pmatrix} = \frac{1}{r^2}\frac{\partial}{\partial r}\left[r^2 \begin{pmatrix} D_{11} & D_{12} & D_{13} \\ D_{21} & D_{22} & D_{23} \\ D_{31} & D_{32} & D_{33} \end{pmatrix} \begin{pmatrix} \frac{\partial X_1}{\partial r} \\ \frac{\partial X_2}{\partial r} \\ \frac{\partial X_3}{\partial r} \end{pmatrix} \right] \tag{1}$$

where X represents the mole fraction of a component, r the radius of the sphere (porphyroblast) and indexes 1, 2 and 3 are any three of the four components (almandine, grossular, pyrope and spessartine).

Diffusivity D is defined by Eq. 2 (Wendt, 1965):

$$D_{ij} = D_i^0 \delta_{ij} - \left[\frac{D_i^0 X_i}{\sum_{k=1}^{n} D_k^0 X_k}\right] \left(D_j^0 - D_n^0\right) \tag{2}$$

and the characteristic time of diffusion is formulate as:

$$t = \frac{\Delta L_D^2}{2D} \tag{3}$$

where D is diffusvity, D^0 self-diffusion coefficient, n is the number of component (n = 4), ΔL_D is the diffusion length, t is the time and δ_{ij}= 0 when $i \neq j$ and 1 when $i = j$.

Euhedral garnet crystals in different sizes (from 3 mm up to 15 mm) were extracted from the rocks samples by hand (hammer and mason). The grains were mounted in epoxy "pills" and polished until exposing the core of the crystal. This procedure was necessary to respect the geometry and warrant the application of radial diffusion numerical modelling. The polished pills were coated with carbon (~30 µm).

3.6.2 Imaging and electron microprobe analyses

Garnet chemical composition maps and profiles were obtained using the electron microprobe JEOL JXA-8200 at the ETH Zürich. Operating conditions for spot analyses were 15 kV accelerating voltage, 20 nA sample current, 20s counting time and beam size < 5 µm. Garnet major element (Mg, Mn, Ca and Fe) concentration maps were performed in order to identify the geometry of growth-diffusion zoning or complete homogenization (Fig. 3.10). Radial garnet composition profiles were analysed for SiO_2, TiO_2, Al_2O_3, FeO, MgO, MnO, CaO, Na_2O, K_2O and Cr_2O_3 avoiding garnet inclusions and cracks. Fe^{3+} was calculated from charge balance. Representative compositional profiles selected for geospeedometry studies are presented in Fig. 3.11.

Garnet crystals from the low-grade LH (*S14-011* and *S14-040*) display similar compositional zoning. From core to rim, almandine (Alm) and pyrope (Prp) increase, whereas spessartine (Sps) and grossular (Grs) decrease (Fig. 3.11a, b). The bell-shape profile of Mn is characteristic of growth zoning without internal diffusion (Hollister, 1969). In these two samples resorption textures at the crystal rim boundaries are not observed. In the kyanite-zone (*S14-015*) and within the MCT shear zone (sillimanite-zone *S14-019*) garnets exhibit a more complex zoning: a compositional discontinuity mark the boundary between the inclusion-rich core and the inclusion-free rim (Fig. 3.10).

Garnet porphyroblasts of sample *S14-015* display four major compositional sectors, from core to rim (Fig. 3.11c): an internal relatively homogenous compositional core, a shell characterized by Mg# decrease, a prograde growing zone represented by Mg# increase and a thin (*c*. 0.1 mm) outermost rim where Mg# drops and *X*Mn increases sharply due to diffusional exchange between garnet and the rock matrix during retrograde metamorphism (Kohn and Spear, 2000). Therefore, the rim was not considered for peak-*T* timescale estimates.

Garnets from sample *S14-019* display an inclusions-rich core with constant major element compositions, a prograde growing zone (increasing of Mg#) and a retrograde outer rim characterized by Mg# decrease and a *X*Mn increase typical of retrograde diffusional cation exchanges with matrix minerals (Fig. 3.11d). These compositional variations in samples *S14-015* and *S14-019* may reflect two different metamorphic stages.

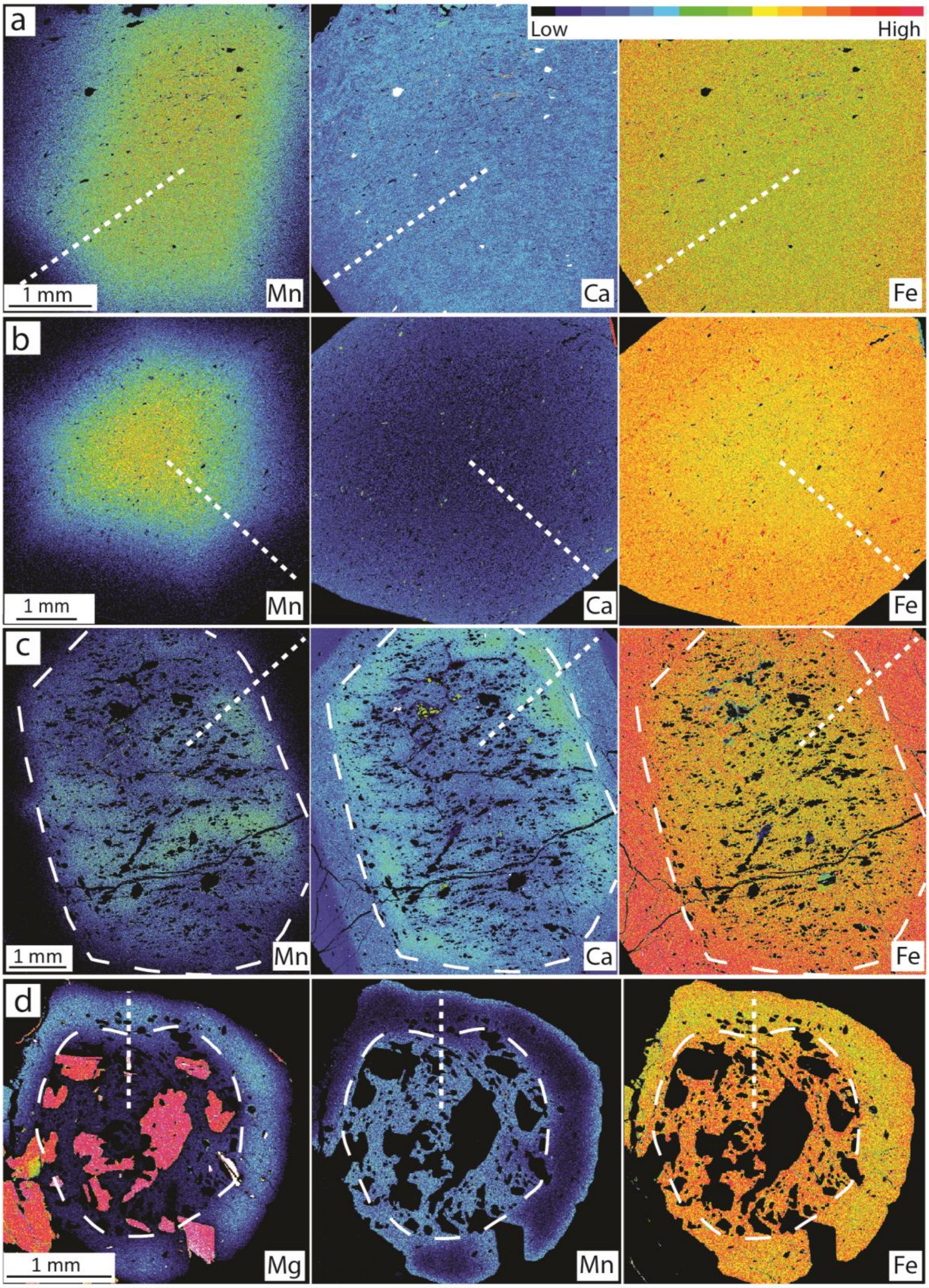

Figure 3.10. Electron microprobe garnet major elements (Ca, Mg, Mn and Fe) concentration maps illustrating varying degrees of compositional zoning. White dots = garnet profile measurements (Fig. 3.11). Dashed white line separates inclusion-rich cores from inclusion-free rims. **a)** Sample *S14-011* and **b)** sample *S14-040* from the LH garnet-zone; **c)** *S14-015* from the kyanite-zone; and **d)** *S14-019* from the sillimanite-zone.

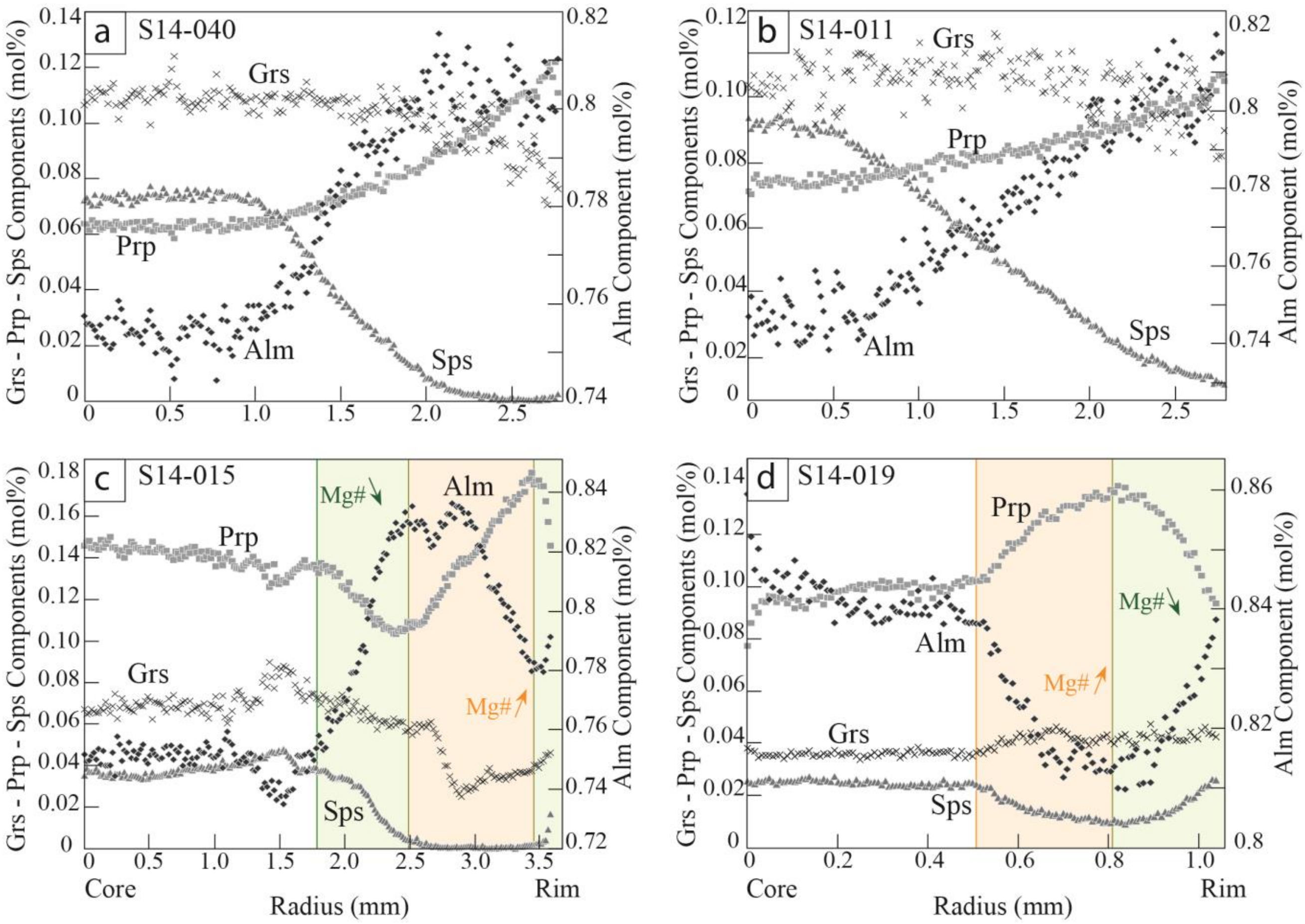

Figure 3.11. Chemical zoning patterns for grossular (Grs), pyrope (Prp), almandine (Alm) and spessartine (Sps) from core to rim (Fig. 3.10) for samples: **a)** *S14-040* (garnet-zone); **b)** *S14-011* (garnet-zone); **c)** *S14-015* (kyanite-zone); **d)** *S14-019* (sillimanite-zone). Orange sector: increase of Mg# indicating prograde growing. Green sector: internal drop in Mg# due to cations exchange with the matrix.

3.*6.3 Garnet fractionation and diffusion modelling*

Inverse fitting model (FRIDGE) considering fractionation and diffusion in garnet for the four major elements simultaneously has been applied to samples *S14-011* and *S14-040* from the LH garnet-zone. Peak-*T* conditions of these two samples are < 600 °C. Consequently, garnet growth compositional profiles were not modified by diffusion providing information about the prograde path experienced by the rock (e.g. Kohn, 2003; Caddick *et al.*, 2010).

The inverse fitting model generates modeled compositional profiles of garnet from a given bulk rock composition assuming chemical fractionation and simultaneous diffusion along a *P*-*T*-*t* path. The *P*-*T* path is not completely arbitrary because it is predicted with the support of phase diagram sections, peak *P*-*T* estimates, petrographic observations and intersections of garnet (from core to rim) compositional contours. Peak-*T* and *P* conditions previously estimated are considered as fix parameters. *P-T* path is changed until the mismatch between calculated and observed profile is minimized. The minimization is evaluated through the following cost function:

$$\chi^2 = \sum \sum \left(C_{r,j}^{mod} - C_{r,j}^{obs}\right)^2$$

The model assumes that the garnet crystal is fractionated from a given bulk rock composition as soon as it crystalizes along a *P-T* path. During each growth step the matrix has a bulk rock composition different from that in the previous step and always in equilibrium with the garnet temporary rim. Along the *P-T* path garnet crystal diffuses as soon as it fractionated (diffusivity efficient at T > 600 °C). Limitations of the model are the assumptions of homogeneous crystal distribution and small variation in garnet sizes.

Garnets from samples *S14-006 (*St-zone*)*, *S14-015* (Ky-zone) and *S14-019* (Sill-zone) exhibit complex compositional zoning representing at least two metamorphic stages (Figs. 3.10 and 3.11). In these cases, FRIDGE numerical model approach is inconvenient because garnet core compositions are almost homogenized (Fig. 3.11) making the prediction of initial *P-T* path impossible. In these cases, garnet radial multicomponent diffusion modelling in a sphere (Eq.1) with the step function method of Ague and Baxter (2007) was employed.

The model estimates the time needed to match the calculated simulation curves with the measured garnet profiles. A step function was defined at the abrupt change in chemical composition (increasing of Mg#). This compositional change corresponds to the transition from an inclusions rich-core and inclusion-free outer shell. It is assumed that the outer shell represents garnet fractionation/diffusion at peak-*T* conditions during the last metamorphic episode. The pre-existing compositional step function undergoes diffusional relaxation during peak-*T* conditions and compositional profiles are considered “frozen” during cooling. This procedure ensures that peak-*T* conditions time extent estimation is maximal. Due the low content of spessartine, i.e. uncertainties in defining the compositional step, it was considered as a dependent variable in the system.

3.6.4 Peak temperature duration estimates

Self-diffusion coefficient D_0 were computed using the values from Carlson (2006) and, for comparison, from Chu and Ague (2015). Representative result of FRIDGE garnet fractionation applied in low-grade rocks (*S14-040*) is shown in Fig. 3.12 (Appendix B2 for *S14-011*). Step function diffusion modelling results for five garnet porphyroblasts from different structural levels of LH are presented in Table 3.7, where time-windows indicate the minimum time that at least one garnet component reaches a good fit, and the maximal time at which at least one component is excessively diffused.

Representative diffusion modelling best-fit solutions for sample *S14-015* and *S14-019* are presented in Fig. 3.13 (Appendix B3 for all garnets considered).

Table 3.7 Step-function diffusion modelling results

			Timescale (t) window	
Sample		Peak *T* [°C]	Carlson (2006)	Chu and Ague (2015)
S14-006	Grt-06-1	640	7 < t < 12 Myr	*X*Mn best-fit at 4 Myr
Staurolite-zone				t > 15 Myr
S14-015	Grt-15-1	660	4.6 < t < 5.4 Myr	4.8 < t < 5.9 Myr
Kyanite-zone	Grt-15-2	660	4.8 < t < 5.7 Myr	5.2 < t < 7 Myr
S14-019	Grt-19-1	680	2.6 < t < 3.5 Myr	No good fit*
Sillimanite-zone	Grt-19-2	680	2.0 < t < 3.2 Myr	No good fit*

*A "good fit" is obtained minimazing the distance between observed and predicted compositional profile.

The estimated *P-T* path history of sample *S14-040* (Fig. 3.12 *left*) was applied to two different garnet porphyroblasts (Grt-1 and Grt2). FRIDGE simulation fit well with the measured garnet profiles for both porphyroblasts (Fig. 3.12 *right*), ratifying the estimated *P-T* evolution. Good-fit results are also obtained in both garnet porphyroblasts from sample *S14-011* (Appendix B2). FRIDGE compositional profile simulations endorses *P-T* conditions for garnet crystallization starting from 0.75 GPa and 540 °C for sample *S14-011* and 0.85 GPa and 550 °C for sample *S14-040*. Pressures in both samples increase up to 1.25 ± 0.05 GPa, whereas temperatures remain < 600 °C. The estimated *P-T* path may be representative conditions experienced by both rocks *S14-011* and *S14-040*. Note that similar *P* at peak-*T* conditions were predicted by phase diagram section calculations combined with mineral composition contours (section 3.4, Fig. 3.8b).

Single step function calculations applied to samples *S14-006* (staurolite-zone), *S14-015* (kyanite-zone) and *S14-019* (sillimanite-zone) with diffusion coefficients of Carlson (2006), predict short-lived peak-*T* conditions for the three zones. Simulations reach best-fit compositional profiles for all components simultaneously (Figs. 3.13a, b). Note the sinusoidal curve of almandine profiles in *S14-015* simulated by the model (Fig. 3.13a).

Best-fit diffusion compositional profiles simulated with diffusion coefficients of Chu and Ague (2015) are imprecise in shape, yields longer time than those estimated with the values of Carlson (2006) and best-fit solutions are not reached for all components simultaneously. Results with diffusivity of Carlson (2006) are more consistent for all components.

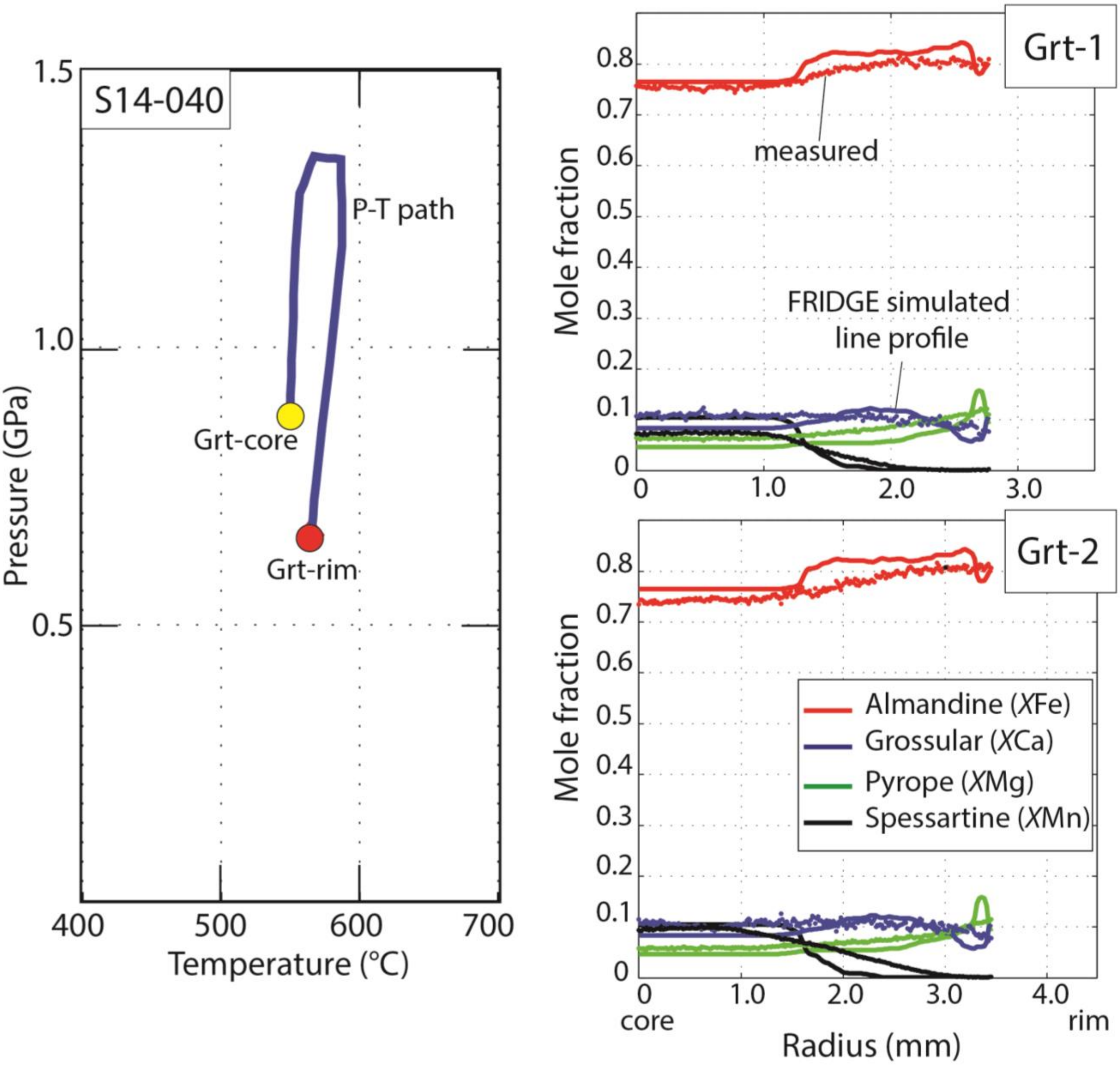

Figure 3.12. Representative FRIDGE results for sample S14-040. *Left*: given P-T path. Yellow dot: P-T conditions for garnet core (Grt-core) composition. Red dot: P-T conditions for garnet rim conditions (Grt-rim). *Right*: FRIDGE garnet compositional simulations, along the given P-T path, compared with measured garnet profiles of Grt-1 (top) and Grt-2 (bottom).

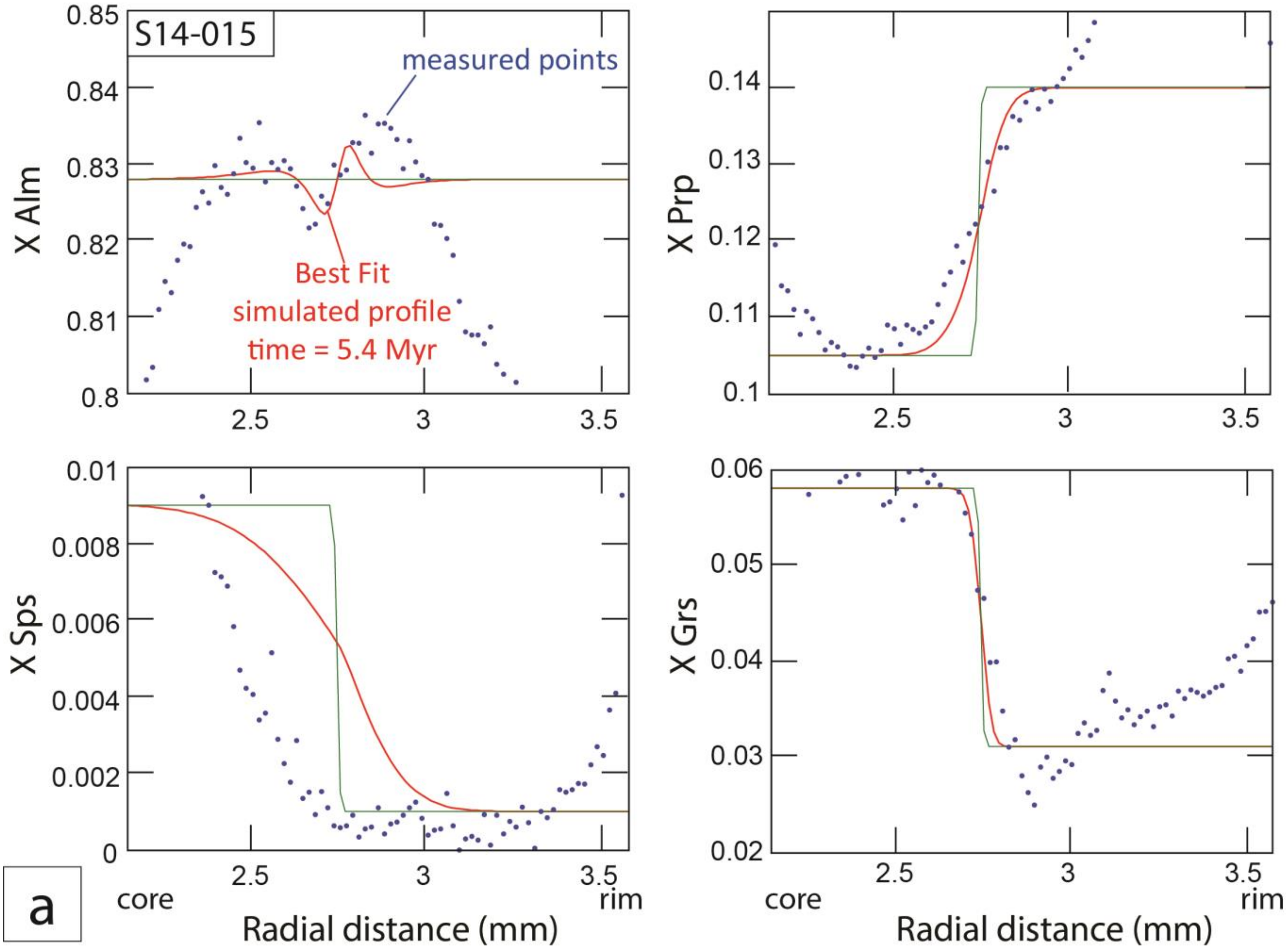

Figure 3.13. Representative diffusion modelling results for almandine (Alm), pyrope (Prp), spessartine (Sps) and grossular (Grs) mole fraction (X). **a)** *S14-015* (kyanite-zone, Grt-15-1); peak-T = 660 °C. Best-fit solution for all components after 5.4 Myr. **b)** *S14-019* (sillimanite-zone, Grt-19-1); peak-T = 680 °C. Best-fit after 3.8 Myr. Green line: Step function initial conditions. Red line: best-fit solutions. Blue dots: measured points.

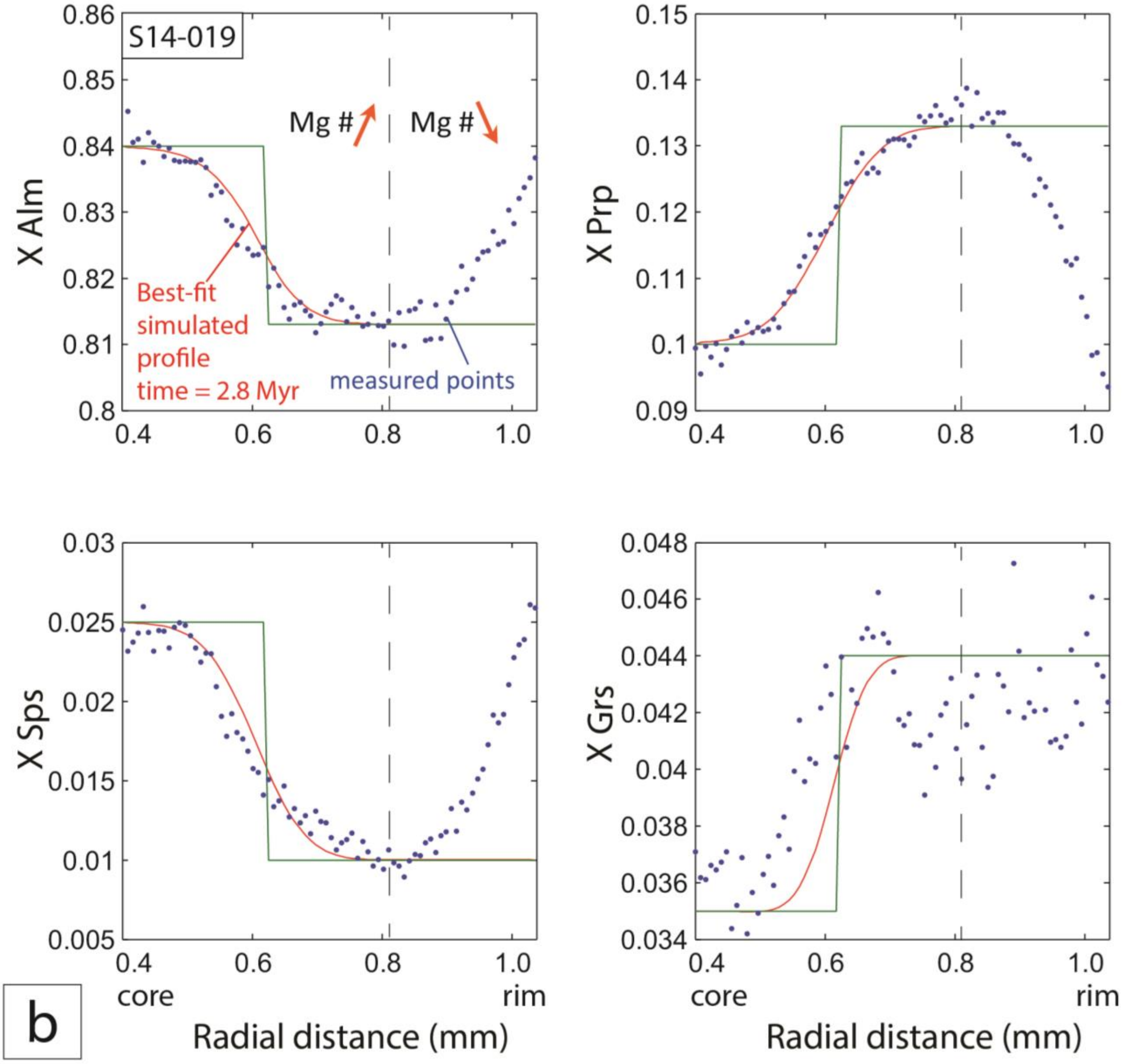

Figure 3.13 Continued

3.7 Discussion

3.7.1 Ages of metamorphic peak

The small number of analysed samples, the restricted amount of dated zircons and the complexity of the crystal domains require careful interpretations.

Samples *S14-026* and *S14-022* collected in the HH (Fig. 3.2) are characterized by heterogeneous (at least three) zircon populations. In both samples core ages are distributed from Late Archean (2745 - 2522 Ma) to Late Proterozoic (825 ± 7 Ma). In sample *S14-026* essentially two rim types were recognized: homogeneous irregular metamorphic rims dated from Cambrian (520 Ma) to Early Miocene (17 Ma), and Oligocene (34 Ma) to Early Miocene (21-18 Ma) thin oscillatory rims. The oscillatory outer rims, attributed to magma crystallisation (Corfu *et al.*, 2003), are interpreted as (re)crystallization during partial melting. Oligocene to Early Miocene (34 - 18 Ma) ages of anatexis in the HH are in agreement with previous dating of HH leucogranites (e.g. Harris *et al.*, 1993; Harrison *et al.*, 1995; Kohn *et al.*, 2010, Rubatto *et al.*, 2013, Mottram *et al.*, 2014).

Zircons from sample *S14-022* collected near the MCT (Fig. 3.2) display thin irregular homogeneous metamorphic rims with three group of ages: from Late Carboniferous to Late Triassic - Early Jurassic (313 - 208 Ma), Late Cretaceous (99 - 65 Ma), and Middle Miocene (16 - 15 Ma). Heterogeneous zircon crystal morphologies coupled with varied U-Pb SHRIMP ages suggest that both leucogranitic intrusions (*S14-0126* and *S14-022*) were generated during partial melting of a continental precursor.

Zircon domains from LH migmatitic lenses (sample *S14-004*) are more homogeneous in size and in shape than previous samples. They display oscillatory zoning. The magmatic precursor may be the Lingtse orthogneiss outcropping near the sampling area (Fig. 3.2) whose Early Proterozoic ages (2030 - 1637 Ma) matches ages obtained by Mottram *et al*. (2014). Homogeneous irregular metamorphic rims are associated to the latest Early- Middle Miocene (between 18 and 15 Ma) metamorphic event.

In the higher portion of the HH (*S14-026*, Fig. 3.2) rock recorded earlier metamorphism (*c*. 34 Ma and 21 - 17 Ma) than in the lower HH structural level near the MCT (*S14-022*), where metamorphic ages are younger with shorter time span (16 - 15 Ma). Similar results were reported by Imayama *et al.* (2012) in eastern Nepal (higher structural level: 33 - 23 Ma; structurally lower domains: 21 - 16 Ma) and by Mottram *et al.* (2014) in western Sikkim (from *c*. 37 to 16 Ma moving toward the MCT).

Investigations of Warren *et al.* (2011, 2013) in north-western Bhutan and north-east India, and the study of Rubatto *et al*. (2013) in north-eastern Sikkim, yielded an opposite age trend, where younger metamorphic rocks thrusted over older rocks. They suggested a major fault separating a younger, structurally higher terrane from an older, structurally lower terrane. This major structure in Sikkim Himalaya was defined between Lachen and Thanggu locality (Rubatto *et al.*, 2013). Field observations support the presence of at least one fault between the two localities in the HH (Figs. 3.2 and 3.3). However, the relatively limited amount of data, the opposite trend of ages arisen between different studies in (or near) the Sikkim HH, require prudence in formulate final statements on the orogenic evolution. In addition, as discussed in Rubatto *et al.* (2013), it is important to consider that individual samples from the same unit/outcrop may record zircon crystallization at slightly different times due to slightly differences in *P*-*T* conditions, in LREE and Zr saturation (Kelsey *et al*., 2008).

3.7.2 Peak metamorphic conditions and duration estimates

Conventional geothermobarometry (garnet-biotite Fe-Mg thermometer, garnet – muscovite – biotite – plagioclase (GMPB) and garnet – aluminosilicate – plagioclase – quartz (GASP) barometers), phase diagram section calculations, garnet-biotite compositional contours indicate that moving up-section in the LH, from the garnet-zone toward the MCT across *c*. 5 km pile of rocks, peak-*T* conditions increase from *c*. 560 °C to *c*. 680 °C, whereas pressure conditions are decreasing from *c*. 1.2 GPa to *c*. 0.6 GPa. This is in disagreement with previous studies that reported an inverted gradient in both temperature and pressure conditions (Dasgupta *et al.,* 2009; Mottram *et al.*, 2014; Gaidies *et al.*, 2015). Discrepancies are largest in pressure estimates in the garnet-zone, whereas peak-*T* and pressure conditions predicted in the staurolite-, kyanite- and sillimanite-zone are consistent with previous studies in east and north Sikkim (Dasgupta *et al.,* 2009; Gaidies *et al.,* 2015).

GMPB pressure estimates were obtained assuming plagioclase in equilibrium with the peak mineral assemblage. However, pseudosections calculations and anorthite content (*X*An) contours point to disequilibrium between plagioclase and peak mineral assemblage (Fig. 3.8a, b), making the GMPB barometer inapplicable for all investigated samples in the LH. This may explain the relatively small Δ*T*s and relatively large Δ*P*s obtained with others studies. The plagioclase may either represent relicts of a previous stable assemblage, or it (re)crystallized during the retrograde part of the *P*-*T* path. Plagioclase recrystallization, nucleation and growth of new grains start to be important at medium grade conditions (450 - 600 °C; e.g. Borges and White, 1980), even more if deformation is active, as in the strongly sheared Main Central Thrust. Consequently, pressure estimates need to be supported with phase equilibria calculations, both garnet and biotite compositional isopleths and their intersections in the *P*-*T* space. In the garnet-zone, peak-*T* are < 600 °C (Fig. 3.8a, b). Therefore, garnet compositional zoning is not modified by diffusion and preserves information about the *P*-*T* evolution during porphyroblast fractionation (e.g. Kohn, 2003; Caddick *et al.,* 2010). Metamorphic *P*-*T* history in the garnet-zone was endorsed with Fractionation and Diffusion in Garnet (FRIDGE) inverse fitting modelling. The optimal *P*-*T* path is estimated with the support of phase diagram sections, peak-*T* estimates and garnet compositional isopleths (from core to rim) considered as steady parameters in the *P*-*T* space. FRIDGE results inferred that sample *S14-011* and *S14-040* in the garnet-zone (Figs. 2.2 and 2.3) pressure estimates (1.1 ± 0.1 GPa) at peak-*T* conditions are effectively higher than concluded in previous studies.

Petrographic observations and garnet compositional profiles from the staurolite-, kyanite- and sillimanite-zone display complex zoning patterns, with two distinct growth zones, suggesting that rocks underwent multiple stages of equilibrium. The qualitative similarity of zonation patterns and inclusions distribution, i.e. inclusion-rich core and inclusion-free rim, suggest that these rocks experienced similar metamorphic evolutions. Inclusion-rich cores display nearly homogeneous compositional profiles (Fig. 3.11c, d) indicating complete equilibration. In the inclusion-free outer shell, petrographic observations and compositional profiles indicate syn-tectonic garnet growth in the prograde path and in equilibrium with the peak mineral assemblage. This support the assumption that garnet porphyroblasts outer shell grew and diffused during peak metamorphic conditions. Staurolite, kyanite and sillimanite define the main lineation parallel to the main N-S shearing movement (Fig. 3.4b). Therefore, peak-metamorphic assemblages are syn-tectonic and associated to foliation formation and top-to-the south thrusting.

The complete metamorphic history, the identification and quantification of possible time gaps between different thermal pulse(s) and their influence on compositional diffusion are impossible to ascertain. In order to estimate the maximal time duration of metamorphic peak conditions, it is assumed that measured chemical concentration profiles resulted from diffusional relaxation active during peak-*T* conditions (e.g. Ague and Baxter, 2007). Best-fit results of simple step function multicomponent diffusion applying diffusion coefficients of Carlson (2006) predict short-lived (2 to 5.7 Myr) peak-*T* conditions in the Himalayan MCT.

3.7.3 Tectonic implication

The complex distribution of ages between different structural levels in the HH reflects distinct metamorphic stages. Slightly diachronous metamorphism and lithological repetitions observed across Sikkim HH, may be due to post metamorphic imbrications (Fig. 3.3). Similar HH faults have been reported by Warren *et al.*, (2011, 2013) and Grujic *et al.*, (2011) in NW Bhutan and Martin *et al.*, (2010) in central Nepal.

This study documents upward pressure decrease and temperature increase in the Sikkim LH. Medium- to high-grade conditions, i.e. from the staurolite- to the sillimanite-zone, are limited in a narrow (3 - 5 km thick) zone parallel to the MCT (Fig. 3.3). Models that predicts inversion of both temperature and pressure gradients are not applied. The thermal inversion may be caused by the emplacement of hot material over the cool footwall (Le Fort, 1975), or by shear/viscous-heating along the thrust (e.g. Graham and England, 1976; England and Molnar, 1993; Stüwe, 1998; Burg and Gerya, 2005; Burg and Schmalholz, 2008; Schmalholz et *al.*, 2014; Schmalholz and Duretz, 2015). Beside the cause of isograds inversion, a debated issue in the metamorphic and tectonic history of the Himalayas is the origin of heat necessary for crustal melting to produce the Miocene leucogranites (e.g. Deniel *et al.* 1987; Copeland *et al.* 1988; Harrison *et al.* 1995). England *et al.* (1992) suggested that shear heating along the MCT may have contributed sufficiently to cause melting in the presence of a fluid.

Thermomechanical model of Burg and Gerya (2005) showed that viscous heating may trigger melting of the subducted crust at the plate interface, increase metamorphic crustal temperatures from 25 to 200 °C, and facilitate the upwelling of lower crustal rocks. The amount of viscous heating in the crust is proportional to convergence rates and it may become the dominant heat source in collision orogens with convergence rates > 1 cm yr^{-1} as in the Himalayas (Burg and Gerya, 2005). Furthermore, the thermal perturbation induced by viscous heating along a shear zones can be about 100 °C and transient in time (few Myr; Schmalholz and Duretz, 2015).

Considering the metamorphic structure of the thrust, the localized high grade zone along the MCT, the transient duration of peak-*T* conditions related to crustal partial melting, viscous heating is hypothesized as most plausible heat source that generated inverted isograds across the MCT.

3.8 Conclusion

This study focused on inverted temperature- and normal pressure-gradients linked to the Main Central Thrust (MCT) in the Sikkim Lower Himalayas. High temperature conditions (kyanite- and sillimanite-zones) are limited to a relatively narrow (few km) zone along the MCT. Differences in peak-*T* estimates between LH high grade rocks and lower grade garnet-zone are *c.* 100 °C across a thickness of about 5 km. Garnet geospeedometry diffusion modelling reveals that peak-*T* conditions persisted for no more than 2 – 5.7 Myr. Considering the normal pressure gradient, the occurrence of significant heating within a short time, viscous-heating along crustal thrusts represents the most persuasive model to explain inverted metamorphic isograds across the MCT. We speculate that peak metamorphic conditions induced by shear-heating may have caused partial melting of magmatic and sedimentary rocks near the MCT between 18 and 15 Ma.

Acknowledgements

We are grateful to Jalutharia Hiten for his precious help and support during field work. Thanks to Lüchinger Remy for his efficient work and high quality thin sections. The authors were supported by ETH Zurich, Research ETH-14 11-1.

4. Garnet multicomponent diffusion applied to the inverted metamorphic sequence in the Champtoceaux Complex, Armorican Massif (France)

Abstract

The aim is to determine the duration (*t*) of peak temperature (*T*) conditions active during crustal-scale thrusting and explain the possible origin of orogenic heat responsible for the inverted metamorphic zonation between the lowest Parautochthon and the Upper Allochthon of the Champtoceaux Complex, Armorican Massif (France). For this purpose, a step function multicomponent (Mg - Fe - Ca and Mn) diffusion in a sphere is applied to garnet porphyroblasts.

Peak temperature conditions, obtained with thermodynamic modelling and garnet isopleths, increase upward from 540 °C in the Lower Micaschist to 640 °C in the Upper Micaschist of footwall units, whereas corresponding pressure conditions are nearly uniform (0.8 ± 0.1 GPa). Geospeedometry results indicate that the maximal duration of peak-*T* conditions was 0.8 - 3.5 Myr.

The transient duration of high *T* conditions, the nearly constant pressure gradient across the investigated section and the narrow (1 km thick) high grade zone, suggest that the origin of the inverted metamorphic zonation was associated with shear heating.

4.1 Introduction

Garnet is a mineral present in a wide range of bulk rock compositions and pressure-temperature (*P*-*T*) metamorphic conditions, ranging from greenschist- to granulite facies. Its isotropic nature, physical strength and abundance make this mineral ideal for investigating fractionation and diffusional processes that are active during metamorphism. Its intracrystalline diffusion rates are slow enough to preserve a complete record of pressure-temperature-time (*P*-*T*-*t*) metamorphic history in the mineral zoning (e.g. Ganguly, 2010), revealing important geological information like heating/cooling rates, pressure variations, changes in fluid content and convection in magmas (e.g. Loomis, 1983; Lasaga, 1983; Spear *et al.*, 1984).

Geospeedometry (Lasaga, 1983) is a technique to estimate the duration of metamorphism by considering modifications in compositional zoning caused by intracrystalline diffusion in garnet (e.g. Lasaga, 1983; Spear *et al.*, 1984; Florence and Spear, 1993; Perchuk and Phillipot, 2000; Ague and Baxter, 2007; Viete *et al.*, 2011, Ague and Carlson, 2013). This technique has the advantage, compared to conventional radiometric dating, to record short-lived events. Such an accuracy is important in interpreting the origin of orogenic heat, tectonic processes and consequent mechanisms responsible for isograds inversion across ductile thrust zones.

Inverted isograds have been investigated in several tectonic settings (e.g. Himalayan belt, Great Caucasus (Russia), Alpine fault (New Zealand), and Scandinavian Caledonides). Diverse numerical models and kinematic simulations have been proposed to explain the inversion of metamorphic zones. A major issue is to determine the thermal source(s) needed to reach peak-*T* recorded by thrust rocks and to constrain the duration (t) of thermal perturbation(s).

Some models attribute inverted metamorphism to local transient syn-kinematic processes such as contact metamorphism generated by magmatic intrusions (e.g. Himmelberg *et al.*, 1991); thrusting (either in one or in multiple steps) of a hot slab over a cold one (‘hot iron’ model of Le Fort, 1975); or shear- or viscous-heating along the thrust (e.g. Graham and England, 1976; Arita, 1983; England and Molnar, 1993; Burg and Schmalholz, 2008). In these scenarios the temperature gradient is reversed, whereas the pressure gradient is normal.

Other authors interpret inversion as post-metamorphic deformation of a former normal sequence. Envisioned processes are brittle/ductile superposition of high grade rocks over lower grade ones (e.g. Brunel and Andrieux, 1980; Andrieux *et al*., 1981); large scale folding of isograds (e.g. Searle and Rex, 1988; Swapp and Hollister, 1991; Stephenson *et al*., 2001); passive ductile thrusting related to ductile extrusion of a wedge (Hodges *et al*., 1993, 1996); or “channel flow” (e.g. Hubbard, 1996; Grujic *et al*., 1996; Vannay and Grasemann, 2001; Beaumont *et al.*, 2001, 2004; Jamieson *et al*., 2002, 2004), where the juxtaposition of outward flowing partially molten mid-crustal channel material contributes to the inverted and right-way-up metamorphic sequence at the base and the top of the extruding channel, respectively (Jamieson *et al*., 2004; Godin *et al.*, 2006). In these models both temperature and pressure gradients are inverted.

In this study, garnet diffusion modelling is applied to garnet micaschists from the Champtoceaux Complex, Armorican Massif, Brittany (France). The Champtoceaux Complex display an inverted metamorphic sequence, where low-grade units are superposed by high-grade metamorphic rocks at the contact between the Lower- and the Upper Allochthons (Ballèvre *et al.* 2009; Pitra *et al.* 2010).

4.2 Geological setting

The Champtoceaux Complex is a crustal-scale thrust zone representing a segment of the Variscan suture zone between Laurussia and Gondwana continents (e.g. Ballèvre et al., 2009; Pitra *et al.*, 2010) in southern Brittany (France; Fig. 4.1). It consists of stacked, strongly deformed eclogite-bearing gneisses and micaschists (Ballèvre *et al.*, 1987) exhumed during Early Carboniferous (e.g. Bosse *et al.*, 2000) and refolded by a large-scale east-west trending antiform (Marchand, 1981).

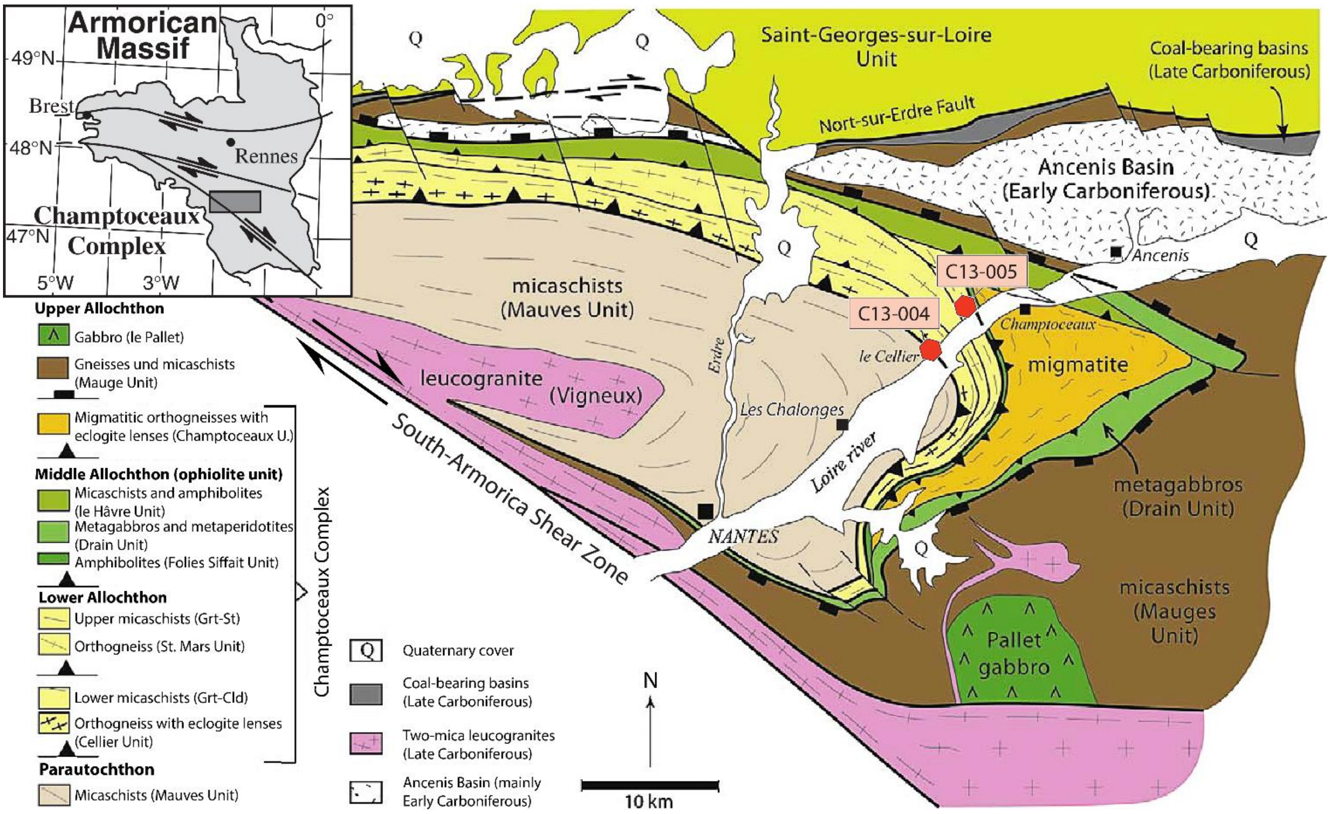

Figure 4.1. Simplified geological and structural map of the Champtoceaux Complex (*modified after Bosse et al., 2000 and Pitra et al., 2010).* Red spots: samples used for geospeedometry study. Inset: Location of the complex in the Armorican Massif.

Four major domains are defined (Figs. 4.1 and 4.2), from the structural bottom to top: the *Parautochthon* (Mauves Unit) composed of metagreywackes of unknown age, overthrust by the *Lower Allochthon* consisting of Ordovician orthogneisses including eclogite lenses derived from doleritic dykes (Godard, 1988), garnet-chloritoid-chlorite micaschists of the Lower Micaschists, fine-grained Ordovician orthogneisses and garnet-staurolite micaschists of the Upper Micaschist. The *Middle Allochthon* is formed, from bottom to top, by strongly deformed garnet-bearing amphibolites with serpentinized peridotite lenses overlain by metaperidotites and metagabbros. The upper part of the Middle Allochthon consists of chloritoid-chlorite micaschists and amphibolites (Pitra *et al.*, 2010).

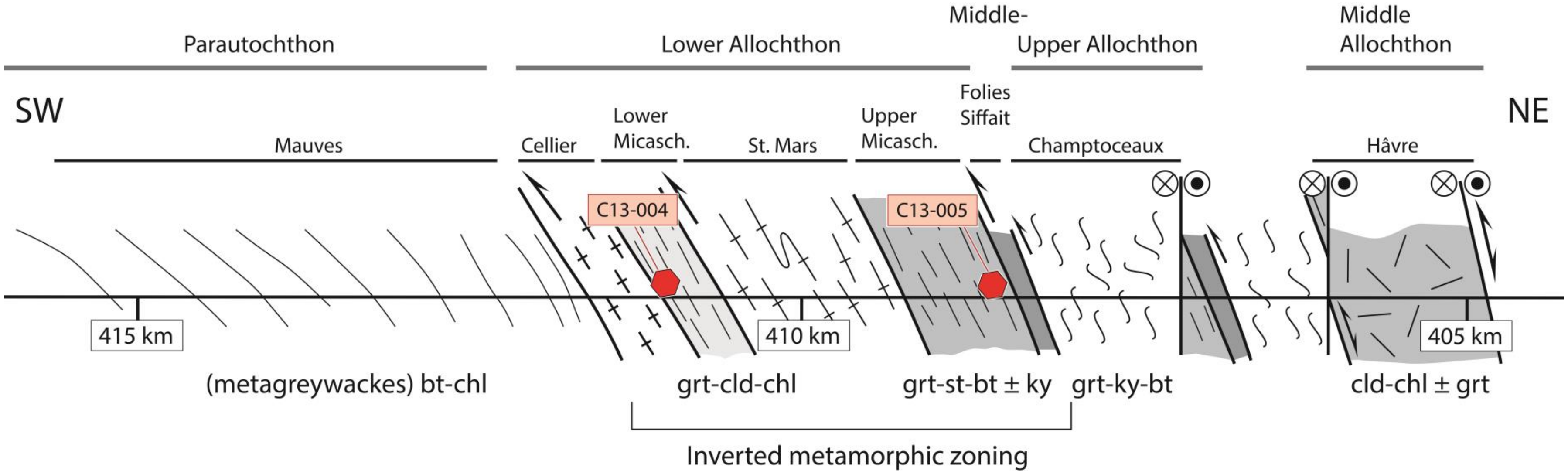

Figure 4.2. Sketch geological cross-section along the Loire River and Nantes-Paris railway with indicative milestone (km; *modified from Pitra et al., 2010*). Red dots: location of the investigated samples.

The *Upper Allochthon* on the top of the Complex is characterized by migmatitic orthogneisses with poorly preserved eclogite lenses and rare metapelites (Pitra *et al.*, 2010) and metagreywackes (Ballèvre *et al.*, 1989, 2002; Bosse *et al.*, 2000; Pitra *et al.*, 2010).

Four main deformational events have been described (Pitra *et al.* 2010; and references therein): ductile deformation (D1) is locally identified in eclogite lenses. Host rocks of eclogites lenses display a penetrative main foliation defined as D2. Localized ductile- to semi-ductile shear bands in the Middle Allochthon and Upper Allochthon units are related to D3. Dextral strike-slip coeval with Late Carboniferous two-mica leucogranites intrusions is associated to D4 (e.g. Carron *et al.*, 1994). A correlated dextral strike-slip fault system in the north-eastern part of the complex resulted in the regional open fold with easterly-plunging axes (e.g. Pitra *et al.*, 2010).

The investigated cross-section follows the Loire River, from Les Chalonges village in the south-west to the Ancenis locality in the north-east (Figs. 4.1 and 4.2). This SW-NE traverse, described in Pitra *et al.* (2010), is well exposed for > 15 km, offering an almost complete exposure of the inverted metamorphic sequence. The structural bottom of the inverted metamorphic zonation starts in the biotite-chlorite metagreywackes of the Parautochthon, where T conditions have been estimates at about 500 °C (Pitra *et al.*, 2010). The metamorphic gradient of the Lower Allochthon garnet micaschists increases upwards from garnet-chloritoid-chlorite to garnet-staurolite-biotite assemblages. Toward the upper boundary with the Upper Allochthon, metamorphic temperatures reach T > 650 °C, in consistency with the overlying migmatitic orthogneisses (e.g. Ballèvre *et al.*, 2009; Pitra *et al.*, 2010). Pitra *et al.* (2010) suggested that the inverted metamorphic zone in the Champtoceaux Complex results from the juxtaposition of a hot thrust unit over colder units.

Garnet-bearing samples were collected across the section for petrographic observation, bulk rock composition, mineral chemistry and geospeedometry studies. Phase diagram section calculations were carried on metapelitic samples to constrain *P*-*T* conditions. Particular attention was paid to garnet porphyroblasts from the Lower- and Upper Micaschists for garnet diffusion modelling.

4.3 Petrology and metamorphic conditions

4.3.1 *Samples description*

Two samples have been selected for peak-*T* estimates and garnet fractionation/diffusion modelling: *C13-004* from the bottom and *C13-005* from the top of the Lower Allochthon unit. The selection of these samples was based on minimal weathering and, after garnet imaging, well-preserved garnet compositional zoning. Sample location and mineral assemblages are summarized in Table 4.1 and located in Figs. 4.1 and 4.2.

Lower Micaschist: Sample *C13-004* was collected in the Lower Micaschist from the bottom of the Lower Allochthon domain (Fig. 4.2). The main foliation is defined by muscovite, chlorite, minor chloritoid, rutile and minor ilmenite. The rock shows compositional layering defined by muscovite (± chlorite) rich thin (few mm) layers and fine grained re-crystallized quartz ± plagioclase (Fig. 4.3a). Sub-euhedral rounded garnet porphyroblasts are from 0.5 up to 6 mm in diameter containing randomly oriented rutile inclusions. Garnet fractures are filled with chlorite. The main foliation is deflected around garnet porphyroblasts with inclusion trails slightly inclined to the rock foliation, which suggests syn- to late deformation (D2) growth. Shear bands at the thin section scale, parallel to white mica (± chlorite) lineation, indicate top-to-the-SW movements.

Upper Micaschist: sample *C13-005* was collected in the Upper Micaschist near the migmatites of the Champtoceaux Unit (Figs. 4.1 and 4.2). The main mylonitic foliation, locally crenulated, is defined by fine grained muscovite, paragonite, minor biotite, accessory ilmenite and recrystallized quartz with relatively uniform grain size and showing at microscope with the gypsum plate inserted, lattice preferred orientation. Sub-euhedral fine grained staurolite crystals (up to 2 mm in size) are parallel to the main foliation and mostly appear in contact with garnet crystals. Sub-euhedral garnet porphyroblasts are 2 to 8 mm in diameter and contain randomly oriented inclusions of quartz, plagioclase, chlorite, chloritoid and rutile (Fig. 4.3b). Garnet fractures and outer rims are occasionally replaced by chlorite and quartz. The deflection of the main foliation around garnet porphyroblasts and bent rutile inclusions continuous with the main foliation indicate syn-tectonic garnet crystallization.

Table 4.1 Provenance, mineral assemblage of investigated samples

Sample	Coordinates	Structural unit	Rock type	Mineral assemblage
C13-004	N 41° 19' 24.9" W 01° 20' 30.0"	Lower Allochthon Lower Micaschist	Grt-Micaschist	grt, qtz, pl, ms, chl, op ± ctd
C13-005	N 47° 20' 54.6" W 01° 17' 39.8"	Lower Allochthon Upper Micaschist	Grt-Micaschist	grt, qtz, ms, pg, chl, st, bt, op

Mineral abbrevation as Kretz (1983): qtz - quartz; pl - plagioclase; bt - biotite; ms - muscovite; chl - chlorite; grt - garnet; st - staurolite; ctd - chloritoid; rt - rutile; pg - paragonite

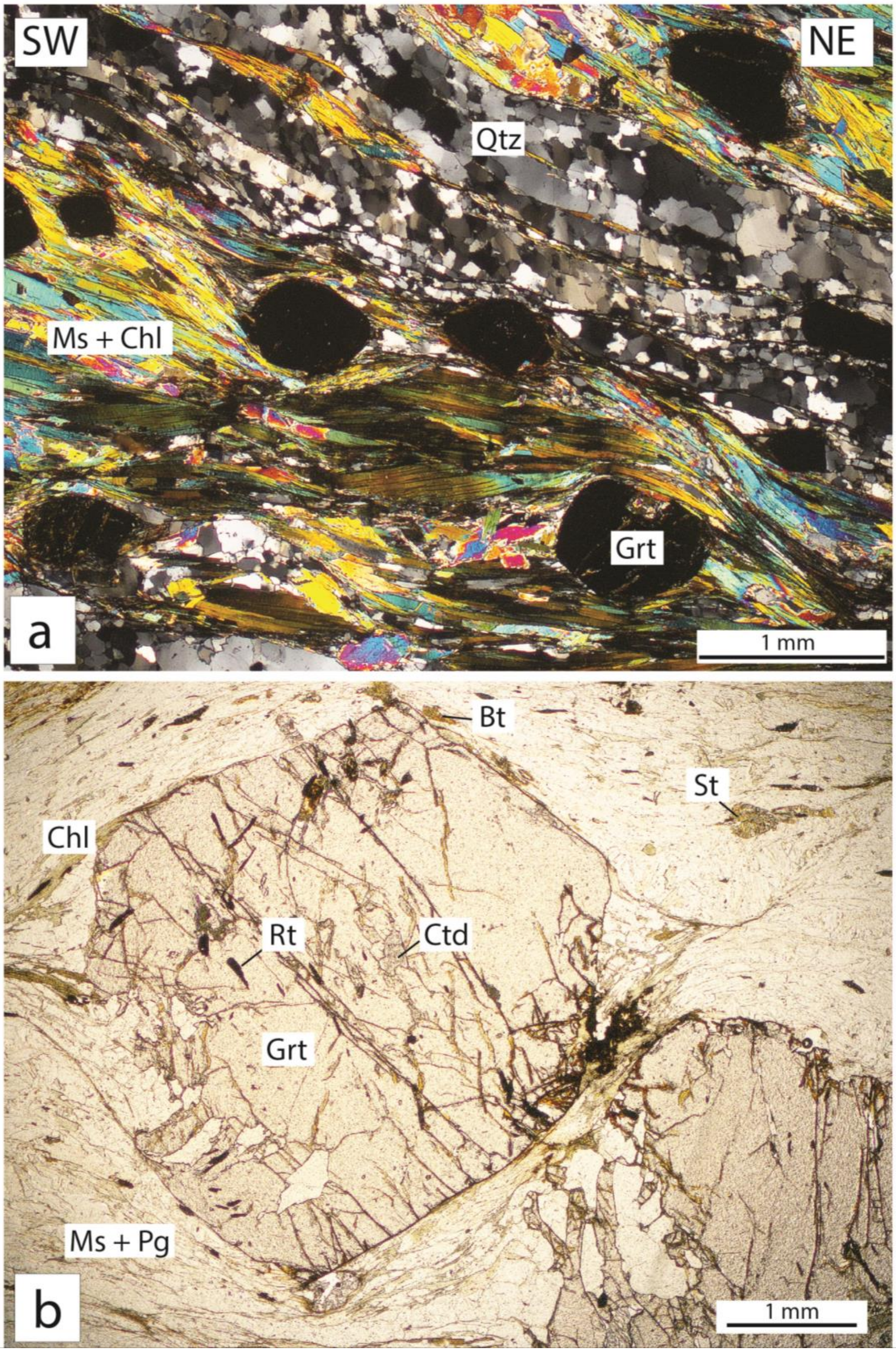

Figure 4.3. Photomicrographs of representative mineral assemblages and textural relationship. Samples are located in Figs. 4.1 and 4.2. Mineral abbreviation after Kretz, (1983). **a)** Lower Micaschist (*C13-004*) displaying a well-developed foliation bended around garnet porphyroblasts (crossed polarised light). **b)** Large sub-euhedral garnet in the Upper Micaschist (*C13-005*) with quartz, chloritoid, chlorite, rutile and minor plagioclase inclusions.

4.3.2 P-T estimates

Accurate peak-*T* estimates are essential for garnet diffusion modelling since cations self-diffusion increase exponentially with temperature and start to be effective at $T > 600$ °C. *P-T* conditions were calculated using the software Perplex_X_07 (http://www.perplex.ethz.ch/; Connolly, 2005), applying the 2004 revised database of Holland and Powell (1998) and mineral solution models listed in Table 4.2. Phase equilibria calculations (pseudosections) are based on minimization of Gibbs free energy, where mineral assemblage stability fields are represented in the *P-T* space for a specific bulk rock composition. Pseudosections of metapelitic compositions were calculated in the NCKFMASHMn system saturated in SiO_2 and H_2O in order to model the prograde path.

Table 4.2 Solid solutions used in the equilibrium phase diagram calculations

Mineral phase	Solution model	Reference
biotite	Bio (TCC)	Tajcmanová *et al*., 2009
chlorite	Chl (HP)	Holland *et al*., 1998
chloritoid	Ctd (HP)	White *et al*., 2000
cordierite	hCrd	Holland and Powell, 1998
feldspar	San	Waldbaum and Thompson 1968
garnet	Gt (GCT)	Ganguly *et al.*, 1996
muscovite	Mica (CHA)	Coggon and Holland, 2002
	Pheng (HP)	modified by Tinkham, 2003
omphacite	Omph(HP)	Holland and Powell, 1998
orthopyroxene	Opx (HP)	Powell and Holland, 1999
plagioclase	Pl (h)	Newton *et al*., 1981
staurolite	St (HP)	Parameters from Thermocalc

Whole-rock bulk compositions were obtained with X-Ray Fluorescence (XRF) analysis at the ETH Zürich and presented in Table 4.3. Core compositions of zoned garnet were extracted from the bulk composition in order to consider the effective bulk rock composition in equilibrium at peak *P-T* conditions (Table 4.3).

Garnet modal proportion was estimated from thin sections and rock sample surface. Volume (vol. %) of garnet cores were estimated from garnet chemical composition maps and profiles obtained from the electron microprobe JEOL JXA-8200 at the ETH Zürich. Assuming a spherical geometry, garnet core average compositions and vol% have been removed from the total XRF bulk analyses. In order to ensure the true radial compositional profiles, separated garnets have been polished until reaching the core of the crystal.

Table 4.3 XRF-derived and effective bulk rock compositions of acidic rocks

Sample	**C13-004**		**C13-005**	
Major oxides (wt%)	XRF	Effective	XRF	Effective
SiO_2	55.99	55.49	55.42	54.87
TiO_2	0.94	0.94	0.91	0.91
Al_2O_3	22.78	22.50	21.58	21.27
FeO	8.04	6.84	7.68	6.44
MgO	2.04	2.02	1.87	1.85
MnO	0.25	0.16	0.34	0.25
CaO	0.60	0.44	0.49	0.44
Na_2O	1.18	1.18	1.00	1.00
K_2O	4.00	4.00	3.71	3.71
LOI	3.39	3.39	5.98	5.98
Total	99.22	96.95	98.98	96.70

Minerals have been analysed for SiO_2, TiO_2, Al_2O_3, FeO, MgO, MnO, CaO, Na_2O, K_2O and Cr_2O_3 with the electron microprobe (ETH Zürich). Operating conditions for spot analyses were 15 kV accelerating voltage, 20 nA sample current, 20 s counting time per element and beam size < 5 µm. Representative mineral analyses are presented in Table 4.4.

Table 4.4 Representative microprobe mineral compositions used to estimate peak-T and P conditions

Sample	**C13-004**				**C13-005**						
	Gt	Chl	Mu	Pl	Gt	Bt	Ms	St	Ilm	Chl	Pg
No. Meas.	3	3	3	2	3	3	3	3	3	5	4
SiO_2	38.31	25.67	46.36	65.96	37.54	35.99	50.27	27.48	0.02	24.94	45.99
TiO_2	0.08	0.12	0.38	0.02	0.10	1.58	0.25	0.46	53.08	0.08	0.35
Cr_2O_3	0.02	0.02	0.01	n.d.	0.02	n.d.	n.d.	0.05	0.04	0.06	0.03
Al_2O_3	21.63	22.23	34.69	20.98	21.20	19.04	30.00	52.73	0.02	22.72	34.97
FeO	31.17	25.79	1.27	0.11	35.95	15.78	1.84	12.28	45.09	25.86	1.07
MnO	0.13	0.29	n.d.	n.d.	0.82	0.04	0.00	0.09	0.27	0.06	0.02
MgO	4.22	13.30	0.92	0.02	3.14	10.56	2.36	1.23	0.15	13.69	0.58
CaO	5.52	0.03	n.d.	0.93	2.28	0.09	0.02	n.d.	0.01	0.02	0.01
Na2O	0.02	0.01	0.93	9.89	0.02	0.15	0.71	n.d.	n.d.	0.02	1.71
K2O	n.d.	0.21	10.11	0.63	n.d.	8.17	9.28	0.01	0.06	0.14	7.34
Total	101.09	87.65	94.67	98.54	101.07	91.39	94.73	94.33	98.73	87.59	92.07

n.d. = not detected

Peak mineral assemblage of sample *C13-004* covers a large stability field between 400 and 600 °C and 0.9 up to > 1.8 GPa (Fig. 4.4a). Garnet *X*Mg# (*X*Mg = Mg/ (Mg + Fe)) ranging between 0.12 and 0.14 and grossular content (*X*grs = Ca/ (Ca+Mg+Mn+Fe)) between 0.08 and 0.12 intersect the stability field at 520 ± 20 °C and 1.7 ± 0.15 GPa. Feldspar has an anorthite content (X_{An}= Ca/ (Ca+Na+K)) of *c.* 0.48 indicating that it is not in equilibrium with the system (out of *P-T* diagram section) and may have (re)crystallized during deformation.

Garnet (*X*Mg# and *X*Grs) and biotite (*X*Mg#) isopleths of sample *C13-005* intersect the peak mineral assemblage stability field at T at 620 ± 20 °C and *P* at 0.8 ± 0.1 GPa (Fig. 4.4b). *P-T* estimates indicate that T conditions are increasing upward, from the Lower to the Upper Micaschists, whereas *P* conditions are decreasing.

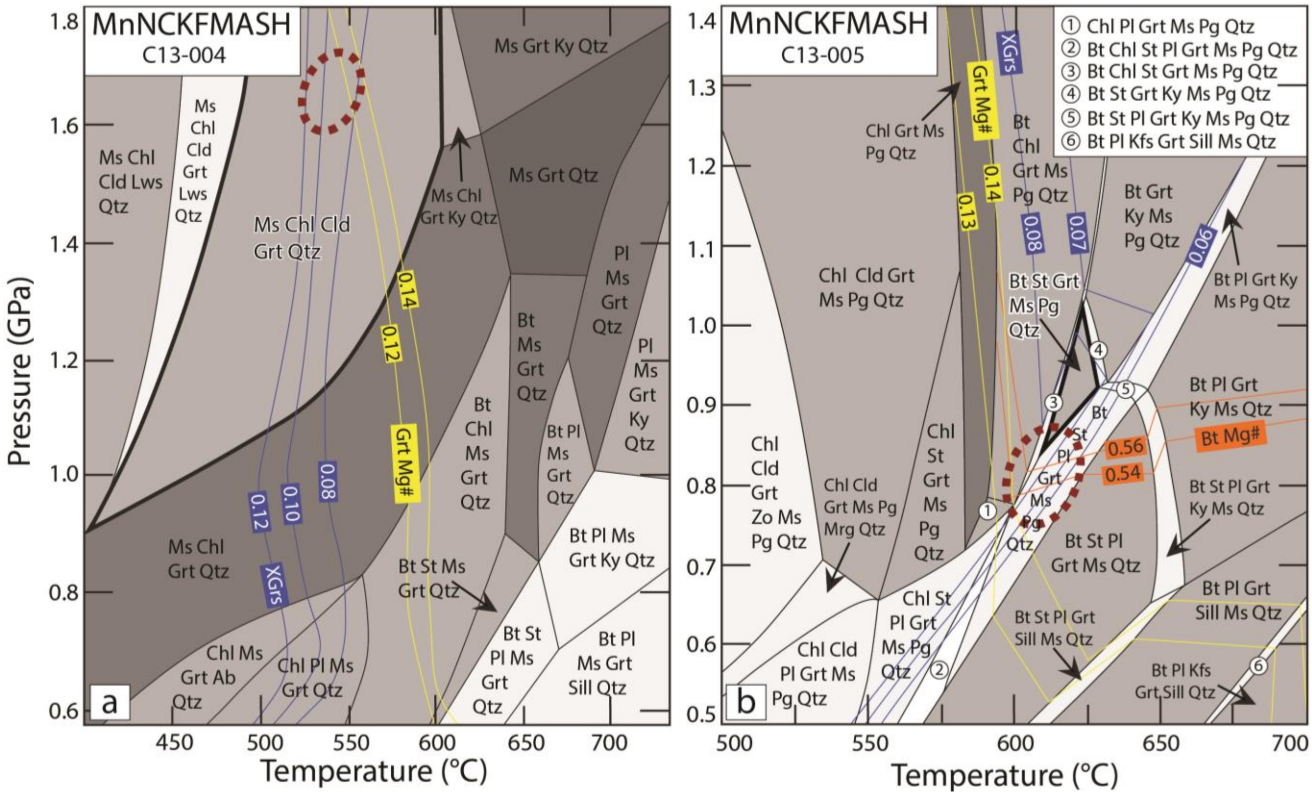

Figure 4.4. *P-T* pseudosections calculated in the MnNCKFMASH system for samples *C13-004* (a) and *C13-005* (b. Bold line: sample assemblage stability field. Orange lines: Mg# biotite composition. Blue lines: garnet grossular (XGrs) composition isopleths. Yellow lines: garnet Mg# (Grt Mg#) composition isopleth. Dashed ellipse: estimated *P-T* conditions. Bulk rock compositions are given in Table 4.3. Greyscale: same shade represents same amount of stable phases.

4.4 Garnet geospeedometry

Mass transfer/diffusion is defined as the flux J $[mol\ m^2\ s^{-1}]$ of a component dependent on both diffusivity D $[m^2\ s^{-1}]$ and chemical gradient dC/dx $[mol\ m^{-3}]$ along a distance x (Fick's first law, 1855):

$$J = -D \cdot \frac{dC}{dx} \tag{1}$$

Intracrystalline diffusion rate is expressed by the Arrhenius (1889) empirical formula, where diffusion is exponentially dependent on temperature T:

$$D = D_0 \cdot e^{-E/RT} \tag{2}$$

where E $[J\ mol^{-1}]$ is the activation energy, R $[J\ K^{-1} mol^{-1}]$ the universal gas constant, T $[K]$ the absolute temperature and D_0 $[m^2\ s^{-1}]$ is a constant (maximal diffusion coefficient). This relation implies that diffusion may be negligible at moderate grades and becomes significant at higher temperature conditions; the maximal diffusion potential occurs at, or near peak-T conditions experienced by the rock.

The effective diffusion length (l_{eff}) is the average distance travelled in one direction by a particle from the point at which it is formed to the point at which it is absorbed. The average distance is proportional to the square root of the time (t); the diffusion coefficient D and all values are temperature-dependent:

$$l_{eff} = \sqrt{Dt} \tag{3}$$

The isotropic nature of garnets is a considerable advantage in multicomponent zoning modelling because diffusion has no directional dependence. Due to the dodecahedral crystal habit the geometry of the crystal may be simplified in a sphere with radial diffusion. In multicomponent diffusion all major cations Fe, Mg, Mn and Ca are treated as dependent on each other in order to maintain the stoichiometry:

$$\begin{pmatrix} \frac{\partial X_1}{\partial t} \\ \frac{\partial X_2}{\partial t} \\ \frac{\partial X_3}{\partial t} \end{pmatrix} = \frac{1}{r^2}\frac{\partial}{\partial r}\left[r^2 \begin{pmatrix} D_{11} & D_{12} & D_{13} \\ D_{21} & D_{22} & D_{23} \\ D_{31} & D_{32} & D_{33} \end{pmatrix} \cdot \begin{pmatrix} \frac{\partial X_1}{\partial r} \\ \frac{\partial X_2}{\partial r} \\ \frac{\partial X_3}{\partial r} \end{pmatrix} \right] \tag{4}$$

where X represents the mole fraction of a component, r the radius of the sphere and index 1, 2 and 3 are any three of the four components (almandine, grossular, pyrope and spessartine).

Euhedral garnet crystals of different sizes (3 mm to 8 mm diameter) were extracted from the rock samples by hand (hammer and mason). In order to respect the geometry and warrant the application of radial diffusion numerical modelling, garnets were mounted in epoxy “pills” and polished until exposure of the crystal core. The polished pills were coated with carbon (~30 µm) for microprobe analysis.

4.4.1 Garnet imaging

Major element (Mg, Mn, Ca and Fe) concentration maps of garnets were performed using the electron microprobe instrument. Radial garnet composition profiles of zoned garnet have been analysed avoiding garnet inclusions and cracks. Representative compositional maps and profiles selected for geospeedometry studies are presented in Figs. 4.5 and 4.6.

Garnet crystals from *C13-004* do not display rim resorption structures at the crystal boundaries. From core to rim, almandine (Alm) and pyrope (Prp) increase, whereas spessartine (Sps) and grossular (Grs) decrease (Fig. 4.5). The bell-shape profile of spessartine is characteristic of growth zoning without internal diffusion (Hollister, 1969).

Garnet porphyroblasts zoning of sample *C13-005* display compositional profiles with similar trends as garnets from the underlying Lower Micaschist *C13-004*. From core to rim the almandine and pyrope content slightly increase whereas grossular and spessartine decrease (Fig. 4.5). Spessartine shows the typical bell-shaped zoning attributed to prograde garnet growth.

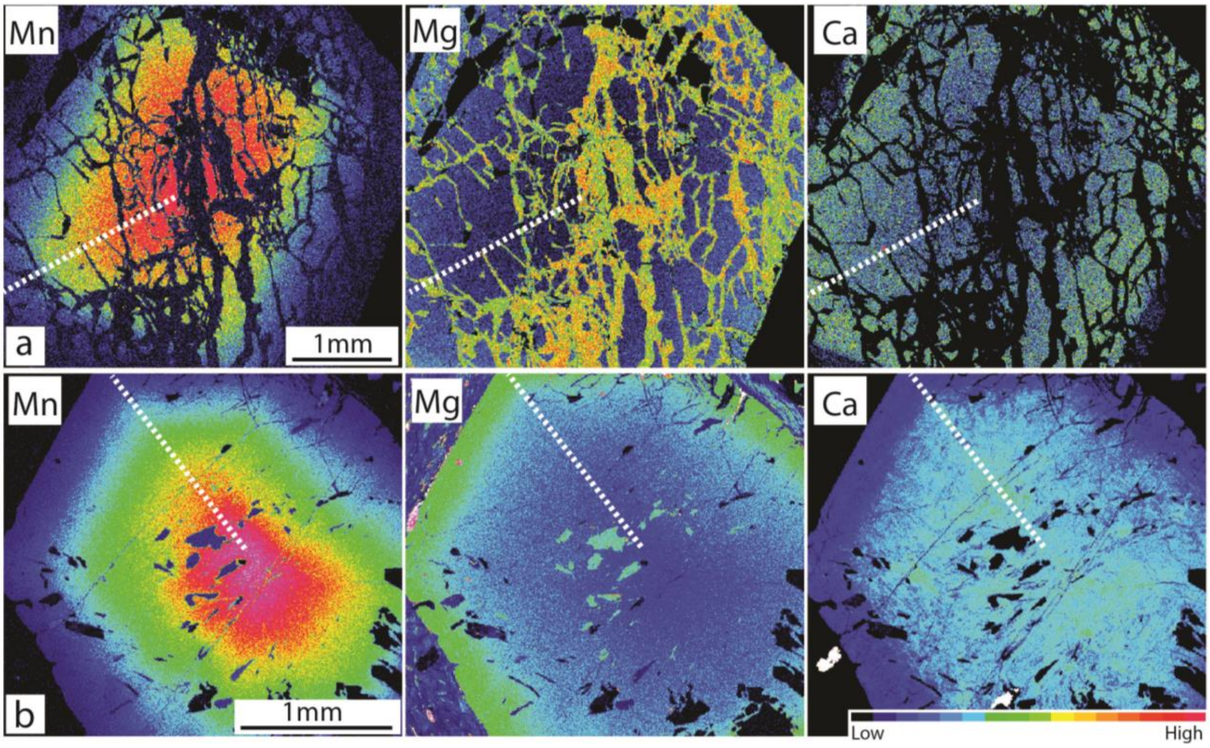

Figure 4.5. Representative garnet major element (Mn, Mg and Ca) concentration maps illustrating compositional zoning. Locations are presented Figs. 4.1 and 4.2. Strait dashed line: measured garnet chemical profile. **a)** Garnet porphyroblast from *C13-004* Lower Micaschist. **b)** Zoned garnet in sample *C13-005* Upper Micaschist.

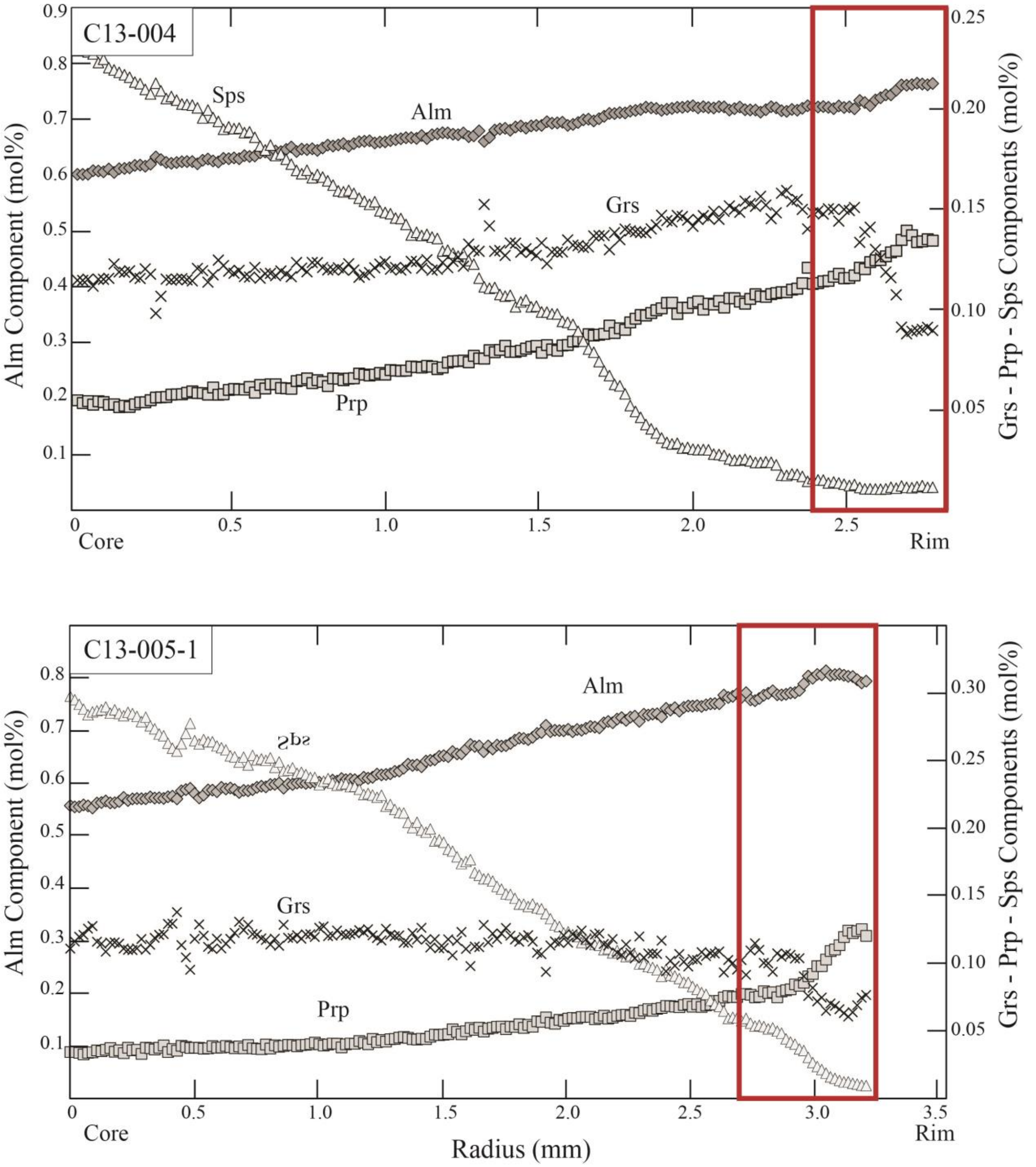

Figure 4.6. Representative chemical zoning profiles for almandine (Alm), pyrope (Prp), spessartine (Sps) and grossular (Grs) from core to rim in samples *C13-004* (top) and *C13-005-1* (garnet 1, bottom). Red sector: near rim compositional discontinuities considered for simple step function garnet diffusion modelling.

4.4.2 Results

Self-diffusion coefficient D_0 were computed using the values from Carlson (2006) and then from Chu and Ague (2015) for comparison. Maximal time (t) duration of peak-*T* conditions for three representative garnet porphyroblasts, one from the Lower (*C13-004*) and two from the Upper Micaschist (*C13-005*), are presented in Table 4.5. Time-windows represent the minimum time from good fit of at least one garnet component and the maximal time for which at least one component is excessively diffused. Due the low content of spessartine, i.e. uncertainties in defining the compositional step, it was considered as a dependent variable in the system. Best-fit diffusion modelling solutions are shown in Fig. 4.7.

Table 4.5 Step-function diffusion modelling results

			Time duration (t) window [Ma]		
Sample		Peak *T* [°C]	Carlson (2006)	Chu and Ague (2015)	
				Alm & Sps	Prp & Grs
C13-004	Grt-1	540	$t > 12.5$	$3.3 < t < 20$	$t > 40$
C13-005	Grt-1	640	$0.8 < t < 1.5$	$0.13 < t < 0.2$	$1.9 < t < 6$
	Grt-2	640	$1.5 < t < 3.5$	$0.3 < t < 1.2$	$2.5 < t < 6.4$

Diffusion best-fit solutions for the two garnets *C13-005-1* and *-2* indicate that the rock was held at peak-*T* conditions for 0.8 to 3.5 Myr (*C13-005 Grt-2* in Appendix C). Simulations reach best-fit compositional profiles for all components simultaneously (Fig. 4.7). The duration of peak conditions is one order of magnitude longer (t > 12.5 Myr) for garnet *C13-004*, for which peak-*T* are 100 °C cooler than those in *C13-005*.

Best-fit diffusion compositional profiles for *C13-005* garnets yield tangibly shorter times (0.13 to 1.2 Myr) for almandine and spessartine components simulated with Chu and Ague (2015) diffusion coefficients, at same peak-*T* conditions and step delimitations as before. Pyrope and grossular reached good fit after longer times (1.9 to 6.4 Myr) while almandine and spessartine are excessively diffused. Applying Chu and Ague (2015) diffusion coefficients to garnet crystal *C13-004*, yields also shorter time estimates for almandine and spessartine (3 to 20 Myr) but t > 40 Myr for pyrope and grossular components.

Results using the calibration of Carlson (2006) are more consistent for all components and durations of thermal perturbation are longer, ensuring maximal time estimates of peak-*T* conditions in the Champtoceaux collisional setting.

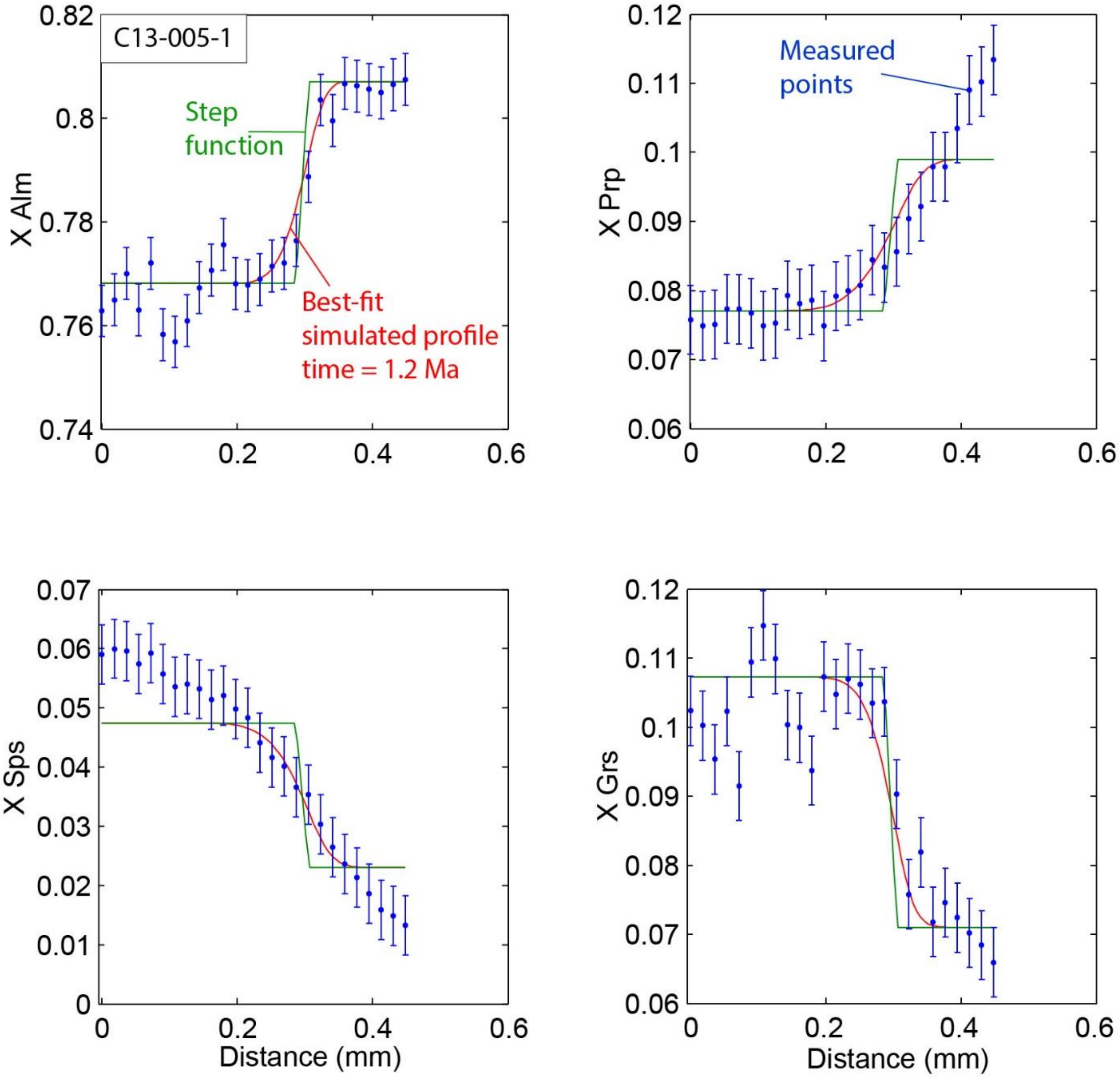

Figure 4.7. Representative diffusion modelling results for garnet C13-005-1 for almandine (Alm), pyrope (Prp), spessartine (Sps) and grossular (Grs) mole fraction (X). Step-function initial conditions (green line) for all major cations are treated dependent on each other. Red line: best-fit solutions at peak temperature of 640 °C. Best-fit solution for all components occurs at 1.2 Myr.

4.5 Discussion

4.5.1 Metamorphic gradient and peak-T duration

Pseudosection calculations and garnet composition contours inferred peak-*T* conditions of *c*. 540 °C in the Lower Micaschist (*C13-004*) and *c*. 640 °C in the Upper Micaschist (*C13-005*). Results indicate that peak-*T* conditions increase by about 100 °C across 3 km thick pile of rocks, whereas pressure conditions are abruptly decreasing from 1.7 ± 0.15 GPa to 0.8 ± 0.1 GPa, revealing an inverted temperature and a decreasing pressure gradient moving upward in the Champtoceaux Complex.

Temperature constraints confirm previous estimates of 500 - 550 °C in the Lower Micaschist and 600 - 650 °C in the Upper Micaschists (e.g. Pitra *et al.,* 2010). Temperature conditions < 600 °C in the Lower Micaschist (*C13-004*) denote that garnet compositional profiles were scarcely modified by diffusion and consequently are convenient for *P-T* paths reconstruction (e.g. Kohn, 2003; Caddick *et al.,* 2010). Therefore, pressures estimates in Lower Micaschists were obtained by the intersection of garnet compositional contours (Fig. 4.4a). The result (*c*. 1.6 GPa) is significantly higher than 0.7 - 1.0 GPa determined by Pitra *et al.* (2010) using THERMOCALC PT-average calculations on several sets of mineral compositions. Possible overestimation due to the steep slope of *X*Mg# and *X*Grs compositional contours has to be taken into account in interpretations. Steep isopleths are sensitive thermometer but imprecise in constraining pressures conditions. In addition, the syn-tectonic mineral assemblage (Ms – Chl – Cld – Grt – Qtz) is stable in a large *P-T* stability field and therefore, not supportive for more accurate pressure constraint (Fig. 4.4a). Consequently, Lower Micaschists pressures estimates made by Pitra *et al.* (2010) are preferred.

The reconstruction of the exact *P-T* path experienced by a rock, the quantification and identification of possible time gaps between different thermal pulse(s) and their influence on compositional diffusion are impossible to determine. Therefore, it is assumed that the measured garnet compositional profiles resulted from diffusion processes at peak-*T* conditions. This assumption ensures that the peak-*T* duration estimations represent the maximum time estimate (e.g. Ague and Baxter, 2007). Petrographic observations and garnet compositional profiles indicate that garnet grows in the prograde path to reach stability with the peak mineral assemblage. This enables the assumption that diffusion occurred during syn-tectonic peak metamorphic conditions.

At T > 600 °C garnet compositional profiles initiate equilibrate faster following the exponential term of Arrhenius relation (Eq. 2). Results confirm the temperature dependency of diffusion, i.e. garnet from the low grade Lower Micaschist (*C13-004*) diffuses up to one order of magnitude slower (> 40 Myr) than garnets from the amphibolite facies peak conditions Upper Micaschist (*C13-005; c.* 1 Myr).

4.5.2 Tectonic implications

Peak-metamorphic assemblages are syn-tectonic and associated to foliation formation and top-to-SW thrusting. Garnets are in equilibrium with the matrix and have grown during the prograde path. Metamorphic temperature increases upward, whereas pressures are nearly uniform across the thrust zone. Models that predicts inversion of both temperature and pressure gradients are not applied.

It is concluded that the heat source responsible for isograds inversion was the hanging-wall during thrusting. Pitra *et al.* (2010) suggested that the Upper Allochthon migmatites were the possible heat source. Monazite ages indicate that migmatization is about 390 Ma (Cocherie *et al.* 2005), i.e. 50 Ma older than the inferred time of thrusting (e.g. Bosse *et al*., 2000; Pitra *et al.*, 2010). Garnet diffusion modelling indicates that peak thermal perturbation at the contact between the Upper Micaschists and the Upper Allochthon may have occurred in one or in a series of shorter pulses that sum up to < 3.5 Myr. Therefore, the heat source responsible for the metamorphic inversion being the migmatites is excluded, unless monazite ages are not migmatization.

Kilometre-scale shear zones during horizontal shortening were simulated by Schmalholz and Duretz (2015). Their thermo-mechanical models predict that viscous heating in shear zones can increase temperatures by about 100 °C in a confined zone parallel to the thrust and it is transient (up to 2 Myr) in time. Accordingly, shear heating may well be the heat source in Champtoceaux, fitting the about 100 °C temperature difference across 3 km thick pile of rocks for a short duration.

4.6 Conclusion

The Champtoceaux Complex displays an inverted temperature- and nearly uniform pressure-gradients linked to a major ductile thrust zone between the Lower Allochthon footwall and the Upper Allochthon hanging-wall. Peak-*T* estimates in footwall Lower- and Upper Micaschists differ by *c.* 100 °C, increasing upward from 540 to 640 °C across a 3 km thick pile of rocks. Garnet geospeedometry diffusion modelling reveals that high grade conditions in the Upper Micaschist lasted less than 3.5 Myr. Considering similar pressures in all units and thermal perturbation over a short time, viscous-heating along the crustal thrust is a persuasive model to explain the inversion of metamorphic isograds in the Champtoceaux collisional setting.

Acknowledgements

We thank Ballèvre M., Pitra P. and Manzotti P. for their assistance and precious help in the field. Zehnder L. for her help and efficient XRF analyses. The authors were supported by ETH Zürich, Research ETH-14 11-1.

5. Conclusions and outlook

5.1 Conclusions

Inverted metamorphic gradients preserved along large-scale thrust zones in continental collisional settings are frequent orogenic features. The Nestos Thrust Zone (NTZ) in the Rhodope Metamorphic Complex (Greece), the Main Central Thrust (MCT) in Sikkim Himalaya (NE India) and the thrust between Lower- and Middle Allochthon in the Champtoceaux Complex (France) are examples of such sequences. These three examples exhibit amphibolite facies grade rocks with migmatites as direct footwall of the thrust unit; the metamorphic grade decreases downward to greenschist facies whereas pressure conditions increase or are nearly uniform across the investigated sections. New structural, petrological, geochronological and geospeedometry results give some insight on the three investigated inverted metamorphic sequences.

5.1.1 Pressures estimates, the plagioclase problem

The reliability of estimating metamorphic *P*-*T* conditions using the conventional geobarometric approach largely depends on the determination of the mineral assemblage in chemical equilibrium and appraisal of the equilibrium composition of all phases involved. The identification of textural evidence proving equilibrium and resetting of mineral chemistry during cooling and/or retrograde metamorphism are major sources of error. Both garnet-plagioclase-biotite-muscovite-quartz (GPBMQ) and garnet-alumosilicate-plagioclase-quartz (GASP) barometers have been employed to infer metamorphic *P*. Phase equilibria modelling in the investigated samples revealed that, in the three studied thrust zones, plagioclase is not part of the peak mineral assemblage. Therefore, its composition is not representative of peak-*T* ($T > 600$ °C) mineral assemblages and GPBMQ and GASP geobarometers may induce pressure estimates different from those actually experienced by the rocks, leading to misleading geological interpretations. The observed fine-grained plagioclase crystals may represent grains relicts of a previous stable assemblage, or (re)crystallized grains during the retrograde part of the *P*-*T* path. At medium grade conditions (450 - 600 °C), recrystallization, nucleation and growth of new plagioclase grains start to be important (e.g. Borges and White, 1980), even more if deformation is active, as expected in strongly sheared rocks. Consequently, pressures at peak-*T* were determined using both garnet and biotite compositional isopleths and their intersections in a contoured *P*-*T* diagram section.

5.1.2 The Nestos Thrust Zone and related inverted metamorphism

In the Rhodope Metamorphic Complex (Greece), higher structural levels of Lower Terrane footwall against the Nestos Thrust Zone (NTZ) reached peak-*T* of 730 ± 20 °C and pressure of 1.1 ± 0.1 GPa. This peak metamorphic event was contemporaneous with anatexis and top-to-SW shearing. Zircon U-Pb SHRIMP dating specifies Early Cretaceous (*c*. 142 Ma) partial melting, whilst granitoids related to the nearby Skaloti pluton are Eocene (*c*. 50 Ma). ^{40}Ar/^{39}Ar geochronology on white mica indicates cooling below 400-300 °C at *c*. 35 Ma. These *P-T* estimates and geochronological results are consistent with previous studies in central and eastern Rhodope Complex, suggesting one orogenic cycle starting in the Jurassic and finished in the Eocene.

Most of the investigated garnet porphyroblasts are equilibrated or display extensively diffused compositional profiles. FRIDGE results revealed that Lower Terrane rocks against the NTZ, have been held at peak-*T* conditions between 2 to 6 Myr in the Drama region, and between 3 and 8.3 Myr in the Komotini area.

5.1.3 Sikkim Himalaya inverted metamorphic sequence

Pressure and temperature estimates in the Sikkim Lesser Himalaya (LH) show increase of temperature conditions by about 100 °C across *c*. 6 km thick NNE-dipping pile of rocks from the garnet- up to the sillimanite zone across the MCT. Peak-*T* conditions are contemporaneous with peak mineral assemblage and top-to-south shearing. U-Pb zircon SHRIMP geochronology dates a polymetamorphic history. The last peak metamorphic event contemporaneous is with partial melting of magmatic and sedimentary rocks during the Middle Miocene (15 - 18 Ma). Garnets from LH staurolite- to sillimanite-zone against the MCT display complex zoning patterns with compositional discontinuity between inclusion-rich cores and inclusion-free rims, suggesting multiple stages of equilibrium. Simple step function multicomponent diffusion in a sphere method (Ague and Baxter, 2007) indicates that peak-*T* conditions persisted for short time (3-5 Myr) in the Sikkim MCT.

5.1.4 Inverted metamorphic zonation in the Champtoceaux Complex

The inverted metamorphic sequence between the Lower- and Upper Allochthon of the Champtoceaux Complex (France) displays syn-tectonic peak metamorphic assemblages contemporaneous with southward shearing. Temperature increases upward from 540 to 640 °C, whereas pressures are nearly uniform within *c*. 1 km thick zone. Radial multicomponent diffusion in garnet, employing the simple step function method, inferred short-lived (t < 3.5 Myr) peak-*T* conditions in the Upper Micaschists footwall in contact with the Upper Allochthon hanging-wall.

5.1.5 Geospeedometry and potential thermal source

Garnet compositional zoning brings information about *P-T* metamorphic history, i.e. duration of intracrystalline diffusion. Sections through garnet crystal centres are required to respect the spherical geometry of the system and legitimate the correlation between measured garnet compositional profiles with those computed with radial diffusion numerical modelling.

Garnet porphyroblasts intracrystalline diffusion starts at T > 600 °C and its influence increase exponentially with temperature. At T > 700 °C, compositional zoning is largely obliterated over few millions years. After longer time, garnet compositional discontinuities are smoothed and initial concentrations drop below their initial values. Garnet compositional profiles fitting with attenuated values as initial conditions in the simple step function method underestimates the duration of diffusion (e.g. Ague and Baxter, 2007; Caddick *et al.*, 2010; Ague and Carlson, 2013). FRIDGE inverse fitting numerical modelling overcomes time underestimation by computing garnet fractionation simultaneous with diffusion along a *P-T-t* path assuming continual equilibration between the growing garnet rim and the matrix. Garnet displaying complex zoning due to multiple equilibration and/or sharp compositional gradients are suitable for the simple initial step function method (Ague and Baxter, 2007).

Both geospeedometry methods yielded short-lived (1 to 6 Myr) peak-*T* conditions in the three investigated thrust zones. The time duration estimate (1 to 6 Myr) represents a range that includes uncertainties in temperature *T* estimates. Other sources of uncertainties may be related to experimental errors, the extrapolation of diffusion coefficients and the geometry of the system which is not perfectly a sphere.

Considering the metamorphic architecture of the studied thrusts, i.e. normal/nearly uniform pressure and inverted temperature gradients, the 1 to 3 km thick high grade zone parallel to the thrust and the transient duration of peak thermal pulse(s), viscous/shear-heating is advocated as a plausible heat source responsible for temperature increase along the investigated thrust zones and consequent metamorphic inversion.

5.2 Outlook

Duration of heating estimates may be supported by Sr diffusion in apatite investigations (Ague and Baxter, 2007). Apatite is a common mineral that grows during prograde metamorphism and has the potential to corroborate results obtained using garnet geospeedometers.

Analytical methods like Sm-Nd and Lu-Hf zoned-garnet geochronology may provide temporal support to fractionation/diffusion investigations. This procedure may constrain with high precision (better than ± 1 Ma) ages of tectono-metamorphic processes (e.g. Baxter and Scherer, 2013). In the Rhodope Metamorphic Complex, this method can be applied to recognize and quantify possible multiple garnet generations along different garnet-micaschist horizons in the Lower Terrane and, therefore, clarify the timing of large amount of homogenized garnet compositional profiles. In the Sikkim Himalaya, Sm-Nd and Lu-Hf zoned-garnet geochronology may better constrain the timing and metamorphic history of garnet porphyroblasts displaying complex compositional profiles, i.e. homogeneous inclusions-rich cores and inclusion-free outer rim.

The preservation of inverted metamorphic sequences denotes that cooling is rapid. Garnet rim compositional diffusion modelling (Spear, 2004) on crystals displaying thin (few µm) retrograde outer rim characterized by Mg# decrease and XMn increase, may be considered to reconstruct the retrograde metamorphic path and gauge information about cooling, exhumation rates and orogenic processes.

In the Champtoceaux Complex, Upper Allochthon migmatization ages, based on monazite dating, can be testified with U-Pb SHRIMP zircon geochronology allowing better understanding between partial melting and thrusting.

Bibliography

Ague, J. J. and Baxter, E. F., 2007. Brief thermal pulses during mountain building recorded by Sr diffusion in apatite and multicomponent diffusion in garnet. *Earth and Planetary Sciences Letters*, 261, 500-516.

Ague, J. J., and Carlson, W. D., 2013. Metamorphism as garnet sees it: the kinetics of nucleation and growth, equilibration, and diffusional relaxation. *Elements*, *9*(6), 439-445.

Anczkiewicz, R., Chakraborty, S., Dasgupta, S., Mukhopadhyay, D., and Kołtonik, K., 2014. Timing, duration and inversion of prograde Barrovian metamorphism constrained by high resolution Lu–Hf garnet dating: A case study from the Sikkim Himalaya, NE India. *Earth and Planetary Science Letters*, *407*, 70-81.

Andersen, D.J. and Lindsley, D.H., 1988. Internally consistent solution models for Fe-Mg-Mn-ti oxides: Fe-Ti oxides. *The American Mineralogist*, *73*(7-8), pp.714-726.

Andreasson, P. G., and Lagerblad, B., 1980. Occurrence and significance of inverted metamorphic gradients in the western Scandinavian Caledonides. *J. Geol. Soc. London* 137, 219-230.

Andrieux, J., Arthaud, F., Brunel, M., and Sauniac, S., 1981. Geometrie et cinematique des chevauchements en Himalaya du Nord-Ouest. *Bulletin de la Société Géologique de France*, *23*(6), 651-661.

Arenas, R., Pascual, F. R., Garcia F., and Catalan, J., 1995. High-pressure micro-inclusions and development of an inverted metamorphic gradient in the Santiago Schists (Órdenes Complex, NW Iberian Massif, Spain): evidence of subduction and syncollisional decompression. *Journal of Metamorphic Geology*, *13*(2), 141-164.

Arita, K., 1983. Origin of the inverted metamorphism of the Lower Himalayas, Central Nepal. *Tectonophysics*, 95, 43-60.

Baker, J. H., and Liati, A., 1991. The Oligocene volcano-sedimentary sequence of the Dipotama basin, N Greece – temporal relationships between tertiary granites and volcanics, and implication for the regional tectonic evolution. *Geologie en Mijnbouw*, *70*(1), 75-83.

Baldwin, J. A., Powell, R., Brown, M., Moraes, R., and Fuck, R. A., 2005. Modelling of mineral equilibria in ultrahigh-temperature metamorphic rocks from the Anápolis–Itauçu Complex, central Brazil. *Journal of Metamorphic Geology*, *23*(7), 511-531.

Ballèvre, M., Bosse, V., Ducassou, C., and Pitra, P., 2009. Palaeozoic history of the Armorican Massif: models for the tectonic evolution of the suture zones. *Comptes Rendus Geoscience*, 341, 174-201.

Ballèvre, M., Capdevila, R., Guerrot, C, and Peucat, J.-J., 2002. Discovery of an alkaline orthogneiss in the eclogite-bearing Cellier Unit (Champtoceaux Complex, Armorican Massif): a new witness of the Ordovician rifting. *Comptes Rendus Geoscience*, 334, 303-311.

Ballèvre, M. and Marchand, J., 1991. Zonation du métamorphisme éclogitique dans la nappe de Champtoceaux (Massif armoricain, France). *Comptes rendus de l'Académie des sciences. Série 2, Mécanique, Physique, Chimie, Sciences de l'univers, Sciences de la Terre*, *312*(7), pp.705-711.

Ballèvre, M., Pinardon, J.-L., Kienast, J.-R., and Vuichard, J.-P., 1989. Reversal of Fe-Mg Partitioning between Garnet and Staurolite in Eclogite-facies Metapelites from the Champtoceaux Nappe (Brittany, France). *Journal of Petrology*, Vol. 30, Part 6, 1321 – 1349.

Barr, S.R., Temperley, S. and Tarney, J., 1999. Lateral growth of the continental crust through deep level subduction–accretion: a re-evaluation of central Greek Rhodope. *Lithos*, *46*(1), pp.69-94.

Bhattacharya, A., Mohanty, L., Maji, A., Sen, S.K. and Raith, M., 1992. Non-ideal mixing in the phlogopite-annite binary: constraints from experimental data on Mg− Fe partitioning and a reformulation of the biotite-garnet geothermometer. *Contributions to Mineralogy and Petrology*, *111*(1), pp.87-93.

Bauer, C., Rubatto, D., Krenn, K., Proyer, A. and Hoinkes, G., 2007. A zircon study from the Rhodope metamorphic complex, N-Greece: time record of a multistage evolution. *Lithos*, *99*(3), pp.207-228.

Baxter, E. F., and Scherer, E. E., 2013. Garnet geochronology: timekeeper of tectonometamorphic processes. *Elements*, *9*(6), 433-438.

Beaumont, C., Jamieson, R. A., Nguyen, M. H., and Lee, B., 2001. Himalayan tectonics explained by extrusion of a low-viscosity crustal channel coupled to focused surface denudation. *Nature*, *414*(6865), 738-742.

Beaumont, C., Jamieson, R. A., Nguyen, M. H., and Medvedev, S., 2004. Crustal channel flows: 1. Numerical models with applications to the tectonics of the Himalayan-Tibetan orogen. *Journal of Geophysical Research: Solid Earth*, *109*(B6).

Bonev, N., Burg, J. P., and Ivanov, Z., 2006. Mesozoic–Tertiary structural evolution of an extensional gneiss dome—the Kesebir–Kardamos dome, eastern Rhodope (Bulgaria–Greece). *International Journal of Earth Sciences*, *95*(2), 318-340.

Bonev, N., Moritz, R., Marton, I., Chiaradia, M. and Marchev, P., 2010. Geochemistry, tectonics, and crustal evolution of basement rocks in the Eastern Rhodope Massif, Bulgaria. *International Geology Review*, *52*(2-3), pp.269-297.

Bonev, N., Ovtcharova-Schaltegger, M., Moritz, R., Marchev, P. and Ulianov, A., 2013. Peri-Gondwanan Ordovician crustal fragments in the high-grade basement of the Eastern Rhodope Massif, Bulgaria: evidence from U-Pb LA-ICP-MS zircon geochronology and geochemistry. *Geodinamica Acta*, *26*(3-4), pp.207-229.

Bonev, N. and Stampfli, G., 2011. Alpine tectonic evolution of a Jurassic subduction-accretionary complex: Deformation, kinematics and 40 Ar/39 Ar age constraints on the Mesozoic low-grade schists of the Circum-Rhodope Belt in the eastern Rhodope-Thrace region, Bulgaria-Greece. *Journal of Geodynamics*, *52*(2), pp.143-167.

Borges, F.S. and White, S.H., 1980. Microstructural and chemical studies of sheared anorthosites, Roneval, South Harris. *Journal of Structural Geology*, *2*(1-2), pp.273-280.

Bosse, V., Féraud, G., Ruffet, G., Ballèvre, M., Peucat, J.-J., and De Jong, K., 2000. Late Devonian subduction and early-orogenic exhumation of eclogite-facies rocks from the Champtoceaux Complex (Variscan belt, France). *Geological Journal*, 35, 297-325.

Brookfield, M. E., 1993. The Himalayan passive margin from Precambrian to Cretaceous times. *Sedimentary Geology*, *84*(1), 1-35.

Brun, J. P., and Faccenna, C., 2008. Exhumation of high-pressure rocks driven by slab rollback. *Earth and Planetary Science Letters*, *272*(1), 1-7.

Brun, J. P., and Sokoutis, D., 2007. Kinematics of the southern Rhodope core complex (North Greece). *International Journal of Earth Sciences*, *96*(6), 1079-1099.

Brunel, M., and Andrieux, J., 1980. A tectonic model for the Himalayas and the inverse metamorphism problem. *COMPTES RENDUS HEBDOMADAIRES DES SEANCES DE L ACADEMIE DES SCIENCES SERIE D*, *291*(7), 609-612.

Bucher, Kurt, and Rodney Grapes, 2011. *Petrogenesis of metamorphic rocks*. Springer Science and Business Media, pp. 428.

Burchfield, B.C., Chen, Z.L., Hodges, K.V. and Liu, Y.P., Royden LI-l, Deng CR, Xu IN, 1992. The South Tibetan Detachment System, Himalayan Orogen. *Geol Soc Am Spec Pap, 269*, pp.1-41.

Burg, J.-P., 2011. Rhodope: From Mesozoic convergence to Cenozoic extension. Review of petro-structural data in the geochronological frame. In (Eds.) Emmanuel Skourtsos and Gordon S. Lister, *Journal of the Virtual Explorer*, volume 39, paper 1, doi: 10.3809/jvirtex.2011.00270.

Burg, J.-P., and Chen, G. M., 1984. Tectonics and structural zonation of southern Tibet, China. *Nature*, *311*, 219-223.

Burg, J.-P., and Gerya, T. V., 2005. The role of viscous heating in Barrovian metamorphism of collisional orogens: thermomechanical models and application to the Lepontine Dome in the Central Alps. *Journal of Metamorphic Geology*, *23*(2), 75-95.

Burg, J.-P., and Schmalholz, S. M., 2008. Viscous heating allows thrusting to overcome crustal-scale buckling: numerical investigation with application to the Himalayan syntaxes. *Earth and Planetary Science Letters*, 274, 189-203.

Burg, J.-P., Brunel, M., Gapais, D., Chen, G. M., and Liu, G. H., 1984. Deformation of leucogranites of the crystalline Main Central Sheet in southern Tibet (China). *Journal of Structural Geology*, *6*(5), 535-542.

Burg, J.-P., Ivanov, Z., Ricou, L. E., Dimov, D., and Klain, L., 1990. Implication of shear sense criteria for the tectonic evolution of the Central Rhodope massif, southern Bulgaria. *Geology*, 18 (5), 451-454.

Burg, J.-P., Leyreloup, A. F., Romney, F. and Delor, C. P., 1989. Inverted metamorphic zonation and Variscan thrust tectonics in the Rouergue area (Massif Central, France): PTt record from mineral to regional scale. *Geological Society, London, Special Publications*, *43*(1), pp.423-439.

Burg, J.-P., Matte, P., Leyreloup, A., and Marchand, J., 1984. Inverted metamorphic zonation and large-scale thrusting in the Variscan Belt: an example in the French Massif Central. *Geological Society, London, Special Publications*, *14*(1), 47-61.

Burg, J.-P., Ricou, L. E., Ivanov, Z., Godfriaux, I., Dimov, D., and Klain, L., 1996. Syn-metamorphic nappe complex in the Rhodope Massif. Structure and kinematics. *Terra Nova*, 8(1), 6-15.

Caddick, M. J., Bickle, M. J., Harris, N. B. W., Holland, T. J. B., Horstwood, M. S. A., Parrish, R. R., and Ahmad, T., 2007. Burial and exhumation history of a Lesser Himalayan schist: Recording the formation of an inverted metamorphic sequence in NW India. *Earth and Planetary Science Letters, 264*(3), 375-390.

Caddick, M. J., Konopásek, J., and Thompson A. B., 2010. Preservation of Garnet Growth Zoning and the Duration of Prograde Metamorphism. *Journal of Petrology,* Volume 3, Number 11, 2327-2347.

Camacho, A., Lee, J. K. W., Hensen, B. J., and Braun, J., 2005. Short-lived orogenic cycles and eclogitization of cold crust by spasmodic hot fluids. *Nature* 435, 1191-1196.

Carlson, W. D., 2006. Rates of Fe, Mg, Mn, and Ca diffusion in garnet. *Am. Mineral*. 91, 1 -11.

Carron, J. P., de Kerneizon, M. L. G., and Nachit, H., 1994. Variscan granites from Brittany. In *Pre-Mesozoic geology in France and related areas* (pp. 231-239). Springer Berlin Heidelberg.

Catlos, E. J., Dubey, C. S., Harrison, T. M., and Edwards, M. A., 2004. Late Miocene movement within the Himalayan Main Central Thrust shear zone, Sikkim, north-east India. *Journal of Metamorphic geology, 22*(3), 207-226.

Catlos, E. J., Harrison, T. M., Kohn, M. J., Grove, M., Ryerson, F. J., Manning, C. E., and Upreti, B. N., 2001. Geochronologic and thermobarometric constraints on the evolution of the Main Central Thrust, central Nepal Himalaya. *Journal of Geophysical Research: Solid Earth, 106*(B8), 16177-16204.

Chakraborty, S., Anczkiewicz, R., Gaidies, F., Rubatto, D., Sorcar, N., Faak, K., Mukhopadhyay, D. K., and Dasgupta, S., 2016. A review of thermal history and timescales of tectonometamorphic processes in Sikkim Himalaya (NE India) and implications for rates of metamorphic processes. *Journal of Metamorphic Geology*.

Chakraborty, A. K., Bratko, D., and Chandler, D., 1994. Diffusion of ionic penetrants in charged disordered media. *The Journal of chemical physics, 100*(2), 1528-1541.

Chakraborty, S., and Ganguly, J., 1991. Compositional zoning and cation diffusion in garnets. In *Diffusion, Atomic Ordering, and Mass Transport* (pp. 120-175). Springer US.

Chakraborty, S., and Ganguly, J., 1992. Cation diffusion in aluminosilicate garnets: experimental determination in spessartine-almandine diffusion couples, evaluation of effective binary diffusion coefficients, and applications. *Contributions to Mineralogy and petrology*, *111*(1), 74-86.

Chemenda, A. I., Burg, J.-P., and Mattauer, M., 2000. Evolutionary model of the Himalaya–Tibet system: geopoem: based on new modelling, geological and geophysical data. *Earth and Planetary Science Letters, 174*(3), 397-409.

Chen, Y., Courtillot, V., Cogné, J.P., Besse, J., Yang, Z. and Enkin, R., 1993. The configuration of Asia prior to the collision of India: Cretaceous paleomagnetic constraints. *Journal of Geophysical Research: Solid Earth*, *98*(B12), pp.21927-21941.

Chu, X., and Ague, J. J., 2015. Analysis of experimental data on divalent cation diffusion kinetics in aluminosilicate garnets with application to timescales of peak Barrovian metamorphism, Scotland. *Contributions to Mineralogy and Petrology*, *170*(2), 1-27.

Cocherie, A., Be Mezeme, E., Legendre, O., Fanning, C. M., Faure, M., and Rossi, P., 2005. Electron-microprobe dating as a tool for determining the closure of Th-U-Pb systems in migmatitic monazites. *American Mineralogist, 90*(4), 607-618.

Coggon, R. and Holland, T.J.B., 2002. Mixing properties of phengitic micas and revised garnet-phengite thermobarometers. *Journal of Metamorphic Geology*, *20*(7), pp.683-696.

Cogné, J., 1990. The Cadomian orogeny and its influence on the Variscan evolution of western Europe. *Geological Society, London, Special Publications*, *51*(1), 305-311.

Connolly, J. A. D., 2005. Computation of phase equilibria by linear programming: a tool for geodynamic modeling and its application to subduction zone decarbonation. *Earth and Planetary Science Letters*, *236*(1), 524-541.

Copeland, P., Parrish, R.R. and Harrison, T.M., 1988. Identification of inherited radiogenic Pb in monazite and its implications for U–Pb systematics. *Nature*, *333*(6175), pp.760-763.

Corfu, F., Hanchar, J.M., Hoskin, P.W. and Kinny, P., 2003. Atlas of zircon textures. *Reviews in mineralogy and geochemistry*, *53*(1), pp.469-500.

Coward, M.P. and Butler, R.W.H., 1985. Thrust tectonics and the deep structure of the Pakistan Himalaya. *Geology*, *13*(6), pp.417-420.

Cygan, R. T., and Lasaga, A. C., 1982. Crystal growth and the formation of chemical zoning in garnets. *Contributions to Mineralogy and Petrology*, *79*(2), 187-200.

Dasgupta, S., Ganguly, J., and Neogi, S., 2004. Inverted metamorphic sequence in the Sikkim Himalayas: crystallization history, P-T gradient and implications. *Journal of Metamorphic Geology*, 22, 395-412.

Dasgupta, S., Chakraborty, S., and Neogi, S., 2009. Petrology of an inverted Barrovian sequence of metapelites in Sikkim, India: constraints on the tectonics of inversion. *American Journal of Science*, 309, 43-84.

DeCelles, P. G., Gehrels, G. E., Najman, Y., Martin, A. J., Carter, A., and Garzanti, E., 2004. Detrital geochronology and geochemistry of Cretaceous–Early Miocene strata of Nepal: implications for timing and diachroneity of initial Himalayan orogenesis. *Earth and Planetary Science Letters*, *227*(3), 313-330.

DeCelles, P. G., Robinson, D. M., Quade, J., Ojha, T. P., Garzione, C. N., Copeland, P., and Upreti, B. N., 2001. Stratigraphy, structure, and tectonic evolution of the Himalayan fold-thrust belt in western Nepal. *Tectonics*, *20*(4), 487-509.

Deniel, C., Vidal, P., Fernandez, A., Le Fort, P. and Peucat, J.J., 1987. Isotopic study of the Manaslu granite (Himalaya, Nepal): inferences on the age and source of Himalayan leucogranites. *Contributions to Mineralogy and Petrology*, *96*(1), pp.78-92.

Dewey, J. F., 2005. Orogeny can be very short. *Proceeding of the National and Academy of Science* 102, 15286-15293.

Didier, A., Bosse, V., Cherneva, Z., Gautier, P., Georgieva, M., Paquette, J. L., and Gerdjikov, I., 2014. Syn-deformation fluid-assisted growth of monazite during renewed high-grade metamorphism in metapelites of the Central Rhodope (Bulgaria, Greece). *Chemical Geology*, *381*, 206-222.

Diener, J. F. A., and Powell, R., 2010. Influence of ferric iron on the stability of mineral assemblages. *Journal of Metamorphic Geology, 28*(6), 599-613.

Dinter, D. A., Macfarlane, A., Hames, W., Isachsen, C., Bowring, S., and Royden, L., 1995. U-Pb and 40Ar/39Ar geochronology of the Symvolon granodiorite: Implications for the thermal and structural evolution of the Rhodope metamorphic core complex, northeastern Greece. *Tectonics, 14*(4), 886-908.

Dinter, D. A., and Royden, L., 1993. Late Cenozoic extension in northeastern Greece: Strymon Valley detachment system Rhodope metamorphic core complex. Geology, 21, 45-48, doi: 10.1130/0091-7613(1993)021<0045:LCEING>2.3CO; 2.

Dodson, M. H., 1973: Closure Temperature in Cooling Geochronological and Petrological Systems. *Contribution to Mineralogy and Petrology*, 40, 259-274.

Efron, B. and Tibshirani, R.J., 1993. An introduction to the bootstrap Chapman & Hall. *New York, 436*.

Engi, M., Berger, A., and Roselle, G. T., 2001. Role of the tectonic accretion channel in collisional orogeny. *Geology*, *29*(12), 1143-1146.

England, P., Le Fort, P., Molnar, P., and Pêcher, A., 1992. Heat sources for Tertiary metamorphism and anatexis in the Annapurna-Manaslu region central Nepal. *Journal of Geophysical Research: Solid Earth*, *97*(B2), 2107-2128.

England, P., and Molnar, P., 1993. The interpretation of inverted metamorphic isograds using simple physical calculations. *Tectonics*, Vol. 12, No. 1, 145-157.

Eskola, P., 1915. On the relations between the chemical and mineralogical composition in the metamorphic rocks of the Orijarvi region. *Bulletin de la Commission géologique de Finlande*, *44*, pp. 109-145.

Eskola, P., 1920. The mineral facies of rocks.

Evans, K. A., 2006. Redox decoupling and redox budgets: Conceptual tools for the study of earth systems. *Geology, 34*(6), 489-492.

Faak, K., Chakraborty, S., and Dasgupta, S., 2012. Petrology and tectonic significance of metabasite slivers in the Lesser and Higher Himalayan domains of Sikkim, India. *Journal of Metamorphic Geology*, 30, 599-622.

Faccenda, M., Gerya, T. V., and Chakraborty, S., 2008. Styles of post-subduction collisional orogeny: influence of convergence velocity, crustal rheology and radiogenic heat production. *Lithos*, *103*(1), 257-287.

Florence, F. P., and Spear, F. S., 1991. Effects of diffusional modification of garnet growth zoning on P-T path calculations. *Contribution to Mineralogy and Petrology*, 107, 487-500.

Florence, F. P., and Spear, F. S., 1993. Influences of reaction history and chemical diffusion on PT calculations for staurolite schists from the Littleton Formation, northwestern New Hampshire. *American Mineralogist*, *78*(3-4), 345-359.

Frank, W., Hoinkes, G., Miller, C., Purtscheller, F., Richter, W., and Thöni, M., 1973. Relations between metamorphism and orogeny in a typical section of the Indian Himalayas. *Tschermaks mineralogische und petrographische Mitteilungen*, *20*(4), 303-332.

French, B.M. and Eugster, H.P., 1965. Experimental control of oxygen fugacities by graphite-gas equilibriums. *Journal of Geophysical Research*, *70*(6), pp.1529-1539.

Frost, B. R., and Chacko, T., 1989. The granulite uncertainty principle: limitations on thermobarometry in granulites. *The Journal of Geology*, 435-450.

Gaidies, F., Abart, R., De Capitani, C., Schuster, R., Connolly, J.A.D. and Reusser, E., 2006. Characterization of polymetamorphism in the Austroalpine basement east of the Tauern Window using garnet isopleth thermobarometry. *Journal of Metamorphic Geology*, *24*(6), pp.451-475.

Gaidies, F., Pattison, D. R. M., and De Capitani, C., 2011. Toward a quantitative model of metamorphic nucleation and growth. *Contributions to Mineralogy and Petrology*, *162*(5), 975-993.

Gaidies, F., Petley-Ragan, A., Chakraborty, S., Dasgupta, S., and Jones, P. 2015. Constraining the conditions of Barrovian metamorphism in Sikkim, India: P–T–t paths of garnet crystallization in the Lesser Himalayan Belt. *Journal of Metamorphic Geology*, *33*(1), 23-44.

Ganguly, J., 2002. Diffusion kinetics in minerals: principles and applications to tectono-metamophic processes, 271-309.

Ganguly, J., 2010. Cation diffusion kinetics in aluminosilicate garnets and geological applications. *Reviews in Mineralogy and Geochemistry*, *72*(1), pp.559-601.

Ganguly, J., Cheng, W., and Chakraborty, S., 1998. Cation diffusion in aluminosilicate garnets: experimental determination in pyrope-almandine diffusion couples. *Contributions to Mineralogy and Petrology*, *131*(2-3), 171-180.

Ganguly, J., Cheng, W. and Tirone, M., 1996. Thermodynamics of aluminosilicate garnet solid solution: new experimental data, an optimized model, and thermometric applications. *Contributions to Mineralogy and Petrology*, *126*(1-2), pp.137-151.

Gansser, A., 1964. Geology of the Himalayas.

Gansser, A., 1981. The geodynamic history of the Himalaya. *Zagros Hindu Kush Himalaya Geodynamic Evolution*, 111-121.

Gerya, T. V., Perchuk, L. L., and Burg, J. P., 2008. Transient hot channels: perpetrating and regurgitating ultrahigh-pressure, high-temperature crust–mantle associations in collision belts. *Lithos*, *103*(1), 236-256.

Ghiorso, M. S., 1987. Chemical mass-transfer in magmatic processes. 3. Crysta;-growth, chemical diffusion and thermal diffusion in multicomponent silicate melts. *Contributions to Mineralogy and Petrology*, *96*(3), 291-313.

Gibson, H. D., Brown, R. L., and Parrish, R. R., 1999. Deformation-induced inverted metamorphic field gradients: an example from the southeastern Canadian Cordillera. *Journal of Structural Geology*, *21*(7), 751-767.

Godard, G., 1988. Petrology of some eclogites in the Hercynides: the eclogites from the southern Armorican Massif, France. *Eclogites and eclogite-facies rocks*, *12*, 451-519.

Godin, L., Grujic, D., Law, R. D., and Searle, M. P., 2006. Channel flow, ductile extrusion and exhumation in continental collision zones: an introduction. *Geological Society, London, Special Publications*, *268*(1), 1-23.

Grasemann, B., Fritz, H. and Vannay, J.C., 1999. Quantitative kinematic flow analysis from the Main Central Thrust Zone (NW-Himalaya, India): implications for a decelerating strain path and the extrusion of orogenic wedges. *Journal of Structural Geology*, *21*(7), pp.837-853.

Graham, C. M., and England, P. C., 1976. Thermal regimes and regional metamorphism in the vicinity of overthrust faults: an example of shear heating and inverted metamorphic zonation from Southern California. *Earth and Planetary Science Letters*, 31, 142-152.

Grujic, D., Casey, M., Davidson, C., Hollister, L. S., Kündig, R., Pavlis, T., and Schmid, S., 1996. Ductile extrusion of the Higher Himalayan Crystalline in Bhutan: evidence from quartz microfabrics. *Tectonophysics*, *260*(1), 21-43.

Grujic, D., Warren, C.J. and Wooden, J.L., 2011. Rapid synconvergent exhumation of Miocene-aged lower orogenic crust in the eastern Himalaya. *Lithosphere*, *3*(5), pp.346-366.

Gumiaux, C., Gapais, D., Brun, J.-P., Chantraine, J., and Ruffet, G., 2004: Tectonic history of the Hercynian Armorican Shear belt (Brittany, France), *Geodinamica Acta*, 17:4, pp. 289-307.

Harris, N. B., Caddick, M., Kosler, J., Goswami, S., Vance, D., and Tindle, G., 2004. The pressure-temperature-time path of migmatites from the Sikkim Himalaya. *Journal of Metamorphic Geology*, 22, 249-264.

Harris, N., Massey, J. and Inger, S., 1993. The role of fluids in the formation of High Himalayan leucogranites. *Geological Society, London, Special Publications*, *74*(1), pp.391-400.

Harrison, T.M., McKeegan, K.D. and LeFort, P., 1995. Detection of inherited monazite in the Manaslu leucogranite by 208Pb232Th ion microprobe dating: crystallization age and tectonic implications. *Earth and Planetary Science Letters*, *133*(3), pp.271-282.

Harrison, T. M., Yin, A., and Ryerson, F. J., 1998. Orographic evolution of the Himalaya and Tibetan plateau. *Oxford Monographs on Geology and Geophysics*, *39*, 39-72.

Heim, A., and Gansser, A., 1939. Central Himalaya.

Himmelberg, G. R., Brew, D. A., and Ford, A. B., 1991. Development of inverted metamorphic isograds in the western metamorphic belt, Juneau, Alaska. *Journal of Metamorphic Geology*, *9*(2), 165-180.

Hodges, K. V., 2000. Tectonics of the Himalaya and southern Tibet from two perspectives. *Geological Society of America Bulletin*, *112*(3), 324-350.

Hodges, K.V. and Crowley, P.D., 1985. Error estimation and empirical geothermobarometry for pelitic systems. *American Mineralogist*, *70*(7-8), pp.702-709.

Hodges, K. V., Burchfiel, B. C., Royden, L. H., Chen, Z., and Liu, Y., 1993. The metamorphic signature of contemporaneous extension and shortening in the central Himalayan orogen: data from the Nyalam transect, southern Tibet. *Journal of Metamorphic Geology*, *11*(5), 721-737.

Hodges, K. V., Parrish, R. R., and Searle, M. P., 1996. Tectonic evolution of the central Annapurna range, Nepalese Himalayas. *Tectonics*, *15*(6), 1264-1291.

Hodges, K. V., and Silverberg, D. S., 1988. Thermal evolution of the greater Himalaya, Garhwal, India. *Tectonics*, *7*(3), 583-600.

Holdaway, M.J. and Lee, S.M., 1977. Fe-Mg cordierite stability in high-grade pelitic rocks based on experimental, theoretical, and natural observations. *Contributions to Mineralogy and Petrology*, *63*(2), pp.175-198.

Holland, T. J. B., and Powell, R., 1998. An internally consistent thermodynamic data set for phases of petrological interest. *Journal of Metamorphic Geology*, Vol. 16, Issue 3, pp. 309-343, doi: 10.1111/j1525-1314.1998.00140.x

Hollister, L. S., 1969. Contact metamorphism in the Kwoiek area of British Columbia: an end member of the metamorphic process. *Geological Society of America Bulletin*, *80*(12), 2465-2494.

Hubbard, M. S., 1996. Ductile shear as a cause of inverted metamorphism: example from the Nepal Himalaya. *The Journal of Geology*, 493-499.

Hughes, N. C., and Jell, P. A., 1999. Biostratigraphy and biogeography of Himalayan Cambrian trilobites. *SPECIAL PAPERS-GEOLOGICAL SOCIETY OF AMERICA*, 109-116.

Imayama, T., Takeshita, T., Yi, K., Cho, D.L., Kitajima, K., Tsutsumi, Y., Kayama, M., Nishido, H., Okumura, T., Yagi, K. and Itaya, T., 2012. Two-stage partial melting and contrasting cooling history within the Higher Himalayan Crystalline Sequence in the far-eastern Nepal Himalaya. *Lithos*, *134*, pp.1-22.

Indares, A. and Martignole, J.A.C.Q.T.I.E.S., 1985. Biotite-garnet geothermometry in granulite-facies rocks: evaluation of equilibrium criteria. *Canadian Mineralogist*, *23*, pp.187-193.

Inger, S., and Harris, N. B. W., 1992. Tectonothermal evolution of the High Himalayan crystalline sequence, Langtang Valley, northern Nepal. *Journal of Metamorphic Geology*, *10*(3), 439-452.

Ivanov, Z., 1988. General framework of the Rhodope massif geological and structural development, in the Balkanides setting. *Bulletin De La Societe Geologique De France*, *4*(2), 227-240.

Jamieson, R. A., Beaumont, C., Fullsack, P., and Lee, B., 1998. Barrovian regional metamorphism: Where’s the heat?. *Geological Society, London, Special Publications*, *138*(1), 23-51.

Jamieson, R. A., Beaumont, C., Medvedev, S., and Nguyen, M. H., 2004. Crustal channel flows: 2. Numerical models with implications for metamorphism in the Himalayan-Tibetan orogen. *Journal of Geophysical Research: Solid Earth*, *109*(B6).

Jamieson, R. A., Beaumont, C., Nguyen, M. H., and Grujic, D., 2006. Provenance of the Greater Himalayan Sequence and associated rocks: predictions of channel flow models. *Geological Society, London, Special Publications*, *268*(1), 165-182.

Jamieson, R. A., Beaumont, C., Nguyen, M. H., and Lee, B., 2002. Interaction of metamorphism, deformation and exhumation in large convergent orogens. *Journal of Metamorphic Geology*, *20*(1), 9-24.

Jégouzo, P., 1980. The South Armorican Shear Zone. *Journal of Structural Geology*, Vol. 2, No. ½, 39-47.

Johnson, D.P., Searle, D.E. and Hopley, D., 1982. Positive relief over buried post-glacial channels, Great Barrier Reef Province, Australia. *Marine Geology*, *46*(1), pp.149-159.

Johnson, N. M., Stix, J., Tauxe, L., Cerveny, P. F., and Tahirkheli, R. A., 1985. Paleomagnetic chronology, fluvial processes, and tectonic implications of the Siwalik deposits near Chinji Village, Pakistan. *The Journal of Geology*, 27-40.

Jolivet, L., and Brun, J. P., 2010. Cenozoic geodynamic evolution of the Aegean. *International Journal of Earth Sciences*, *99*(1), 109-138.

Jones, C. E., Tarney, J., Baker, J. H., and Gerouki, F., 1992. Tertiary granitoids of Rhodope, northern Greece: magmatism related to extensional collapse of the Hellenic Orogen? *Tectonophysics*, *210*(3-4), 295-314.

Kaus, B. J., and Podladchikov, Y. Y., 2006. Initiation of localized shear zones in viscoelastoplastic rocks. *Journal of Geophysical Research: Solid Earth*, *111*(B4).

Kaiser-Rohrmeier, M., Handler, R., Quadt, A.V. and Heinrich, C., 2004. Hydrothermal Pb–Zn ore formation in the central Rhodopian dome, south Bulgaria: review and new time constraints from Ar–Ar geochronology. *Swiss Bulletin of Mineralogy and Petrology*, *84*(1), pp.37-58.

Kelsey, D.E., Clark, C. and Hand, M., 2008. Thermobarometric modelling of zircon and monazite growth in melt-bearing systems: Examples using model metapelitic and metapsammitic granulites. *Journal of Metamorphic Geology*, *26*(2), pp.199-212.

Kelsey, D. E., White, R. W., Powell, R., Wilson, C. J. L., and Quinn, C. D., 2003. New constraints on metamorphism in the Rauer Group, Prydz Bay, east Antarctica. *Journal of Metamorphic Geology*, *21*(8), 739-759.

Ketcham, R. A., and Carlson, W. D., 2012. Numerical simulation of diffusion-controlled nucleation and growth of porphyroblasts. *Journal of Metamorphic Geology*, *30*(5), 489-512.

Kilias, A., and Mountrakis, D., 1990. Kinematics of the crystalline sequences in the western Rhodope massif. *Geologica Rhodopica*, *2*, 100-116.

Kohn, M. J., 2003. Geochemical zoning in metamorphic minerals. *The Crust*, *3*, 229-261.

Kohn, M.J., 2008. PTt data from central Nepal support critical taper and repudiate large-scale channel flow of the Greater Himalayan Sequence. *Geological Society of America Bulletin*, *120*(3-4), pp.259-273.

Kohn, M. J., 2014. Himalayan metamorphism and its tectonic implications. *Annual Review of Earth and Planetary Sciences*, *42*, 381-419.

Kohn, M. J., Paul, S. K., and Corrie, S. L., 2010. The lower Lesser Himalayan sequence: A Paleoproterozoic arc on the northern margin of the Indian plate. *Geological Society of America Bulletin*, *122*(3-4), 323-335.

Kohn, M. J., and Spear, F., 2000. Retrograde net transfer reaction insurance for pressure-temperature estimates. *Geology*, *28*(12), 1127-1130.

Kolceva, K., Zeljaskova-Panajotova, M., Bobrecov, N.L. and Stojanova, V., 1986. Eclogites in Central Rhodope Metamorphic Group and their retrograde metamorphism. *Geochem Mineral Petrol (Sofia)*, *20*(21), pp.130-144.

Koziol, A.M. and Newton, R.C., 1988. Redetermination of the anorthite breakdown reaction and improvement of the plagioclase-garnet-Al2SiO5-quartz geobarometer. *American Mineralogist*, *73*(3-4), pp.216-223.

Krenn, K., Bauer, C., Proyer, A., Klötzli, U., and Hoinkes, G., 2010. Tectonometamorphic evolution of the Rhodope orogen. *Tectonics*, *29*(4).

Kretz, R., 1983. Symbols of rock-forming minerals. American Mineralogist, 68, 277–279.

Krohe, A., and Mposkos, E., 2002. Multiple generations of extensional detachments in the Rhodope Mountains (northern Greece): Evidence of episodic exhumation of high-pressure rocks, in *The Timing and Location of Major Ore deposits in an Evolving Orogen*, edited by D. J. Blundell, F. Neubauer, and A. von Quadt, *Geol. Soc. Spec. Publ*, 204, 151-178.

Kröner, A., and Willner, A. P. (1998). Time of formation and peak of Variscan HP-HT metamorphism of quartz-feldspar rocks in the central Erzgebirge, Saxony, Germany. *Contributions to Mineralogy and Petrology*, *132*(1), 1-20.

Lasaga, A. C., 1979. The treatment of multi-component diffusion and ion pairs in diagenetic fluxes. *American Journal of Science*, *279*(3), 324-346.

Lasaga, A. C., 1983. Geospeedometry: An extension of geothermometry. *Kinetics and Equilibrium in Mineral Reactions*, S. K., Saxena, ed., Advances in Physical Geochemistry, Vol. 3, Springer, New York, pp. 81-114.

Lasaga, A. C., and Jiang, J., 1995. Thermal history of rocks; PTt paths for geospeedometry, petrologic data, and inverse theory techniques. *American Journal of Science*, *295*(6), 697-741.

Lee, J. K., and Tromp, J., 1995. Self-induced fracture generation in zircon. *Journal of Geophysical Research: Solid Earth*, *100*(B9), 17753-17770.

Le Fort, P., 1975. Himalaya: the collided range. Present knowledge of the continental arc. *American Journal of Science*, Vol. 275-A, 1-44.

Liati, A., 1986. *Regional metamorphism and overprinting contact metamorphism of the Rhodope zone, near Xanthi (N. Greece): petrology, geochemistry, geochronology*. na.

Liati, A., 2005. Identification of repeated Alpine (ultra) high-pressure metamorphic events by U–Pb SHRIMP geochronology and REE geochemistry of zircon: the Rhodope zone of Northern Greece. *Contributions to Mineralogy and Petrology*, *150*(6), 608-630.

Liati, A. and Kreuzer, H., 1990. K-Ar dating of metamorphic and magmatic rocks from the Xanthi and Drama areas, Greek part of the Rhodope zone. *Eur J Mineral*, *2*(Bh 1), p.161.

Liati, A., Gebauer, D., and Fanning, C. M., 2004. The age of ophiolitic rocks of the Hellenides (Vourinos, Pindos, Crete): first U–Pb ion microprobe (SHRIMP) zircon ages. *Chemical Geology*, *207*(3), 171-188.

Loomis, T.P., 1983. Compositional zoning of crystals: a record of growth and reaction history. In *Kinetics and Equilibrium in Mineral Reactions* (pp. 1-60). Springer New York.

Machev, P. and Kolcheva, K., 2008. Eclogites from Arda tectonic unit—mineralogy and evidence for short leaved granulite facies overprint. In *Proceedings of national conference GEOSCIENCES* (pp. 49-50).

Marchand, J., 1981. Ecaillage d’un “mélange tectonique” profond: le complexe cristallophyllien de Champtoceaux (Bretagne méridionale). *CR Acad. Sci., Paris*, *293*, pp.223-228.

Martin, A.J., Ganguly, J. and DeCelles, P.G., 2010. Metamorphism of Greater and Lesser Himalayan rocks exposed in the Modi Khola valley, central Nepal. *Contributions to Mineralogy and Petrology*, *159*(2), pp.203-223.

Massonne, H.J. and Willner, A.P., 2008. Phase relations and dehydration behaviour of psammopelite and mid-ocean ridge basalt at very-low-grade to low-grade metamorphic conditions. *European Journal of Mineralogy*, *20*(5), pp.867-879.

Mohan, A., Windley, B. F., and Searle, M. P., 1989. Geothermobarometry and development of inverted metamorphism in the Darjeeling-Sikkim region of the eastern Himalaya. *Journal of Metamorphic Geology*, 7, 95-110.

Molnar, P., and England, P., 1990. Temperatures, heat flux, and frictional stress near major thrust faults. *Journal of Geophysical Research: Solid Earth*, *95*(B4), 4833-4856.

Molnar, P., England, P., and Martinod, J., 1993. Mantle dynamics, uplift of the Tibetan Plateau, and the Indian monsoon. *Reviews of Geophysics*, *31*(4), 357-396.

Mottram, C. M., Warren, C. J., Regis, D., Roberts, N. M., Harris, N. B., Argles, T. W., and Parrish, R. R., 2014. Developing an inverted Barrovian sequence; insights from monazite petrochronology. *Earth and Planetary Science Letters*, *403*, 418-431.

Moulas, E., Podladchikov, Y.Y., Aranovich, L.Y. and Kostopoulos, D., 2013. The problem of depth in geology: When pressure does not translate into depth. *Petrology*, *21*(6), pp.527-538.

Moulas, E., Schenker, F.L., Aranovich, L.Y. and Burg, J.-P., 2016. Metamorphic conditions and exhumation of the Kesebir-Kardamos dome – Rhodope Metamorphic Complex (Greece-Bulgaria). *International Journal of Earth Sciences*. Submitted.

Mposkos, E., 1989. High-pressure metamorphism in gneisses and pelitic schists in the East Rhodope Zone (N. Greece). *Mineralogy and Petrology*, *41*(1), 25-39.

Mposkos, E. D., and Kostopoulos, D. K., 2001. Diamond, former coesite and supersilicic garnet in metasedimentary rocks from the Greek Rhodope: a new ultrahigh-pressure metamorphic province established. *Earth and Planetary Science Letters, 192*(4), 497-506.

Mposkos, E.V.R.I.P.I.D.I.S. and Liati, A.N.T.H.I., 1993. Metamorphic evolution of metapelites in the high-pressure terrane of the Rhodope zone, Northern Greece. *Canadian Mineralogist*, *31*, pp.401-401.

Mungall, J. E., Romano, C., and Dingwell, D. B., 1998. Multicomponent diffusion in the molten system K2O-Na2O-Al2O3-SiO2-H2O. *American Mineralogist*, *83*(7-8), 685-699.

Nagel, T. J., Schmidt, S., Janák, M., Froitzheim, N., Jahn-Awe, S., and Georgiev, N., 2011. The exposed base of a collapsing wedge: The Nestos Shear Zone (Rhodope Metamorphic Province, Greece). *Tectonics*, Vol. 30, TC4009, doi: 10.1029/2010TC002815.

Naydenov, K., von Quadt, A., Peytcheva, I., Sarov, S., and Dimov, D., 2009. U-Pb zircon dating of metamorphic rocks in the region of Kostenets-Kozarsko villages: constraints on the tectonic evolution of the Maritsa strike-slip shear zone. *Bulgarian Geological Society*, 70(1-3), 5-21.

Neogi, S., Dasgupta, S., and Fukuoka, M., 1998. High P-T Polymetamorphism, Dehydration Melting, and Generation of Migmatites and Granites in the Higher Himalayan Crystalline Complex, Sikkim, India. *Journal of Petrology*, Vol. 39, No. 1, 61-99.

Newton, R.C. and Haselton, H.T., 1981. Thermodynamics of the garnet—plagioclase—Al2SiO5—quartz geobarometer. In *Thermodynamics of minerals and melts* (pp. 131-147). Springer New York.

Newton, R.C., Charlu, T.V. and Kleppa, O.J., 1980. Thermochemistry of the high structural state plagioclases. *Geochimica et Cosmochimica Acta*, *44*(7), pp.933-941.

Oliver, G. J. H., Chen, F., Buchwaldt, R., and Hegner, E., 2000. Fast tectonometamorphism and exhumation in the type area of the Barrovian and Buchan zones. *Geology*, *28*(5), 459-462.

Ovtacharova, M., von Quadt, A., Heinrich, C. A., Frank, M., Keiser-Rhomeier, M., Peytcheva, I., and Cherneva, Z., 2003. Triggering of hydrothermal ore mineralization in the central Rhodope core complex (Bulgaria) – Insight from isotope and geochronological studies on Tertiary magmatism and migmatization. *Mineral Exploration and Sustainable Development,* vol. 1, 367-370.

Pandey, M.R., Tandukar, R.P., Avouac, J.P., Lave, J. and Massot, J.P., 1995. Interseismic strain accumulation on the Himalayan crustal ramp (Nepal). *Geophysical Research Letters*, *22*(7), pp.751-754.

Papanikolaou, D., and Panagopoulos, A., 1981. On the structural style of southern Rhodope, Greece. *Geologica Balcanica*, *11*(3), 13-22.

Patriat, P. and Achache, J., 1984. India–Eurasia collision chronology has implications for crustal shortening and driving mechanism of plates.

Patzelt, A., Li, H., Wang, J. and Appel, E., 1996. Palaeomagnetism of Cretaceous to Tertiary sediments from southern Tibet: evidence for the extent of the northern margin of India prior to the collision with Eurasia. *Tectonophysics*, *259*(4), pp.259-284.

Peacock, S., 1987. Creation and preservation of subduction-related inverted metamorphic gradients. *J. Geophys. Res.*, 92, 12763-12782.

Pêcher, A., 1977. Geology of the Nepal Himalaya: deformation and petrography in the Main Central Thrust zone. *Ecologie et Géologie de l'Himalaya*, *268,* 301-318.

Pêcher, A., 1989. The metamorphism in the central Himalaya. *Journal of Metamorphic Geology*, *7*(1), 31-41.

Perchuk, L.L. and Lavrent'Eva, I.V., 1983. Experimental investigation of exchange equilibria in the system cordierite-garnet-biotite. In *Kinetics and equilibrium in mineral reactions* (pp. 199-239). Springer New York.

Perchuk, A., and Philippot, P., 1997. Rapid cooling and exhumation of eclogitic rocks from the Great Caucasus, Russia. *Journal of Metamorphic Geology*, *15*(3), 299-310.

Perchuk, A.L. and Philippot, P., 2000. Geospeedometry and time scales of high-pressure metamorphism. *International Geology Review*, *42*(3), pp.207-223.

Perchuk, L.L., Aranovich, L.Y., Podlesskii, K.K., LAvRANT'EvA, I.V., Gerasimov, V.Y., Fed'Kin, V.V., Kitsul, V.I., Karsakov, L.P. and Berdnikov, N.V., 1985. Precambrian granulites of the Aldan shield, eastern Siberia, USSR. *Journal of metamorphic Geology*, *3*(3), pp.265-310.

Perraki, M., Proyer, A., Mposkos, E., Kaindl, R. and Hoinkes, G., 2006. Raman micro-spectroscopy on diamond, graphite and other carbon polymorphs from the ultrahigh-pressure metamorphic Kimi Complex of the Rhodope Metamorphic Province, NE Greece. *Earth and Planetary Science Letters*, *241*(3), pp.672-685.

Pitra, P., Ballèvre, M., and Ruffet, G., 2010. Inverted metamorphic field gradient towards a Variscan suture zone (Champtoceaux Complex, Armorican Massif, France). *Journal of metamorphic Geol*ogy, 28, 183-208.

Powell, R. and Holland, T., 1999. Relating formulations of the thermodynamics of mineral solid solutions: activity modeling of pyroxenes, amphiboles, and micas. *American Mineralogist*, *84*(1-2), pp.1-14.

Reischmann, T. and Kostopoulos, D., 2002. Timing of UHPM in metasediments from the Rhodope Massif, N Greece. *Geochim. Cosmochim. Acta*, *66*, p.A634.

Richter, F. M., Rowley, D. B., and DePaolo, D. J., 1992. Sr isotope evolution of seawater: the role of tectonics. *Earth and Planetary Science Letters*, *109*(1), 11-23.

Ricou, L. E., Burg J.-P., Godfriaux, I., and Ivanov, Z., 1998. Rhodope and Vardar: the metamorphic and the olistostromic paired belts related to the Cretaceous subduction under Europe. *Geodinamica Acta*, 11(6), 285-309.

Rieser, A. B., Neubauer, F., Handler, R., Velichkova, S. H., and Ivanov, I., 2008. New 40Ar/39Ar age constraints on the timing of magmatic events in the Panagyurishte region, Bulgaria. *Swiss J. Geosci*., 101(1), 107-123, doi: 10.1007/s0015-007-1243-z.

Robertson, A. H. F., Clift, P. D., Degnan, P. J., and Jones, G., 1991. Palaeogeographic and palaeotectonic evolution of the Eastern Mediterranean Neotethys. *Palaeogeography, Palaeoclimatology, Palaeoecology*, *87*(1), 289-343.

Robinson, D. M., DeCelles, P. G., and Copeland, P., 2006. Tectonic evolution of the Himalayan thrust belt in western Nepal: Implications for channel flow models. *Geological Society of America Bulletin*, *118*(7-8), 865-885.

Rowley, D. B., 1996. Age of initiation of collision between India and Asia: A review of stratigraphic data. *Earth and Planetary Science Letters*, *145*(1), 1-13.

Rubatto, D., Chakraborty, S., Dasgupta, S., 2013. Timescales of crustal melting in the Higher Himalayan Crystallines (Sikkim, Eastern Himalaya) inferred from trace element-constrained monazite and zircon chronology. Contrib. Mineral Petrol., 165: 349-372, DOI 10.1007/s00410-012-0812-y

Rudnick, R. L., and Williams, I. S., 1987. Dating the lower crust by ion microprobe. *Earth and Planetary Science Letters*, *85*(1), 145-161.

Ruppel, C., and Hodges, K. V., 1994. Pressure-temperature-time paths from two-dimensional thermal models: Prograde, retrograde, and inverted metamorphism. *Tectonics*, Vol. 13, No. 1, 17-44.

Sangode, S. J., and Bloemendal, J., 2004. Pedogenic transformation of magnetic minerals in Pliocene–Pleistocene palaeosols of the Siwalik Group, NW Himalaya, India. *Palaeogeography, Palaeoclimatology, Palaeoecology*, *212*(1), 95-118.

Sangode, S. J., Kumar, R., and Ghosh, S. K., 1996. Magnetic polarity stratigraphy of the Siwalik sequence of Haripur area (HP), NW Himalaya. *Geological Society of India*, *47*(6), 683-704.

Schelling, D., 1992. The tectonostratigraphy and structure of the eastern Nepal Himalaya. *Tectonics*, *11*(5), 925-943.

Schelling, D., and Arita, K., 1991. Thrust tectonics, crustal shortening, and the structure of the far-eastern Nepal Himalaya. *Tectonics*, *10*(5), 851-862.

Schmalholz, S. M., and Duretz, T., 2015. Shear zone and nappe formation by thermal softening, related stress and temperature evolution, and application to the Alps. *Journal of Metamorphic Geology*, *33*(8), 887-908.

Schmalholz, S.M., Duretz, T., Schenker, F.L. and Podladchikov, Y.Y., 2014. Kinematics and dynamics of tectonic nappes: 2-D numerical modelling and implications for high and ultra-high pressure tectonism in the Western Alps. *Tectonophysics*, *631*, pp.160-175.

Schmidt, S., Nagel, T.J. and Froitzheim, N., 2010. A new occurrence of microdiamond-bearing metamorphic rocks, SW Rhodopes, Greece. *European Journal of Mineralogy*, *22*(2), pp.189-198.

Schott, B., Yuen, D. A., and Schmeling, H., 2000. The significance of shear heating in continental delamination. *Physics of the Earth and Planetary Interiors*, *118*(3), 273-290.

Schenker, F. L., Gerya, T., and Burg, J. P., 2012. Bimodal behavior of extended continental lithosphere: Modeling insight and application to thermal history of migmatitic core complexes. *Tectonophysics*, *579*, 88-103.

Schwarz, J. O., Engi, M., and Berger, A., 2011. Porphyroblast crystallization kinetics: the role of the nutrient production rate. *Journal of Metamorphic Geology*, *29*(5), 497-512.

Searle, M.P., 1986. Structural evolution and sequence of thrusting in the High Himalayan, Tibetan—Tethys and Indus suture zones of Zanskar and Ladakh, Western Himalaya. *Journal of Structural Geology*, *8*(8), pp.923-936.

Searle, M. P., Cooper, D. J. W., Rex, A. J., Herren, E., and Colchen, M., 1988. Collision Tectonics of the Ladakh--Zanskar Himalaya [and Discussion]. *Philosophical Transactions of the Royal Society of London A: Mathematical, Physical and Engineering Sciences*, *326*(1589), 117-150.

Searle, M. P., Law, R. D., Godin, L., Larson, K. P., Streule, M. J., Cottle, J. M., and Jessup, M. J., 2008. Defining the Himalayan main central thrust in Nepal. *Journal of the Geological Society*, *165*(2), 523-534.

Searle, M. P., and Rex, A. J., 1989. Thermal model for the Zanskar Himalaya. *Journal of Metamorphic Geology*, 7, 127-134.

Searle, M. P., and Szulc, A. G., 2005. Channel flow and ductile extrusion of the high Himalayan slab-the Kangchenjunga–Darjeeling profile, Sikkim Himalaya☆. *Journal of Asian Earth Sciences*, *25*(1), 173-185.

Seeber, L., Armbruster, J. G., and Quittmeyer, R. C., 1981. Seismicity and continental subduction in the Himalayan arc. *Zagros Hindu Kush Himalaya Geodynamic Evolution*, 215-242.

Sheng, Y. J., Wasserburg, G. J., and Hutcheon, I. D., 1992. Self-diffusion of magnesium in spinel and in equilibrium melts: Constraints on flash heating of silicates. *Geochimica et Cosmochimica Acta*, *56*(6), 2535-2546.

Singh, I. B., 1981. A critical review of the fossil records in the Krol Belt succession and its implications on the biostratigraphy and paleogeography of the Lesser Himalaya: Palaeontological Society of India. *Journal*, *25*, 148-169.

Sinha Roy, S., 1974. Polymetemorphism in Daling rocks from a part of Eastern Himalaya and some problems of Himalayan metamorphism. *Him. Geol*, *4*(1), 74-101.

Sinha Roy, S., 1982. Interactions of Tethyan blocks and evolution of Asian fold belts. *Tectonophysics*, 82, 277-297.

Sinha-Roy, S., and Gupta, S. S., 1986. Precambrian deformed granites of possible basement in the Himalayas. *Precambrian research*, *31*(3), 209-235.

Sokoutis, D., Brun, J. P., Van Den Driessche, J., and Pavlides, S., 1993. A major Oligo-Miocene detachment in southern Rhodope controlling north Aegean extension. *Journal of the Geological Society*, *150*(2), 243-246.

Sorcar, N., Hoppe, U., Dasgupta, S., and Chakraborty, S., 2014. High-temperature cooling histories of migmatites from the High Himalayan Crystallines in Sikkim, India: rapid cooling unrelated to exhumation?. *Contributions to Mineralogy and Petrology*, *167*(2), 1-34.

Spear, F.S., 2004. Fast cooling and exhumation of the Valhalla metamorphic core complex, southeastern British Columbia. *International Geology Review*, *46*(3), pp.193-209.

Spear, F. S., 2014. The duration of near-peak metamorphism from diffusion modelling of garnet zoning. *Journal of Metamorphic Geology*, *32*(8), 903-914

Spear, F. S., and Selverstone, J., 1983. Quantitative P-T Paths from Zoned Minerals: Theory and Tectonic Applications. *Contribution to Mineralogy and Petrology*, 83, pp. 348-357.

Spear, F. S., Selverstone, J., Hickmott, D., Crowley, P., and Hodges, K. V., 1984. P-T path from garnet zoning: A new technique for deciphering tectonic processes in crystalline terranes. *Geology*, 12, 87-90.

Srivastava, P., and Mitra, G., 1994. Thrust geometries and deep structure of the outer and lesser Himalaya, Kumaon and Garhwal (India): Implications for evolution of the Himalayan fold-and-thrust belt. *Tectonics*, *13*(1), 89-109.

Stephenson, B. J., Waters, D. J., and Searle, M. P., 2000. Inverted metamorphism and the Main Central Thrust: field relations and thermobarometric constraints from the Kishtwar Window, NW Indian Himalaya. *Journal of Metamorphic Geology*, *18*(5), 571-590.

Stephenson, B. J., Searle, M. P., Waters, D. J., and Rex, D. C., 2001. Structure of the Main Central Thrust zone and extrusion of the High Himalayan deep crustal wedge, Kishtwar–Zanskar Himalaya. *Journal of the Geological Society*, *158*(4), 637-652.

Štípská, P., and Schulmann, K., 1995. Inverted metamorphic zonation in a basement-derived nappe sequence, eastern margin of the Bohemian Massif. *Geological Journal*, *30*(3-4), 385-413.

Stöcklin, J., 1980. Geology of Nepal and its regional frame Thirty-third William Smith Lecture. *Journal of the Geological Society*, *137*(1), 1-34.

Stüwe, K., 1998. Heat sources of Cretaceous metamorphism in the Eastern Alps—a discussion. *Tectonophysics*, *287*(1), pp.251-269.

Swapp, S. M., and Hollister, L. S., 1991. Inverted metamorphism within the Tibetan slab in Bhutan: evidence for a tectonically transported heat source. *Canadian Mineralogist*, 29, 1019-1041.

Tajčmanová, L., Connolly, J.A.D. and Cesare, B., 2009. A thermodynamic model for titanium and ferric iron solution in biotite. *Journal of Metamorphic Geology*, *27*(2), pp.153-165.

Thompson, A. B., and England, P. C., 1984. Pressure-Temperature-Time Path of Regional Metamorphism II. Their Interference and Interpretation using Mineral Assemblages in Metamorphic Rocks. *Journal of Petrology*, Vol. 25, Part 4, 929-955.

Thompson, A.B., Ridley, J.R. and Mason, R., 1987. Pressure--Temperature--Time (P--T--t) Histories of Orogenic Belts [and Discussion]. *Philosophical Transactions of the Royal Society of London A: Mathematical, Physical and Engineering Sciences*, *321*(1557), pp.27-45.

Tilley, C. E., 1924. The facies classification of metamorphic rocks. *Geological Magazine*, *61*(04), 167-170.

Turpaud, P., 2006. Characterization of igneous terranes by zircon dating: implications for the UHP relicts occurrences and suture identification in the Central Rhodope, Northern Greece. *Unpublished Ph. D. Thesis*.

Turpaud, P. and Reischmann, T., 2010. Characterisation of igneous terranes by zircon dating: implications for UHP occurrences and suture identification in the Central Rhodope, northern Greece. *International Journal of Earth Sciences*, *99*(3), pp.567-591.

Vannay, J.C. and Grasemann, B., 1998. Himalayan inverted metamorphism in the High Himalaya of Kinnaur (NW India): petrography versus thermobarometry. *Schweizerische Mineralogische und Petrographische Mitteilungen*, *78*, pp.107-132.

Vannay, J. C., and Grasemann, B., 2001. Himalayan inverted metamorphism and syn-convergence extension as a consequence of a general shear extrusion. *Geological Magazine*, *138*(03), 253-276.

Viete, D. R., Hermann, J., Lister, G. S., and Stenhouse, I. R., 2011. The nature and the origin of the Barrovian metamorphism, Scotland: diffusion length scales in garnet and inferred thermal time scales. Journal of the Geological Society, Vol. 168, 115-132, doi: 10.1144/0016-76492009-087.

Waldbaum, D.R. and Thompson, J.B., 1968. Mixing properties of sanidine crystalline solutions. 2. Calculations based on volume data. *American Mineralogist*, *53*(11-1), p.2000.

Wang, Y., Xu, Y., Khawaja, S., Passey, B. H., Zhang, C., Wang, X., ... and Xie, G., 2013. Diet and environment of a mid-Pliocene fauna from southwestern Himalaya: Paleo-elevation implications. *Earth and Planetary Science Letters*, *376*, 43-53.

Warren, C.J., 2013. Exhumation of (ultra-) high-pressure terranes: concepts and mechanisms. *Solid Earth*, *4*(1), p.75.

Warren, C.J., Grujic, D., Kellett, D.A., Cottle, J., Jamieson, R.A. and Ghalley, K.S., 2011. Probing the depths of the India-Asia collision: U-Th-Pb monazite chronology of granulites from NW Bhutan. *Tectonics*, *30*(2).

Watson, E.B., Harrison, T.M. and Ryerson, F.J., 1985. Diffusion of Sm, Sr, and Pb in fluorapatite. *Geochimica et Cosmochimica Acta*, *49*(8), pp.1813-1823.

Wetherill, G. W., 1956. Discordant uranium-lead ages, I. *EOS, Transactions American Geophysical Union*, *37*(3), 320-326.

Wendt, R. P., 1965. The estimation of diffusion coefficients for ternary systems of strong and weak electrolytes. *J. Phys. Chem*., 69, 1227-1237.

White, R.W., Powell, R., Holland, T.J.B. and Worley, B.A., 2000. The effect of TiO~ 2 and Fe~ 2O~ 3 on metapelitic assemblages at greenschist and amphibolite facies conditions: mineral equilibria calculations in the system K~ 2O-FeO-MgO-Al~ 2O~ 3-SiO~ 2-H~ 2O-TiO~ 2-Fe~ 2O~ 3. *Journal of Metamorphic Geology*, *18*(5), pp.497-512.

Winter, John D., 2010. An introduction to igneous and metamorphic petrology.

Yin, J., and Enay, R., 2004. Tithonian ammonoid biostratigraphy in eastern Himalayan Tibet. *Geobios*, *37*(5), 667-686.

Yin, A., and Harrison, T. M., 2000. Geologic evolution of the Himalayan-Tibetan orogen. *Annual Review of Earth and Planetary Sciences*, *28*(1), 211-280.

Zhang, Y., 2008. *Geochemical kinetics*. Princeton University Press, pp. 631.

Zhang, Y., 2010. Diffusion in minerals and melts: theoretical background. *Reviews in Mineralogy and Geochemistry*, *72*(1), 5-59.

Zhao, W., Nelson, K. D., and Team, P. I., 1993. First Deep Seismic Reflection Profile in Himalaya/Tibet Plateau: Initial Results of Project IN DEPTH. *Nature*, *366*, 557-559.

Appendix A

Supplementary material Chapter 2

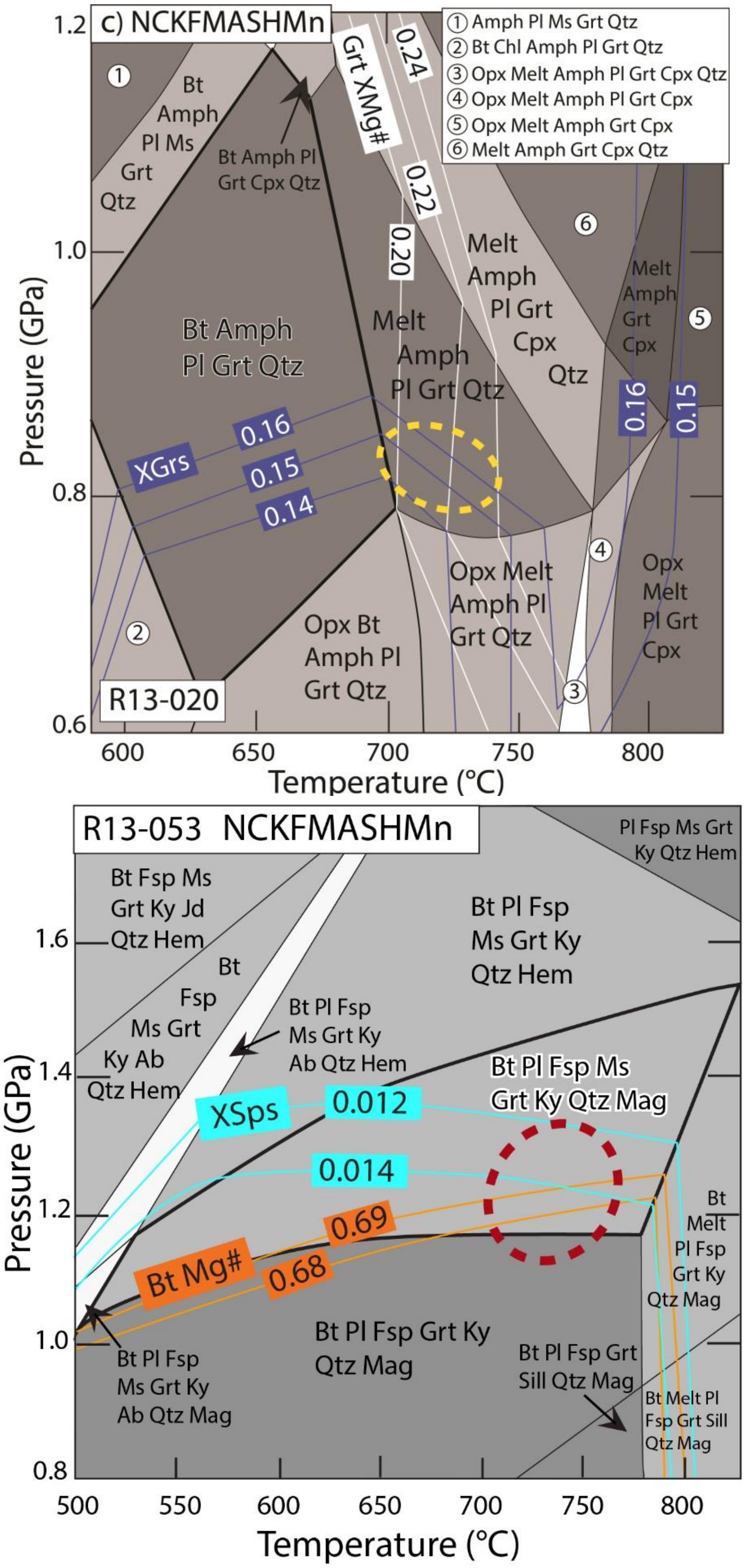

Appendix A.1. *P-T* pseudosections calculated in the NCKFMASHMn system for samples *R13-020* (top) and sample *R13-053* (bottom). Blue lines: garnet grossular (XGrs) composition isopleths. Green lines: garnet Mg# (Grt XMg#) chemical contour. Orange lines: biotite Mg# contours. Light blue lines: garnet spessartine (XSps) composition isopleths. Dashed ellipse: estimated *P-T* conditions. Bulk rock compositions are given in Table 2.3. Greyscale: same shade represents same amount of stable phases.

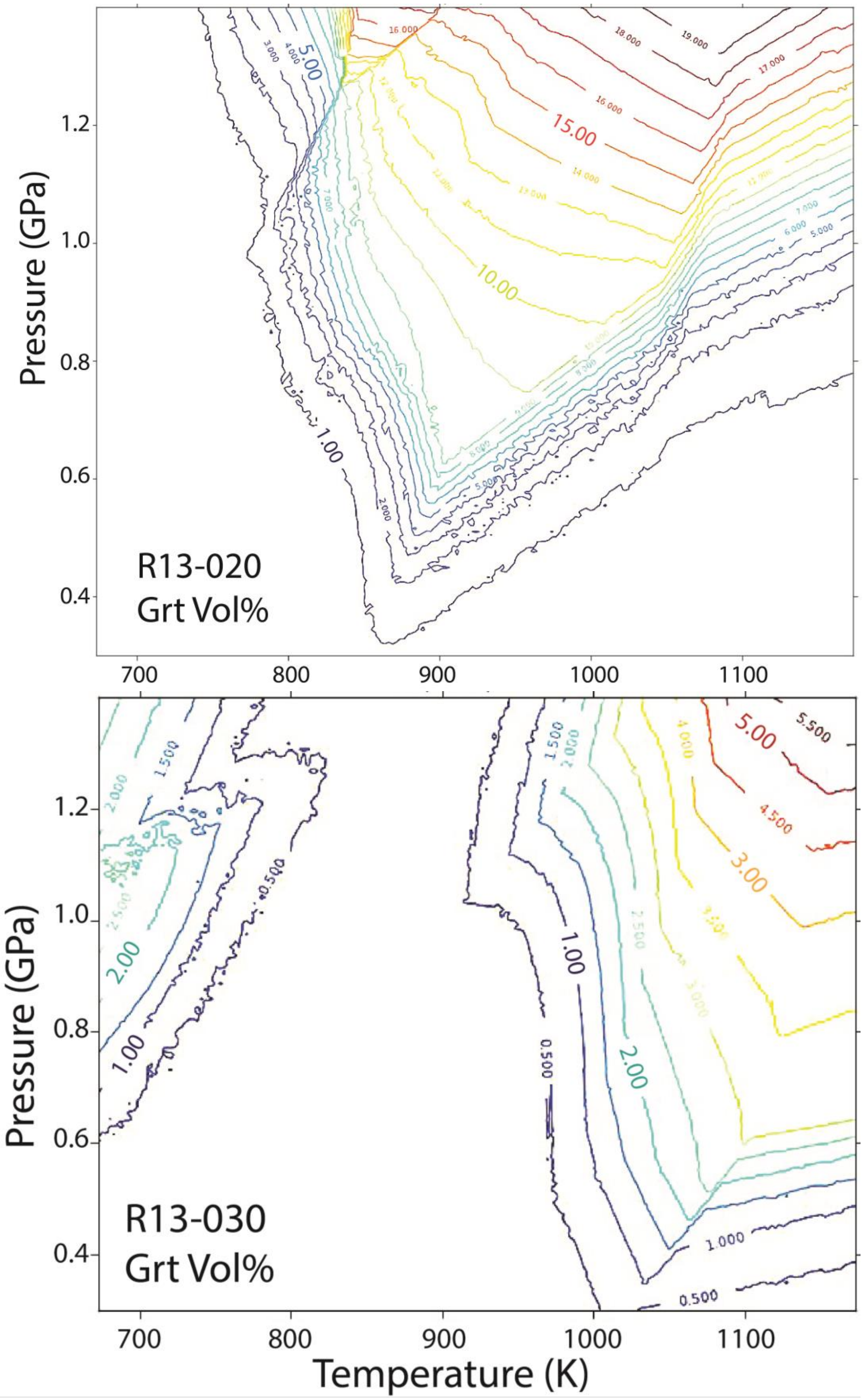

Appendix A.2. Garnet modal proportion (vol%).

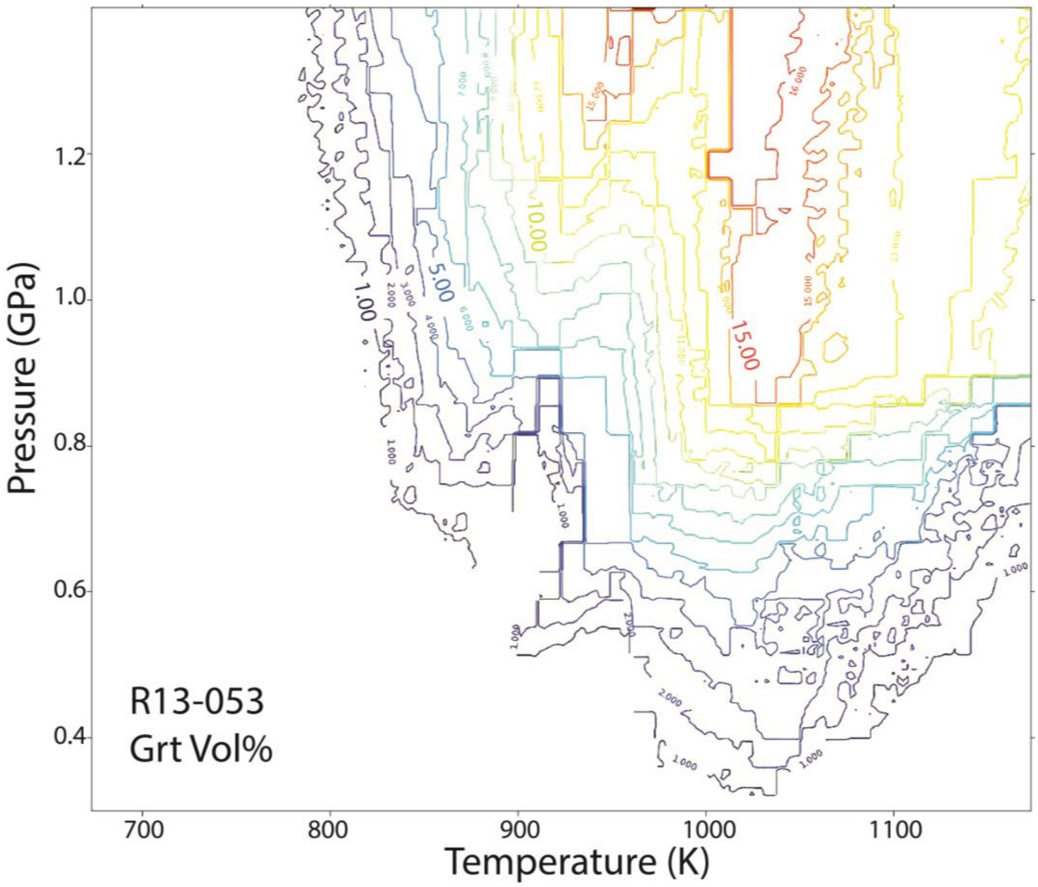

Appendix A.2. Continued

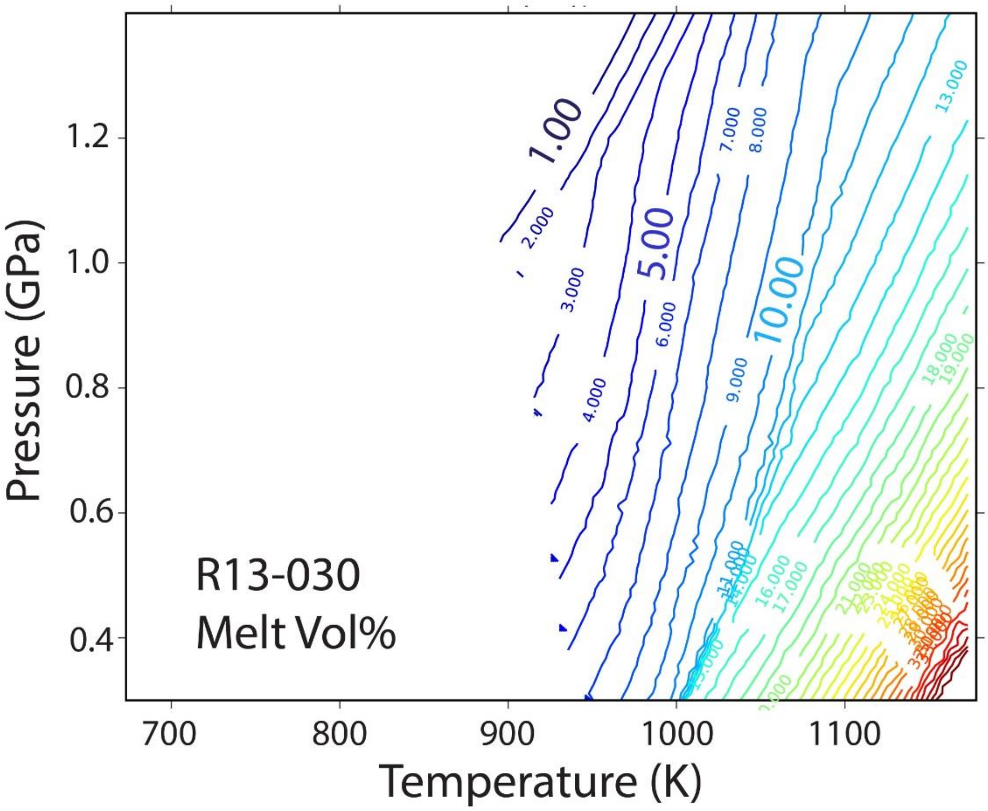

Appendix A.3. Melt modal proportion (vol%) for sample R13-030.

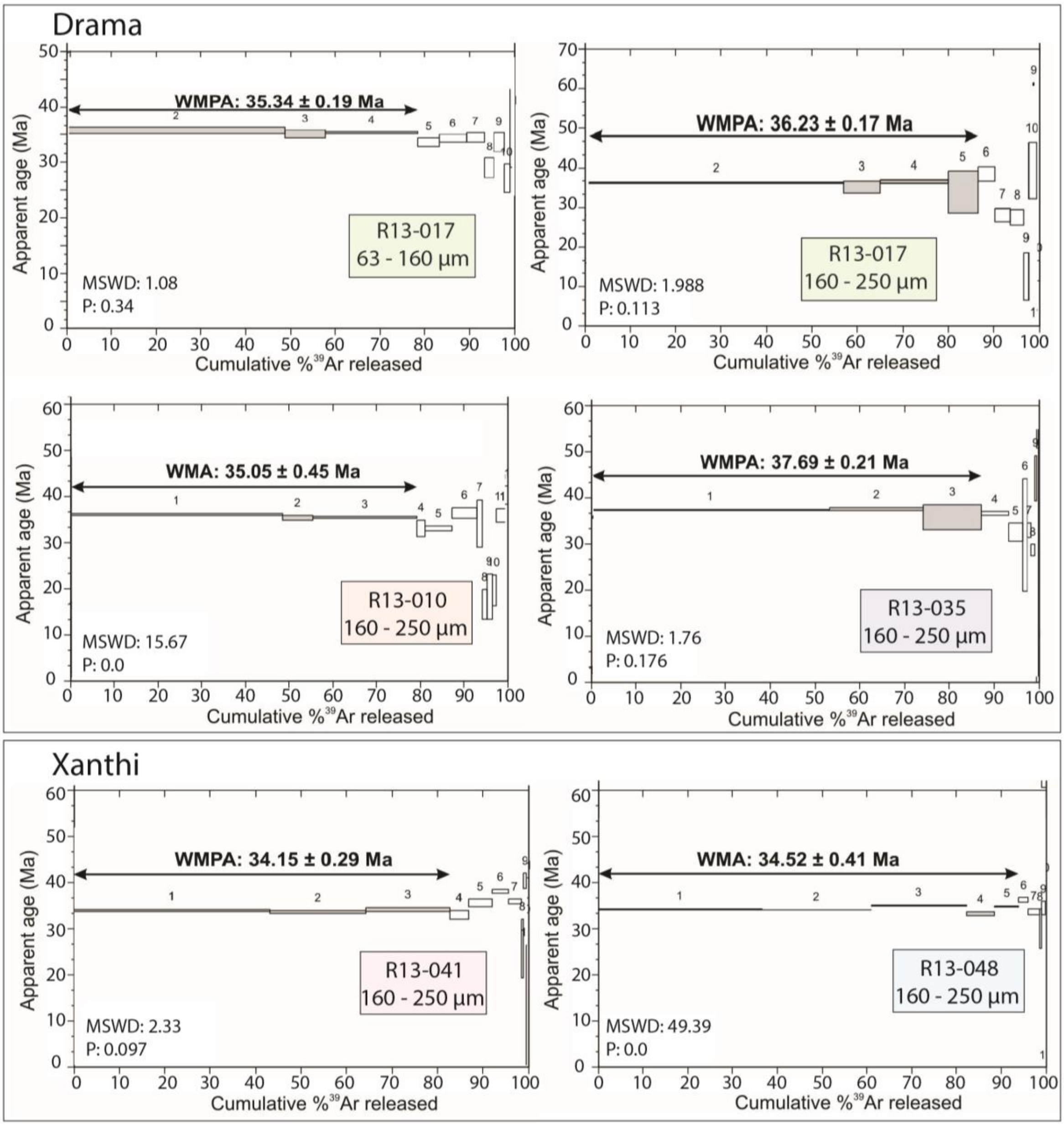

Appendix A.4. Representative ^{40}Ar/^{39}Ar step-heating ages. Uncertainties are given at 2σ level. (**a**) Drama-Sidironero section and (**b**) Xanthi region. Constant concentration profiles indicate no diffusion or later heating events. Plateau ages are similar for different grain sizes from same sample (*R13-017*). ^{40}Ar/^{39}Ar dating with step-heating technique was performed at the Geological Survey of Norway, Trondheim.

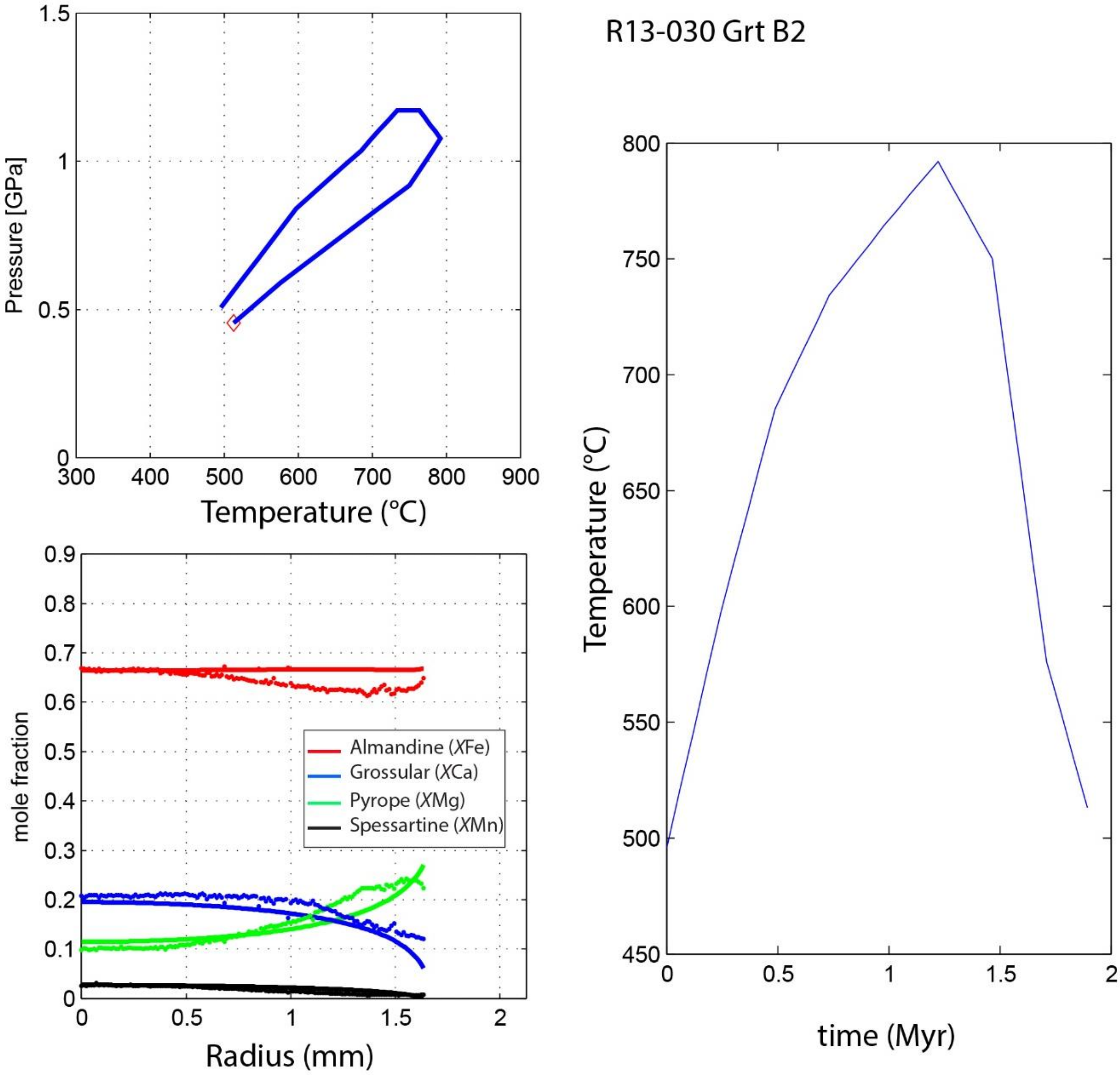

Appendix A.5. FRIDGE numerical model results for samples *R13-030* (Grt – B2), *R13-20* (Grt A), *R13-053* (Grt C1). *Left top*: estimated pressure-temperature-time (*P*-*T*-*t*) path from petrographic observation, phase diagram sections and *P*-*T* estimates. *Left bottom*: Result of garnet fractionation with diffusivity activated at *T* = 600 °C. *Right*: Temperature-time (*T*-*t*) diagram representing the duration (Myr) of peak-*T* conditions.

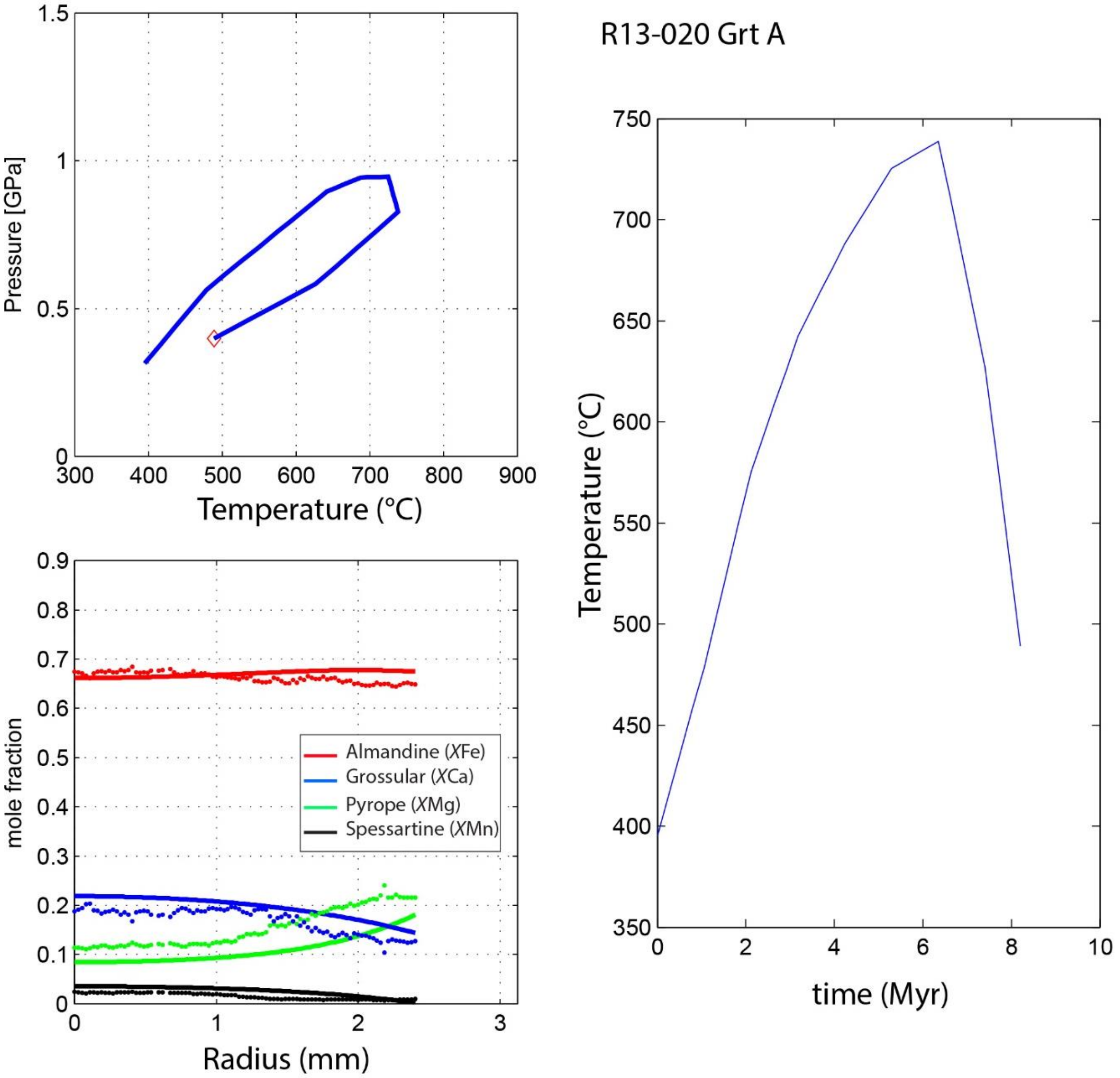

Appendix A.5. Continued

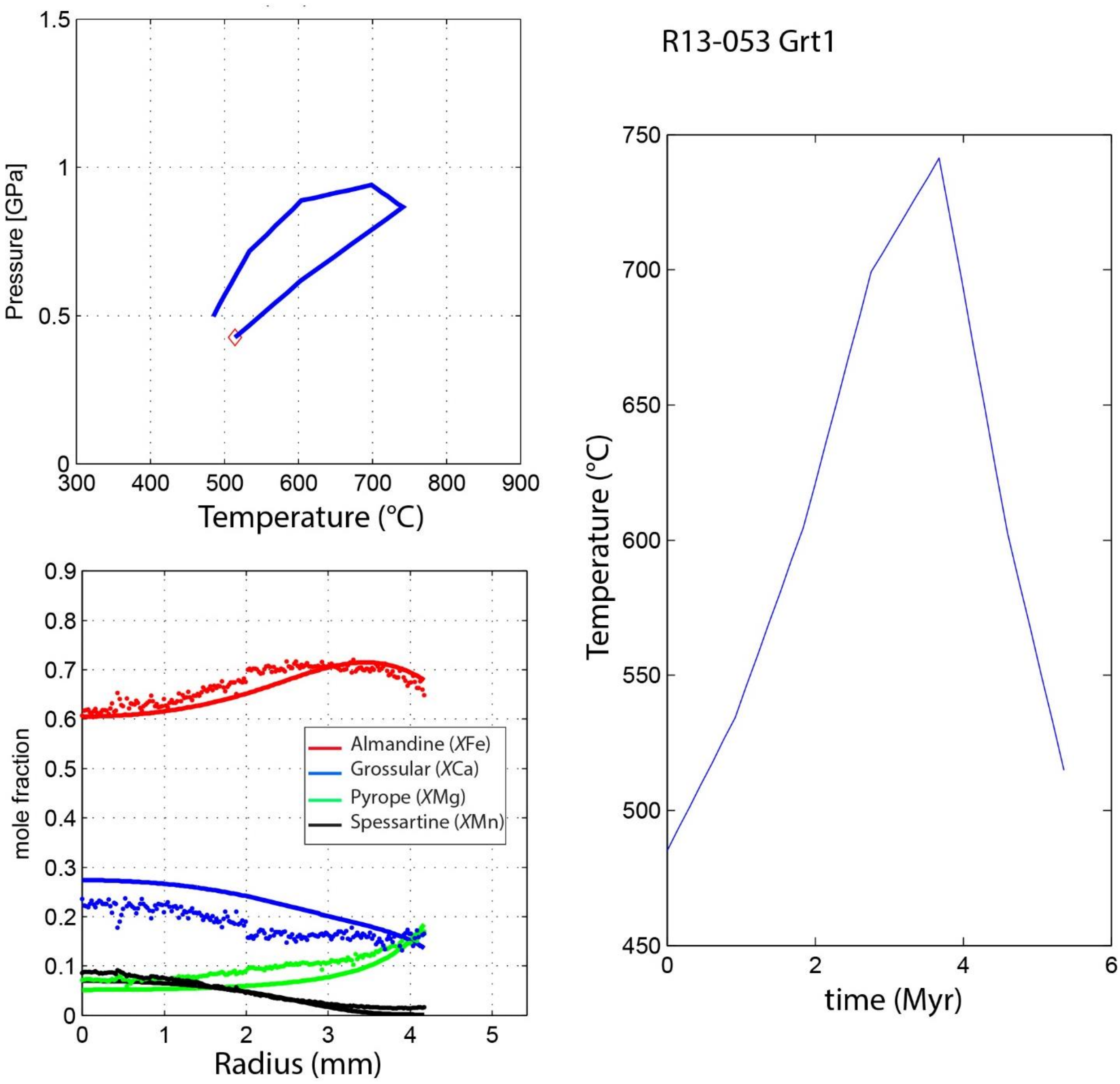

Appendix A.5. Continued

Appendix B

Supplementary material Chapter 3

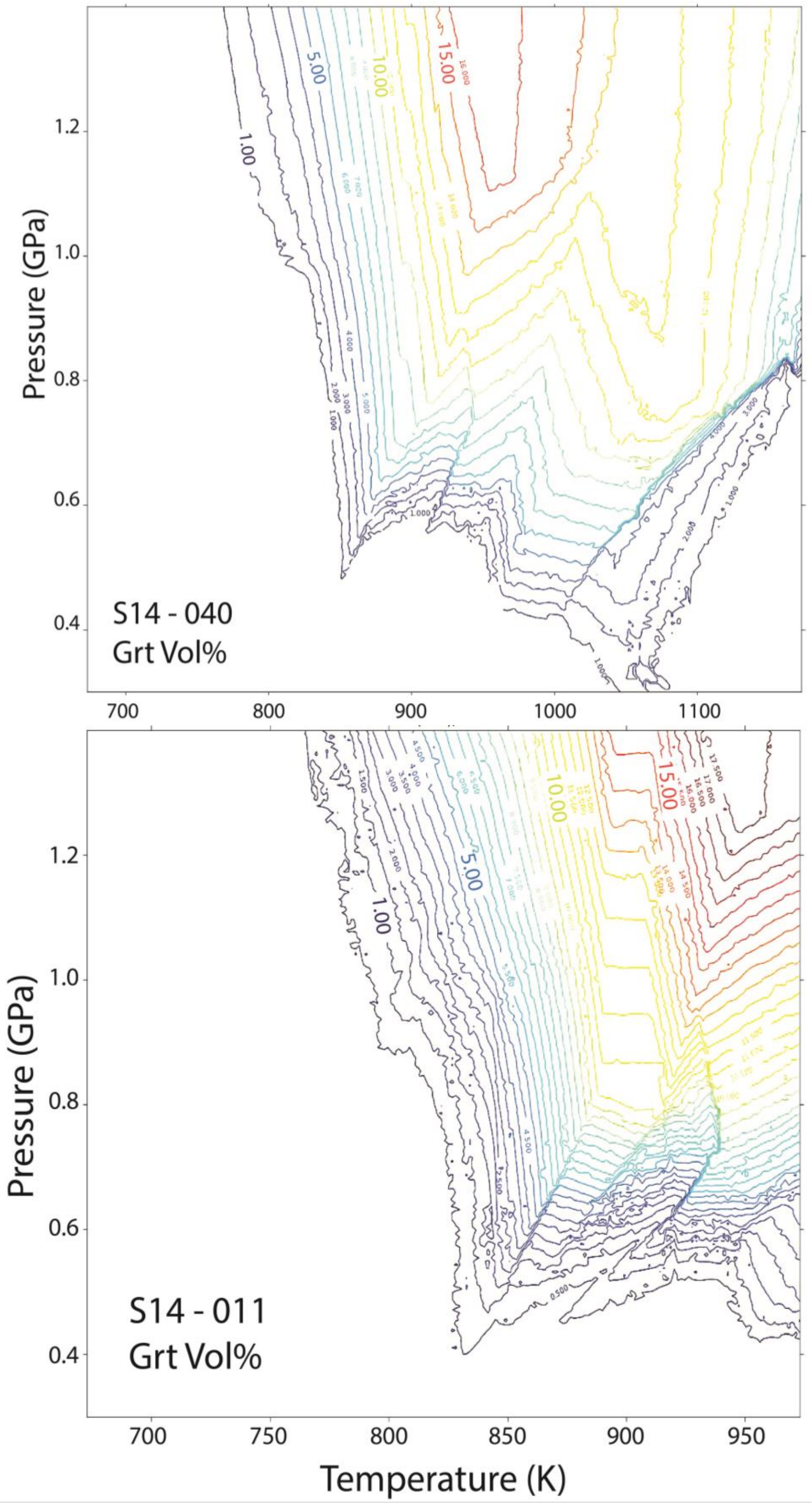

Appendix B.1. Garnet modal proportion (vol%)

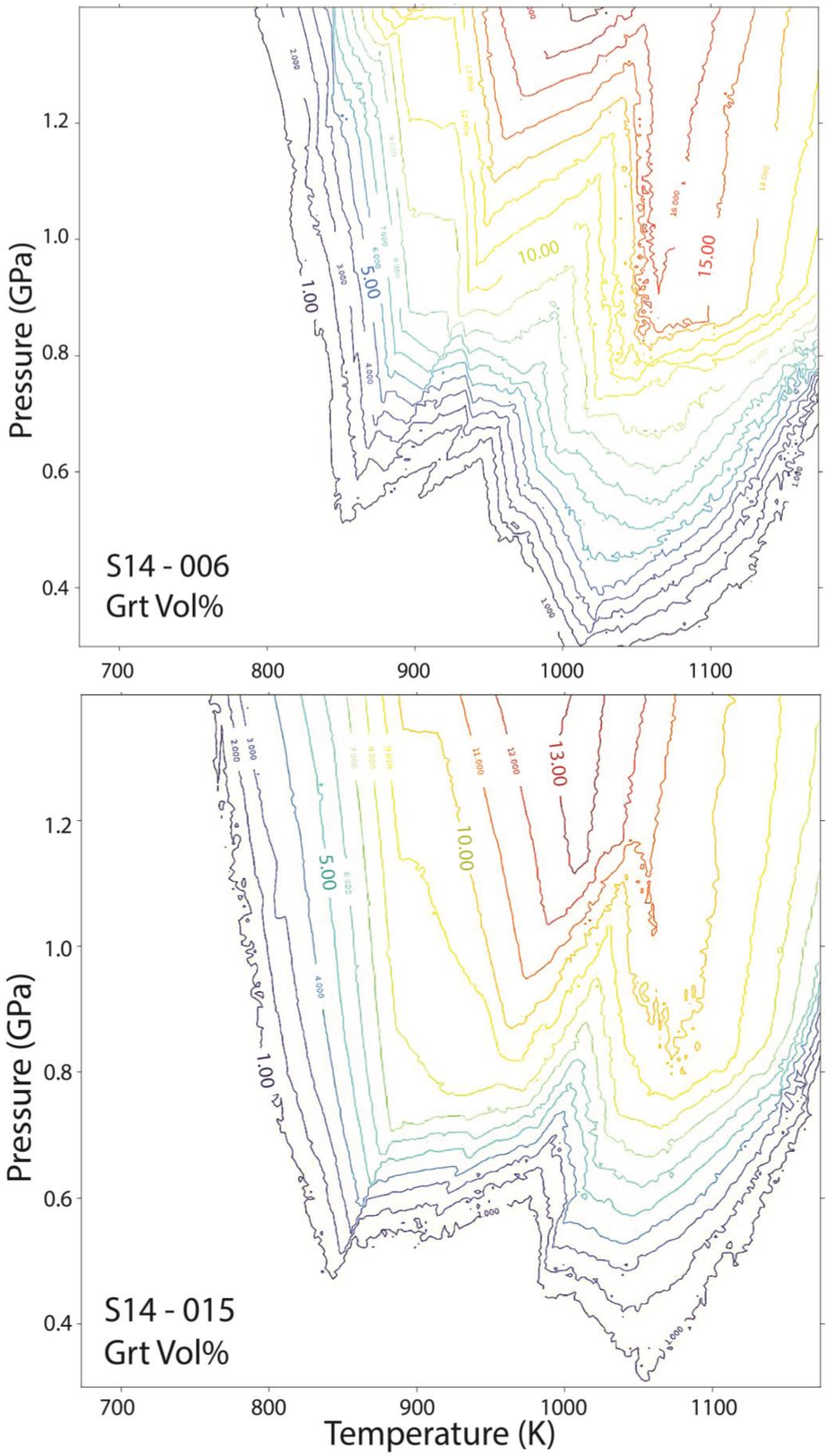

Appendix B.1. Continued

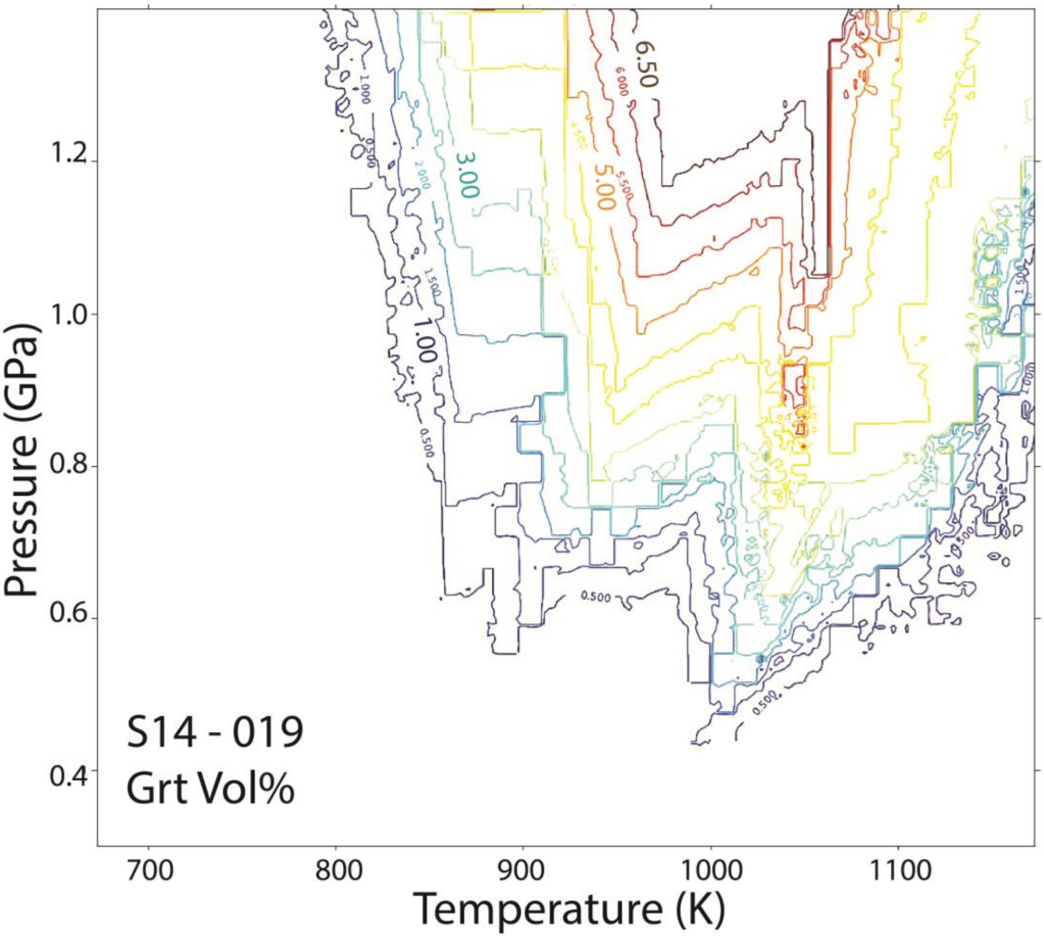

Appendix B.1. Continued

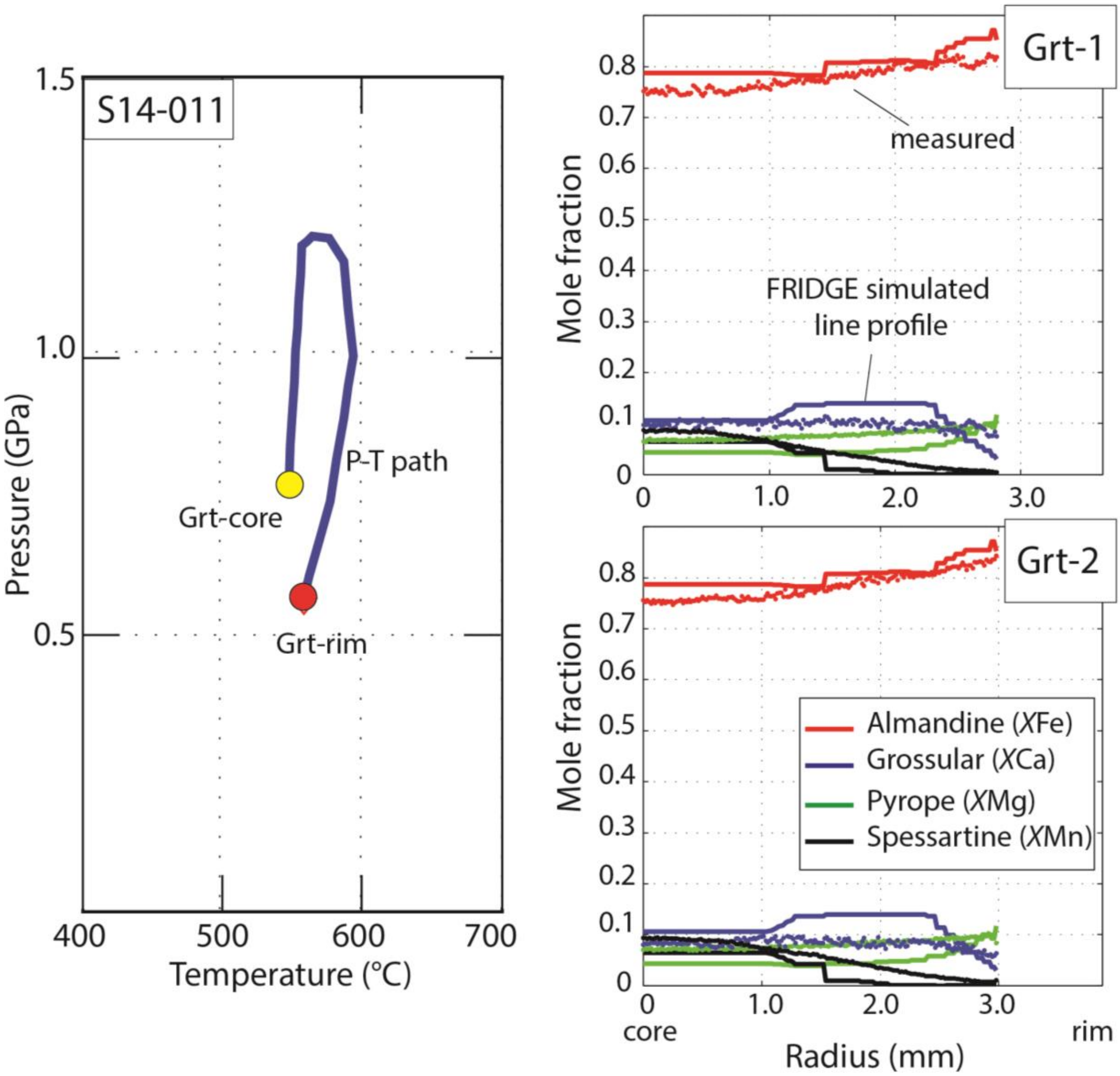

Appendix B.2. Representative FRIDGE results for sample *S14-011*. *Left*: given P-T path. Yellow dot: P-T conditions for garnet core (Grt-core) composition. Red dot: P-T conditions for garnet rim conditions (Grt-rim). *Right*: FRIDGE garnet compositional simulations, along the given P-T path, compared with measured garnet profiles of Grt-1 (top) and Grt-2 (bottom).

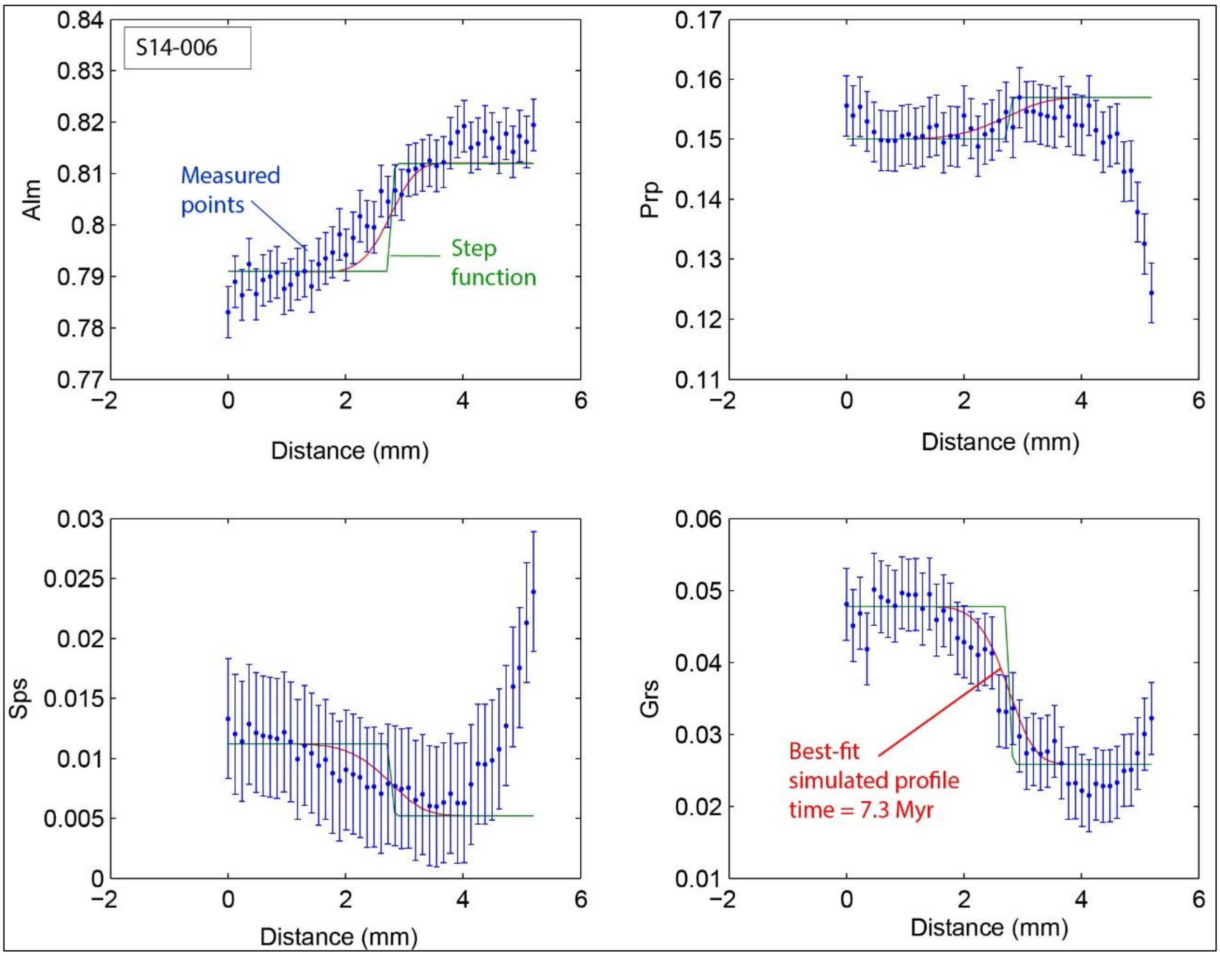

Appendix B.3. Representative diffusion modelling results for garnet S14-006 for almandine (Alm), pyrope (Prp), spessartine (Sps) and grossular (Grs) mole fraction (X). Step-function initial conditions (green line) for all major cations are treated dependent on each other. Red line: best-fit solutions at peak temperature of 640 °C. Best-fit solution for all components occurs at 1.2 Myr.

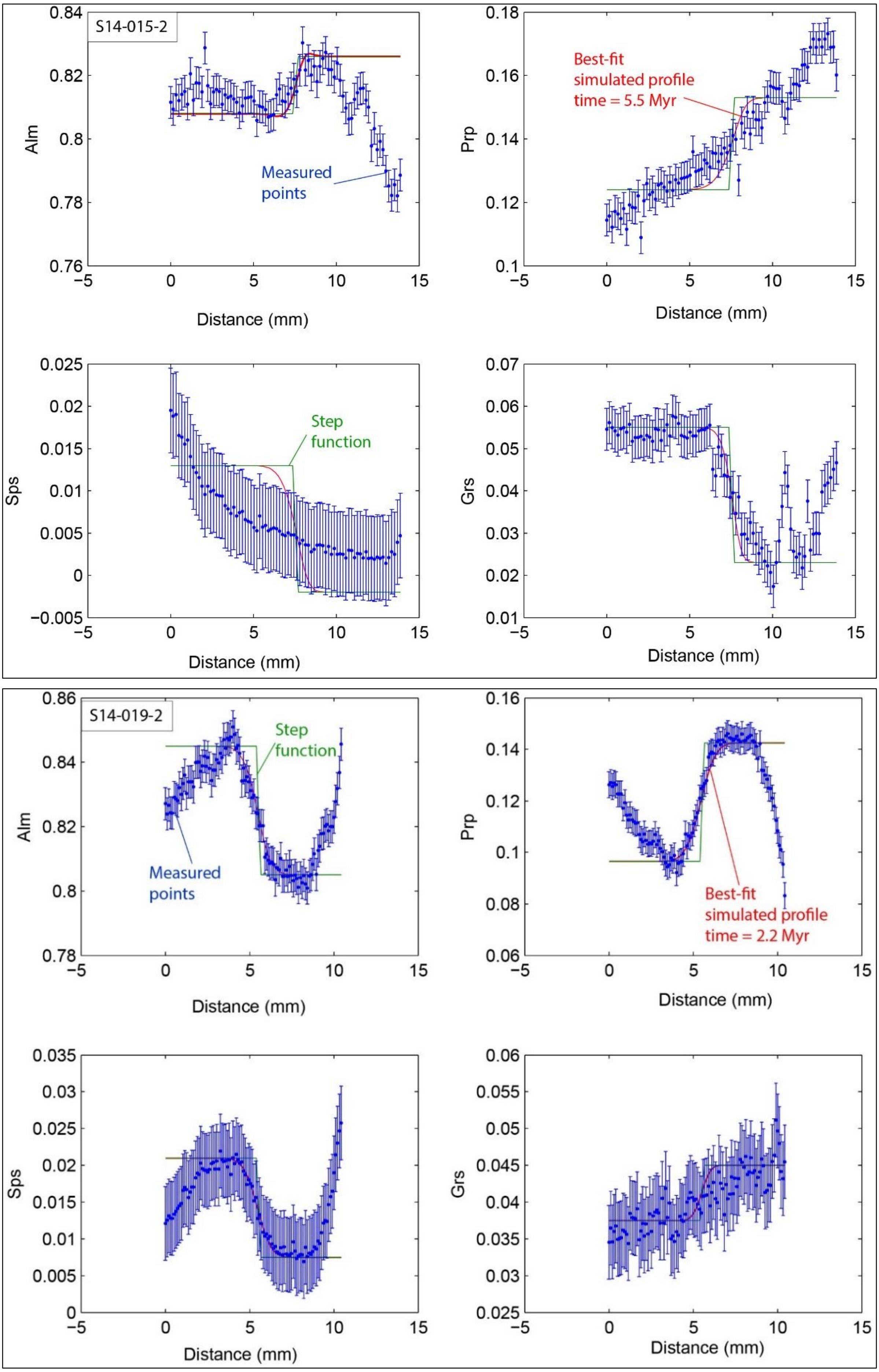

Appendix B.3. Continued

Appendix C

Supplementary material Chapter 4

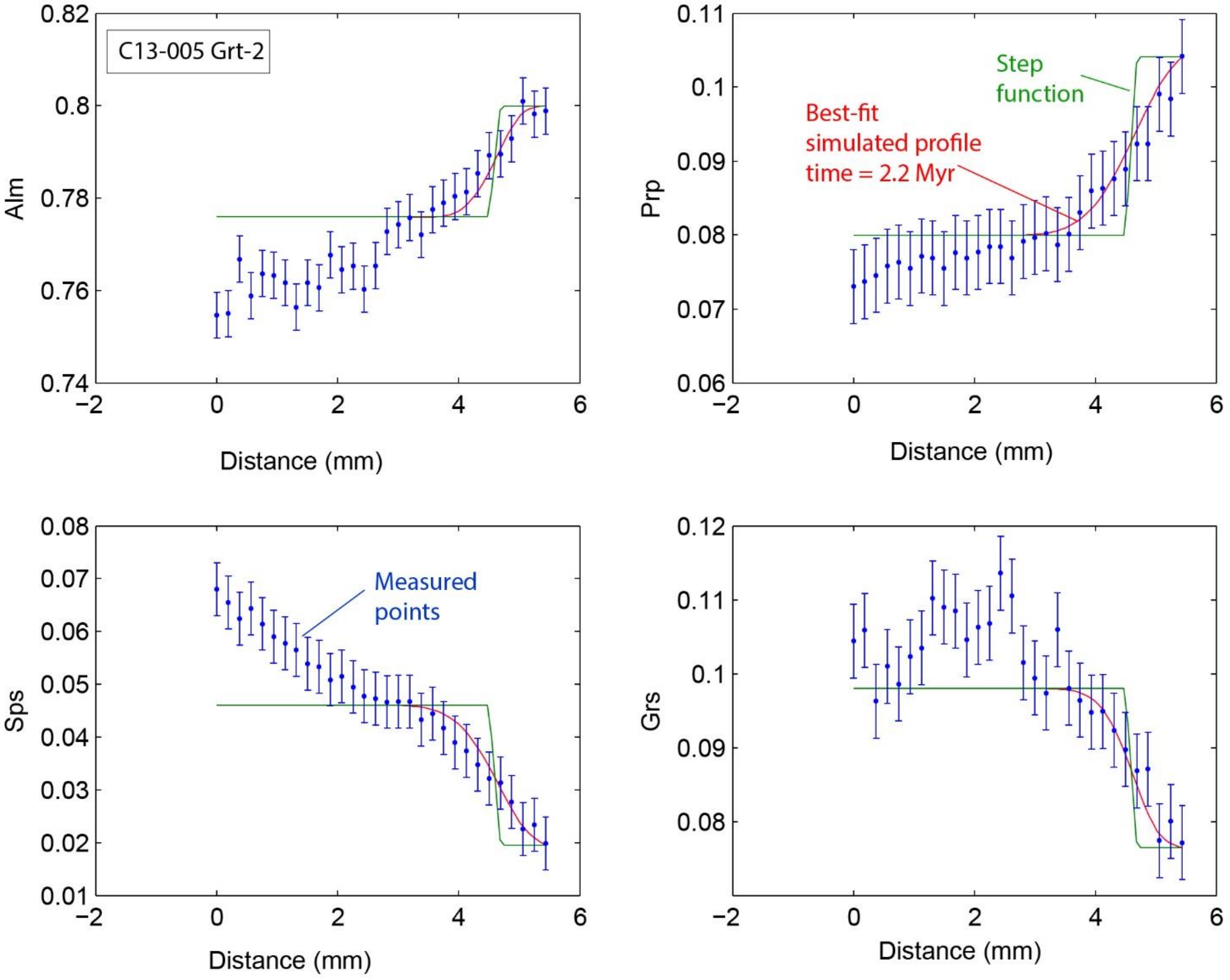

Appendix C.1. Representative diffusion modelling results for *C13-005* Grt-2 for almandine (Alm), pyrope (Prp), spessartine (Sps) and grossular (Grs) mole fraction (X). Step-function initial conditions (green line) for all major cations are treated dependent on each other. Red line: best-fit solutions at peak temperature of 640 °C. Best-fit solution for all components occurs at 2.2 Myr.

Acknowledgements

First I would like to thank Prof. Jean-Pierre Burg for giving me the opportunity to do a PhD thesis at the Geological Institute at the ETH. I am very grateful for the confidence and freedom he gave me during these years and for his help in the different field trips. I want also to thank Prof. Lucie Tajcmanová for the great help in organizing the Sikkim field trip and her extraordinary diplomatic performance to obtain the necessary visas.

My best thanks go to Vango for his fundamental help, the patience, the great user-monkey friendly numerical code and delicious *arnaki*. Thank you Marlon! Special acknowledgments are given to all the people that helped me during these years, especially Giuditta for introducing me the different mineral separation methods, Lydia for the efficient XRF analyses, Pirovino and Remy for the high quality thin sections, Nievi for his help with the microscope, Markus and Marcel for their support at the laser, Eric and Lukas for saving me from time to time at the microprobe and Dawid for the short SEM introduction.

I would like to thank Marilù for all the funny moments (che risate!). Pippo, for the precious support in the field and happy emergency landing. I am very grateful to Monica for introducing me John and Jamie. Sarete sempre nel mio cuore! Omar, for teaching me that “who goes slow and steady, wins”. Galli, for the geological and psycho(patho)logical support during these years, from the Insubric line to the Andes (belisim!). Grazie Andrew!

I want to thank Quinn Clinton for the help in improving my English and all the nice people of the group I met during these years: Nicola, Nima, Matteo, Sanjay, Marine, Alba (Comaneci), Claudio, Jonas, Daniela, Negar, Marie, Julien, Sarah, Beatrix, Richard, Neil, Marcel, Friedrich, Stephane, Wen, Rita, Shankar, Mahmoud, Sebastian (thanks for the conversations in Esperanto), Xiaoyu, Tomaso and Ingrid. But special thanks go to the “triple A”: Anna, Ali and Amaneh. Thank you my dear *jigar* friends for the loughs, beers and chips!

I would like to thank my dear friends Ghazy, Angi, Sheila, Pietro, Manuela and Patrick for their understanding and positive energy during these years in Zürich. Without you it would not be the same.

My heartfelt thanks go to my dear parents, Ramona and Gabriele, and my sister Natasha for the great patience, for supporting and always encouraging me. Vi voglio bene! Ora parto in viaggio!